METAL ORGANIC FRAMEWORKS AND CONDUCTING POLYMER BASED MATERIALS FOR ENERGY AND SENSING APPLICATIONS

Thesis Submitted to
the University of Calicut for the Award
of

DOCTOR OF PHILOSOPHY IN CHEMISTRY

By

ROOPASRI R

Under the Supervision of

Prof. YAHYA A. I.

DEPARTMENT OF CHEMISTRY UNIVERSITY

OF CALICUT

KERALA-673 635

FEBRUARY 2026

Department of Chemistry
University of Calicut
Malappuram, Kerala, India
673 635

Dr. Yahya A.I.
Professor

aiyahya@uoc.ac.in
Mob: 7558059506
https://www.intelligentpolymerlab.com/

CERTIFICATE

This is to certify that the thesis entitled **"Metal organic frameworks and conducting polymer based materials for energy and sensing applications"** submitted by **Roopasri R** to the University of Calicut for the award of the degree of Doctor of Philosophy in Chemistry, is an authentic record of research work carried out at the Department of Chemistry, of the University of Calicut under my guidance and supervision. The contents of the thesis have been checked for plagiarism using the software 'iThenticate,' and the similarity index falls under the permissible limit. I further certify that the thesis or part has not previously formed the basis for the award of any degree/diploma,/ associate ship of any other University or Institute.

I also certify that the adjudicators have not suggested any major changes or corrections in the scientific content, results and interpretations of the thesis. However, minor suggestions recommended by the examiners is incorporated in the revised thesis

University of Calicut

Dr. Yahya A.I.
Professor
Department of Chemistry
University of Calicut

DECLARATION

I, **Roopasri R**, hereby declare that the work presented in the thesis entitled **"Metal organic frameworks and conducting polymer based materials for energy and sensing applications"** is based on the original work done by me under the guidance of Dr**. Yahya A. I**, has not been included in any other thesis submitted previously for the award of any degree. The contents of the thesis are undergone a plagiarism check using 'iThenticate' software at C.H.M.K. Library, University of Calicut, and the similarity index found within the permissible limit. I also declare that the thesis is free from AI generated contents.

University of Calicut

Roopasri R

Dedicated to...

My Parents

Rajamany and Ambika

ACKNOWLEDGEMENT

I would like to express my deepest and most heartfelt gratitude to all those who stood beside me, supported me, and encouraged me throughout the journey of completing this doctoral dissertation. The path toward earning this PhD has been long and challenging, and I remain profoundly indebted to everyone who guided, inspired, and motivated me at every step. Words alone cannot fully express the depth of my appreciation and respect for the remarkable individuals whose unwavering support, constant encouragement, and belief in me made this achievement possible.

First and foremost, I express my deepest gratitude to my supervisor, ***Prof. Yahya A. I., Professor, Department of Chemistry, University of Calicut****, for his invaluable guidance, constant encouragement, and endless support throughout this research work. His profound knowledge, insightful suggestions, and inspiring mentorship greatly enriched my academic journey. I am truly thankful for the trust, freedom, and motivation he provided, which enabled me to complete this work successfully. It has been a great privilege and honor to work under his guidance.*

I would like to express my sincere gratitude to Dr. Binitha N., Head of the Department of Chemistry, and the former Heads of the Department for providing an excellent academic environment and the necessary facilities to carry out my research. I am also grateful to Dr. P. Raveendran professor and Honourable Vice Chancellor of the University of Calicut, Dr. Abraham Joseph, Dr. N. K. Renuka, and Dr. M. T. Ramesan for their valuable guidance, insightful suggestions, and constant encouragement. My appreciation extends to all the faculty members of the department for their support and inspiration.

I am deeply thankful to the laboratory assistants and other non-teaching staff for their invaluable help and cooperation. A special word of appreciation and love goes to all the present and former office staff and the department librarian, whose prompt and sincere assistance greatly facilitated my work.

I also acknowledge the financial assistance received from E-grantz, Govt.of Kerala. I extend my profound gratitude to CSIF, University of Calicut, CIF IISER TVM, STIC Kochi for carrying out the analyses necessary for my research work. I also convey my heartfelt thanks to Dr. Mohamed Shahin Thayyil, Professor, Department of Physics, University of Calicut, and his research group for their generous support in electrical characterization.

I am deeply thankful to my research group members, Dr. Shabeeba, Dr. Sidheekha, Dr. Lijin Rajan, Siva, Afi, Farsana, Madav, Anu, Sruthi, and Neethu, for their companionship, encouragement, and care, which made my research journey more memorable. I am especially indebted to Afi, whose warmth, kindness, and cheerfulness have made my journey more colourful. I extend my hearty thanks to our former M. Phil scholars, Geethu E R, Thasneem C, and Athira A for their valuable support. My loving appreciation goes to my project students Nithya, Mizna, and Shabeeh for their love, care and affection.

It is also a pleasure to acknowledge Dr. Deepak Joshy and Dr. Jijil C. P. for their enthusiastic support and for helping me in every possible way with their valuable advice throughout my Ph.D. I express my heartfelt thanks to my friends in the department, Amrutha T.P, Dheeraj, Anila, Linda, Sankar, Arathi, Anju, Gopika, Labeeba, Aysha, Amritha, Ritu, Arya, Sudhishna, Aswini, Anagha, Jai, Haritha, Dani and Saji who became my extended family. I extend my sincere gratitude to Meera Krishna for her love and sisterly care. I will always cherish those hostel days we shared, filled with endless conversations and laughter. I am deeply indebted to my friend Dr. Dipin T for the constant

support, genuine care, and invaluable help he extended, especially during the most challenging moments of this journey.

I express my profound gratitude to my dear friends Dr. Anjitha, Dr. Parvathi, Dr. Anjali, Dr.Neethudas, Manju and Aiswarya who have been my pillars of support since my degree days and have walked beside me throughout every stage of this journey. Their constant encouragement and genuine friendship have always been a source of strength in my life, and I remain forever grateful for their presence

This journey would not have been possible without my husband, Vicky, whose love, understanding, and unwavering support strengthened me through every challenge and inspired me to move forward. From the depths of my heart, I also express my most heartfelt gratitude to my beloved daughter, Anvika, whose innocent sacrifices, patience, and silent understanding gave me the courage to pursue my dreams. Her presence has been my greatest source of joy, motivation, and emotional strength, and every achievement of mine is deeply intertwined with her love. I also express my gratitude to my father-in-law and mother-in-law for their understanding, support, and care.

I fondly remember my beloved sister, Divya, whose love and constant support have always been a source of strength in my life. I am deeply grateful for her care and affection for my daughter, which helped me continue this journey with peace of mind. I also extend my heartfelt thanks to my brother-in-law, Jithin S. Anand, for his unwavering support and encouragement.

Above all, I offer in profound gratitude to my parents, Appa and Amma, whose unconditional love, selfless sacrifices, and constant prayers have been the very foundation of my life. Their unwavering faith in me gave me strength in moments of struggle and hope in times of uncertainty. Every step of this achievement is a reflection of their endless support, and I dedicate this success

with deepest love and reverence to them. Though many have not been mentioned, none is forgotten

Above all, I thank God Almighty, without whose blessings and mercy, I would never have completed this venture.

Roopasri R

ABSTRACT

Supercapacitors are promising energy-storage devices owing to their high power density, rapid charge-discharge capability, and excellent cycling stability, but their relatively low energy density limits their applications. This thesis focuses on the development of metal-organic frameworks (MOFs) and conducting polymer (CP)-based composites for energy storage, with the conducting polymer-based composites further investigated for self-sensing applications. We synthesised a nitrogen-enriched Ni MOF using polyvinylpyrrolidone (PVP) as a nitrogen source and morphology-directing agent. Polypyrrole (PPy) and polyaniline (PANI) were combined with nitrogen-doped graphene quantum dots (NGQDs) to improve their electrochemical stability. NGQDs were synthesized by a simple hydrothermal method using PPy as the precursor and incorporated into PPy and PANI matrices through chemical oxidative polymerization. Among the NGQDs/PPy composites, the NPP-50 composite exhibited a specific capacitance of 664 F g^{-1} at 0.8 A g^{-1}, an energy density of 90.2 Wh kg^{-1}, a power density of 600.4 W kg^{-1}, and 93% capacitance retention after 3000 cycles. Among the NGQDs/PANI composites, the NPA-25 composite achieved 947 F g^{-1} at 1 A g^{-1}, an energy density of 67.6 Wh kg^{-1}, a power density of 599.7 W kg^{-1}, and 94% retention after 3000 cycles. Furthermore, both composites demonstrated current-sensing capability, highlighting their potential for integrated energy-storage and sensing applications. Overall, the developed Ni MOF and NGQD-based conducting polymer composites show promise as multifunctional electrode materials for advanced supercapacitors and self-sensing devices.

Keywords: Supercapacitors, Conducting polymers, Cyclic Voltammetry, polyaniline, Polypyrrole

TABLE OF CONTENTS

		Page No.
Preface		i
List of abbreviations		vi
Chapter 1		**1 – 60**
Introduction		
1.	Introduction	1
1.1	Supercapacitors	1
1.1.1.	Comparison of supercapacitors with conventional capacitors and batteries	2
1.1.2.	Mechanism of energy storage supercapacitors	3
1.1.3.	Electrode materials commonly adopted in supercapacitor applications	6
1.2.	An overview of metal organic frameworks	7
1.2.1.	Historical background	8
1.2.2.	Linkers/ligands used in MOFs	9
1.2.3.	Transition metal ions	11
1.2.4.	Synthesis strategies of MOFs	12
1.2.5.	MOFs-based electrodes for supercapacitors	14
1.2.6.	Applications of MOFs	16
1.2.7.	Nickel metal-organic frameworks: A potential material for supercapacitors	18
1.3.	Conducting polymers	20
1.3.1.	Major Conducting Polymers	21
1.3.2.	Doping Mechanisms in Conducting Polymers	22

1.3.3.	Mechanistic insights into charge transport in conducting polymers	24
1.3.4.	Applications of conducting polymers	26
1.4	Polypyrrole: A Concise Historical Perspective	27
1.4.1.	Structure of polypyrrole	28
1.4.2.	Synthesis of polypyrrole	29
1.4.3.	Doping in polypyrrole	30
1.5.	Polyaniline (PANI)	31
1.5.1.	Structure of polyaniline	32
1.5.2.	Doping in polyaniline	33
1.5.3.	Various synthesis routes for polyaniline	34
1.5.4.	Conducting polymer based supercapacitors	35
1.6.	Graphene Quantum Dots (GQDs)	36
1.6.1.	Nitrogen-doped Graphene quantum dots (NGQDs)	36
1.6.2.	Synthesis of GQDs and NGQDs	37
1.7	Polypyrrole/carbon nanostructure composites for supercapacitor applications	38
1.8	Polyaniline/carbon nanostructure composites for supercapacitor applications	40
1.9	A comprehensive overview of conducting polymer electrochemistry	41
	References	45
Chapter 2		**61 – 79**
Materials and methods		

2.1. Materials 61

2.2. Synthetic methods 62

2.2.1. Synthesis of Ni MOF and N-Ni MOF 62

2.2.2. Synthesis of polypyrrole 63

2.2.3. Synthesis of NGQDs 63

2.2.4. Synthesis of NGQDs/PPy composites 64

2.2.5. Synthesis of NGQDs/PANI Composites 65

2.3. Characterization techniques 66

2.3.1. Fourier Transform Infrared (FTIR) Spectroscopy 66

2.3.2. X-Ray diffraction Analysis (XRD) 66

2.3.3. UV-Visible Spectroscopy 67

2.3.4. UV-Visible-NIR Diffuse Reflectance Spectroscopy (DRS) 67

2.3.5. Raman Spectroscopy 68

2.3.6. Field Emission Scanning Electron Microscopy (FE-SEM) 69

2.3.7. Energy dispersive X-ray spectroscopy (EDX) 69

2.3.8. High Resolution Transmission Electron Microscopy (HR-TEM) 70

2.3.9. Conductivity studies 70

2.3.10 Photoluminescence spectroscopy (PL) 71

2.3.11 Brunauer-Emmett-Teller analysis (BET) 71

2.3.12 X-ray photoelectron spectroscopy (XPS) 72

2.4. Electrochemical Characterizations 72

2.4.1. Cyclic voltammetry (CV) 73

2.4.2. Galvanostatic Charge-Discharge(GCD) 74

2.4.3. Electrochemical Impedance Spectroscopy(EIS) 76

2.4.4 Chronopotentiometry 76

2.5 Fabrication of a symmetric supercapacitor device 77

References 78

Chapter 3 **80 – 106**

Polyvinylpyrrolidone Assisted Synthesis of Ni MOF as an Electrode Material for Supercapacitor Applications

3.1. Introduction 80

3.2. Results and Discussion 81

3.2.1. XRD Analysis 81

3.2.2. FTIR Spectroscopy 82

3.2.3. DRS spectra 83

3.2.4. SEM and TEM Analysis 84

3.2.5. EDX Spectral Analysis 85

3.2.6. BET Surface area analysis 86

3.2.7. Contact angle 88

3.2.8. XPS Analysis 88

3.2.9. Electrochemical characterization 90
3.2.9.1. Cyclic voltammetry 90
3.2.9.2. Charge storage kinetic studies 91
3.2.9.3. Galvanostatic charge-discharge studies 93
3.2.9.4. Electrochemical impedance spectra 95
3.2.9.5. Cyclic stability 96
3.2.9.6. Symmetric supercapacitor device 97
3.3. Conclusion 100
References 100

Chapter 4 **107 – 145**

Polypyrrole Derived Nitrogen-Doped Graphene Quantum Dots /Polypyrrole Composites for High Energy Density Supercapacitor

4.1. Introduction 107
4.2. Results and Discussion 109
4.2.1. HR-TEM Analysis 110
4.2.2. SEM Analysis 112
4.2.3. UV-Visible absorption and PL spectral analysis 113
4.2.4. FTIR and Raman spectra 115
4.2.5. XRD Analysis 118
4.2.6. Conductivity studies 119

4.2.7. XPS Analysis 120

4.2.8. BET Surface area Analysis 123

4.2.9. Electrochemical Analysis 125

4.2.10. Symmetric supercapacitor device 135

4.3. Conclusions 138

References 139

Chapter 5 **146 – 173**

Polypyrrole Derived Nitrogen-Doped Graphene Quantum Dots/Polyaniline Composites for Supercapacitor Applications

5.1. Introduction 146

5.2. Results and Discussion 146

5.2.1. TEM Analysis 147

5.2.2. FTIR Analysis 147

5.2.3. XRD Analysis 148

5.2.4. UV-Visible Absorption spectra 149

5.2.5. SEM Analysis 150

5.2.6. Conductivity Studies 152

5.2.7. XPS Analysis 153

5.2.8. BET Surface area Analysis 154

5.2.9. Electrochemical Characteristics 155

5.2.10 Symmetric supercapacitor device 165

5.3. Conclusion 168

References 168

Chapter 6

NGQDs integrated Polypyrrole and Polyaniline as Sensors of Electrical Energetic Condition **174 – 190**

6.1. Introduction 174

6.2. Results and Discussion 176

6.2.1. Coulovoltammogram of NGQDs/PPy composites 176

6.2.2. Sensing working electrical energetic condition: Current Sensor 177

6.2.3. Theoretical description 180

6.2.4. Coulovoltammogram of NGQDs/PANI Composites 184

6.2.5. Sensing working electrical energetic condition: Current Sensor 185

6.3. Conclusion 188

References 188

Chapter 7

Conclusions and Future Outlook **191 -194**

List of publications and presentations 195

Preface

Energy forms the foundation of modern society, powering industries, economic growth, and daily activities. As global attention increasingly shifts toward sustainable and efficient energy solutions, the need for advanced energy storage technologies has become more significant than ever. Among the various energy storage systems, supercapacitors have gained considerable prominence for applications such as electric vehicles, portable electronics, and industrial equipment. Supercapacitors, in particular, have attracted great interest due to their high power density, excellent cyclic stability, and rapid charge-discharge capability, making them highly suitable for applications that demand frequent and instantaneous energy delivery. The performance of supercapacitors largely depends on factors such as electrode material, electrolyte composition, and electrode surface area. Consequently, the design and engineering of advanced electrode materials, especially metal organic frameworks (MOFs) and conducting polymers (CPs), play a crucial role in enhancing key performance parameters, including specific energy, power density, and cyclic stability. Furthermore, the growing demand for flexible energy storage devices, particularly for wearable technologies, has opened new research avenues, highlighting the importance of developing novel and efficient materials.

Metal-organic frameworks are promising electrode materials because of their high surface area, porous structure, and tunable properties. Their large surface area provides more active sites for charge storage, while their three-dimensional porous network enables efficient ion transport, enhancing supercapacitor performance. Although MOFs face challenges such as low electrical conductivity and limited cyclic stability. Recent advances show that

functionalization with heteroatoms has improved their electrochemical behavior. These developments highlight the potential of MOFs for future flexible energy storage applications, especially in wearable and portable devices.

Conducting polymers have emerged as a promising field of research due to their remarkable electrical conductivity, distinctive structural features, and potential to form innovative composite materials with exceptional properties. Their diverse applications range from optoelectronics to materials science. The present research primarily focuses on the development of novel CP-based composites as electrode materials for supercapacitor applications. Polypyrrole (PPy) and polyaniline (PANI) are being explored and developed as possible candidates for supercapacitor applications due to their ease of synthesis, environmental stability, excellent biocompatibility, tunable electrical conductivity, and strong redox behavior. During repeated charge-discharge cycles, PPy and PANI undergo mechanical stress and volumetric changes, leading to cracking, loss of conductivity, and degradation of their electrochemical properties. To overcome these limitations PPy and PANI were composited with novel nitrogen doped graphene quantum dots (NGQDs) and explored as an electrode for supercapacitor applications

Beyond their role in energy storage, conductive polymers have attracted considerable interest in the scientific community due to their unique electrical and electrochemical properties, which enable a wide range of applications. Most of these applications have focused on their behavior as dry materials, where their composition remains constant. However, in the wet state, conductive polymers (CPs) behave like gels, and their properties are largely governed by their composition. This thesis focuses on investigating the composition-dependent, properties of CPs, aiming to demonstrate their

inherent biomimetic reactive sensing characteristics under various electrochemical reaction conditions. The ultimate goal is to contribute to the realization of devices or self-sensing motors that can simultaneously sense their surrounding environment while operating, without the need for additional connections. While our research group has previously established the reactive sensing capabilities of polypyrrole and polyaniline, this study aims to demonstrate that composites of polypyrrole and polyaniline with nitrogen-doped graphene quantum dots also exhibit similar reactive sensing properties.\

The thesis is divided into 7 Chapters

Chapter 1 provides a general introduction to the present work, including details on the importance of supercapacitors. A detailed description of electrode materials such as MOFs, PPy, PANI and NGQDs. The comprehensive overview of electrochemistry of conducting polymers for sensing application also briefly described.

Chapter 2 presents the materials, experimental procedures, and characterization techniques employed throughout this study. It describes the synthesis methods for MOFs, NGQDs, NGQDs/PPy, and NGQDs/PANI composites, along with the fabrication of symmetric supercapacitor devices. In addition, the experimental approach adopted for sensing studies is discussed, providing the methodological approaches for the investigations presented in the subsequent chapters.

Chapters 3 to 6 are the working chapters focusing on our research objectives.

Chapter 3 presents the synthesis, characterization, and electrochemical evaluation of nitrogen-enriched Nickel-based metal-organic frameworks (Ni MOFs) for supercapacitor applications. The chapter focuses on enhancing the electrochemical performance of Ni MOFs by incorporating nitrogen through

polyvinylpyrrolidone (PVP), which acts both as a nitrogen source and a morphology-directing agent. The influence of nitrogen incorporation on the structural, morphological, and electrochemical properties of the prepared materials is systematically investigated. Furthermore, the chapter discusses the improvement in specific capacitance and cyclic stability of the modified Ni MOF, highlighting its potential as an efficient electrode material for high-performance energy storage devices.

Chapter 4 describes the synthesis and electrochemical evaluation of NGQDs/PPy composite electrodes for supercapacitor applications. The chapter focuses on overcoming the limitations of PPy by incorporating NGQDs to improve conductivity, charge transport, and cyclic stability. It discusses the preparation of NGQDs through a one-step hydrothermal method and examines the structural and electrochemical performance of the resulting composite, highlighting its potential for advanced energy storage applications.

Chapter 5 presents the synthesis and electrochemical investigation of NGQDs/PANI composites for supercapacitor applications. Extending the work of the previous chapter, this study focuses on improving the cyclic stability and electrochemical performance of PANI by incorporating NGQDs. The composites were synthesized via chemical oxidative polymerization, and their structural and electrochemical properties were systematically analyzed. The enhanced specific capacitance, rate performance, and cyclic stability of the NGQDs/PANI composites demonstrate their potential as efficient electrode materials for next-generation energy storage devices.

Chapter 6 investigates the reactive sensing behavior of NGQDs based conducting polymer composites, specifically NGQDs/PPy and NGQDs/PANI. Building on the supercapacitive performance discussed in the previous chapters, this chapter explores their ability to respond to changes in

electrical energetic conditions and function as current sensors. The current sensing properties of NGQDs/PPy and NGQDs/PANI composites are systematically examined for the first time, highlighting their potential for the development of soft, wet, and reactive sensing devices.

Chapter 7 provides an overview of the key findings and significant outcomes of the present study. It summarizes the major discoveries and discusses the future prospects of the research. In addition, the chapter explores the potential applications of the developed system in self-sensing motors.

LIST OF ABBREVIATIONS

SCs	*Supercapacitors*
EDLC	*Electrical Double Layer Capacitors*
HSC	*Hybrid Supercapacitors*
BDS	*Broadband Dielectric Spectroscopy*
MOFs	*Metal organic frameworks*
COFs	*Covalent organic frameworks*
CPs	*Conducting polymers*
PA	*Polyacetylene*
PP	*Poly (para-phenylene)*
PPy	*Polypyrrole*
PANI	*Polypyrrole*
PEDOT	*Poly (3,4-ethylenedioxythiophene)*
PIN	*Polyindole*
PTh	*Polythiophene*
PQ	*Polyquilonine*
CNT(s)	*Carbon Nanotube(s)*
AC	*Activated carbon*
CSD	*Cambridge Structural Database*
RCSR	*Reticular Chemistry Structure Resource*
ZIFs	*Zeolitic imidazolate frameworks*
MIL	*Materials of the Institute Lavoisier*
BDC	*Benzene-1,4-dicarboxylic acid*
BPC	*4,4'-biphenyldicarboxylic acid*
BPYDC	*2,2'-Bipyridine-5,5'-dicarboxylic acid*
HITP	*2,3,6,7,10,11-hexaiminotriphenylene*
HTTP	*2,3,6,7,10,11-hexathiotriphenylene*
CVD	*Chemical Vapour Deposition*
ICP(s)	*Intrinsically conducting polymer(s)*
GQDs	*Graphene quantum dots*
NGQDs	*Nitrogen-doped graphene quantum dots*
CQDs	*Carbon quantum dots*
CDs	*Carbon dots*
GO	*Graphene oxide*
rGO	*Reduced graphene oxide*

CV(s)	*Cyclic Voltammogram(s)*
APS	*Ammonium persulfate*
DMF	*Dimethy formamide*
EDX	*Energy Dispersive X-ray Spectroscopy*
EIS	*Electrochemical Impedance Spectroscopy*
ES	*Emeraldine Salt*
ESCR	*Electrochemically Stimulated Conformational Relaxation*
AC	*Alternating current*
DC	*Direct current*
FESEM	*Fourier Transform Scanning Electron Microscopy*
FTIR	*Fourier Transform Infra-red spectroscopy*
GCD	*Galvanostatic Charge-Discharge*
GCE	*Glassy Carbon Electrode*
HOMO	*Highest Occupied Molecular Orbital*
HR-TEM	*High-Resolution Transmission Electron Microscope*
ITO	*Indium tin oxide*
LE	*Leucoemeraldine*
Cu MOF	*Copper metal organic frameworks*
Ni MOF	*Nickel metal organic frameworks*
N-Ni MOF	*Nitrogen-enriched Ni MOF*
PVP	*Polyvinyl pyrrolidone*
PVA	*Polyvinyl alcohol*
C_{sp}	*Specific capacitance*
NPP	*Nitrogen-doped graphene quantum dots/ Polypyrrole composites*
NPA	*Nitrogen doped graphene quantum dots/ Polyaniline composites*
LED(s)	*Light Emitting Diode(s)*
QV	*Coulovoltammogram*
RE	*Reference Electrode*
TGA	*Thermogravimetric Analysis*
WE	*Working Electrode*

Chapter 1

Introduction and Literature Review

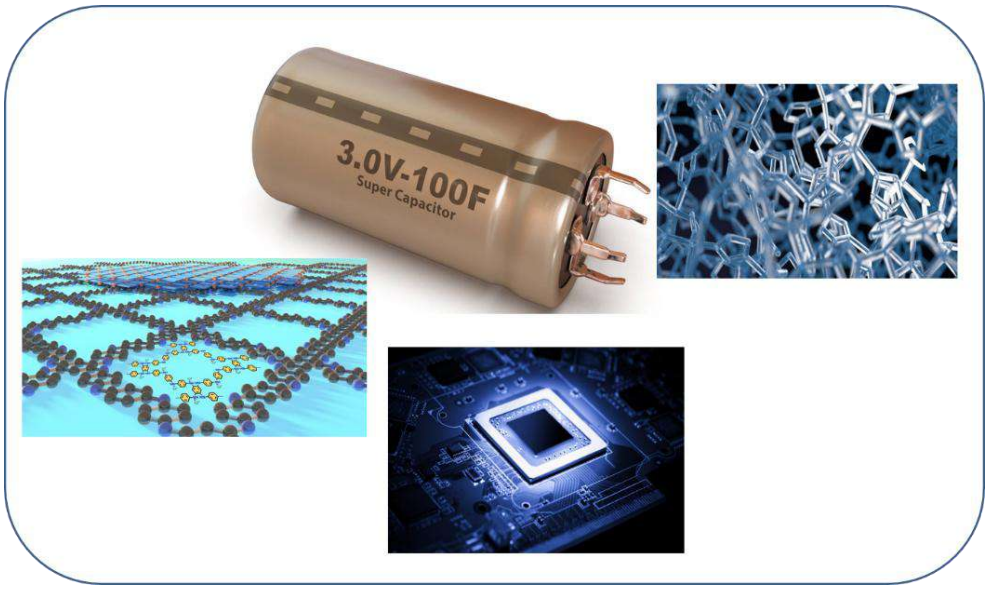

This chapter begins by highlighting the importance of energy storage devices, with particular emphasis on supercapacitors. A concise overview of supercapacitors and their operating mechanisms is presented. Various electrode materials, including metal-organic frameworks, conducting polymers such as polypyrrole and polyaniline, and their composites with nitrogen-doped graphene quantum dots, are discussed. In addition, the scope of biomimetic current-sensing applications of conducting polymer composites is briefly addressed. A comprehensive literature survey on these materials is incorporated in this chapter.

The growing energy demands of modern society, along with increasing environmental concerns, have increased the search for alternative energy sources. Developing clean and sustainable energy systems requires the integration of innovative technologies with reliable methods of energy conversion and storage [1]. While renewable energy sources such as solar, wind, hydro, and ocean energy are widely exploited, their intermittent nature highlights the need for advanced storage technologies [2, 3]. Different energy storage devices, including capacitors, supercapacitors, batteries, and fuel cells, have been developed. Among these, supercapacitors play a crucial role in the scientific community.

1.1. Supercapacitors

Supercapacitors (SCs), also called ultracapacitors or electrochemical capacitors [4]. Due to their simple operating mechanisms, remarkable cyclic stability (exceeding 1 million cycles), fast charge-discharge kinetics, and high power efficiency, SCs are considered a promising alternative in energy storage research. Compared to traditional capacitors, SCs provide excellent power densities but suffer from low energy densities, whereas batteries, though offering superior energy storage capacity, are hindered by slower energy delivery rates [5, 6]. SCs are emerging as an intermediate energy storage solution, effectively bridging the gap between conventional capacitors and electrochemical batteries [7].

Today, supercapacitors are used in a wide range of applications, from energy storage and consumer electronics to industrial power systems, and memory backup devices. An example is their role in the emergency doors of Airbus, which highlights their importance in critical situations where rapid energy delivery is essential. As research and technology continue to advance, supercapacitors are expected to play an even bigger role in next-generation

energy storage, potentially challenging the dominance of traditional batteries [8, 9].

1.1.1. Comparison of supercapacitors with conventional capacitors and batteries

Simply, supercapacitors are devices that store energy with high capacity and lower internal resistance than conventional capacitors. Unlike batteries, they can be rapidly charged and deliver longer cycles without significant loss of performance.

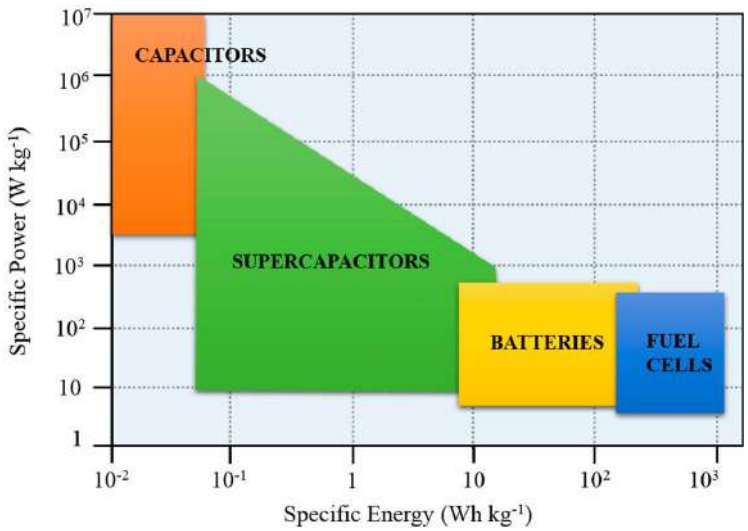

Figure 1.1 *Ragone plot for different energy storage devices [10]*

The performance of an energy storage device is evaluated by using parameters such as charge-discharge duration, cycle life, energy density and power density. The energy density (amount of energy stored per unit mass) and power density (amount of energy delivered per unit mass) can be calculated using the following formula,

$$E = \frac{0.5 \times C \times V^2}{3.6} \quad (1.1)$$

$$P = \frac{3600 \times E}{t} \quad (1.2)$$

In these equations, t (s) refers to the discharge time, while V (V) indicates the applied potential window during operation. The Ragone plot shows the relationship between energy density and power density that compares the performance of various energy storage devices, as shown in Figure 1.1.

1.1.2. Mechanism of energy storage in supercapacitors

The operation of supercapacitors can be explained through three distinct charge storage mechanisms, as shown in Figure 1.2.

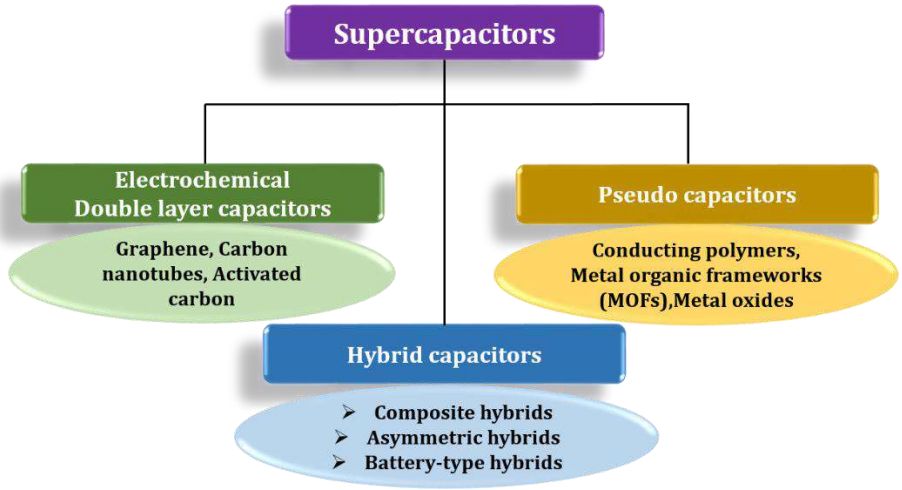

Figure 1.2 *Classification of different types of supercapacitors*

a) Electrochemical double-layer capacitors

The energy storage mechanism involves electrostatic accumulation of charges at the electrode-electrolyte interface without any faradaic reactions [11-14]. When a potential is applied, ions from the electrolyte migrate toward oppositely charged electrodes, forming two parallel layers of charge: one on the electrode surface and the other in the electrolyte, thereby acting as capacitor for energy storage. This process is characterized by the rapid

adsorption and desorption of ions. This resulting in excellent power performance due to fast charge-discharge kinetics [15]. The schematic representation of EDLC is shown in Figure 1.3 (a).

The concept of the electrical double layer was first proposed by Helmholtz (1853), who visualised it as two parallel sheets of opposite charge separated by a fixed distance comparable to the ionic radius. Later, the Gouy-Chapman refined this idea by incorporating the effect of thermal motion of ions, describing a *diffuse layer* in which ion concentration gradually decreases with distance from the electrode surface according to Boltzmann statistics. Subsequently, the Stern model combined both approaches, retaining the compact, immobile layer of specifically adsorbed ions (Helmholtz layer) near the electrode, and adding a diffuse region of mobile solvated ions extending into the electrolyte. Thus, in the Stern model, the EDL consists of two distinct regions: the Stern layer**,** which represents a compact zone of specifically adsorbed ions located directly on the electrode surface, and the diffuse layer**,** which consists of thermally agitated and solvated ions that gradually extend away from the electrode into the bulk of the electrolyte [16, 17].

b) Pseudocapacitors

In pseudocapacitors, a faradaic process (redox reactions) occurs at the electrode-electrolyte interface. Thus, the charge storage functions through electrosorption, reversible redox reactions, and faradaic charge transfer occurring at or near the electrode surface [18]. During the charging process, ions from the electrolyte engage in redox reactions with the electrode material; for example, in MOFs, metal ions can reversibly shift between oxidation states. When an external potential is applied to a pseudocapacitor, specifically adsorbed electrolyte ions migrate into the electric double layer

and undergo charge transfer with the electrode surface. The schematic diagram depicting a pseudocapacitor is shown in Figure 1.3 (b). The electrode materials used are redox-active and capable of fast, reversible reactions with electrolyte ions, including conducting polymers [19], transition metal oxides [20], layered double hydroxides (LDHs) [21], metal nitrides [22], and porous crystalline materials such as MOFs [23] and covalent organic frameworks (COFs) [24]. Owing to these mechanisms, pseudocapacitors combine the advantages of electrochemical double-layer capacitors (EDLCs) and batteries, offering higher energy densities than EDLCs, quick charge-discharge rates, enhanced specific power and energy, long cycle life, and improved safety, making them highly suitable for advanced energy storage applications [25, 26].

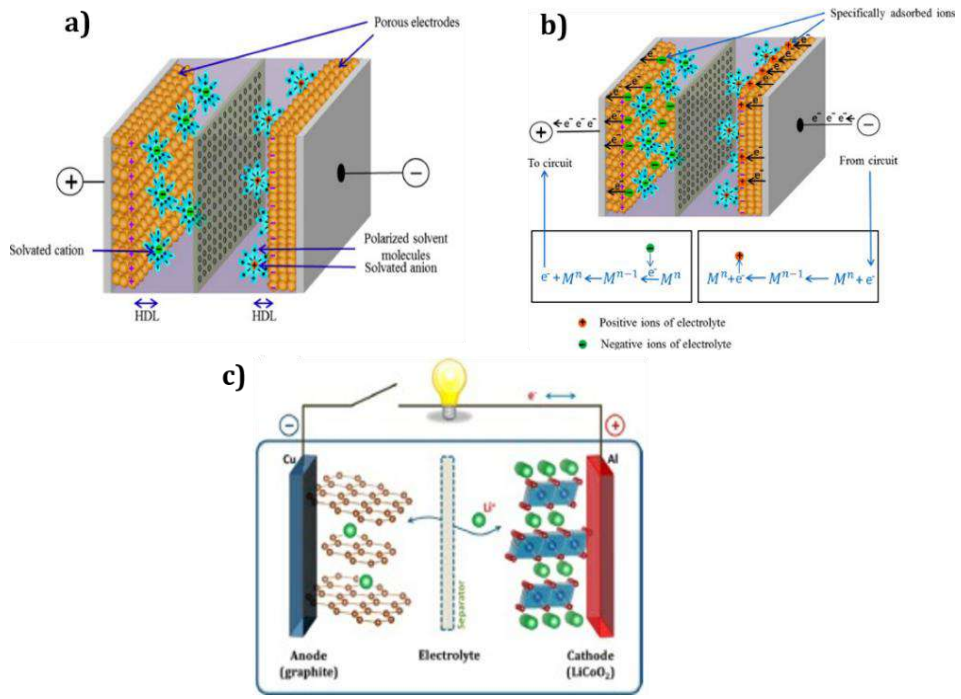

Figure 1.3 *Schematic representation of charge storage mechanisms in* ***(a)*** *EDLCs,* ***(b)*** *pseudocapacitors, and* ***(c)*** *hybrid supercapacitors*

c) Hybrid supercapacitors

A hybrid supercapacitor (HSC) combines the advantages of both capacitive and faradaic charge storage mechanisms. This helps it to achieve high energy density without compromising power density, rate capability, or cyclic stability [27, 28]. The schematic representation of a hybrid capacitor is shown in Figure 1.3(c). Structurally, it consists of two types of electrodes, one is a polarizable carbon-based electrode material, which provides electrical conductivity, a large surface area, and remarkable chemical stability. The other is a non-polarizable redox-active electrode made up of metal oxides or conducting polymers. While the carbon electrode stores charge through electrostatic accumulation, the redox-active component contributes additional capacitance through fast and reversible faradaic reactions [29].

1.1.3. Electrode Materials Commonly Adopted in Supercapacitor Applications

Common electrode materials for supercapacitor applications include conducting polymers, carbon-based materials, transition metal oxides, crystalline materials such as MOFs and COFs, and metal sulfides and nitrides. Conducting polymers like polyaniline (PANI), polypyrrole (PPy) and poly (3, 4-ethylenedioxythiophene) (PEDOT), are considered as promising electrode materials for supercapacitors due to their reversible redox reactions [30]. Carbon-based materials such as activated carbon (AC), carbon nanotubes (CNTs), graphene, and carbon aerogels are widely employed as electrode materials in supercapacitors. These materials mainly operate through EDLC mechanism and enable rapid charge-discharge processes [31]. Transition metal oxides, including RuO_2, MnO_2, NiO, and Co_3O_4, are an important class

of electrode materials for supercapacitors due to their pseudocapacitive behavior.

MOFs are a unique class of crystalline materials made by linking metal ions or clusters interconnected by organic linkers. Their high porosity, adjustable structures, redox-active metal sites, and well-defined pathway for ion diffusion make them attractive candidates for supercapacitor applications [32, 33]. Covalent organic frameworks (COFs) are a distinctive class of porous crystalline materials constructed from organic building units connected through strong covalent bonds. Their highly ordered structure, large surface area, and strong chemical stability make them promising candidates for electrode materials in supercapacitors [34] [35, 36].

By combining different materials such as carbon with conducting polymers, metal oxides, or other nanostructures, researchers have found an effective approach to boost supercapacitor performance. These composites take advantage of the strengths of each component, offering a high surface area, good electrical conductivity, and reversible redox activity, while reducing their individual limitations. This results in higher energy density and power density, along with improved cyclic stability for a wide range of energy-storage applications.

1.2. An overview of metal organic frameworks

MOFs are an intriguing class of crystalline materials formed by the coordination of metal ions or clusters with organic ligands, resulting in one, two, or three-dimensional architectures as shown in Figure 1.4 [37]. These materials are distinguished for their exceptionally high surface area, tunable porosity, and versatile functionalization, which make them suitable for a

wide range of applications, including energy storage, gas storage, separation, catalysis, and sensing [38]. The concept of MOFs emerged in 1990 to overcome the limitations of conventional zeolites and activated carbons.

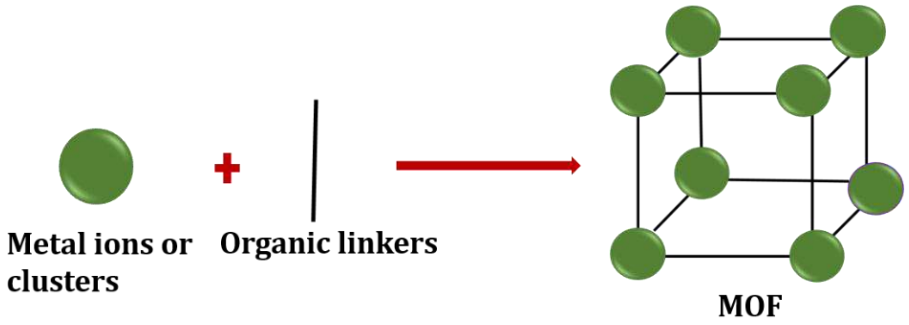

Figure 1.4 *Schematic illustration of the metal-organic framework architecture*

In 1999, Yaghi and his team synthesized MOF-5, a material notable for its large surface area and adjustable pore sizes [39]. This breakthrough discovery marked a key milestone in the development of MOF, which was recognized with the Nobel Prize in Chemistry in 2025. MOFs are named using the abbreviation "MOF" followed by a number or distinctive name that reflects either the order of discovery or specific characteristics. For example, MOF-5 is one of the first and most studied frameworks. MIL-53, derived from "Materials of the Institute Lavoisier" and HKUST-1, named after the Hong Kong University of Science and Technology. The development of specialized databases and repositories, such as the Cambridge Structural Database (CSD), Reticular Chemistry Structure Resource (RCSR), and MOF Portal, has enabled the systematic organization on MOFs information. These resources provide researchers with easy access to detailed information on MOF structures, properties, synthesis strategies, and potential applications [40].

1.2.1. Historical background

The development of MOFs can be considered as the stunning result of the progress in interdisciplinary research. In 1756, Axel Frederik Cronstedt discovered porous natural zeolite stilbite [41]. That creates widespread interest in porous solids. In 1990, Robson and co-workers reported porous coordination polymers with ion-exchange properties[42]. This was followed by the pioneering work of Omar M. Yaghi and colleagues, who developed MOF-5, widely recognized as the first robust and highly porous MOF, outperforming the conventional materials such as zeolites and activated carbon [43]. Structurally, MOF-5 exhibits a primitive cubic (pcu) topology and is synthesized using zinc acetate and benzene-1,4-dicarboxylic acid (BDC) as building units [44]. Shortly thereafter, in 1997, Kitagawa et al. reported a three-dimensional MOF capable of adsorbing gas at ambient temperature. The field advanced rapidly with the synthesis of landmark structures such as MOF-5 and HKUST-1 in 1999, which remain among the most extensively studied MOFs.

In 2002, Férey and colleagues reported both rigid and flexible porous frameworks, including MIL-47 and the MIL-53/MIL-88 series. The same year also witnessed the emergence of isoreticular chemistry, initially demonstrated with zinc dicarboxylate frameworks and later extended to numerous other systems. In addition, MOF chemistry expanded to comprise imidazolate-based linkers, giving rise to zeolitic imidazolate frameworks (ZIFs). Owing to their structural diversity, tunable pore dimensions, permanent porosity, and versatile functionalities, more than 20,000 distinct MOFs have been synthesized and explored over the past few decades [33, 45].

1.2.2. Linkers/Ligands used in MOFs

Organic linkers are essential components in the rational design of MOFs, as they serve as key structural building blocks. To construct targeted frameworks and expand the diversity of MOF architectures, significant effort has been focused on the design and synthesis of multifunctional organic bridging ligands, onto which various functional moieties have been incorporated [46]. In some studies, these organic linkers are directly introduced through one-pot MOF synthesis. Alternatively, mixed-linker approaches, linker installation, and post-synthetic modification strategies are employed to overcome diffusion limitations associated with bulky ligands used in direct synthesis. These methods enable the fabrication of MOFs with multiple active components [47].

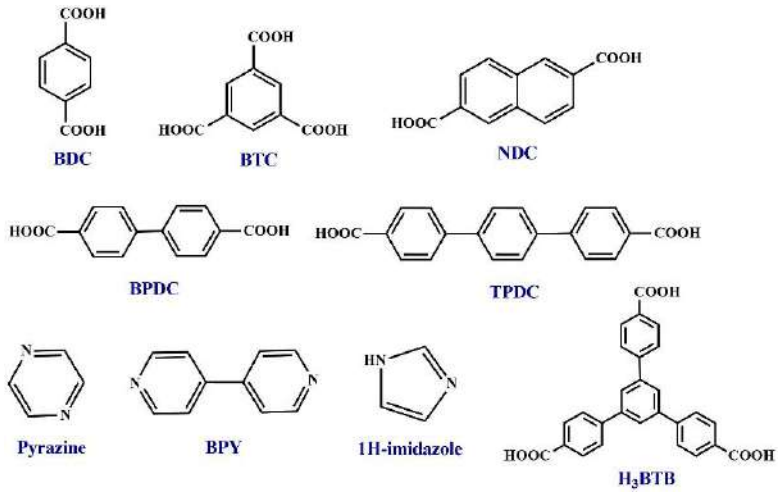

Figure 1.5 *Commonly used ligands in the synthesis of MOFs*

A wide range of organic linkers, including neutral, anionic, and cationic species, can be employed in MOF synthesis as shown in Figure 1.5. Rigid ligands are often favored because they allow easier prediction of framework

geometry and help retain porosity after solvent removal. Carboxylate functional groups play a key role in coordinating metal ions, producing stiff and geometrically well-defined clusters. In addition, ligands with different connectivity and coordination modes can bind metal ions in multiple ways, leading to diverse MOF architectures [48]. However, optimizing the conditions required for metal cluster formation remains a significant challenge. A large number of studies have focused on MOFs incorporating carboxylic acid functionalities, as these groups provides robust and predictable coordination modes [49].

1.2.3. Transition metal ions

MOFs are constructed from two fundamental components organic ligands (linkers) and metal sources. The metal nodes are typically introduced in the form of various salts, such as nitrates, chlorides, perchlorates, or sulfates, and may originate from rare-earth elements, transition metals, as well as s-block or p-block metals [50]. The choice of metal, particularly its oxidation state and accessible coordination geometries, plays a crucial role in directing the formation of MOFs with one , two, or three-dimensional architectures [51]. Each metal ion exhibits a characteristic preference for specific coordination numbers and geometrical arrangements, including linear, T or Y-shaped, tetrahedral, square-planar, square-pyramidal, trigonal-bipyramidal, octahedral, trigonal-prismatic, or pentagonal-bipyramidal configurations. For instance, Cu(II) ions commonly favour square-planar or tetrahedral environments, although their coordination number and geometry can vary significantly depending on the nature of the ligands and the solvent system employed [52]. In both basic and applied chemistry, MOFs based on s-block elements such as alkali and alkaline-earth metals have been studied less. This is mainly because these materials often show low stability and limited

chemical flexibility. Therefore, most MOFs are built using transition metal ions as the inorganic components. Lanthanide ions are also commonly used since their high coordination numbers, usually between 7 and 10, allow the formation of unique and complex framework structures. However, lanthanide-based MOFs have several disadvantages, including high cost, toxicity concerns, and possible environmental contamination. In comparison, transition metal ions are more attractive due to their lower toxicity, reduced cost, and wider availability [53].

Many transition metal-based MOFs have been studied for a wide range of applications. These include MOFs constructed from metals such as Sc, Ti, V, Cr, Mn, Fe, Cu, Zn, Co, and Ni. In the present work, we mainly focused on the d-block transition metal Ni. Nickel is one of the most abundant transition metals on earth and exhibits outstanding catalytic, electrical, optical, and magnetic properties, especially when engineered at the nanoscale. It is the fourth most abundant transition metal after Fe, Ti, and Zr and is also economically favorable. In particular, Ni MOFs have attracted significant research interest due to their intrinsic redox activity, good electrical conductivity, excellent structural stability, abundant active sites, high theoretical capacitance and a high specific surface area. Consequently, because of these excellent physicochemical properties, Ni MOFs have been widely explored for diverse electrochemical applications [54, 55].

1.2.4. Synthesis strategies of MOFs

The synthesis of MOFs has attracted great attention over the past few decades because of their unique properties and diverse applications. Many studies have focused on the bottom-up approach, where metal ions or clusters combine with organic ligands to form well-defined crystalline structures [37].

Several common synthesis methods for MOFs are illustrated in Figure 1.6. The solvothermal method is one of the most widely used techniques. In this process, metal salts and organic ligands are dissolved in an organic solvent such as DMF, DEF, ethanol, methanol, or acetone and heated in a sealed vessel at high temperature and pressure for an extended period to form crystals [56]. Recently, water has also been employed as a greener solvent alternative in MOF synthesis, offering an environmental friendly approach while maintaining good crystallinity and structural integrity [57, 58].

Figure 1.6 *Various synthetic methods adopted for MOFs*

In electrochemical synthesis, electrochemical reactions are used to produce MOFs under mild conditions. This method allows better control over the reaction, shorter synthesis times, and often results in materials with higher surface area and improved properties. The mechano-chemical method involves grinding reactants together with little or no solvent, both manually using a mortar and pestle or by ball milling (which offers better reproducibility). This solvent-free technique is especially useful for preparing

bulk MOFs and for systems where the components are poorly soluble [59]. In microwave-assisted synthesis, rapid and uniform heating enables faster crystallization and smaller particle sizes compared to solvothermal synthesis. It can also yield highly crystalline MOFs from homogeneous solutions or directly on the substrate surfaces [60].

The slow evaporation method produces high-quality crystals by allowing the solvent to evaporate gradually. However, it often requires large amounts of solvent, depends on solubility, and takes a long time to complete. Finally, the sonochemical method uses ultrasonic waves to provide the energy needed for the reaction. This approach converts metal ions into hydroxides in the presence of an oxidizing agent and promotes rapid nucleation [61]. It offers advantages such as short synthesis time, low temperature, uniform particle size, and high porosity. MOFs prepared by this method are flexible and suitable for applications including catalysis, gas storage, and sensing [62].

1.2.5. MOFs-based electrodes for supercapacitors

The first pristine MOF used as a supercapacitor electrode was Co_8-MOF-5, which exhibited EDLC behavior in 0.1 M $TBAPF_6$ [63]. But delivered a very low capacitance of 0.30 F g^{-1} at 10 mA g^{-1} due to poor electrical conductivity. Subsequently, several pristine MOFs such as Co-MOF-71[64], Zn_6 $(BPC)_6$ $(L)_3 \cdot 9DMF$[65], and MIL-100(Fe) [66] were explored in aqueous electrolytes, showing pseudocapacitive behavior but limited cyclic stability.

In 2014, Yaghi's group systematically studied 23 different nanoscale MOFs for supercapacitor application [67]. It is identified that $Zr_6O_4(OH)_4(BPYDC)_6$ as a promising electrode, delivering high stack and areal capacitances and excellent stability over 10,000 cycles, attributed to sp^2-nitrogen-rich ligands.

In addition, Ni-based MOFs, particularly $Ni_3(OH)_2(C_8H_4O_4)_2(H_2O)_4.2H_2O$, have accordion like structure and exhibited a high capacitance of 988 F g^{-1} and good cyclic stability of 96.5% after 5000 cycles in alkaline electrolyte [68].

The electrochemical performance of most MOFs are limited due to their lower electrical conductivity. To address this limitation, researchers have shifted their attention toward conductive MOFs and explored their direct use as electrode materials in supercapacitors. In 2017, Ni_3 $(HITP)_2$ was reported as the first non-carbon electrode material for EDLCs, exhibiting an exceptionally high electrical conductivity (>5000 S m^{-1}). This breakthrough confirmed the effectiveness of purely conductive MOFs in EDLC applications. The material delivers a high area-capacitance of 18 μF cm^{-2} and excellent cyclic stability 91% after 10,000 charge-discharge cycles.

Following this pioneering work, several conductive MOFs with similar coordination structures have been reported as active electrode materials for supercapacitors. Li et al. introduced a model system using Cu-catecholate (Cu-CAT) MOFs to enhance capacitance by incorporating pseudocapacitive contributions. Cu-CAT consists of Cu ions coordinated with HHTP (2, 3, 6, 7, 10, 11-hexahydroxytriphenylene ligands), forming a honeycomb-like porous framework built from stacked two-dimensional hexagonal layers. A symmetric supercapacitor fabricated using Cu-CAT nanowires achieved an areal capacitance of 22 μF cm^{-2}. Although the capacitance of conductive MOFs is comparable to that of most porous carbon materials, they still exhibit a gap in performance compared with conventional materials such as holey graphene. To address this, Feng *et al.* designed a highly redox-active conductive MOF to introduce pseudocapacitance [69]. Using a ligand hexaaminobenzene (HAB) coordinated with Ni^{2+} or Cu^{2+}, they obtained 2D

honeycomb MOFs with sub-nanometre pores (approximately 0.8 nm), which possess high electrical conductivity and excellent chemical stability in both acidic and alkaline electrolytes. Notably, Ni-HAB and Cu-HAB delivered high specific capacitances of 420 and 215 F g^{-1} in 1 M KOH. Beyond conjugated conductive MOFs, MIL-47 (V IV (O) (BDC)) with a paddle-wheel structure has also demonstrated excellent pseudocapacitive behavior in a neutral Na_2SO_4 electrolyte. A high specific capacitance of 572.1 F g^{-1} was achieved at 0.5 Ag^{-1}, along with outstanding cyclic stability over 10,000 cycles [70].

Yang et al. first reported the supercapacitive behavior of amorphous UiO-66, which exhibited a higher capacitance than its crystalline counterpart [71]. To address the low thermal stability of conductive MOFs and the high sublimation temperature of organic ligands, Du et al. developed a dual-temperature-zone CVD method to grow conductive Cu_3 $(HHTP)_2$ nanowire arrays in situ, offering a promising route for synthesizing diverse conductive MOFs [72]. Rajak and co-workers prepared a novel Na/Co-based MOF via slow diffusion, achieving 97.4 % capacitance retention after 5000 cycles [73].

1.2.6. Applications of MOFs

The exceptional properties of MOFs render them highly promising materials for a wide range of multidisciplinary applications, as depicted in Figure 1.7. Beyond their role in supercapacitors, MOFs have been widely explored across various fields. Their exceptionally high surface area, tunable porosity, and low dead volume make them especially attractive for gas storage applications [74]. As a result, MOFs have been extensively used for energy-related gas storage, including hydrogen and methane storage and carbon dioxide capture [75, 76]. Beyond gas storage, the structural tunability and

crystalline nature of MOFs also make them compelling candidates for electrocatalysis, particularly in electrochemical hydrogen production via water splitting [77]. Compared with conventional semiconductor catalysts, MOFs exhibit superior catalytic activity arising from their design flexibility and structural robustness after modification [78, 79].

Figure 1.7 *Different applications of MOFs*

In addition to energy conversion applications, MOFs have demonstrated excellent performance in membrane-based separation processes due to their precisely controllable pore sizes, which enable high molecular selectivity. Key requirements for wastewater treatment include high selectivity and permeability, uniform pore structures, strong adsorption affinity, and long-term reusability [80-82]. More recently, MOFs have attracted substantial interest as advanced photocatalytic materials. Structurally, they are three-dimensional crystalline micro-mesoporous hybrids composed of metal nodes interconnected by multidentate organic ligands, and their modular architecture enables facile integration of photoactive components. The

photocatalytic performance of MOFs can be optimized by independently tuning the metal nodes, organic linkers, and guest species confined within the pores [83]. The metal nodes can function as isolated semiconductor-like centers that are either directly photoexcited or sensitized by light-harvesting ligands [84, 85]. MOF based catalyst are also used to converting CO_2 into value-added products such as CO, HCOOH, CH_3OH, and CH_4 showing potential for both solar and electrically driven CO_2 conversion [86, 87].

1.2.7. Nickel metal-organic frameworks: A potential material for supercapacitors

Ni MOFs have attracted considerable attention as promising electrode materials for supercapacitors due to their excellent redox activity, tunable structures, and favorable electrochemical properties. The structural flexibility of Ni MOFs allows the formation of diverse morphologies, such as nanosheets, nanoflowers, and microspheres, which enhance ion diffusion and electrolyte accessibility, thereby improving electron transfer and overall energy storage performance. For instance, it has been reported that Ni MOF synthesized from nickel ions and trimesic acid via a hydrothermal route could deliver a higher specific capacitance of 726 F g^{-1} [88]. For instance, Gao *et al.* synthesized a cuboid Ni MOF exhibited a mesoporous layered structure, resulting in a high specific capacitance of 804 F g^{-1} at 1 A g^{-1} [89]. An asymmetric Ni MOF//activated carbon (AC) device based on this electrode delivered an energy density of 31.5 Wh kg^{-1} at a power density of 800 W kg^{-1}. Wang *et al.* reported ultrathin nanosheet-assembled Ni MOF microflowers featuring a three-dimensional hierarchical framework, which facilitated rapid ion transport and reduced charge-transfer resistance. This electrode exhibited an impressive specific capacitance of 1093 F g^{-1} at 1 A g^{-1} [90]. Similarly, hierarchically structured pillared Ni MOFs, delivering

552 F g^{-1} at 1 A g^{-1} and retaining 438 F g^{-1} even at a high current density of 20 A g^{-1} [91]. Accordion-like Ni MOFs exhibited high specific capacitances of 988 F g^{-1} and 823 F g^{-1} at current densities of 1.4 and 7.0 A g^{-1}, respectively, along with outstanding cyclic stability, retaining 96.5% of their initial capacitance after 5000 cycles as shown in Figure 1.8 [92].

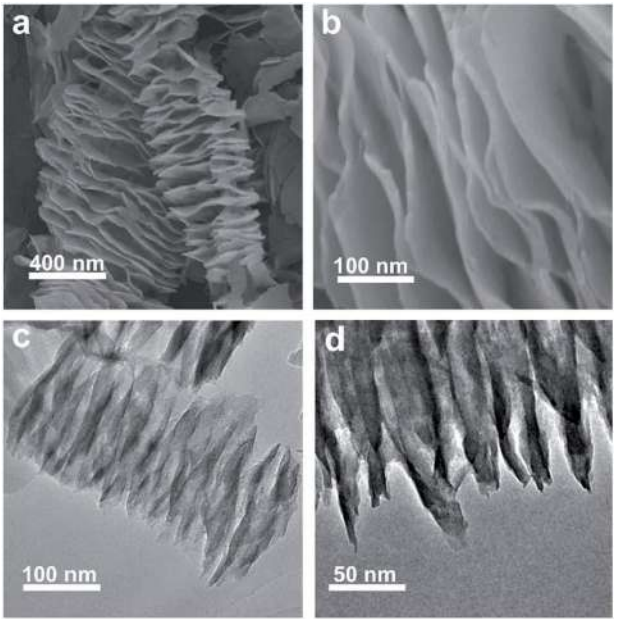

Figure 1.8 ***(a-b)*** *FESEM images of the accordion-like morphology of Ni MOF and* ***(c-d)*** *TEM images of the accordion-like morphology*

Hierarchically porous Ni MOFs constructed from interconnected nanosheets via optimized ligand-to-metal ratios demonstrated a large surface area and abundant electroactive sites, yielding a high specific capacitance of 1057 F g^{-1} at 1 A g^{-1} and 70% capacitance retention after 2500 cycles [93]. Yang *et al.* synthesized Ni MOF-12 and Ni MOF-24 and employed them as supercapacitor electrodes in aqueous electrolytes, achieving high rate performance, large capacitance, and long-term stability. In particular, a layered Ni MOF electrode delivered an outstanding specific capacitance of

1127 F g^{-1} at 0.5 A g^{-1}, along with a notable energy density of 19.17 Wh kg^{-1} and a power density of 1750 W kg^{-1} [94]. Collectively, these studies demonstrate that simple hydrothermal products to complex hierarchical and layered architectures, plays a critical role in enhancing specific capacitance, rate capability, and cyclic stability for high-performance supercapacitor applications.

1.3. Conducting polymers

Until the mid-20th century, organic polymers were regarded primarily as insulators. Researchers mainly focused on their insulating and anti-corrosion properties, making them valuable for various applications of plastic [95]. The perception was challenged with the discovery of polyacetylene (PA) in 1958. In the late 1970s, Hideki Shirakawa, Alan J. Heeger, and Alan G. MacDiarmid demonstrated that doping polyacetylene with iodine could drastically increase its electrical conductivity, transforming it from an insulator to a conductor [96-98]. This breakthrough marked the birth of CPs and opened a new era in materials science. Their work was honoured with the Nobel Prize in Chemistry in 2000 for the "discovery and development of conducting polymers," highlighting their significant influence on modern electronics and technology [99, 100].

Cps offer unique advantages such as tunable conductivity, lightweight structure, corrosion resistance, and ease of synthesis, making them highly attractive for both academic research and industrial applications [101]. Intrinsically conducting polymers (ICPs), often referred to as “synthetic metals,” derive their electrical conductivity from their unique electronic structures [102]. These polymers feature alternating or conjugated double bonds along their backbone are critical characteristic that enables electrical

conduction. In ICPs, the polymer chain consists of a π-conjugated system where the unpaired electrons in the carbon atoms overlap and delocalize across the entire polymer backbone [103]

This extended π-electron conjugation facilitates chemical and electrochemical redox reactions, allowing precise tuning of the electrical and optical properties of polymers through controlled oxidation and reduction. The remarkable redox behavior of ICPs offers vast potential for designing materials with tailored conductivity and optical characteristics, making them highly versatile for applications in electronics, optoelectronics, and electrochemical technologies. In their undoped state, CPs behave as insulators, however their electrical conductivity can be dramatically enhanced through a process called "doping". By controlling the type and level of doping, the conductivity of CPs can be finely tuned, ranging from insulating to semiconducting or even metallic behavior [104]. For instance, the conductivity of PA increased by a remarkable ten million-fold when oxidized with iodine vapour, reaching values high as 10^3 S cm^{-1} [105]. Typical conductivity ranges are depicted in Figure 1.9.

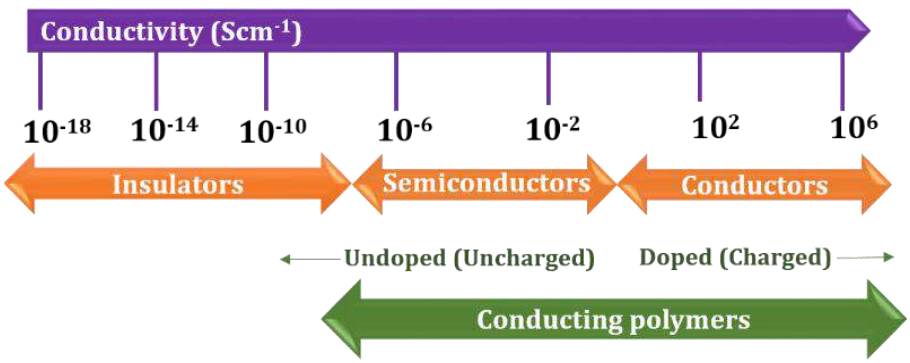

Figure 1.9 *Conductivity ranges of CPs*

1.3.1. Major Conducting Polymers

The pioneering studies on conductive polymers began with the discovery of PA. Although PA is inherently semiconducting, its conductivity increases by nearly ten million times upon iodine doping. However, its practical use was limited due to infusibility, poor solubility, and instability in air. These shortcomings motivated the development of a wide range of alternative CPs, such as PPy, PANI, polythiophene (PTh), polyindole (PIN), poly(3,4-ethylenedioxythiophene) (PEDOT) poly(para-phenylene) (PP), polyquilonine (PQ), and poly(para-phenylenevinylene) (PPV). Notably, PPy and PTh are composed of five-membered heterocyclic rings containing nitrogen (PPy) or sulfur (PTh), with monomers ideally coupled at the α–α′ positions, enabling effective π-bond delocalization [101]. The structures of some important CPs are given in Figure 1.10.

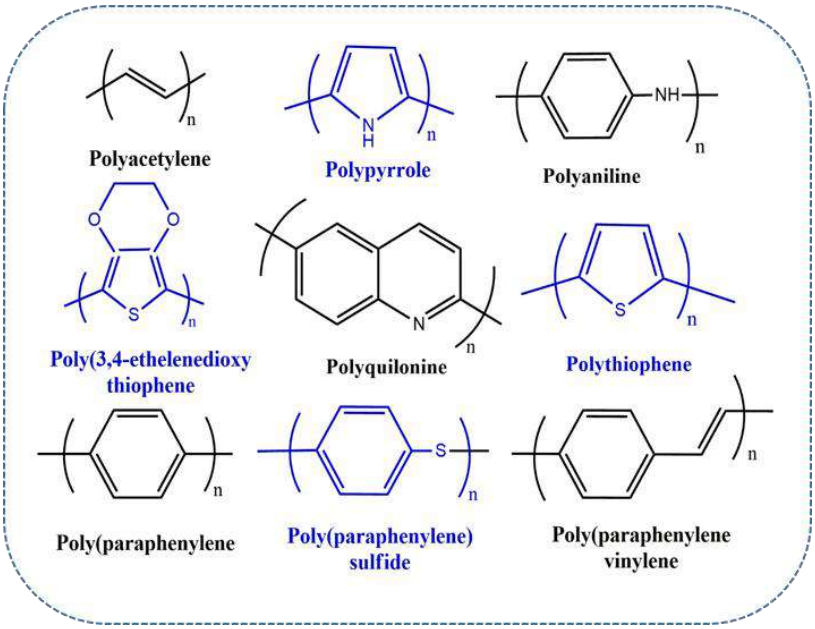

Figure 1.10 *Examples of commonly used conducting polymers*

1.3.2. Doping Mechanisms in Conducting Polymers

Doping is the process by which a π-conjugated polymer is converted from its insulating state into a semiconductor or conductor. Unlike conventional inorganic semiconductors, the doping mechanism in conducting polymers is unique. In their undoped form, CPs behave as insulators; however, upon treatment with appropriate oxidizing or reducing agents, their carrier concentration increases, resulting in enhanced electrical conductivity. Doping in conducting polymers introduces conjugation-related irregularities within the polymer backbone, leading to the formation of charge carriers such as solitons, polarons, and bipolarons [106, 107]. Various techniques are employed to achieve this doping process, some of which are outlined below.

(a) Redox Doping

Redox doping represents the most prevalent method for modifying the electronic properties of conducting polymers. This approach can be carried out either chemically or electrochemically. In chemical redox doping, two pathways are possible such as p-type doping, achieved through oxidation with electron-accepting species, and n-type doping, achieved via reduction using electron-donating agents. Typical p-type dopants include $FeCl_3$, HNO_3, H_2SO_4, HCl, AsF_5, $HClO_4$, CH_3COOH, H_3PO_4 and NH_4BF_4, while common n-type dopants are alkali metals such as Na, K, and Li. A notable example is the oxidation of PA with iodine, which enhances its [90] conductivity dramatically from 10^{-5} S cm^{-1} up to 10^{2} S cm^{-1} [108, 109].

De-doping is the reverse process of doping, in which conducting polymers are transformed back into their neutral or insulating state. For p-type polymers in the oxidized form, de-doping is achieved by treatment with

electron donors, while for n-type polymers in the reduced state, electron acceptors are employed. Since the nature of the dopant and the selected doping strategy strongly govern the conductivity, stability, and overall performance of conducting polymers, doping remains a crucial step in tailoring their synthesis and practical applications [110].

b) Non-Redox Doping

In the case of non-redox doping, the doping process does not involve electron transfer reactions within the polymer chain. Instead, it leads to a reorganisation of the energy levels of the CP, while the total number of electrons in the backbone remains unchanged. A well-known example is the protonic acid doping of PANI (emeraldine base form), which generates conducting polysemiquinone radical cations [111].

1.3.3. Mechanistic insights into charge transport in conducting polymers

Conducting polymers readily undergo redox reactions due to their π-conjugated backbone. Upon doping, charge carriers such as solitons, polarons, and bipolarons are generated, which are delocalized along the polymer chains and exhibit high mobility, thereby enhancing electrical conductivity [112]. Doping involves either the removal of electrons from the highest occupied molecular orbital (HOMO) or their injection into the lowest unoccupied molecular orbital (LUMO). Based on their bond structure, CPs can exist in degenerate or non-degenerate ground states. Degenerate CPs possess two equivalent ground-state geometries and conduct via solitons, whereas non-degenerate CPs exhibit energetically distinct benzenoid and quininoid structures, with polarons and bipolarons acting as charge carriers [113]. A soliton is a localized defect in a conjugated polymer chain that possesses zero

charge and a spin of ±½. It forms when a carbon atom does not share its π-electron with neighbouring atoms, resulting in the formation of a radical. The π-bond can shift between neighbouring atoms, allowing the soliton to move along the polymer backbone due to the degeneracy of these bonding states. Solitons serve as fundamental charge carriers in conjugated polymers and are highly delocalized along the chain. Unlike conventional electrons, they exhibit fermionic spin (±½) while remaining electrically neutral, which distinguishes them from traditional charge carriers [114].

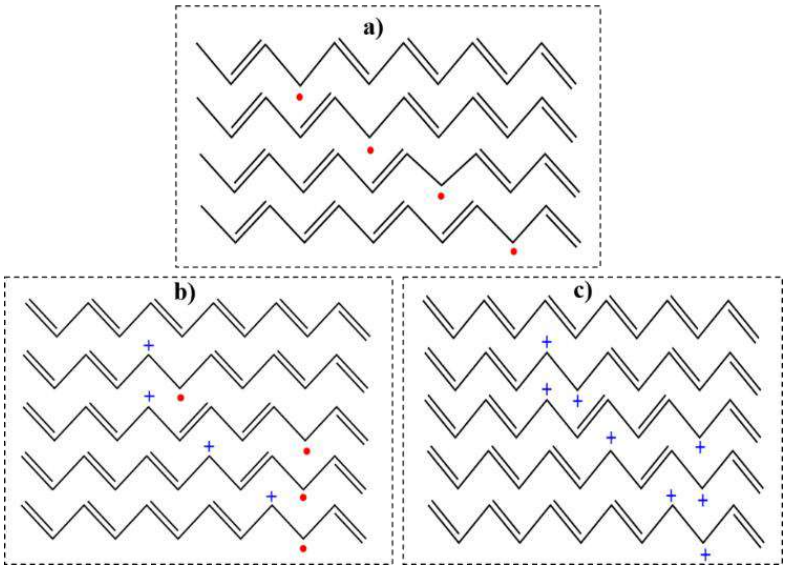

Figure 1.11 ***(a)*** *Charge transport in trans-polyacetylene occurs through the hopping motion of solitons along the polymer backbone,* ***(b)*** *the charge transfer mechanism involving a polaron in trans-polyacetylene,* ***(c)*** *the charge transfer mechanism involving a bipolaron in trans-polyacetylene*

A polaron is a quasiparticle consisting of a charged site coupled with a free radical, accompanied by local lattice distortion arising from polarization of the surrounding medium. It carries a spin of ±½ and an electric charge of ±e. Accordingly, a polaron may exist as either a radical cation, formed through

electron-acceptor doping, or a radical anion, generated via electron-donor doping. The formation of polarons introduces new localized electronic states within the band gap of the polymer. In contrast to solitons, polarons exhibit a finite spatial extent defined by the separation between the associated electron and hole, which decreases with increasing dopant ion concentration [115]. In most non-degenerate conducting polymers, electrical conductivity is predominantly spinless, indicating the involvement of bipolarons formed through polaron-polaron interactions. When the dopant concentration exceeds a critical level, two polarons couple to generate a self-localized quasiparticle known as a bipolaron (dication or dianion). The separation between the two positively charged sites defines the bipolaron length. Upon further oxidation of a polymer chain containing a polaron, electron removal can occur either from the polymer backbone, producing two polarons, or directly from the polaron, resulting in bipolaron formation. Bipolarons are spinless bosonic carriers with a charge of ±2e and are thermodynamically more stable than two isolated polarons due to reduced ionisation energy [113, 116]. The formation of solitons, polarons, and bipolarons is illustrated in Figure 1.11.

1.3.4. Applications of conducting polymers

The CPs have been employed in numerous fields owing to their unique properties. Some of its major applications are listed below.

a) **Supercapacitors and Batteries:** CPs are considered a promising electrode material for batteries and supercapacitors due to their high theoretical capacitance, low cost, light weight, tunable electrical conductivity and excellent doping-dedoping properties. Current

research efforts aim to improve the energy density and rate capability of conducting polymer-based energy storage devices [117, 118].

b) **Corrosion Protection:** CPs provide corrosion resistance to metallic substrates by forming protective coatings that inhibit electrochemical degradation in corrosive environments. Such coatings effectively extend the operational lifespan of metals [119].

c) **Sensors:** CPs are widely used in chemical, electrochemical, physical, and biological sensing applications due to their stimuli-responsive behavior. Variations in its electrical conductivity upon exposure to gases, humidity, or chemical analytes enable its effective use in environmental monitoring, industrial safety, and healthcare diagnostics [120].

d) **Actuators:** When an external potential is applied to CPs, ions move within the polymer matrix, causing volumetric expansion or contraction. This property makes CP actuators highly suitable for applications such as artificial muscles, microfluidic systems, and controlled drug delivery platforms [105].

e) **Smart Textiles:** Coating textiles with CPs, making the fabric electrically conductive, allowing the development of smart fabrics with integrated electronic features. Such materials are widely used in wearable devices, biomedical monitoring systems, and military uniforms equipped with sensors for signal tracking and sense surrounding environmental condition [121].

f) **Biomedical Applications:** In the biomedical field, CPs are widely explored for drug delivery systems, tissue scaffolds, and biosensors for detecting biomolecules. Its biocompatible nature, tunable characteristics, and stimulus-responsive behavior contribute to its

suitability for biomedical use. A detailed discussion of PPy and PANI is presented in this thesis.

1.4. Polypyrrole: A Concise Historical Perspective

PPy plays an important role in the history of conducting polymers. It was the first organic polymer to exhibit significant electrical conductivity was also the first conjugated polymer prepared in the form of a plastic film. Pyrrole was discovered by Runge in 1834, around the same time as aniline, but its redox chemistry remained unexplored for many years[122]. Later in 1915, Angelo Angeli, who oxidized pyrrole using hydrogen peroxide in acetic acid and similar oxidants. The reaction produced a black insoluble solid, known as "pyrrole black." Due to its insolubility, its exact structure could not be predicted. Angeli's proposed a structure was to the oxidized backbone of present day PPy, which paid a foundation and later recognized PPy as a conducting polymer. The conductive behavior of PPy was first demonstrated in 1963 by Weiss, McNeill, and Bolto during studies on the pyrolysis of tetraiodopyrrole, which revealed appreciable electrical conductivity [123].

1.4.1 Structure of polypyrrole

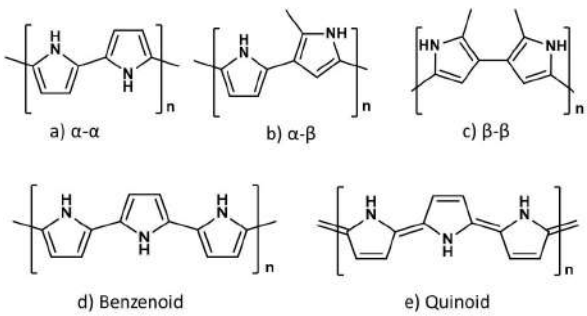

Figure 1.12 *Schematic depiction of **(a-c)** bonding between PPy repeat units, highlighting the **(d)** benzenoid and **(e)** quinonoid forms [124]*

In PPy, polymer chain growth occurs predominantly through α–α coupling between adjacent monomer units (Figure 1.12a), although a small fraction of linkages involving α-β and β-β positions are also observed (Figure 1.12 b-c) [124]. The presence of an extended π-conjugated backbone endows PPy with electrical conductivity by enabling delocalization of charge carriers along the polymer chain. In its de-doped or neutral state, PPy adopts a benzenoid (aromatic) configuration and behaves as an electrical insulator, exhibiting a relatively wide band gap of about 3.16 eV. Electrical conductivity is induced upon doping, which involves the removal of π-electrons from the polymer backbone, thereby transforming the molecular structure from the benzenoid form to a quinonoid configuration.

1.4.2 Synthesis of polypyrrole

a) Electrochemical synthesis

PPy can be prepared electrochemically through the oxidation of pyrrole monomers under an applied electric current at an inert electrode. One major advantage of this method is the cost effective deposition of PPy nanostructures directly onto metal electrodes. Generally electropolymerization of PPy is generally carried out using potentiostatic, galvanostatic, or potentiodynamic modes. This method follows irreversible chain-growth polymerization mechanism. The selection of electrode material plays a critical role for the targeted application. Electrochemical method offer great control over film thickness, morphology and uniformity of the deposited films compared with conventional electrochemical chemical oxidative polymerization [125, 126].

b) Oxidative polymerization

In conventional chemical synthesis, pyrrole monomers are directly oxidized using different oxidizing agents. Typically, PPy is produced by reacting pyrrole with a strong oxidant under acidic conditions. Among the oxidizing, Ferric chloride is the most commonly employed. But its high oxidizing power requires harsh reaction conditions. To overcome this limiation, milder oxidizing agents such as hydrogen peroxide, often combined with a catalyst are used as an environmental friendly alternative. PPy can be obtained in different morphologies such as irregular agglomerates, granular particles or nanofibres depending on the synthesis condition [127-129].

1.4.3. Doping in polypyrrole

The extended π-conjugated backbone of PPy allows transport of charge along the polymer chain. However, this conjugation does not result in high electrical conductivity. To achieve better conductivity, PPy needs to be doped. Doping is usually achieved by oxidation and less commonly by reduction. After doping, PPy changes from an insulating material to a metallic or highly conducting material.

In its neutral state, PPy mainly contains benzenoid structures. During oxidative doping, one electron is removed from the valence band. This process forms a positively charged radical called polaron, which is stabilized by charge delocalization. With further oxidation, a second electron is removed from the polymer chain, leading to the formation of a bipolaron. Bipolarons are more stable than two separate polarons because they have lower energy. Both polarons and bipolarons are delocalized over about four pyrrole units along the polymer chain [113]. Due to the extended π

conjugation, these charge carriers can move easily along the backbone. Their movement is mainly responsible for the electrical conductivity of PPy. In the dedoped state, PPy has a wide band gap of about 3.16 eV. This large band gap prevents electrons moving from the valence band to the conduction band at room temperature, making PPy insulating. When polarons are formed, two new energy levels appear inside the band gap such as bonding and antibonding states. As a result, the HOMO level moves upward, and the LUMO level moves downward. With further oxidation, bipolaron states are created, which further reduce the band gap [130]. At high doping levels, the overlap of bipolaron states forms two broad bipolaron bands. This significantly narrows the energy gap, leading to a substantial increase in electrical conductivity.

1.5. Polyaniline (PANI)

PANI is one of the earliest and most extensively studied CPs, with its origins tracing back to the 19th century. The polymer was initially recognized as *aniline black*, a dark-colored product formed by the oxidation of aniline, first reported in 1835 and later studied in detail by Dr Henry Letheby in 1862 during the electrolysis of aniline sulphate [131]. Early structural investigations in the early 20th century, particularly by Willstätter and co-workers, attempted to explain the nature of aniline black. A breakthrough came between 1910 and 1912 when Green and Woodhead systematically described the polymerization of aniline and identified distinct oxidation states of PANI, proposing a para-linked head-to-tail chain structure composed of aniline units. They also highlighted the presence of amine (-NH-) and imine (-N=) groups, which play a crucial role in determining the electrical properties of the polymer. The conductivity of PANI can be reversibly tuned through protonation-deprotonation and redox processes,

enabling interconversion between different oxidation states. Although early studies paid little attention to its electrical properties, the concept of electrical conduction in organic polymers was later suggested, and a systematic understanding of redox chemistry of PANI and oxidation states was further developed by Alan MacDiarmid and his group, leading to renewed scientific interest in PANI during the mid-20th century [132].

1.5.1. Structure of polyaniline

PANI possesses a conjugated backbone composed of repeating benzene rings linked through nitrogen atoms. These nitrogen atoms can exist in two forms, amine or imine, depending on how much the polymer is oxidized. The ratio of these two nitrogen forms changes with the oxidation level of PANI. PANI mainly exists in three oxidation states.

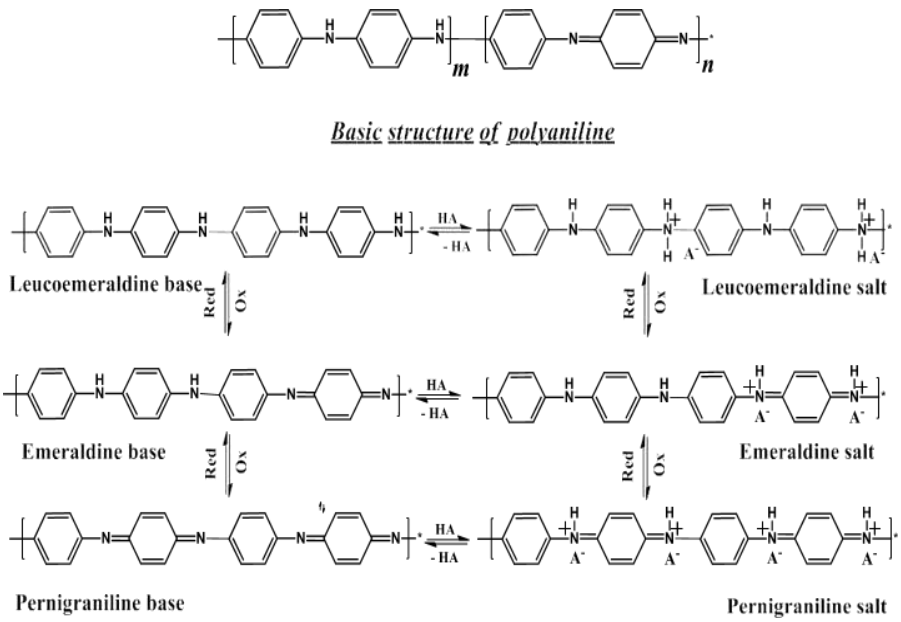

Figure 1.13 *Various oxidation states of PANI*

In the fully reduced form, called leucoemeraldine, the polymer chain contains only benzenoid rings, and all nitrogen atoms are in the amine form with hydrogen attached. In the fully oxidized form, known as pernigraniline, the structure contain alternating benzenoid and quinonoid form, and the nitrogen atoms are in the imine form without hydrogen atoms .The nitrogen atoms in PANI can be either protonated or unprotonated depending on the pH of the environment. When they are unprotonated, PANI is referred to as being in the base form. Between the fully reduced and fully oxidized states lies the emeraldine form, which contains both benzenoid and quinonoid units [133]. This intermediate form is the most stable and widely used form of PANI in practical applications are shown in Figure 1.13.

1.5.2. Doping in polyaniline

PANI shows a special type of doping that is different from most other conducting polymers, such as PA, PPy, and PTh, which mainly undergo oxidation (p-doping). In PANI, the electrical properties can be controlled by changing both the number of electrons and the number of protons in the polymer chain. In aqueous solutions, the electrochemical activity of PANI strongly depends on pH, and it decreases significantly when the pH is higher than 4. Similar behavior is observed in aprotic solvents, where the redox response disappears when a strong base is added [133].

A large decrease in electrical conductivity is observed when the pH increases from acidic to neutral conditions, showing that protons play a major role in charge transport. Unlike redox doping, PANI can be doped simply by protonation, where the emeraldine base form reacts with protonic acids such as HCl, H_2SO_4, or organic sulfonic acids to form the conducting polyaniline salt [134]. In this process, the oxidation state of the polymer remains

unchanged. Earlier reports suggested that protonation occurs mainly at imine nitrogen. But later it was found that amine sites can also be protonated, depending on the acid strength and oxidation state. The counterions from the acid stay remain close to the polymer chain to maintain charge balance and influence the conductivity [135].

1.5.3. Various synthesis routes for polyaniline

PANI can be synthesized using either chemical or electrochemical methods. Chemical synthesis produce PANI in powdered form and provides a higher yield compared with electrochemical routes. In contrast, electrochemical polymerization allows for the direct deposition of PANI as uniform thin films on various conductive substrates, making it particularly suitable for electronic and device-oriented applications [136]. In chemical synthesis, aniline monomers are usually polymerized in an acidic aqueous medium using oxidizing agents such as ammonium persulfate [137], hydrogen peroxide [138], ferric chloride [137], or ceric nitrate/sulfate [139]. During the process, oxidizing agent removes electrons from the aniline molecules, initiating polymerization and resulting in the coupling of monomer units into polymer chains. This approach is highly favorable for large-scale production of PANI. Under acidic conditions (pH < 3-4), the resulting polymer is oxidized at a lower potential than the aniline monomer itself. Moreover, conducting the reaction at lower temperatures, close to 0 °C, promotes the formation of high molecular-weight PANI. Overall, chemical polymerization of aniline requires an aqueous electrolyte medium to ensure efficient monomer oxidation and polymer growth [133, 140]. Electropolymerization of PANI has been successfully carried out via electrodeposition, commonly using a potentiostatic technique in which a constant potential in the range of 0.5-0.9 V is applied for durations ranging from a few seconds to several

minutes. This process is carried out in a three-electrode configuration comprising a working, counter, and reference electrode immersed in an electrolyte solution containing aniline monomers and acids such as HCl or H_2SO_4 [141]. In addition to potentiostatic deposition, galvanostatic and potentiodynamic approaches are also employed for PANI electrodeposition. Typically, a platinum electrode serves as the counter electrode, Ag/AgCl as the reference electrode, and substrates such as ITO, Cu, Fe, Au, or graphite are used as working electrodes.

1.5.4. Conducting polymer based supercapacitors

Among various conducting polymers, PPy and PANI have attracted considerable attraction for advanced supercapacitor applications. This is mainly due to its ease of synthesis, environmental stability, excellent biocompatibility, tunable conductivity, strong redox behavior, and inherent flexibility. Despite these advantages, Both PPy and PANI suffers from certain drawbacks to prevent their long term electrochemical performance. During repeated charge-discharge cycles, the repeated insertion and extraction of counterions, induce swelling and shrinkage of the polymer chains, leading to structural instability and mechanical degradation. This volumetric changes results deterioration of the electrode material, limits the long-term electrochemical performance and practical applicability of PANI and PPy in energy storage systems.

Inorder to overcome the inherent limitations of poor cyclic stability and limited rate capability in CPs such as PPy and PANI. One effective strategy is the formation of composites with suitable carbon-based materials, including CNTs, graphene, graphene quantum dots (GQDs), carbon quantum dots (CQDs), and activated carbon. These materials offer a large specific

surface area, which improves electrolyte accessibility and enhances the pseudocapacitive contribution of the polymers. They also improve the electrical conductivity of PPy and PANI, leads to better rate performance. Further, the presence of surface functional groups, particularly in carbon nanostructured materials, strengthens interfacial interactions with the polymer chains. This helps to prevent structural degradation during repeated charge-discharge cycles and improves the cyclic stability of both PPy and PANI.

1.6. Graphene Quantum Dots (GQDs)

Graphene quantum dots is a class of zero-dimensional graphene-based nanomaterials that combine the key features of both graphene and carbon dots (CDs). They usually have lateral dimensions below 20 nm. GQDs consist of few graphene layers (usually 2-3) along with abundant surface defects and oxygen containing functional groups [142]. GQDs possess an extended π-π conjugated network composed of sp^2 and sp^3 hybridized carbon atoms, with oxygen functional groups, particularly carboxyl groups at the edges similar to graphene. This enhances surface area and facilitates efficient surface modification and interfacial interactions. These surface functional groups serve as active sites for binding polymers, inorganic species and biomolecules. GQDs are typically produced by cutting down graphene sheets into nanoscale fragments smaller than the exciton Bohr radius, which give rise to quantum confinement effects. Due to their large number of edge sites, GQDs can effectively function as both electron donors and acceptors. Therefore, GQDs are considered as promising materials for a wide range of applications, particularly in energy storage and conversion systems, as well as in sensing, biomedicine, and optoelectronic devices [143].

1.6.1. Nitrogen doped Graphene quantum dots (NGQDs)

Heteroatom doping is considered as an effective approach to tune the intrinsic properties of GQDs. Among various heteroatoms, nitrogen has been most commonly employed for GQD modification. This is attributed to the comparable atomic radii of nitrogen and carbon along with the higher electronegativity of nitrogen compared to carbon, which facilitates easy incorporation of N into the carbon lattice. NGQDs comprises of three types of nitrogen , graphitic N, where nitrogen atoms substitute carbon atoms within the hexagonal graphene framework, and pyridinic N and pyrrolic N, both of which are typically located at edge defects. The incorporation of N into GQDs alters the electronic distribution , leading to enhanced electrical conductivity and improved functional versatility [144]. As a result, NGQDs have attracted considerable interest for applications in supercapacitors, sensing devices, electronics, and catalysis. In this work, we emphasize the synthesis of NGQDs via a simple hydrothermal method and systematically investigated their electrochemical properties for supercapacitor applications.

1.6.2. Synthesis of GQDs and NGQDs

Generally, GQDs are prepared using two main approaches, top-down and bottom-up strategies [145]. The top-down approach involves breaking down bulk carbon materials such as graphene, graphite, carbon nanotubes, graphene oxide (GO), through methods including hydrothermal treatment, electrochemical exfoliation, and strong acid oxidation [146]. However, this method suffers has certain drawbacks including non-uniform particle size distribution, low product yield, harsh reaction conditions [147]. In contrast, the bottom-up strategy focuses on building GQDs from small molecular precursors via thermal or catalytic processes. This approach offers better size

control, morphology, and lattice structure [148]. During hydrothermal or solvothermal synthesis, the small molecular precursors undergo dehydrogenation and carbonization, leading to the formation of uniform GQDs [144, 149]. NGQDs can also be prepared using both top-down and bottom-up approaches. In the top-down approach, carbon-based materials are broken down in the presence of nitrogen-containing agents, such as ammonia solution. Most commonly used carbon sources include GO, rGO, C_{60}, and CNTs. For example, Santiago et al.[150] reported the synthesis of NGQDs via pulsed laser ablation using GO as the carbon precursor and diethylenetriamine (DETA) as the nitrogen source. Similarly, Hu et al. [151] Fabricated NGQDs through a one-step hydrothermal treatment of GO in an ammonia solution. In recent years, bottom-up strategies have attracted increasing attention for NGQD synthesis, wherein NGQDs are constructed from small organic molecules such as citric acid, glucose, and glycine, combined with nitrogen-rich compounds including ammonia, glycine, dicyandiamide, tris (hydroxymethyl) aminomethane, and 3,4-dihydroxy-L-phenylalanine. These methods, which typically employ hydrothermal treatment, microwave irradiation, or pyrolysis, involve the simultaneous polymerization , carbonization, and nitrogen incorporation within a single reaction system [152]. Safardoust-Hojaghan et al. [153] demonstrated the hydrothermal synthesis of NGQDs using citric acid and ethylenediamine, where initial carbonisation of the precursors was followed by their conversion into NGQDs. In a related study, Ramachandran et al.[154] prepared NGQDs via a single-step hydrothermal route using PANI, a nitrogen-containing polymer that promotes the formation of an aromatic framework and enhances nitrogen doping. In the present work, PPy was employed as both the carbon and nitrogen source for the facile synthesis of NGQDs.

1.7. Polypyrrole/carbon nanostructure composites for supercapacitor applications

PPy has attracted considerable attention as a pseudocapacitive electrode material due to its high theoretical capacitance and fast redox kinetics. However, its practical application is hindered by poor mechanical integrity and limited cyclic stability arising from volumetric changes during repeated charge-discharge processes. To overcome these drawbacks, carbon-based nanostructures, particularly graphene quantum dots, carbon quantum dots and other graphene derivatives, have been extensively incorporated into PPy matrices to improve conductivity, structural stability, and electrochemical performance. PPy/GQD composites have been reported to deliver a high specific capacitance of 487 F g^{-1} at a current density of 1 A g^{-1}, along with an energy density of 43 Wh kg^{-1} at a power density of 812 W kg^{-1}. Moreover, these electrodes exhibit excellent cyclic stability, maintaining about 92% of their initial capacitance after 5000 cycles, thereby outperforming pristine PPy-based systems [155]. Similarly, electrochemically reduced GQDs (ERGQDs) integrated with PPy combined the electric double-layer capacitance of ERGQDs with the pseudocapacitance of PPy, resulting in a specific capacitance of 418 F g^{-1} at 1 A g^{-1} and improved rate capability, with 75.8% retention at 10 A g^{-1} and 86% capacitance retention after 1000 cycles [156].

Zhou et al. demonstrated that chemical bonding between the carbonyl (C=O) groups of GQDs and the N-H groups of PPy facilitates efficient charge transfer while simultaneously improving the structural integrity of the composite. As a result of these synergistic interactions, PPy-GQD composites have been demonstrated to deliver high specific capacitance values of up to 647 F g^{-1}, together with notable energy density (93 Wh kg^{-1})

and power density (1430 W kg^{-1}) [157]. Rahimpour and Teimuri-Mofrad developed a ferrocenyl-modified graphene quantum dot/polypyrrole (GQD-Fc/PPy) nanocomposite as a hybrid supercapacitor electrode. The optimized electrode delivered a specific capacitance of 284.01 F g^{-1} at 2.5 Ag^{-1}, along with a high energy density of 81.79 Wh kg^{-1} and a power density of 18.17 kW kg^{-1}. In addition, the nanocomposite exhibited good cyclic stability, retaining about 86% of its initial capacitance after 5000 charge-discharge cycles [158]. Carbon quantum dots (CQDs) have also been shown to effectively enhance PPy-based electrodes. Malik et al. synthesized PPy/CQD composites via galvanostatic electropolymerization. The optimized PQD 0.5 composite achieved an exceptionally high specific capacitance of 1073.5 F g^{-1} at 10 mV s^{-1}, although the capacitance retention was limited to 62% after 2000 cycles [159]. A ternary composite comprising SnO_2 quantum dots, GO, and PPy (SGP) demonstrated a remarkably high specific capacitance of 928.56 F g^{-1} at 40 mV s^{-1}. This enhancement was attributed to the synergistic contribution of pseudocapacitance from SnO_2 and the conductive GO/PPy network. The symmetric SGP3 device achieved an energy density of 25.6 Wh kg^{-1} at a high power density of 4098 W kg^{-1}, while maintaining excellent cyclic stability over 11,000 charge-discharge cycles at a current density of 1 A g^{-1} [160].

1.8. Polyaniline/carbon nanostructure composites for supercapacitor applications

Recent studies have highlighted the effectiveness of incorporating GQDs into PANI-based architectures to enhance supercapacitor performance. Breczko et al. [161] reported the synthesis of sulfonated polyaniline nanotubes (s-PANI-NTs) decorated with GQDs as advanced supercapacitor electrode materials exhibited specific capacitance of 245F g^{-1}. Muhiuddin et al.[162] reported the

synthesis of neodymium-NGQDs (Nd-GQDs) via a microwave-assisted hydrothermal method and their integration with PANI for supercapacitor applications. The Nd-GQDs delivering a high specific capacitance of 618 F g^{-1} at 5 mV s^{-1} in a three-electrode configuration. The optimized Nd-GQDs/PANI composite (20 mL Nd-GQDs) achieved a specific capacitance of 354 F g^{-1} at 1 A g^{-1}, along with an energy density of 49.15 Wh kg^{-1} and a power density of 2000 W kg^{-1} in a symmetric supercapacitor. Moreover, the device demonstrated excellent cyclic stability with nearly 99% capacitance retention after 2000 cycles [162]. Arthisree and Madhuri developed a green-synthesized GQD-doped PAN/PANI polymer nanocomposite for supercapacitor applications. Owing to strong synergistic interactions, the optimized composite (1.5 wt% GQD) exhibited a high specific capacitance of 589.3 F g^{-1} cm^{-2} and good electrical conductivity. A prototype device delivered a stable output voltage of ~1.4 V, demonstrating its potential for low-cost energy storage [163].

1.9. A comprehensive overview of conducting polymer electrochemistry

In the late 1970s, MacDiarmid, Heeger, and Shirakawa discovered that conducting polymers can undergo reversible redox reactions, a breakthrough that was later recognized with the Nobel Prize in Chemistry in 2000. CPs can be oxidized or reduced by chemical or electrochemical methods, during which ions move in and out of the polymer from the surrounding electrolyte. This process, known as doping and de-doping, changes the polymer's composition and can increase or decrease its electrical conductivity by several orders of magnitude, along with changes in its optical and volume properties. CPs undergo transition between neutral, oxidized, and reduced states when an electric field is applied in an electrolyte. During these redox reactions, charge balance is maintained not only by ion movement but also

by the transport of solvent molecules due to osmotic balance. These reversible reactions cause structural changes in the polymer chains, such as transitions between benzenoid and quinonoid forms, which alter the polymer shape. Because of this electrochemically induced structural flexibility, CPs are considered reactive materials and generally exhibit three main types of electrochemical reaction mechanisms [164].

a) Oxidation (p-doping)

Among the various doping processes in conducting polymers, p-type doping is the most prevalent. This process involves the formation of positive charge carriers (holes) along the polymer backbone through electron removal under an applied anodic potential. To balance electrical neutrality, counter-ions from the electrolyte diffuse into the polymer matrix to balance the generated charges. The transition of the polymer from its electrically neutral form to the oxidized state can occur via two distinct pathways.

The prevailing anion exchange

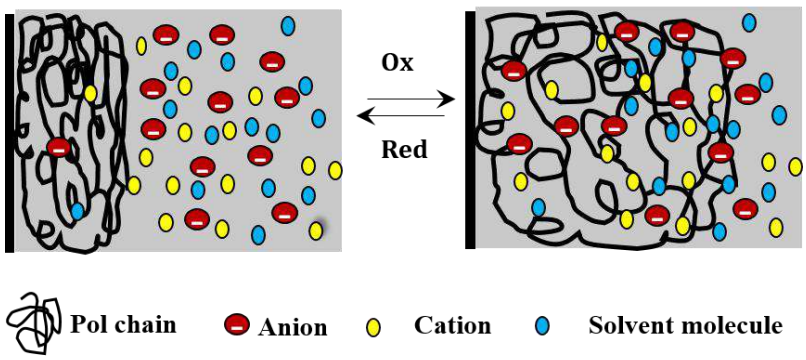

Figure 1.14 *Schematic diagram showing polymer swelling and contraction associated with p-doping via anion exchange*

This behavior is usually seen in CPs with small counterions. When the polymer is oxidized, positive charges form on the polymer chains, causing the polymer chain to rearrange. These conformational changes generate additional volume inside the polymer.To balance the charges and maintain osmotic balance, anions and solvent molecules from the electrolyte enter the polymer, leading to swelling [165]. In contrast, upon reduction, anions are expelled, leading to a contraction or decrease in the polymer volume, as shown in the reaction 1.3.

$$(\boldsymbol{Pol^0})_s + \boldsymbol{n}(\boldsymbol{X^-})_{aq} + \boldsymbol{m}(\boldsymbol{Solv}) \rightleftarrows [(\boldsymbol{Pol^{n+}})_s\,(\boldsymbol{X^-})_n(\boldsymbol{Solv})_m]_{gel} + \boldsymbol{ne^-} \quad (1.3)$$

In this reaction, the subscripts s and aq denote the solid state and aqueous solution, respectively. Pol^0 refers to the reactive sites present along the polymer chains, while X^- represents the anions. Figure 1.14 illustrates the volume transition of the polymer from a compact, densely packed solid state to a swollen gel state as a result of reaction 1.3.

Prevailing cation exchange

If the polymer is formed in the presence of a large macro-anion, the anion becomes permanently trapped within the polymer matrix, irrespective of the oxidation state. During reduction, cations enter the polymer to maintain charge neutrality, while during oxidation, they are expelled, as shown in reaction 1.4. As a result, the polymer swells upon reduction and shrinks upon oxidation, which is evident in Figure 1.15.

$$[(\boldsymbol{Pol^0})\,(\boldsymbol{MA^-})_n(\boldsymbol{C^+})_n]_s \rightleftarrows [(\boldsymbol{Pol^{n+}})_s\,(\boldsymbol{MA^-})_n]_s + (\boldsymbol{nC^+})_{aq} + \boldsymbol{n}(\boldsymbol{e^-})_{metal} \quad (1.4)$$

Here, MA^- corresponds to a large macroanion confined inside the polymer

matrix during synthesis, while C^+ denotes the balancing cation. In reactions 1.3 and 1.4, positive charges are present on the polymer chains; therefore, this process is referred to as p-doping.

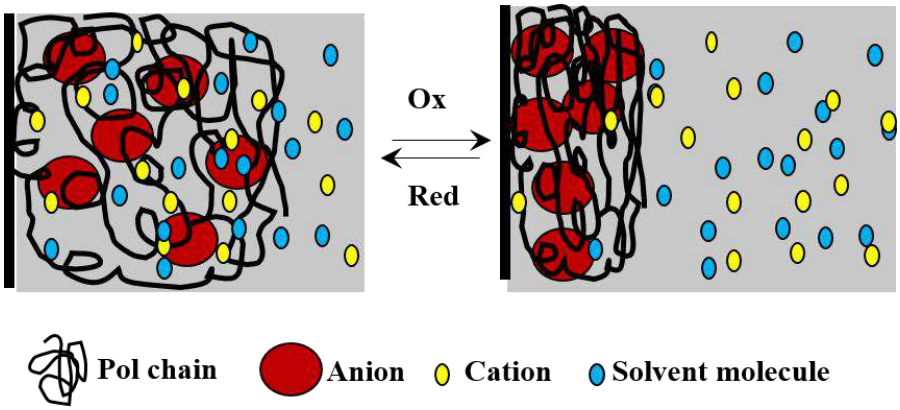

Figure 1.15 *Schematic diagram showing polymer swelling and contraction associated with p-doping via cation exchange*

N-doping (reduction)

Conducting polymers with high electronic affinity undergo *n-doping*, enabling transitions from a neutral to a reduced state. Under high cathodic potentials, electrons are injected into the polymer chains, generating and storing negative charges. Polymers such as PEDOT, polythiophene, and polyfluorenes exhibit this behavior. The execution of reaction (1.6) requires highly stable solvents and supporting salts. During reduction, these materials undergo volumetric swelling due to structural rearrangements associated with charge uptake, while neutralisation leads to contraction of the polymer matrix. It is shown in the reaction.1.5.

$$(\boldsymbol{Pol^0})_s + \boldsymbol{n}(\boldsymbol{C^+})_{aq} + \boldsymbol{ne^-} \rightleftarrows [(\boldsymbol{Pol^{n-}})_s\,(\boldsymbol{C^+})_n(\boldsymbol{Solv})_m]_{gel} \qquad (1.5)$$

Very recently, the electrochemistry of CPs has been revisited by Toribio's group [166, 167]. Toribio proposed the concept of structural electrochemistry and the electrochemically stimulated conformation relaxation (ESCR) model, thereby considering the CPs as composition-dependent materials and their applicability as biomimetic sensors of the surrounding condition [168]. This thesis also explores the electrochemistry of CPs composited with NGQDs and tries to explore their applicability as simultaneous sensors of surrounding environmental conditions.

Objectives of the work

- To improve the supercapacitor performance of Ni MOF-based materials through nitrogen enrichment using PVP as a nitrogen source and structure directing agent, and fabricate a symmetric supercapacitor.
- With an objective to enhance the supercapacitive performance of conducting polymers using graphene quantum dots.
- To study the reaction-driven biomimetic sensing characteristics of NGQDs/PPy and NGQDs/PANI composites.

References

[1] R.K. Baranwal, N. Biswas, B. Oraon, G. Majumdar, Advances in surface engineering for improved energy storage, (2020).
[2] A. Schneuwly, R. Gallay, Properties and applications of supercapacitors from the state-of-the-art to future trends, in: Proceeding PCIM, Citeseer, 2000, pp. 1.
[3] N. Singh, V. Singh, N. Bisht, P. Negi, A. Dhyani, R.K. Sharma, B. Tewari, A comprehensive review on supercapacitors: Basics to recent advancements, Journal of Energy Storage, 121 (2025) 116498.

[4] C. Largeot, C. Portet, J. Chmiola, P.-L. Taberna, Y. Gogotsi, P. Simon, Relation between the ion size and pore size for an electric double-layer capacitor, Journal of the American Chemical Society, 130 (2008) 2730-2731.
[5] S.G. Krishnan, H.D. Pham, D.P. Dubal, Supercapacitors: Materials, Design, and Commercialization, Elsevier, 2024.
[6] M.E. Şahin, F. Blaabjerg, A. Sangwongwanich, A comprehensive review on supercapacitor applications and developments, Energies, 15 (2022) 674.
[7] C.V.M. Gopi, S. Alzahmi, V. Narayanaswamy, R. Vinodh, B. Issa, I.M. Obaidat, Supercapacitors: A promising solution for sustainable energy storage and diverse applications, Journal of Energy Storage, 114 (2025) 115729.
[8] S.C. Smith, P. Sen, B. Kroposki, Advancement of energy storage devices and applications in electrical power system, in: 2008 IEEE Power and Energy Society General Meeting-Conversion and Delivery of Electrical Energy in the 21st Century, IEEE, 2008, pp. 1-8.
[9] M.M. Rahman, I. Khan, K. Alameh, The role of energy storage technologies for sustainability in developing countries, in: Renewable Energy and Sustainability, Elsevier, 2022, pp. 347-376.
[10] S. Kulandaivalu, Y. Sulaiman, Recent advances in layer-by-layer assembled conducting polymer based composites for supercapacitors, Energies, 12 (2019) 2107.
[11] J. Tan, Z. Li, M. Ye, J. Shen, Nanoconfined space: Revisiting the charge storage mechanism of electric double layer capacitors, ACS Applied Materials & Interfaces, 14 (2022) 37259-37269.
[12] S. Najib, E. Erdem, Current progress achieved in novel materials for supercapacitor electrodes: mini review, Nanoscale Advances, 1 (2019) 2817-2827.
[13] E.E. Miller, Y. Hua, F.H. Tezel, Materials for energy storage: Review of electrode materials and methods of increasing capacitance for supercapacitors, Journal of Energy Storage, 20 (2018) 30-40.
[14] S.Y. Attia, S.G. Mohamed, Y.F. Barakat, H.H. Hassan, W.A. Zoubi, Supercapacitor electrode materials: addressing challenges in mechanism and charge storage, Reviews in Inorganic Chemistry, 42 (2022) 53-88.
[15] W. Hsieh, T.-L.A. Horng, H.-C. Huang, H. Teng, Facile simulation of carbon with wide pore size distribution for electric double-layer capacitance

based on Helmholtz models, Journal of Materials Chemistry A, 3 (2015) 16535-16543.
[16] M. Salanne, B. Rotenberg, K. Naoi, K. Kaneko, P.-L. Taberna, C.P. Grey, B. Dunn, P. Simon, Efficient storage mechanisms for building better supercapacitors, Nature Energy, 1 (2016) 1-10.
[17] J. Libich, J. Máca, J. Vondrák, O. Čech, M. Sedlaříková, Supercapacitors: Properties and applications, Journal of energy storage, 17 (2018) 224-227.
[18] S. Fleischmann, J.B. Mitchell, R. Wang, C. Zhan, D.-e. Jiang, V. Presser, V. Augustyn, Pseudocapacitance: from fundamental understanding to high power energy storage materials, Chemical Reviews, 120 (2020) 6738-6782.
[19] A.M. Bryan, L.M. Santino, Y. Lu, S. Acharya, J.M. D'Arcy, Conducting polymers for pseudocapacitive energy storage, Chemistry of Materials, 28 (2016) 5989-5998.
[20] N.S. George, L.M. Jose, A. Aravind, Review on transition metal oxides and their composites for energy storage application, in: Updates on Supercapacitors, IntechOpen, 2022.
[21] M. Sarfraz, I. Shakir, Recent advances in layered double hydroxides as electrode materials for high-performance electrochemical energy storage devices, Journal of energy storage, 13 (2017) 103-122.
[22] C. Huang, P. Qin, D. Li, Q. Ruan, H. Song, L. Liu, Y. Wu, Y. Ma, Q. Li, K. Huo, Origin of superior pseudocapacitive mechanism of transition metal nitrides, Journal of Energy Chemistry, 69 (2022) 561-568.
[23] S. Cheng, W. Gao, Z. Cao, Y. Yang, E. Xie, J. Fu, Selective center charge density enables conductive 2D metal− organic frameworks with exceptionally high pseudocapacitance and energy density for energy storage devices, Advanced Materials, 34 (2022) 2109870.
[24] N.M. Chola, R.K. Nagarale, A pseudocapacitor from redox active covalent organic framework, Journal of The Electrochemical Society, 168 (2021) 100501.
[25] R. Chen, M. Yu, R.P. Sahu, I.K. Puri, I. Zhitomirsky, The development of pseudocapacitor electrodes and devices with high active mass loading, Advanced Energy Materials, 10 (2020) 1903848.

[26] Y.-M. Wei, K.D. Kumar, L. Zhang, J.-F. Li, Pseudocapacitive materials for energy storage: properties, mechanisms, and applications in supercapacitors and batteries, Frontiers in Chemistry, 13 (2025) 1636683.
[27] D.P. Chatterjee, A.K. Nandi, A review on the recent advances in hybrid supercapacitors, Journal of Materials Chemistry A, 9 (2021) 15880-15918.
[28] A. Afif, S.M. Rahman, A.T. Azad, J. Zaini, M.A. Islan, A.K. Azad, Advanced materials and technologies for hybrid supercapacitors for energy storage–A review, Journal of Energy Storage, 25 (2019) 100852.
[29] H. Liu, X. Liu, S. Wang, H.-K. Liu, L. Li, Transition metal based battery-type electrodes in hybrid supercapacitors: A review, Energy Storage Materials, 28 (2020) 122-145.
[30] G.A. Snook, P. Kao, A.S. Best, Conducting-polymer-based supercapacitor devices and electrodes, Journal of power sources, 196 (2011) 1-12.
[31] L.L. Zhang, X. Zhao, Carbon-based materials as supercapacitor electrodes, Chemical society reviews, 38 (2009) 2520-2531.
[32] D.-G. Wang, Z. Liang, S. Gao, C. Qu, R. Zou, Metal-organic framework-based materials for hybrid supercapacitor application, Coordination Chemistry Reviews, 404 (2020) 213093.
[33] Y. Xu, Q. Li, X. Guo, S. Zhang, W. Li, H. Pang, Metal organic frameworks and their composites for supercapacitor application, Journal of Energy Storage, 56 (2022) 105819.
[34] R. Li, J. Li, Q. Liu, T. Li, D. Lan, Y. Ma, Recent progress on covalent organic frameworks and their composites as electrode materials for supercapacitors, Advanced Composites and Hybrid Materials, 8 (2025) 86.
[35] H. Hegazy, S.S. Sana, T. Ramachandran, Y.A. Kumar, D.K. Kulurumotlakatla, H.S. Abd-Rabboh, S.C. Kim, Covalent organic frameworks in supercapacitors: Unraveling the pros and cons for energy storage, Journal of Energy Storage, 74 (2023) 109405.
[36] S. Xu, J. Wu, X. Wang, Q. Zhang, Recent advances in the utilization of covalent organic frameworks (COFs) as electrode materials for supercapacitors, Chemical Science, 14 (2023) 13601-13628.
[37] C.P. Raptopoulou, Metal-organic frameworks: synthetic methods and potential applications, Materials, 14 (2021) 310.

[38] N. Rabiee, Metal-organic frameworks (MOFs): an introduction, in: Logic for Metal− Organic Framework Selection: MOFs for Biomedical Applications, ACS Publications, 2024, pp. 1-5.
[39] E. Salehi, M. Khajavian, N. Sahebjamee, M. Mahmoudi, E. Drioli, T. Matsuura, Advances in nanocomposite and nanostructured chitosan membrane adsorbents for environmental remediation: A review, Desalination, 527 (2022) 115565.
[40] P. Li, F.-F. Cheng, W.-W. Xiong, Q. Zhang, New synthetic strategies to prepare metal–organic frameworks, Inorganic Chemistry Frontiers, 5 (2018) 2693-2708.
[41] C. Colella, The fascinating story of porous materials, Current Physical Chemistry, 2 (2012) 126-135.
[42] S.R. Batten, S.M. Neville, D.R. Turner, Coordination polymers: design, analysis and application, Royal Society of Chemistry, 2009.
[43] X. Zhang, Z. Chen, X. Liu, S.L. Hanna, X. Wang, R. Taheri-Ledari, A. Maleki, P. Li, O.K. Farha, A historical overview of the activation and porosity of metal–organic frameworks, Chemical Society Reviews, 49 (2020) 7406-7427.
[44] E.V. Perez, C. Karunaweera, I.H. Musselman, K.J. Balkus Jr, J.P. Ferraris, Origins and evolution of inorganic-based and MOF-based mixed-matrix membranes for gas separations, Processes, 4 (2016) 32.
[45] M. Muslim, M. Ahmad, Historical developments in synthesis approaches and photocatalytic perspectives of metal-organic frameworks, in: Photocatalysts-New Perspectives, IntechOpen, 2022.
[46] T.-H. Chen, I. Popov, W. Kaveevivitchai, O.S. Miljanić, Metal–organic frameworks: rise of the ligands, Chemistry of materials, 26 (2014) 4322-4325.
[47] P. Rocío-Bautista, I. Taima-Mancera, J. Pasán, V. Pino, Metal-organic frameworks in green analytical chemistry, Separations, 6 (2019) 33.
[48] M. Kim, Y. Lee, H.R. Moon, Carboxylate-Based Metal–Organic Framework and Coordination Polymer Glasses: Progress and Perspectives, Accounts of Chemical Research, 57 (2024) 2347-2357.
[49] V.F. Yusuf, N.I. Malek, S.K. Kailasa, Review on metal–organic framework classification, synthetic approaches, and influencing factors: applications in energy, drug delivery, and wastewater treatment, ACS omega, 7 (2022) 44507-44531.

[50] N. Stock, S. Biswas, Synthesis of metal-organic frameworks (MOFs): routes to various MOF topologies, morphologies, and composites, Chemical reviews, 112 (2012) 933-969.
[51] S. Kitagawa, Metal–organic frameworks (MOFs), Chemical Society Reviews, 43 (2014) 5415-5418.
[52] T. De Villenoisy, X. Zheng, V. Wong, S.S. Mofarah, H. Arandiyan, Y. Yamauchi, P. Koshy, C.C. Sorrell, Principles of design and synthesis of metal derivatives from MOFs, Advanced Materials, 35 (2023) 2210166.
[53] Q. Wang, D. Astruc, State of the art and prospects in metal–organic framework (MOF)-based and MOF-derived nanocatalysis, Chemical reviews, 120 (2019) 1438-1511.
[54] S. Vignesh, K. Ahmad, T.H. Oh, Progress in nickel MOF-based materials for electrochemical biosensor and supercapacitor applications, Biosensors, 15 (2025) 560.
[55] G. Chaturvedi, R. Jaiswal, S. Ilangovan, S. Sujatha, K. Ajeesh, S.S.V. Tatiparti, A systematic approach for selecting suitable morphologies for supercapacitor applications through morphological stability map–A case of Ni-MOF, Ceramics International, 49 (2023) 9382-9394.
[56] W. Chen, L. Du, C. Wu, Hydrothermal synthesis of MOFs, in: Metal-organic frameworks for biomedical applications, Elsevier, 2020, pp. 141-157.
[57] Y.-R. Lee, J. Kim, W.-S. Ahn, Synthesis of metal-organic frameworks: A mini review, Korean Journal of Chemical Engineering, 30 (2013) 1667-1680.
[58] H. Reinsch, N. Stock, Synthesis of MOFs: A personal view on rationalisation, application and exploration, Dalton Transactions, 46 (2017) 8339-8349.
[59] A. Ghoorchian, A. Afkhami, T. Madrakian, M. Ahmadi, Electrochemical synthesis of MOFs, in: Metal-organic frameworks for biomedical applications, Elsevier, 2020, pp. 177-195.
[60] V.V.e. Butova, M.A. Soldatov, A.A. Guda, K.A. Lomachenko, C. Lamberti, Metal-organic frameworks: structure, properties, methods of synthesis and characterization, Russian Chemical Reviews, 85 (2016) 280.
[61] W.-J. Son, J. Kim, J. Kim, W.-S. Ahn, Sonochemical synthesis of MOF-5, Chemical Communications, (2008) 6336-6338.

[62] N. Al Amery, H.R. Abid, S. Al-Saadi, S. Wang, S. Liu, Facile directions for synthesis, modification and activation of MOFs, Materials Today Chemistry, 17 (2020) 100343.
[63] R. Díaz, M.G. Orcajo, J.A. Botas, G. Calleja, J. Palma, Co8-MOF-5 as electrode for supercapacitors, Materials letters, 68 (2012) 126-128.
[64] D.Y. Lee, S.J. Yoon, N.K. Shrestha, S.-H. Lee, H. Ahn, S.-H. Han, Unusual energy storage and charge retention in Co-based metal–organic-frameworks, Microporous and Mesoporous Materials, 153 (2012) 163-165.
[65] Y. Gong, J. Li, P.-G. Jiang, Q.-F. Li, J.-H. Lin, Novel metal (II) coordination polymers based on N, N′-bis-(4-pyridyl) phthalamide as supercapacitor electrode materials in an aqueous electrolyte, Dalton Transactions, 42 (2013) 1603-1611.
[66] N. Campagnol, R. Romero-Vara, W. Deleu, L. Stappers, K. Binnemans, D.E. De Vos, J. Fransaer, A hybrid supercapacitor based on porous carbon and the metal-organic framework MIL-100 (Fe), ChemElectroChem, 1 (2014) 1182-1188.
[67] K.M. Choi, H.M. Jeong, J.H. Park, Y.-B. Zhang, J.K. Kang, O.M. Yaghi, Supercapacitors of nanocrystalline metal–organic frameworks, ACS nano, 8 (2014) 7451-7457.
[68] D. Sheberla, J.C. Bachman, J.S. Elias, C.-J. Sun, Y. Shao-Horn, M. Dincă, Conductive MOF electrodes for stable supercapacitors with high areal capacitance, Nature materials, 16 (2017) 220-224.
[69] D. Feng, T. Lei, M.R. Lukatskaya, J. Park, Z. Huang, M. Lee, L. Shaw, S. Chen, A.A. Yakovenko, A. Kulkarni, Robust and conductive two-dimensional metal− organic frameworks with exceptionally high volumetric and areal capacitance, Nature Energy, 3 (2018) 30-36.
[70] Y. Yan, Y. Luo, J. Ma, B. Li, H. Xue, H. Pang, Facile synthesis of vanadium metal-organic frameworks for high-performance supercapacitors, Small, 14 (2018) 1801815.
[71] F. Yang, W. Li, B. Tang, Facile synthesis of amorphous UiO-66 (Zr-MOF) for supercapacitor application, Journal of Alloys and Compounds, 733 (2018) 8-14.
[72] X. Du, J. Zhang, H. Wang, Z. Huang, A. Guo, L. Zhao, Y. Niu, X. Li, B. Wu, Y. Liu, Solid–solid interface growth of conductive metal–organic framework nanowire arrays and their supercapacitor application, Materials Chemistry Frontiers, 4 (2020) 243-251.

[73] R. Rajak, M. Saraf, S.M. Mobin, Mixed-ligand architected unique topological heterometallic sodium/cobalt-based metal–organic framework for high-performance supercapacitors, Inorganic chemistry, 59 (2020) 1642-1652.
[74] V. Aggarwal, S. Solanki, B.D. Malhotra, Applications of metal–organic framework-based bioelectrodes, Chemical Science, 13 (2022) 8727-8743.
[75] H. Furukawa, K.E. Cordova, M. O'Keeffe, O.M. Yaghi, The chemistry and applications of metal-organic frameworks, Science, 341 (2013) 1230444.
[76] M.M. Salehi, F. Esmailzadeh, F. Hassanzadeh-Afruzi, Applications of MOFs, in: Physicochemical Aspects of Metal-Organic Frameworks: A New Class of Coordinative Materials, Springer, 2023, pp. 197-305.
[77] Y. Peng, S. Sanati, A. Morsali, H. García, Metal–organic frameworks as electrocatalysts, Angewandte Chemie International Edition, 62 (2023) e202214707.
[78] C. Li, H. Zhang, M. Liu, F.-F. Lang, J. Pang, X.-H. Bu, Recent progress in metal–organic frameworks (MOFs) for electrocatalysis, Industrial Chemistry & Materials, 1 (2023) 9-38.
[79] Y. Pan, R. Abazari, Y. Wu, J. Gao, Q. Zhang, Advances in metal–organic frameworks and their derivatives for diverse electrocatalytic applications, Electrochemistry Communications, 126 (2021) 107024.
[80] M.U. Shahid, T. Najam, M. Islam, A.M. Hassan, M.A. Assiri, A. Rauf, A. ur Rehman, S.S.A. Shah, M.A. Nazir, Engineering of metal organic framework (MOF) membrane for waste water treatment: synthesis, applications and future challenges, Journal of water process engineering, 57 (2024) 104676.
[81] V. Russo, M. Hmoudah, F. Broccoli, M.R. Iesce, O.-S. Jung, M. Di Serio, Applications of metal organic frameworks in wastewater treatment: a review on adsorption and photodegradation, Frontiers in Chemical Engineering, 2 (2020) 581487.
[82] M.H. Manzoor, N. Naz, S.M.G. Naqvi, S. Ashraf, M.Z. Ashiq, F. Verpoort, Wastewater treatment using metal-organic frameworks (MOFs), Applied Materials Today, 40 (2024) 102358.
[83] Y. Qian, F. Zhang, H. Pang, A review of MOFs and their composites-based photocatalysts: synthesis and applications, Advanced Functional Materials, 31 (2021) 2104231.

[84] Y. Shi, A.-F. Yang, C.-S. Cao, B. Zhao, Applications of MOFs: Recent advances in photocatalytic hydrogen production from water, Coordination Chemistry Reviews, 390 (2019) 50-75.
[85] M.Z. Hussain, Z. Yang, Z. Huang, Q. Jia, Y. Zhu, Y. Xia, Recent advances in metal–organic frameworks derived nanocomposites for photocatalytic applications in energy and environment, Advanced Science, 8 (2021) 2100625.
[86] J. Chen, R. Abazari, K.A. Adegoke, N.W. Maxakato, O.S. Bello, M. Tahir, S. Tasleem, S. Sanati, A.M. Kirillov, Y. Zhou, Metal–organic frameworks and derived materials as photocatalysts for water splitting and carbon dioxide reduction, Coordination Chemistry Reviews, 469 (2022) 214664.
[87] N. Kornienko, Y. Zhao, C.S. Kley, C. Zhu, D. Kim, S. Lin, C.J. Chang, O.M. Yaghi, P. Yang, Metal–organic frameworks for electrocatalytic reduction of carbon dioxide, Journal of the American Chemical Society, 137 (2015) 14129-14135.
[88] H. Guo, H. Zhang, N. Wu, Z. Pan, C. Li, Y. Chen, Y. Cao, W. Yang, Trimesic acid-modified 2D NiCo-MOF for high-capacity supercapacitors, Journal of Alloys and Compounds, 934 (2023) 167779.
[89] S. Gao, Y. Sui, F. Wei, J. Qi, Q. Meng, Y. He, Facile synthesis of cuboid Ni-MOF for high-performance supercapacitors, Journal of materials science, 53 (2018) 6807-6818.
[90] C.-H. Wang, D.-W. Zhang, S. Liu, Y. Yamauchi, F.-B. Zhang, Y.V. Kaneti, Ultrathin nanosheet-assembled nickel-based metal–organic framework microflowers for supercapacitor applications, Chemical Communications, 58 (2022) 1009-1012.
[91] C. Qu, Y. Jiao, B. Zhao, D. Chen, R. Zou, K.S. Walton, M. Liu, Nickel-based pillared MOFs for high-performance supercapacitors: design, synthesis and stability study, Nano Energy, 26 (2016) 66-73.
[92] Y. Yan, P. Gu, S. Zheng, M. Zheng, H. Pang, H. Xue, Facile synthesis of an accordion-like Ni-MOF superstructure for high-performance flexible supercapacitors, Journal of Materials Chemistry A, 4 (2016) 19078-19085.
[93] P. Du, Y. Dong, C. Liu, W. Wei, D. Liu, P. Liu, Fabrication of hierarchical porous nickel based metal-organic framework (Ni-MOF) constructed with nanosheets as novel pseudo-capacitive material for

asymmetric supercapacitor, Journal of colloid and interface science, 518 (2018) 57-68.
[94] J. Yang, P. Xiong, C. Zheng, H. Qiu, M. Wei, Metal–organic frameworks: a new promising class of materials for a high performance supercapacitor electrode, Journal of Materials Chemistry A, 2 (2014) 16640-16644.
[95] H. Shirakawa, E.J. Louis, A.G. MacDiarmid, C.K. Chiang, A.J. Heeger, Synthesis of electrically conducting organic polymers: halogen derivatives of polyacetylene,(CH) x, Journal of the Chemical Society, Chemical Communications, (1977) 578-580.
[96] H. Shirakawa, A. McDiarmid, A. Heeger, Twenty-five years of conducting polymers, Chemical communications, 2003 (2003) 1-4.
[97] G. Marsh, Electronic polymers revolution, Materials Today, 4 (2001) 4-6.
[98] Y. Cao, P. Smith, A.J. Heeger, Mechanical and electrical properties of polyacetylene films oriented by tensile drawing, Polymer, 32 (1991) 1210-1218.
[99] A.G. MacDiarmid, Nobel Lecture:"Synthetic metals": A novel role for organic polymers, Reviews of Modern Physics, 73 (2001) 701.
[100] S.C. Rasmussen, Early history of conductive organic polymers, in: Conductive Polymers, CRC Press, 2018, pp. 1-22.
[101] T.A. Skotheim, Handbook of conducting polymers, CRC press, 1997.
[102] A.G. MacDiarmid, "Synthetic metals": a novel role for organic polymers (Nobel lecture), Angewandte Chemie International Edition, 40 (2001) 2581-2590.
[103] F.G. Córdova, Y.A. Ismail, J.G. Martinez, A.S. Al Harrasi, T.F. Otero, Conducting polymers are simultaneous sensing actuators, in: Electroactive Polymer Actuators and Devices (EAPAD) 2013, SPIE, 2013, pp. 29-43.
[104] A.G. MacDiarmid, A.J. Heeger, Organic metals and semiconductors: The chemistry of polyacetylene,(CH) x, and its derivatives, Synthetic Metals, 1 (1980) 101-118.
[105] Y.A. Ismail, A. Shabeeba, M.P. Sidheekha, L. Rajan, Conducting polymer/hydrogel systems as soft actuators, Actuators: Fundamentals, Principles, Materials and Applications, (2020) 211-252.
[106] C. Chiang, M. Druy, S. Gau, A. Heeger, E. Louis, A.G. MacDiarmid, Y. Park, H. Shirakawa, Synthesis of highly conducting films of derivatives

of polyacetylene,(CH) x, Journal of the American Chemical Society, 100 (1978) 1013-1015.
[107] C.K. Chiang, C. Fincher Jr, Y.W. Park, A.J. Heeger, H. Shirakawa, E.J. Louis, S.C. Gau, A.G. MacDiarmid, Electrical conductivity in doped polyacetylene, Physical review letters, 39 (1977) 1098.
[108] L. Dai, Intelligent macromolecules for smart devices: from materials synthesis to device applications, Springer, 2004.
[109] S. Ghosh, J. Majhi, S. Sharma, K. Priya, A. Bandyopadhyay, A review on the development of electron and ion conductive polymer hydrogels and their composites for flexible and smart supercapacitors, Journal of Energy Storage, 74 (2023) 109423.
[110] A.G. MacDiarmid, A.J. Epstein, Polyanilines: a novel class of conducting polymers, Faraday discussions of the Chemical Society, 88 (1989) 317-332.
[111] A. MacDiarmid, J. Chiang, A. Richter, Epstein, AJ, Polyaniline: a new concept in conducting polymers, Synthetic Metals, 18 (1987) 285-290.
[112] A. Heeger, Charge storage and charge transport in conducting polymers: solitons, polarons and bipolarons, Philosophical Transactions of the Royal Society of London. Series A, Mathematical and Physical Sciences, 314 (1985) 17-35.
[113] J.L. Bredas, G.B. Street, Polarons, bipolarons, and solitons in conducting polymers, Accounts of chemical research, 18 (1985) 309-315.
[114] A.J. Heeger, S. Kivelson, J.R. Schrieffer, W.-P. Su, Solitons in conducting polymers, Reviews of Modern Physics, 60 (1988) 781.
[115] D.L. Gochnauer, T. Gilani, Conduction Mechanism in Electrically Conducting Polymers, American Journal of Undergraduate Research, 14 (2018).
[116] A.K. Singh, R. Prakash, Conduction mechanism in electronic polymers: Effect of morphology, in: 2008 2nd National Workshop on Advanced Optoelectronic Materials and Devices, IEEE, 2008, pp. 65-74.
[117] S.K. Simotwo, V. Kalra, Polyaniline-based electrodes: recent application in supercapacitors and next generation rechargeable batteries, Current Opinion in Chemical Engineering, 13 (2016) 150-160.
[118] J. Banerjee, K. Dutta, M.A. Kader, S.K. Nayak, An overview on the recent developments in polyaniline-based supercapacitors, Polymers for Advanced Technologies, 30 (2019) 1902-1921.

[119] Y. Wei, J. Wang, X. Jia, J.-M. Yeh, P. Spellane, Polyaniline as corrosion protection coatings on cold rolled steel, Polymer, 36 (1995) 4535-4537.
[120] N. Shoaie, M. Daneshpour, M. Azimzadeh, S. Mahshid, S.M. Khoshfetrat, F. Jahanpeyma, A. Gholaminejad, K. Omidfar, M. Foruzandeh, Electrochemical sensors and biosensors based on the use of polyaniline and its nanocomposites: A review on recent advances, Microchimica Acta, 186 (2019) 465.
[121] L. Abilevitch, L. Mizrahi, G. Cohen, S. Kenig, E. Amir, Polyaniline for Smart Textile Applications, Trends and Developments in Modern Applications of Polyaniline, (2023).
[122] A. Dallolio, G. Dascola, V. Varacca, V. Bocchi, Electronic paramagnetic resonance and conductivity of a black electrolytic oxypyrrole, Comptes Rendus Hebdomadaires Des Seances De L Academie Des Sciences Serie C, 267 (1968) 433-&.
[123] C. He, C. Yang, Y. Li, Chemical synthesis of coral-like nanowires and nanowire networks of conducting polypyrrole, Synthetic metals, 139 (2003) 539-545.
[124] A. Shabeeba, Electrochemical investigation of polypyrrole and polypyrrole/hydrogel hybrid materials for sensing and supercapacitor applications, in, Deparment of Chemistry, University of Calicut, 2023.
[125] E. Gutierrez Pineda, F. Alcaide, M.a.J. Rodríguez Presa, A.n.E. Bolzán, C.A. Gervasi, Electrochemical preparation and characterization of polypyrrole/stainless steel electrodes decorated with gold nanoparticles, ACS Applied Materials & Interfaces, 7 (2015) 2677-2687.
[126] M.M. Gvozdenović, B. Jugović, J. Stevanović, B.N. Grgur, Electrochemical synthesis of electroconducting polymers, Hemijska industrija, 68 (2014) 673-684.
[127] A.S. Saraç, B. Ustamehmetoğlu, M.I. Mustafaev, C. Erbil, G. Uzelli, Oxidative polymerization of pyrrole in polymer matrix, Journal of Polymer Science Part A: Polymer Chemistry, 33 (1995) 1581-1587.
[128] R.E. Myers, Chemical oxidative polymerization as a synthetic route to electrically conducting polypyrroles, Journal of electronic materials, 15 (1986) 61-69.

[129] H.C. Kang, K. Geckeler, Enhanced electrical conductivity of polypyrrole prepared by chemical oxidative polymerization: effect of the preparation technique and polymer additive, Polymer, 41 (2000) 6931-6934.
[130] G. Verbist, F. Peeters, J. Devreese, Large bipolarons in two and three dimensions, Physical Review B, 43 (1991) 2712.
[131] A.G. Green, A.E. Woodhead, CCXLIII.—Aniline-black and allied compounds. Part I, Journal of the Chemical Society, Transactions, 97 (1910) 2388-2403.
[132] A.G. Green, A.E. Woodhead, CXVII.—Aniline-black and allied compounds. Part II, Journal of the Chemical Society, Transactions, 101 (1912) 1117-1123.
[133] M. Khalid, A.M.B. Honorato, H. Varela, Polyaniline: synthesis methods, doping and conduction mechanism, Polyaniline—From Synthesis to Practical Applications; IntechOpen: London, UK, (2018).
[134] A. MacDiarmid, J. Chiang, A. Richter, N. Somasiri, A. Epstein, Polyaniline: synthesis and characterization of the emeraldine oxidation state by elemental analysis, Conducting polymers, 105 (1987).
[135] C. Menardo, M. Nechtschein, A. Rousseau, J. Travers, P. Hany, Investigation on the structure of polyaniline: 13C nmr and titration studies, Synthetic metals, 25 (1988) 311-322.
[136] N.P.S. Chauhan, M. Mozafari, Polyaniline: An introduction and overview, in: Fundamentals and Emerging Applications of Polyaniline, Elsevier, 2019, pp. 1-15.
[137] S. David, Y. Nicolau, F. Melis, A. Revillon, Molecular weight of polyaniline synthesized by oxidation of aniline with ammonium persulfate and with ferric chloride, Synthetic metals, 69 (1995) 125-126.
[138] Z. Sun, Y. Geng, J. Li, X. Wang, X. Jing, F. Wang, Catalytic oxidization polymerization of aniline in an H2O2 Fe2+ system, Journal of applied polymer science, 72 (1999) 1077-1084.
[139] H. Ding, M. Wan, Y. Wei, Controlling the diameter of polyaniline nanofibers by adjusting the oxidant redox potential, Advanced Materials, 19 (2007) 465-469.
[140] Z.A. Boeva, V.G. Sergeyev, Polyaniline: Synthesis, properties, and application, Polymer Science Series C, 56 (2014) 144-153.

[141] T. Girija, M. Sangaranarayanan, Investigation of polyaniline-coated stainless steel electrodes for electrochemical supercapacitors, Synthetic Metals, 156 (2006) 244-250.
[142] M. Bacon, S.J. Bradley, T. Nann, Graphene quantum dots, Particle & Particle Systems Characterization, 31 (2014) 415-428.
[143] P. Tian, L. Tang, K. Teng, S. Lau, Graphene quantum dots from chemistry to applications, Materials today chemistry, 10 (2018) 221-258.
[144] M. Kaur, M. Kaur, V.K. Sharma, Nitrogen-doped graphene and graphene quantum dots: A review onsynthesis and applications in energy, sensors and environment, Advances in colloid and interface science, 259 (2018) 44-64.
[145] Z. Ji, E. Dervishi, S.K. Doorn, M. Sykora, Size-dependent electronic properties of uniform ensembles of strongly confined graphene quantum dots, The journal of physical chemistry letters, 10 (2019) 953-959.
[146] C. Xia, X. Hai, X.-W. Chen, J.-H. Wang, Simultaneously fabrication of free and solidified N, S-doped graphene quantum dots via a facile solvent-free synthesis route for fluorescent detection, Talanta, 168 (2017) 269-278.
[147] C. Zhao, X. Song, Y. Liu, Y. Fu, L. Ye, N. Wang, F. Wang, L. Li, M. Mohammadniaei, M. Zhang, Synthesis of graphene quantum dots and their applications in drug delivery, Journal of Nanobiotechnology, 18 (2020) 142.
[148] T. Van Tam, N.B. Trung, H.R. Kim, J.S. Chung, W.M. Choi, One-pot synthesis of N-doped graphene quantum dots as a fluorescent sensing platform for Fe3+ ions detection, Sensors and Actuators B: Chemical, 202 (2014) 568-573.
[149] N. Sohal, B. Maity, S. Basu, Recent advances in heteroatom-doped graphene quantum dots for sensing applications, RSC advances, 11 (2021) 25586-25615.
[150] S. Santiago, T.N. Lin, C.-H. Chang, Y.-A. Wong, C.-A.J. Lin, C.-T. Yuan, J. Shen, Synthesis of N-doped graphene quantum dots by pulsed laser ablation with diethylenetriamine (DETA) and their photoluminescence, Physical Chemistry Chemical Physics, 19 (2017) 22395-22400.
[151] C. Hu, Y. Liu, Y. Yang, J. Cui, Z. Huang, Y. Wang, L. Yang, H. Wang, Y. Xiao, J. Rong, One-step preparation of nitrogen-doped graphene quantum dots from oxidized debris of graphene oxide, Journal of Materials Chemistry B, 1 (2013) 39-42.

[152] B. Zheng, Y. Chen, P. Li, Z. Wang, B. Cao, F. Qi, J. Liu, Z. Qiu, W. Zhang, Ultrafast ammonia-driven, microwave-assisted synthesis of nitrogen-doped graphene quantum dots and their optical properties, Nanophotonics, 6 (2017) 259-267.
[153] H. Safardoust-Hojaghan, M. Salavati-Niasari, O. Amiri, M. Hassanpour, Preparation of highly luminescent nitrogen doped graphene quantum dots and their application as a probe for detection of Staphylococcus aureus and E. coli, Journal of Molecular Liquids, 241 (2017) 1114-1119.
[154] A. Ramachandran, A.N. JS, S. Karunakaran Yesodha, Polyaniline-derived nitrogen-doped graphene quantum dots for the ultratrace level electrochemical detection of trinitrophenol and the effective differentiation of nitroaromatics: structure matters, ACS Sustainable Chemistry & Engineering, 7 (2019) 6732-6743.
[155] P. Wilczewska, J. Breczko, D.M. Bobrowska, M. Wysocka-Żołopa, J. Goclon, A. Basa, K. Winkler, Enhancement of polypyrrole electrochemical performance with graphene quantum dots in polypyrrole nanoparticle/graphene quantum dot composites, Journal of electroanalytical chemistry, 923 (2022) 116767.
[156] X. Shi, Z.-Z. Yin, J. Xu, S. Li, C. Wang, B. Wang, Y. Qin, Y. Kong, Preparation, characterization and the supercapacitive behaviors of electrochemically reduced graphene quantum dots/polypyrrole hybrids, Electrochimica Acta, 385 (2021) 138435.
[157] M. Vandana, H. Vijeth, S. Ashokkumar, H. Devendrappa, Hydrothermal synthesis of quantum dots dispersed on conjugated polymer as an efficient electrodes for highly stable hybrid supercapacitors, Inorganic Chemistry Communications, 117 (2020) 107941.
[158] K. Rahimpour, R. Teimuri-Mofrad, Novel hybrid supercapacitor based on ferrocenyl modified graphene quantum dot and polypyrrole nanocomposite, Electrochimica Acta, 345 (2020) 136207.
[159] R. Malik, S. Lata, U. Soni, P. Rani, R.S. Malik, Carbon quantum dots intercalated in polypyrrole (PPy) thin electrodes for accelerated energy storage, Electrochimica Acta, 364 (2020) 137281.
[160] M. Vandana, S. Veeresh, H. Ganesh, Y. Nagaraju, H. Vijeth, M. Basappa, H. Devendrappa, Graphene oxide decorated SnO2 quantum

dots/polypyrrole ternary composites towards symmetric supercapacitor application, Journal of Energy Storage, 46 (2022) 103904.
[161] J. Breczko, B. Grzeskiewicz, E. Gradzka, D.M. Bobrowska, A. Basa, J. Goclon, K. Winkler, Synthesis of polyaniline nanotubes decorated with graphene quantum dots: Structural & electrochemical studies, Electrochimica Acta, 388 (2021) 138614.
[162] M. Muhiuddin, N. Bharadishettar, N.A. Devi, A. Gautam, S.S. Chauhan, A.B. Siddique, M.I. Ahmad, M. Satyanarayan, U. Bhat, W. Akhtar, Neodymium doped graphene quantum dots/PANI composite for supercapacitor application, Journal of Alloys and Compounds, 1012 (2025) 178516.
[163] D. Arthisree, W. Madhuri, Optically active polymer nanocomposite composed of polyaniline, polyacrylonitrile and green-synthesized graphene quantum dot for supercapacitor application, International Journal of Hydrogen Energy, 45 (2020) 9317-9327.
[164] T.F. Otero, Structural and conformational chemistry from electrochemical molecular machines. Replicating biological functions. A review, The Chemical Record, 18 (2018) 788-806.
[165] T.F. Otero, Conducting polymers, electrochemistry, and biomimicking processes, in: Modern Aspects of Electrochemistry, Springer, 1999, pp. 307-434.
[166] L. Rajan, M.P. Sidheekha, A. Shabeeba, T.F. Otero, Y.A. Ismail, Structural electrochemistry of poly (3, 4-ethylenedioxythiophene) and its applicability as simultaneous sensor of environmental surroundings: self-sensing electrical, thermal, and chemical working conditions, Journal of Materials Chemistry A, 12 (2024) 4583-4600.
[167] L. Rajan, T.F. Otero, A. Ajayan, Y.A. Ismail, Electrochemistry of Poly (3, 4-ethylenedioxythiophene) coated polyvinyl alcohol (PEDOT/PVA) films as a model for the muscle functions quantification and triggering of sensing neuron pulses, Electrochimica Acta, (2025) 146561.
[168] T. Otero, I. Boyano, Comparative study of conducting polymers by the ESCR model, The Journal of Physical Chemistry B, 107 (2003) 6730-6738.

Chapter 2

Materials and Methods

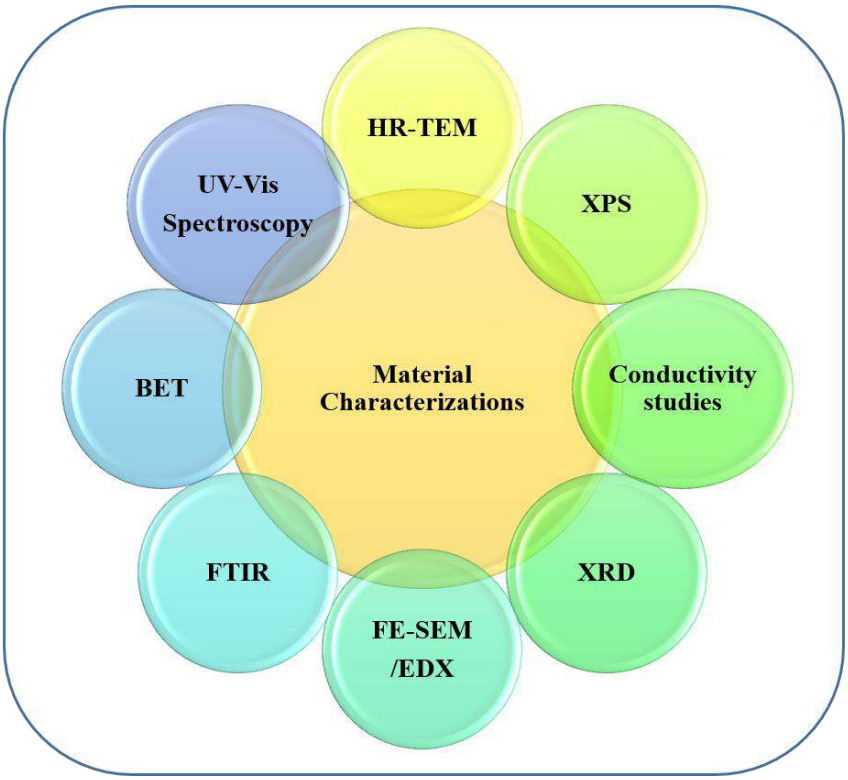

This chapter describes the materials and methods, including the characterization techniques employed in this study. It outlines the procedures used for the synthesis of MOFs, NGQDs, NGQDs/PPy, and NGQDs/PANI composites, as well as the fabrication of symmetric supercapacitor devices. In addition, the methods adopted for biomimetic sensing studies are clearly presented.

2.1. Materials

The materials and chemicals used in this study are listed in Table 2.1. All reagents were of analytical grade and used as received unless otherwise specified. Pyrrole and aniline monomers were purified by vacuum distillation before use. Double-distilled water was employed throughout all experiments.

Table 2.1 List of chemicals used for the entire study and their manufacturer

Chemicals	Manufacturer
Nickel nitrate ($Ni(NO_3)_2.6H_20$)	SRL, India
1,4-Benzene dicarboxylic acid (BDC)	Merck, India
Polyvinyl pyrrolidone (PVP)	Spectrochem
Dimethyl formamide	Merck, India
Ethanol	Merck, India
Pyrrole	Spectrochem, India
Ferric chloride ($FeCl_3$)	Merck, India
Acetone	Merck, India
Aniline	Merck, India
Ammonium persulfate	Qualigens, India
Polyvinyl alcohol (PVA)	Himedia, India
Sodium chloride (NaCl)	Merck, India
Sulphuric acid (H_2SO_4)	Merck, India
Sodium hydroxide (NaOH)	Merck, India
Potassium hydroxide (KOH)	Merck, India
Conductive carbon paste	MG chemicals, USA
Isopropanol (C_3H_8O)	Merck, India
Conducting carbon cloth	Fuel Cell Earth, USA

2.2. Synthetic methods

2.2.1. Synthesis of Ni MOF and N-Ni MOF

For the synthesis of the materials, $Ni(NO_3)_2.6H_2O$ (2.32g), 1,4-benzenedicarboxylicacid (BDC) (0.664g), and polyvinylpyrrolidone (PVP) (0.6 g) were dissolved in DMF (60ml), and their homogenous solution was prepared through sonication for 20 minutes. This mixed liquid autoclaved 160°C for 24 hours. The product was separated by centrifugation after cooling to ambient temperature. It was then washed repeatedly with DMF and ethanol before being dried overnight at 60 °C in a vacuum to produce N-Ni MOF. A bare Ni MOF was also prepared by adopting the same technique without the addition of PVP to examine the impact of PVP introduction on MOF morphology and supercapacitor performance [1, 2]. The schematic representation of the synthesis of both Ni MOF and N-Ni MOF is shown in Figure 2.1.

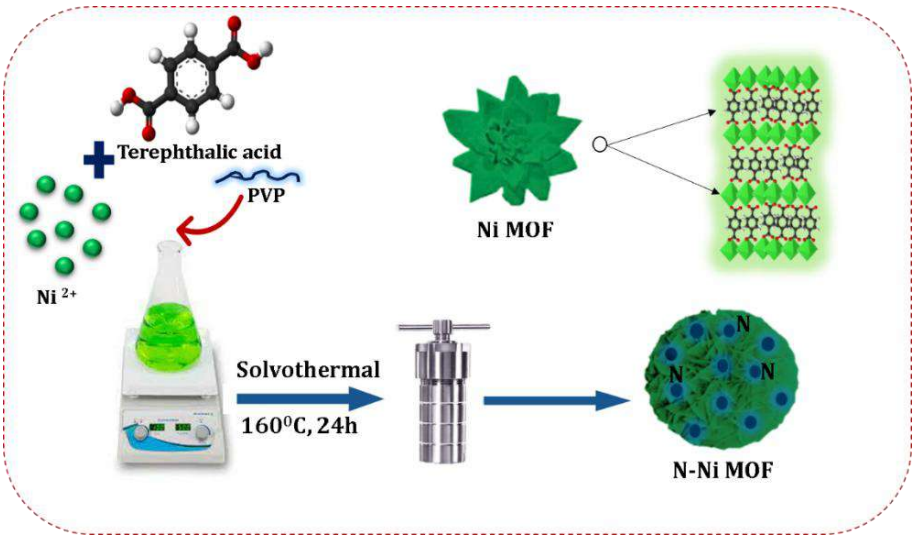

Figure 2.1 *Schematic representation of the synthesis of N-Ni MOF*

2.2.2. Synthesis of Polypyrrole

PPy powder was synthesized via in situ chemical oxidative polymerization of pyrrole using anhydrous $FeCl_3$ as the oxidizing agent. Polymerization was carried out by dissolving 0.01 mol of pyrrole in 100 mL of distilled water at 0-4 °C. The $FeCl_3$ solution (0.0125 mol in 100 mL water) was added dropwise to the pyrrole solution at 1 mL min^{-1} with constant stirring. The molar ratio of monomer to oxidant was maintained at 1:1.25. The reaction mixture was continuously stirred for 24 hours. The resulting fine black PPy precipitate was filtered using Whatman No. 1 filter paper, thoroughly washed with double-distilled water to remove residual oxidants, followed by acetone to eliminate low molecular weight oligomers. The purified product was dried in a hot air oven at 55 °C for 24 hours and subsequently ground into fine powder [3, 4]. The schematic representation of the synthesis of PPy is depicted in Figure 2.2.

Figure 2.2 *Schematic representation of the synthesis process of PPy*

2.2.3. Synthesis of NGQDs

The synthesis of NGQDs was carried out using PPy powder as the starting material. Initially, 300 mg of freshly prepared PPy powder was dispersed in 60 mL of distilled water using an ultrasonicator for 1 hour to achieve a

uniform dispersion. Subsequently, 1 mL of 2M NaOH solution was added to the mixture. The resulting solution was transferred into a 100 mL Teflon-lined autoclave, sealed, and heated at 200 °C for 12 hours. After the reaction, a pale-yellow colored liquid containing the NGQDs was carefully collected from the supernatant, while the unreacted PPy sediment was discarded from the bottom of the container [5, 6].

2.2.4. Synthesis of NGQDs/PPy composites

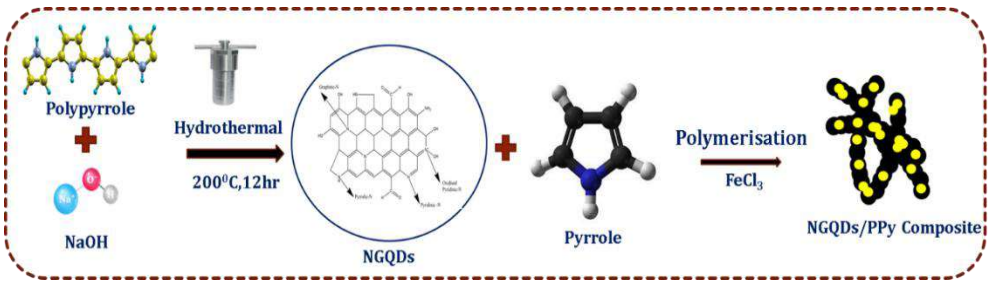

Figure 2.3 *Synthesis Scheme of NGQDs and NGQDs/PPy Composites*

The NGQDs/PPy composite was synthesized via an in-situ chemical oxidative polymerization process. Initially, 0.002 mol of pyrrole monomer was dissolved in 100 mL of a 1:1 ethanol-water mixture and stirred continuously for 1 hour to obtain a homogeneous solution. Subsequently, varying volumes of NGQDs solution (25, 50, 75, and 100 mL) of constant composition (1 mg/mL) were added to the pyrrole solution and stirred until a uniform dispersion was achieved. In parallel, 0.0025 mol of $FeCl_3$ dissolved in 100 mL of deionized water was added dropwise to the above mixture, maintained at 0-4 °C for 1 hour. The reaction mixture was then allowed to stand for 24 hours. The resulting product was thoroughly washed with deionized water to remove unreacted species and dried at 60 °C for 12 hours to obtain the NGQDs/PPy composites. The synthetic procedure adopted for the same is depicted in Figure 2.3 [7, 8]. The final composites, prepared

using 25, 50, 75, and 100 mL of NGQDs solution, were designated as NPP-25, NPP-50, NPP-75, and NPP-100, respectively.

2.2.5. Synthesis of NGQDs/PANI Composites

The NGQDs/PANI composite was synthesized by dispersing 25 mL of the NGQDs solution into 1 M H_2SO_4. To initiate oxidative polymerization, 0.002 mol of aniline was introduced into the mixture, which was maintained at 0-4 °C using an ice bath. Ammonium persulfate (APS, 0.0025 mol), previously dissolved in 1 M H_2SO_4, was then added dropwise at a controlled rate of 1 mL min^{-1} under continuous stirring, ensuring a molar ratio of aniline to APS of 1:1.25. The polymerization reaction was allowed to proceed for 12 hours. A black precipitate formed, was separated using Whatman No. 41 filter paper. The product was thoroughly washed with double-distilled water and followed by acetone and then dried in a hot-air oven at 55 °C for 24 hours [9, 10]. The dried product was finely ground and kept in a desiccator for further studies. The synthetic procedures adopted in Figure 2.4. The same procedure was adopted to synthesize four various compositions of NGQDs (10, 50 and 75 mL), and the resulting samples were designated as NPA-10, NPA-50, and NPA-75.

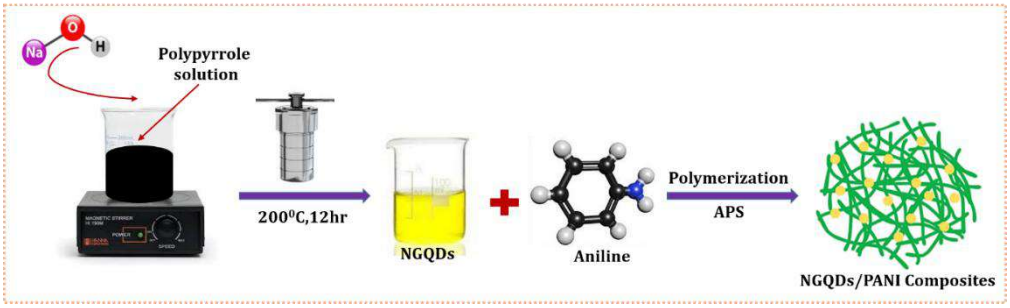

Figure 2.4 *Synthesis scheme illustrating the formation of NGQDs/PANI composites*

2.3. Characterization Techniques

2.3.1. Fourier transform infrared (FTIR) spectroscopy

FTIR spectroscopy is a commonly used analytical technique which offers comprehensive insights into molecular structure and chemical composition. In this study, JASCO FTIR-4100 was used for recording the spectra (using KBr disc method). This approach includes the interaction of infrared radiation with the samples, leading to changes in their dipole moment and corresponding vibrational levels. The FTIR spectrometer measures the intensity of transmitted or reflected radiation across a range of wavelengths to produce the spectrum. The spectrum offers a unique fingerprint of a sample, showcasing peaks that correspond to the vibrational frequencies of the chemical bonds within the sample.

2.3.2. X-Ray diffraction Analysis (XRD)

The crystal structure and phase purity of the synthesized samples were examined using powder XRD analysis. The diffraction pattern of the samples were measured using the X'pert3 powder with a Cu Kα (λ=1.5406A^0) radiation source over a range of 0^0 to 90^0. For the analysis, the samples were scanned in the 2θ range of 5-90^0.

XRD analysis was carried out to obtain information about the lattice parameters, crystalline size and phase composition of the samples. When a sample is irradiated with X-rays of wavelength λ, the X-rays interact with the electrons in the sample and produce a characteristic diffraction pattern. These patterns arise due to constructive interference of the scattered X-rays and obey Bragg's law, which relates the incident angle to the wavelength of the X-rays and the spacing between the crystal planes. According to Bragg's law,

$$n\lambda = 2d\sin\theta \quad (2.1)$$

where n is the order of the reflection, λ is the wavelength of x-rays, d is the interplanar spacing between two lattice planes, and θ is the angle of incidence. The diffraction pattern obtained by the instrument is typically compared with the standard reference pattern in the ICDD database (International Centre for Diffraction Data) to identify the determination of the crystal structure of the material.

2.3.3. UV-Visible Spectroscopy

UV-Visible spectroscopy studies the interaction of UV and visible light with matter to determine the electronic structure of the material. Based on the Beer-Lambert law,

$$A = \varepsilon cl \quad (2.2)$$

Where the absorbance (A) depends on the molar extinction coefficient (ε), concentration (c), and path length (l). UV-Vis Absorption spectra of NGQDs/PPy and NGQDs/PANI composites were recorded using a JASCO UV-Vis spectrophotometer (Model V-750, USA). A typical spectrometer consists of a light source, monochromator, quartz cuvette, and detector, and may operate in single or double-beam mode. In this technique, the monochromatic light passes through the sample, and the transmitted light intensity is measured.

2.3.4. UV-Visible-NIR Diffuse Reflectance Spectroscopy (DRS)

DRS is a technique used to obtain spectroscopic information of materials in the UV, visible, and near-infrared regions. UV-Vis DRS was conducted using a UV-Vis-NIR spectrophotometer (JASCO V-55). When light strikes a material, part of it is absorbed, transmitted, or reflected either as specular

(mirror-like) or diffuse (scattered) reflection. In DRS, the diffusely reflected light is collected using an integrating sphere coated with a reflective material such as barium sulfate. The sample is placed at the reflectance port, and the reflected light is directed to the detector after multiple internal reflections. Barium sulfate or teflon is used as a reference for baseline correction. The reflectance data are converted to an absorption-like spectrum using the Kubelka-Munk function,

$$F(R) = \frac{(1-R)^2}{2R} = \frac{k}{s} \quad (2.3)$$

Here, *R* denotes the reflectance, *k* represents the molar absorption coefficient, and *s* corresponds to the scattering coefficient. The Kubelka-Munk remission function enables the accurate estimation of a material's band gap by converting diffuse reflectance data into an equivalent absorption spectrum, thereby providing valuable insights into its optical properties. The band gap energy of the samples can be calculated using the relation.

$$E_g = \frac{hC}{\lambda} \quad (2.4)$$

2.3.5. Raman Spectroscopy

Raman spectroscopy is a non-destructive analytical technique widely used to obtain detailed information about a material's chemical structure, crystallinity, and molecular interactions. For recording the Raman spectra a laser confocal micro-Raman spectrometer (Bruker RFS 27 MultiRAM) was employed. The principle behind this method is Raman scattering, which involves inelastic scattering of photons. In this process, a monochromatic light source, typically a laser operating in the visible or near-infrared region, is directed onto the sample. When the laser light interacts with the molecules, the scattered photons experience an energy shift, either higher or lower than

the incident light energy. This shift corresponds to the vibrational modes of the sample, offering valuable insight into its molecular composition.

2.3.6. Field Emission Scanning Electron Microscopy (FE-SEM)

FE-SEM is an advanced analytical tool widely employed to observe the surface morphology and structural details of materials. It functions by directing a focused beam of high-energy electrons onto the sample surface, where their interaction with the atoms generates various signals that are converted into high-resolution images. In this study, a CARL ZEISS GeminiSEM-300 (Germany) operated at an accelerating voltage of 5 kV was utilized for surface morphological analysis. The instrument primarily consists of an electron gun, condenser lenses, scanning coils, detectors, a specimen stage, and a display unit. When the electron beam strikes the sample, it interacts with the surface atoms, resulting in the emission of secondary, backscattered, and Auger electrons. Among these, secondary electrons produced through inelastic collisions are primarily collected by the detector to form images with superior resolution and depth of detail, revealing both surface topography and compositional variations. Since electrical conductivity is essential for accurate imaging, non-conductive samples are commonly coated with a thin conductive layer, such as gold or silver, using a sputter-coating process before observation.

2.3.7. Energy dispersive X-ray spectroscopy (EDX)

Energy dispersive X-ray spectroscopy (EDX) was employed to determine the elemental composition of the prepared sample. In the present work, elemental analysis of the prepared samples was performed using an EDX detector attached to a Gemini 300 SEM system. Upon exposure to the focused electron beam, characteristic X-rays were generated due to the interaction between the incident electrons and the atoms of the sample.

The emitted X-rays possess energies specific to the element present, enabling their identification and quantification. The resulting EDX spectrum exhibited distinct peaks corresponding to constituent elements, confirming elemental composition of the sample.

2.3.8. High Resolution Transmission Electron Microscopy (HR-TEM)

The morphology, particle size, and shape of prepared samples were examined using transmission electron microscopy (TEM). The analysis was carried out using JEM-2100/JEOL high-resolution TEM instrument. TEM images provided direct information about the structural features and size distribution of the samples. It is also used to analyze nanostructures, providing valuable information on their elemental composition and electronic structure.

High-resolution TEM (HRTEM) was further employed to obtain detailed structural information at the nanoscale. The recorded HRTEM images revealed well-defined lattice features, confirming the crystalline nature of the material. The TEM and HRTEM results together offered clear insight into the morphology and structural characteristics of the prepared sample.

2.3.9. Conductivity studies

The electrical conductivity of the samples was measured using a two-point probe method at room temperature and ambient pressure within a frequency range of 10^{-2} to 10^{7} Hz, employing a broadband dielectric spectrometer (Novocontrol Technologies, Germany). For the measurement, each powdered sample was compressed into pellets using a stainless-steel die (1.3 cm diameter) and a hydraulic press. These pellets were placed between a pair of gold-plated parallel copper electrodes. The DC electrical conductivity was obtained by fitting the frequency-dependent conductivity data using the

universal power law, commonly known as Jonscher's power law, which is expressed as

$$\sigma_{AC} = \sigma_{DC} + A\omega^{s} \quad (2.5)$$

where ω is the angular frequency ($\omega = 2\pi f$), A, and s are constants. The value of 's' usually lies between 0 and 1.

2.3.10. Photoluminescence spectroscopy (PL)

PL spectroscopy is a widely used and effective technique to determine the optoelectronic properties of semiconductor materials. In this study, the PL spectra of the prepared samples were recorded using an Agilent Cary Eclipse spectrophotometer. PL analysis provides valuable insight into the fluorescence behaviour of materials by monitoring the light emitted after excitation. When a material is irradiated with energy above its optical band gap, a large number of excitons are generated. Analysis of the resulting emission spectra helps reveal the recombination behaviour of the photogenerated electrons and holes. Intense PL emission generally signifies a higher rate of electron–hole recombination, suggesting that fewer excitons are available to participate in chemical reactions.

2.3.11. Brunauer-Emmett-Teller analysis (BET)

Brunauer-Emmett-Teller (BET) analysis was carried out to determine the specific surface area and pore size distribution of the samples. Nitrogen adsorption/desorption isotherms were recorded using the BELSORP max analyzer. The method is based on the physical adsorption of nitrogen molecules onto the material surface. Because nitrogen can penetrate surface pores and interparticle spaces, overall surface area can be accurately estimated. The pore size distribution is further evaluated using the Barrett-Joyner-Halenda (BJH) method. The BET results showed that the samples

possess a relatively high surface area and well-defined porous structure, supporting their suitability for super capacitor applications.

2.3.12. X-ray photoelectron spectroscopy (XPS)

X-ray Photoelectron Spectroscopy (XPS), also referred to as Electron Spectroscopy for Chemical Analysis (ESCA), was employed to examine the surface composition and chemical states of the prepared materials. This surface-sensitive technique provides information from a depth of approximately 10 nm. It operates based on the photoelectric effect, in which incident X-rays with sufficient energy eject core-level electrons from the material surface.

The binding energy of these electrons is determined from their measured kinetic energy using the relation:

$$E_k = h\upsilon - E_{binding} - \phi \qquad (2.6)$$

Where $E_{binding}$ is the binding energy and ϕ represents the work function of the material. Since each element exhibits characteristic binding energy values, the XPS spectrum (binding energy against photoelectron intensity) allows identification and quantification of elements present (except hydrogen and helium) along with their oxidation states. Peak intensity comparison further enables semi-quantitative surface analysis and helps in understanding surface reaction mechanisms.

2.4. Electrochemical Characterizations

The electrochemical workstation used in this study is capable of performing various techniques such as cyclic voltammetry (CV), galvanostatic charge-discharge (GCD), electrochemical impedance spectroscopy (EIS), and chronopotentiometry. These methods are widely employed for evaluating the

electrochemical characteristics of supercapacitors, batteries, sensors, and solar cells. All experiments were conducted using a Zahner Zennium Pro electrochemical workstation (Germany) equipped with a galvanostat-potentiostat system and operated through the Thales XT software. The electrochemical measurements were carried out in a conventional three-electrode configuration, where Ag/AgCl (3 M KCl) was used as the reference electrode and a platinum wire served as the counter electrode. During the electrochemical experiments, a current was applied between the working and counter electrodes, while the potential of the working electrode was accurately measured with respect to the reference electrode. This configuration enabled precise evaluation of electrochemical processes, providing detailed insights into charge transfer, electrode kinetics, and the overall electrochemical behaviour of the materials.

For the electrochemical evaluation of the powder samples, a glassy carbon electrode (GCE) coated with the sample was utilised as the working electrode. Initially, the GCE surface was finely polished using alumina powder on a moistened microcloth until a bright, reflective finish was obtained. The electrode was then subjected to ultrasonic cleaning in ethanol water mixture to eliminate any surface impurities. Subsequently, 0.5 mg of the sample was dispersed in conductive carbon paste and evenly applied onto the GCE surface, forming a uniform active layer for electrochemical testing.

2.4.1. Cyclic Voltammetry (CV)

CV is one of the most widely used potentiodynamic electrochemical techniques for probing the redox characteristics and electron transfer behaviour of electroactive materials. In this method, the potential of the working electrode is systematically swept between two predetermined limits in a cyclic manner while recording the resulting current response. The

potential is linearly varied with time, first in the forward direction, where oxidation occurs, and then reversed to induce reduction, thus generating a characteristic cyclic voltammogram, a plot of current versus applied potential. The shape and position of the peaks in this voltammogram provide valuable insights into the redox reversibility, kinetics, and diffusion processes of the electroactive species involved. The rate at which the potential is scanned, known as the scan rate, plays a crucial role in determining the time scale of the electrochemical processes; higher scan rates result in faster potential sweeps and shorter cycle durations. Owing to its sensitivity and versatility, CV serves as a fundamental tool for investigating electron transfer mechanisms, interfacial reactions, and electrochemical performance in diverse applications such as supercapacitors, batteries, sensors, corrosion analysis, and electrocatalysis.

In this study, cyclic voltammetry (CV) was employed to assess the supercapacitive behaviour of the prepared samples. The specific capacitance (C_{sp}) was calculated from the obtained CV curves using Equation 2.7.

$$C_{sp} = \int_{v1}^{v2} \frac{I\Delta V}{m\vartheta\Delta v} \qquad (2.7)$$

In this expression, $\int I\Delta V$ denotes the integrated area enclosed by the CV curve, m corresponds to the mass of the active material, ϑ is the scan rate, and ΔV represents the applied potential window.

2.4.2. Galvanostatic Charge Discharge (GCD)

The GCD technique is a fundamental electrochemical method employed to evaluate the energy storage performance of supercapacitors and battery-type devices. In this experiment, a constant current is applied to the electrochemical cell, inducing either the charging or discharging process. During charging, electrons are driven into the electrode material, resulting in

charge accumulation, whereas during discharging, the stored charge is released as current flows in the reverse direction. The voltage response of the system is continuously recorded as a function of time, providing valuable insights into its electrochemical behavior. From the obtained charge-discharge curves, essential parameters such as specific capacitance or capacity, energy and power densities, coulombic efficiency, and cyclic stability can be derived. These measurements are crucial for understanding the intrinsic properties of electrode materials, optimizing their design, and assessing their suitability for advanced energy storage applications such as electric vehicles, renewable energy systems, and portable electronic devices. The specific capacitance (C_{sp}) of the electrode material was determined from the galvanostatic charge-discharge (GCD) profiles using Equation 2.8.

$$C_{sp} = \frac{I\Delta t}{m\Delta V} \tag{2.8}$$

Where I denotes the discharge current, Δt is the discharge time, m represents the mass of active material, and ΔV corresponds to the potential window of discharge. In a supercapacitor system, the energy storage capability per unit mass is expressed as the energy density (E), while the rate at which the stored energy can be delivered is described by the power density (P). For the solid-state symmetric supercapacitor device, the energy density and power density were determined using Equations 2.9 and 2.10, respectively.

$$E = \frac{0.5 \times C \times V^2}{3.6} \tag{2.9}$$

$$P = \frac{3600 \times E}{t} \tag{2.10}$$

In these equations, t (s) refers to the discharge duration, while V (V) indicates the applied potential window during operation.

2.4.3. Electrochemical Impedance Spectroscopy (EIS)

An electrochemical method for examining the electrical and interfacial characteristics of materials in electrochemical systems is electrochemical impedance spectroscopy (EIS). This technique measures the current response across a variety of frequencies after applying a tiny sinusoidal voltage signal at a constant potential. The impedance is calculated from the ratio of the applied voltage to the measured current and provides information related to charge transfer resistance, double-layer capacitance, and diffusion processes at the electrode–electrolyte interface.EIS data are generally presented in the form of Nyquist and Bode plots. The Nyquist plot displays the real and imaginary components of impedance, with the inclined linear region at low impedance and the semicircular region linked to charge transfer resistance.frequencies is related to diffusion-controlled processes. In the present study, EIS measurements were carried out at an open-circuit potential with an applied AC amplitude of 10 mV in the frequency range from 0.1 Hz to 100 kHz. The obtained data were analyzed using an equivalent circuit model with Zman software.

Supercapacitors, batteries, sensors, and corrosion-resistant coatings are just a few examples of the electrochemical systems that are frequently evaluated using EIS. It is possible to learn more about the system's capacitive and resistive characteristics by examining the frequency-dependent response.

2.4.4. Chronopotentiometry

Chronopotentiometry is a galvanostatic electrochemical technique in which a constant square-wave current is applied between two electrodes, and the resulting potential response is recorded as a function of time. In the present study, this technique is employed to investigate the reaction-driven sensing behaviour of the prepared materials, including current sensing.

Chronopotentiometry is a well-established method for understanding the kinetics and mechanisms of electrochemical reactions. The variation of potential with time is represented as a chronopotentiogram. Initially, a sudden potential jump is observed, which arises from various resistive components such as solution resistance, film resistance, counter-ion resistance, and interfacial resistance associated with the electrode system. Following this, the potential changes gradually with time. When the applied current exceeds the limiting current, diffusion alone is unable to supply sufficient reactants to sustain the imposed current, leading to a sharp increase in potential until the electrode potential of the subsequent reaction is reached. Upon reversing the applied current from anodic to cathodic, the anodic species undergo reduction, causing the potential to shift in the cathodic direction. The electrical energy consumed (U) during the reaction at any given time can be expressed in terms of the evolved potential (E) and the applied current.

$$U = I \int Edt \qquad (2.11)$$

Where $\int Edt$ denotes the area enclosed by the chrononopotentiograms

2.4. Fabrication of a symmetric supercapacitor device

A symmetric supercapacitor device was fabricated by sandwiching two carbon cloth electrodes coated with the sample, each having an active area of 2 cm^2, using Whatman filter paper No. 2 as the separator. The filter paper was impregnated with a PVA-based gel electrolyte, where KOH, NaCl, and H_2SO_4 were used as electrolytes in this thesis. The gel electrolyte was prepared by dissolving equal amounts of PVA and the electrolyte in 30 mL of deionized water under constant stirring. A piece of filter paper was immersed in the gel electrolyte, removed, and allowed to dry until the excess

water evaporated. The electrolyte-impregnated filter paper thus served as both the separator and the solid electrolyte and was carefully placed between the two electrodes to complete the device assembly.

References

[1] C.-H. Wang, D.-W. Zhang, S. Liu, Y. Yamauchi, F.-B. Zhang, Y.V. Kaneti, Ultrathin nanosheet-assembled nickel-based metal–organic framework microflowers for supercapacitor applications, Chemical Communications, 58 (2022) 1009-1012.
[2] S.A. Hira, D. Annas, S. Nagappan, Y.A. Kumar, S. Song, H.-J. Kim, S. Park, K.H. Park, Electrochemical sensor based on nitrogen-enriched metal–organic framework for selective and sensitive detection of hydrazine and hydrogen peroxide, Journal of Environmental Chemical Engineering, 9 (2021) 105182.
[3] A. Shabeeba, L. Rajan, M.P. Sidheekha, M.S. Thayyil, Y.A. Ismail, Polypyrrole/hydrogel hybrid films as multi sensing supercapacitor electrodes, Journal of Energy Storage, 55 (2022) 105724.
[4] A. Shabeeba, Y.A. Ismail, Chitosan/polypyrrole hybrid film as multistep electrochemical sensor: sensing electrical, thermal and chemical working ambient, Materials Research Bulletin, 152 (2022) 111817.
[5] A. Thadathil, D. Thacharakkal, Y.A. Ismail, P. Periyat, Polyindole-derived nitrogen-doped graphene quantum dots-based electrochemical sensor for dopamine detection, Biosensors, 12 (2022) 1063.
[6] A. Ramachandran, A.N. JS, S. Karunakaran Yesodha, Polyaniline-derived nitrogen-doped graphene quantum dots for the ultratrace level electrochemical detection of trinitrophenol and the effective differentiation of nitroaromatics: structure matters, ACS Sustainable Chemistry & Engineering, 7 (2019) 6732-6743.
[7] S. Sharanappa, S. Vijaykumar, D. Suresh, A.B. Shbil, H. Ganesha, S. Veeresh, Y. Nagaraju, H. Devendrappa, Synthesis of water-soluble nitrogen doped carbon quantum dots-polypyrrole nanocomposite via in-situ polymerization for high performance supercapacitor application, Journal of Energy Storage, 74 (2023) 109371.

[8] X. Jian, J.-g. Li, H.-m. Yang, L.-l. Cao, E.-h. Zhang, Z.-h. Liang, Carbon quantum dots reinforced polypyrrole nanowire via electrostatic self-assembly strategy for high-performance supercapacitors, Carbon, 114 (2017) 533-543.
[9] N. Punnakkal, S. Naneena, S.L. CP, A. Pradeep, S.B. TG, P.V. Suneesh, Nitrogen-doped graphene quantum dot embedded polyaniline for the fabrication of high-performance flexible supercapacitor with enhanced cycling stability, Journal of Energy Storage, 100 (2024) 113527.
[10] Q. Wang, H. Wang, D. Liu, P. Du, P. Liu, Synthesis of flake-shaped nitrogen-doped carbon quantum dot/polyaniline (N-CQD/PANI) nanocomposites via rapid-mixing polymerization and their application as electrode materials in supercapacitors, Synthetic Metals, 231 (2017) 120-126.

Chapter 3

Polyvinylpyrrolidone Assisted Synthesis of Ni MOF as an Electrode Material for Supercapacitor Applications

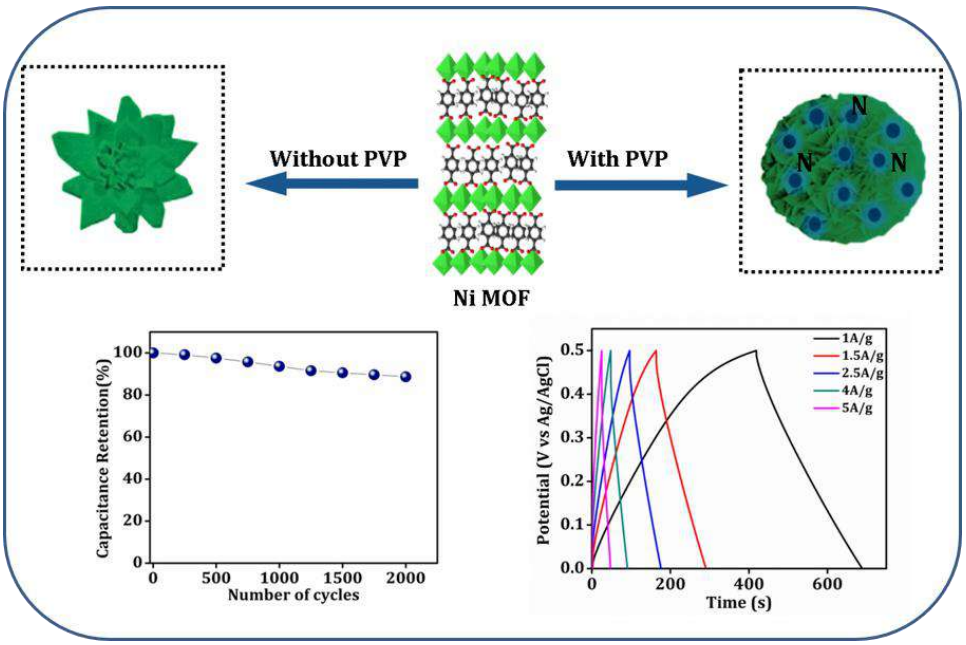

This chapter focuses on enhancing the supercapacitive performance of Ni MOF through nitrogen enrichment, using PVP, which acts as both a nitrogen source and a structure-directing agent. The structure, porosity, and morphology of the N-Ni MOF were characterized using XRD, BET surface area analysis, and SEM. Detailed electrochemical characterization and supercapacitive performance were evaluated using CV, GCD, and EIS techniques. Furthermore, the practical applicability of the material was demonstrated by fabricating a symmetric supercapacitor device.

3.1. Introduction

MOFs are a family of porous, crystalline materials composed of metal ions or clusters interconnected by organic ligands [1-4]. Their customizable pore sizes, vast surface areas, and substantial pore volumes render them excellent candidates for supercapacitor applications [5-7]. It is reported that MOFs can be employed as electrode materials for supercapacitors in many ways; MOFs can be utilized directly because of their distinctive architectures that offer numerous pseudocapacitive redox centers or can be used as templates via carbonization for EDLC electrodes or as precursors to make metal oxides for pseudocapacitor application [8-13].

Ni MOFs, in particular, are regarded as highly favorable electrode candidates for supercapacitor applications due to their well-ordered porous architecture, plentiful active sites for ion movement, flexible oxidation state (Ni^{2+}, Ni^{3+}), and tunable frameworks [2, 14-16]. These result in a high theoretical specific capacitance for Ni-based MOFs. For example, Wang. et al. reported a Ni-based MOF microflowers for supercapacitor application, delivering a specific capacitance of 1093 F g^{-1} [17]. However, the weak conductivity of Ni MOFs prevents their active usage as supercapacitors [18, 19].

To address this limitation, functionalizing MOFs by incorporating hetero-atoms, functional groups, polymers or other metal ions has proven to be an efficient strategy [20-22]. This approach enhances the inherent activity of pristine MOFs and improves the specific desired attributes. For instance, Chen et al. developed a nitrogen-doped Cu MOF utilizing PVP, which functions as an electrochemical sensor for detecting dopamine and sulfanilamide [23]. Notably, the strong electron-attracting nitrogen atom can change the electrical characteristics of the intrinsic material significantly, boosting the performance of MOF [20, 23]. The MOF morphology can be changed by doping it with nitrogen atom, which results from an optimum

distance for ion diffusion and a sufficient number of accessible active sites. Moreover, it can change the electron distribution of material and boost its wettability. This allows the electrode material and electrolyte to come into contact more efficiently [24-26].

In the present study, we explored for the first time, the impact of nitrogen enrichment in the Ni MOF framework achieved using PVP. PVP plays a dual role by acting as a source of nitrogen through its C-N functional group and as a morphology-directing agent. The nitrogen incorporation facilitated by PVP improved both specific capacitance and cyclic stability of the Ni MOF.

3.2. Results and Discussions

3.2.1. XRD Analysis

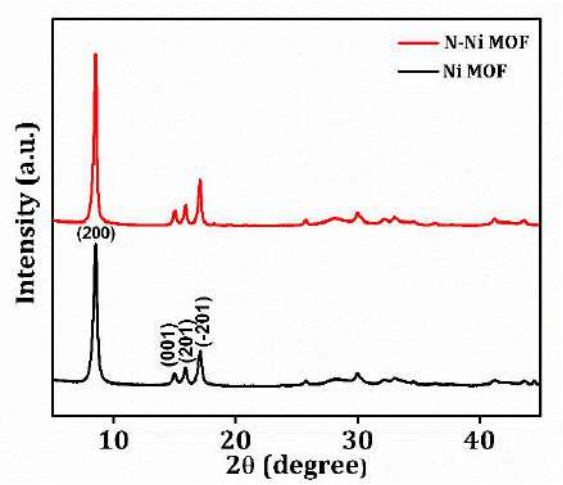

Figure 3.1 *XRD pattern of Ni MOF and N-Ni MOF*

Figure 3.1 presents the XRD patterns for Ni MOF and N-Ni MOF, revealing four distinct diffraction peaks for the $Ni_2(OH)_2$ BDC complex, marked as (001), (200), (201), and (201) planes in the 7.5-20 2θ range. The structure consists of two nickel atoms coordinated with six oxygen atoms, forming an octahedron. These octahedra are connected at the edges or corners within the

(200) plane, creating two-dimensional layers of nickel, which are interconnected with BDC molecules (CCDC 985792) [27, 28]. The distinct peaks of Ni MOF observed in both compounds confirm the successful synthesis of Ni MOF. Moreover, the XRD patterns of N-Ni MOF closely match those of Ni MOF in terms of peak geometry and position, with only minor variations in Bragg intensities. This indicates that the inclusion of PVP does not alter the fundamental architecture and texture of the Ni MOF structure [29-31].

3.2.2. FTIR Spectroscopy

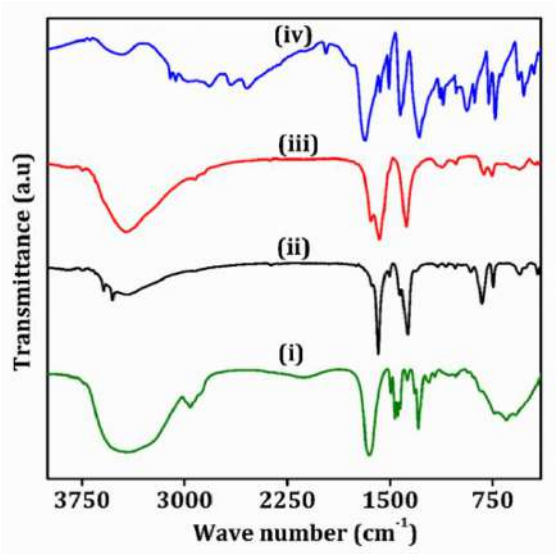

Figure 3.2 *FTIR spectra of **(i)** pure PVP **(ii)** Ni MOF **(iii)** N-Ni MOF **(iv)** Ligand (BDC)*

Figure 3.2 presents the FTIR spectra for pure PVP, Ni-MOF, N-Ni MOF, and the ligand BDC. The distinct differences in FTIR peaks among N-Ni MOF, Ni MOF, and BDC highlight the formation of the MOF structure. In both N-Ni MOF and Ni MOF, a broad band at 3300-3600 cm^{-1} range

corresponds to OH^- bond stretching, and the absorption bands at 1300-1700 cm^{-1} region are attributed to the asymmetric (1574, 1581 cm^{-1}) and symmetric (1373, 1369 cm^{-1}) vibrations of carboxyl groups [32]. In addition to those bands, several additional peaks appeared around 754 and 749cm^{-1} due to the C-H bending vibration of the phenyl group. A prominent band at 554 cm^{-1} is attributed to the O-Ni-O vibrational mode. Strikingly, several distinct bands can be noticed in the N-Ni MOF in contrast to Ni MOF and BDC. Specifically, unlike Ni MOF, the C-H stretching vibration (2835-3000 cm^{-1}) of N Ni MOF is identical to that of PVP [25, 33].

3.2.3. DRS spectra

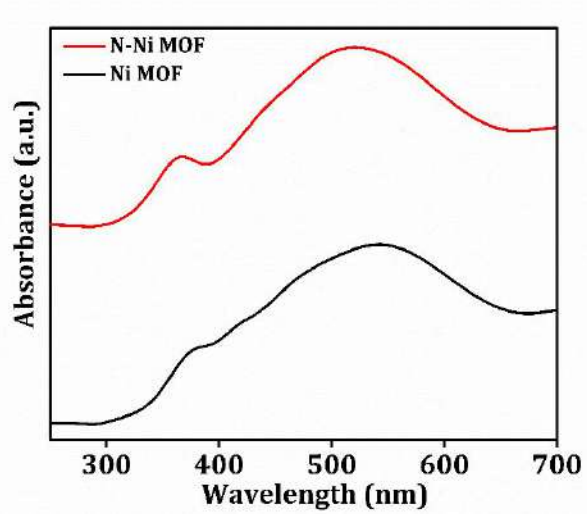

Figure 3.3 *DRS spectra of Ni MOF and N-Ni MOF*

The optical absorption properties of the materials were examined in the range of 200-900 nm using DRS. As depicted in Figure 3.3, UV-Vis DRS spectra of Ni MOF and N-Ni MOF reveal two peaks at 363 and 520 nm, corresponding to the characteristic transitions of Ni^{2+} [18]. It is apparent from Figure 3.3 that both two peaks at nearly matching wavelengths but with

heightened intensities. This similarity suggests that the fundamental structure of N-Ni MOF remained unchanged in the presence of PVP. Notably, Ni MOF and N-Ni MOF possess band gap energies of 2.85 eV and 2.87 eV, respectively [34].

3.2.4. SEM and TEM Analysis

SEM and TEM analyses were conducted to investigate the morphologies of the synthesized samples. Interestingly, the morphology of Ni MOF changes significantly with the introduction of PVP as a synthetic regulator. As depicted in Figure 3.4 (a-b), without PVP, Ni MOF displayed a flower-like structure.

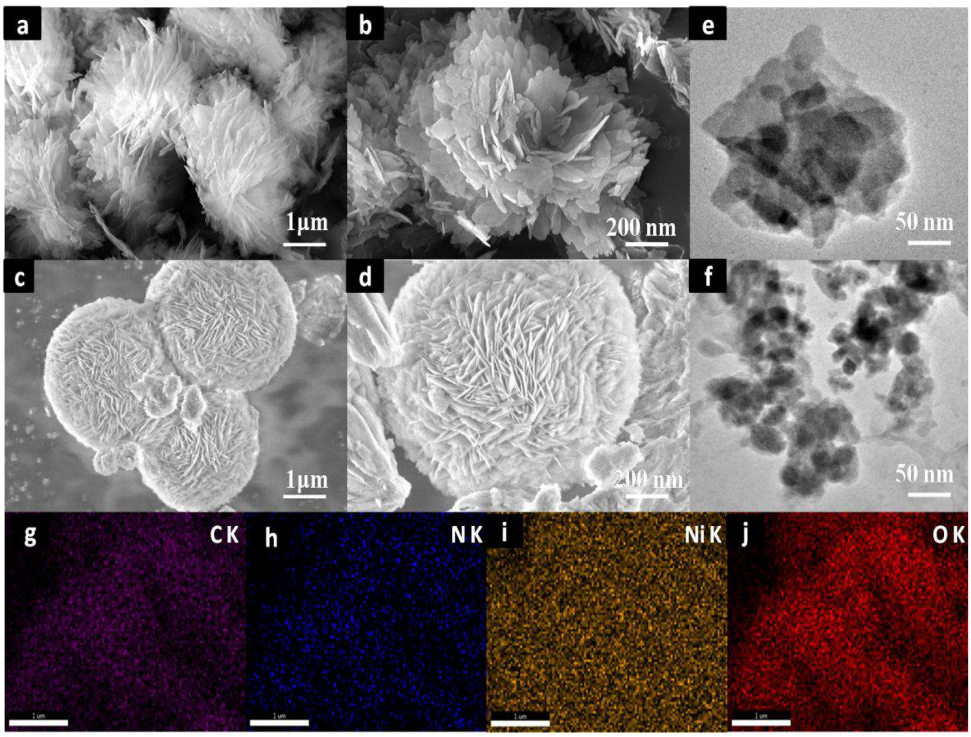

Figure 3.4 *SEM images of Ni MOF* ***(a-b)*** *and N-Ni MOF* ***(c-d)****, TEM images of* ***e)*** *Ni MOF and* ***f)*** *N-Ni MOF and* ***(g-j)*** *elemental mapping images C, N, Ni and O of N-Ni MOF*

Conversely, upon the introduction of PVP, N-Ni MOF exhibited hierarchical flower-like microspheres as shown in Figure 3.4(c-d). Here, PVP also functions as a capping agent, offering steric stabilization to the growing Ni MOF crystals. It adsorbs onto the MOF surface, inhibiting excessive growth in specific directions, which results in more uniform and controlled shapes providing substantial surface area for storing additional charges and ample space for active metal centers [35]. The findings demonstrated the impact of PVP on morphological control.

Figure 3.4 (e, f) shows TEM images of Ni MOF and N-Ni MOF, the particles have smooth surfaces and sharp edges, suggesting that the synthesized Ni MOF has enough crystallinity. Moreover, it indicates that PVP was densely coated on the surface of Ni MOF with high density. TEM analysis reveals that the addition of PVP increases the dispersion of Ni MOF particles, effectively minimizing aggregation. This improvement is vital for preserving the high surface area and achieving uniformity in electrochemical applications. The reduced aggregation is evident in TEM images, where the particles appear as individual entities or small clusters, rather than forming large agglomerates. The presence and consistent distribution of C, N, O, and Ni throughout the framework were revealed in the elemental mapping images depicted in Figure 3.4 (g-j).

3.2.5. EDX Spectral Analysis

The EDX spectrum of the synthesized N-Ni MOF illustrates the atom ratios of C, N, O, and Ni elements, which are 28.42, 2.23, 35.26, and 33.29% respectively (Figure 3.5). This eloquently showcases the harmonious dispersion of these elements within the entire MOF architecture, underscoring the pivotal role of the N element in shaping the intricate N-Ni MOF structure [36].

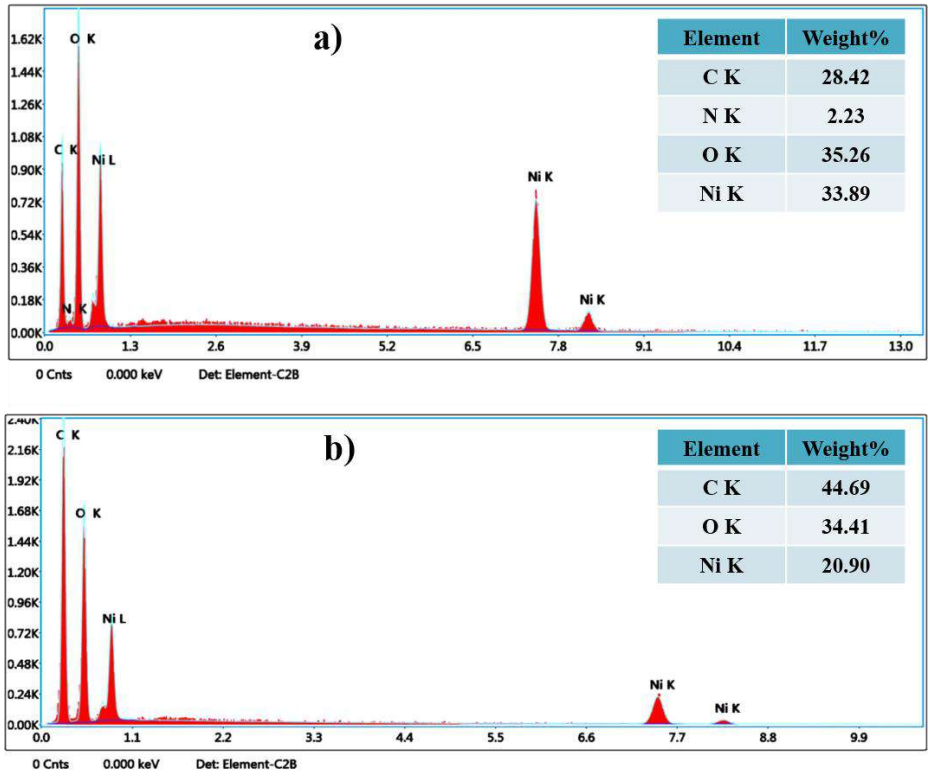

Figure 3.5 *EDX spectrum of* ***(a)*** *N-Ni MOF and* ***(b)*** *Ni MOF*

3.2.6. BET Surface area analysis

The electrochemical traits of active materials are greatly impacted by their porosity and surface area. Figure 3.6 shows the typical N_2 adsorption-desorption isotherms for Ni MOF and N-Ni MOF and the corresponding pore size distribution plots were investigated.

Table 3.1 Surface area and pore size of Ni MOF and N-Ni MOF

Sample	BET surface area ($m^2 g^{-1}$)	Total pore volume ($cm^3 g^{-1}$)	Average pore diameter (nm)
Ni MOF	64.80	0.065	1.26
N-Ni MOF	108.18	0.129	1.96

The findings reveal that the BET-specific surface areas of Ni MOF and N-Ni MOF are 64.80 and 108.18 m^2 g^{-1}, respectively, showing that N-Ni MOF offers a greater surface area. Table 3.1 shows the specific surface area, average pore diameter, and pore volume.

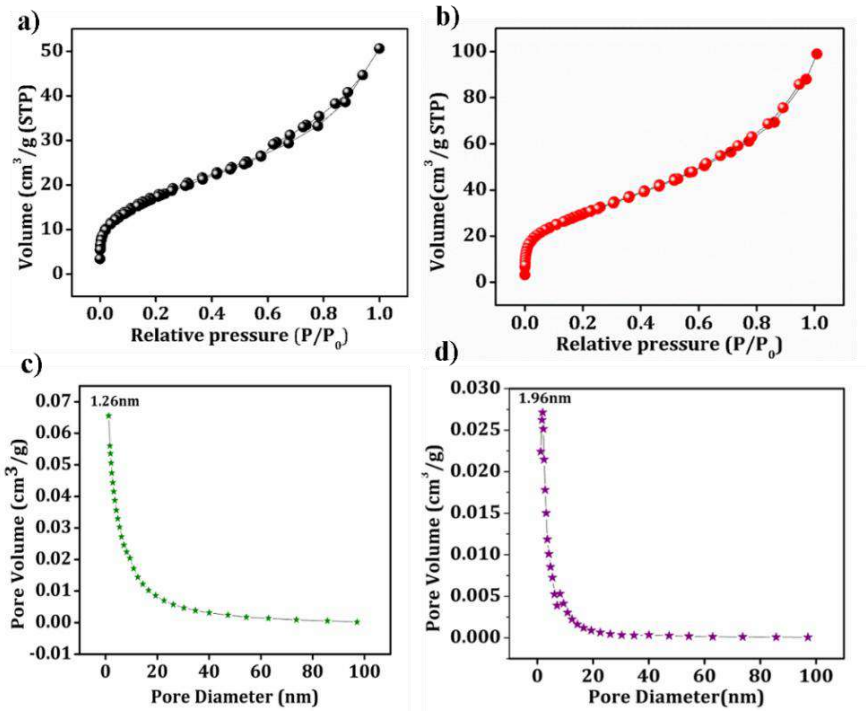

Figure 3.6 *N_2 adsorption-desorption isotherms of* ***(a)*** *Ni MOF,* ***(b)*** *N-Ni MOF and BJH pore size distribution plot of* ***(c)*** *Ni MOF and* ***(d)*** *N-Ni MOF*

Recently it was reported that PVP can improve the specific surface area, average pore size and pore volume [37, 38]. Additionally, based on the BJH method, the pore diameter of all the samples was less than 2 nm demonstrating the microporous nature. The increased surface area improves faradaic redox reactions at surface sites, thereby augmenting the supercapacitive performance of the electrode material. The N-Ni MOF electrode material has a superior microporous structure that allows higher transit of electrolyte ions into the active sites, potentially improving the high

rate capabilities of the material [23]. Furthermore, nitrogen incorporation could improve wettability and ion accessibility, leading to more stable electrochemical performance.

3.2.7. Contact angle

The better wettability of N-Ni MOF was assessed through contact angle measurement using water as the solvent. The results are presented in Figure 3.7. The average contact angles for Ni MOF and N-Ni MOF were found to be 31.7° and 24.2°, respectively. The data indicate a reduction in the contact angle for N-Ni MOF compared to Ni MOF, confirming improved wettability.

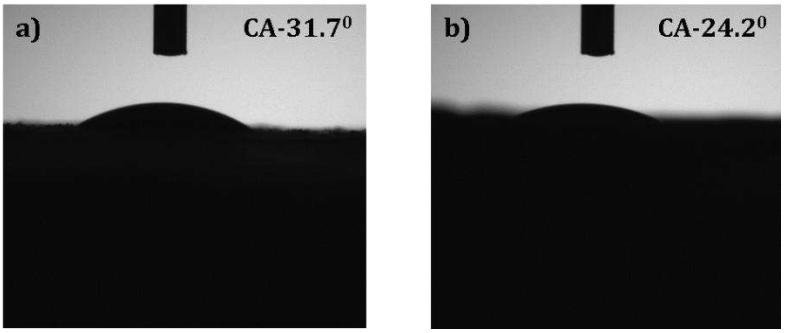

Figure 3.7 *The contact angle images for* ***(a)*** *Ni MOF,* ***(b)*** *N-Ni MOF*

3.2.8. XPS Analysis

To understand the surface chemistry of the samples, XPS was employed. The results are presented in Figure 3.8(a) and (b), which reveal that the survey spectra of the surfaces of Ni MOF and N-Ni MOF are composed of carbon, oxygen, and nickel. Notably, a minor presence of nitrogen was detected on the surface of the N-Ni MOF. In the high-resolution C1s spectra of N-Ni MOF in Figure 3.8c, three peaks with energies around 284.1, 285.3, and 288.1 eV are evident, indicative of C-C or C=C, C-OH, and C=O bonds, respectively [39, 40]. In the O1s spectra, there are two discernible peaks

around 530.7 and 532.4 eV, representing Ni-O and C=O bonds, respectively (Fig. 3.8d). The N1s spectrum of N-Ni MOF has two peaks at 399.7 and 400.6 eV respectively (Figure 3.8e). Especially noteworthy is the confirmation of PVP molecule in N-Ni MOF, indicated by the presence of pyrrolic N peak at 400.6eV.

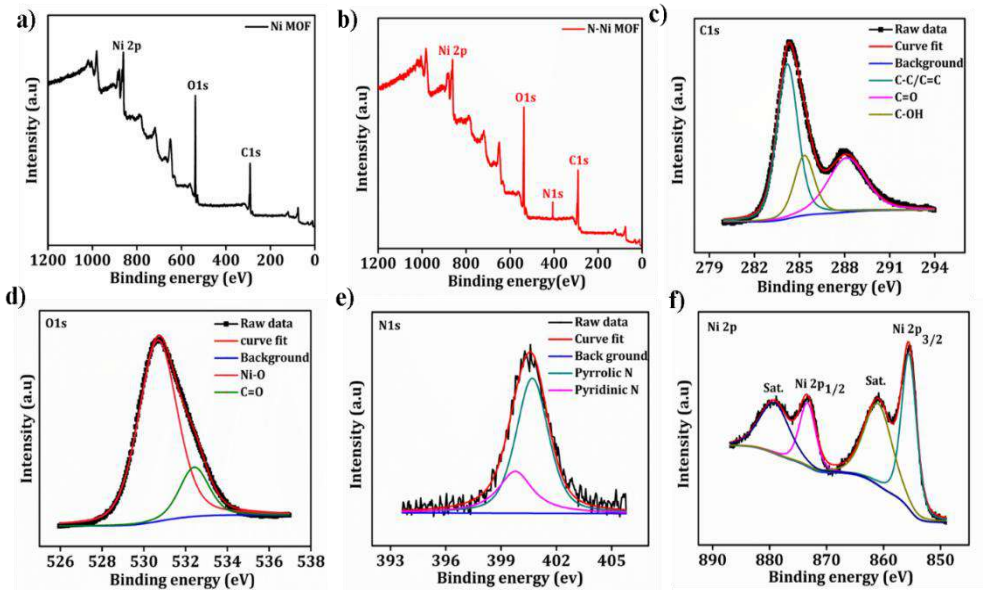

Figure 3.8 *XPS of* ***(a)*** *Ni MOF,* ***(b)*** *N-Ni MOF and high-resolution* ***(c)*** *C1s* ***(d)*** *O1s* ***(e)*** *N1s* ***(f)*** *Ni 2p spectra of N-Ni MOF*

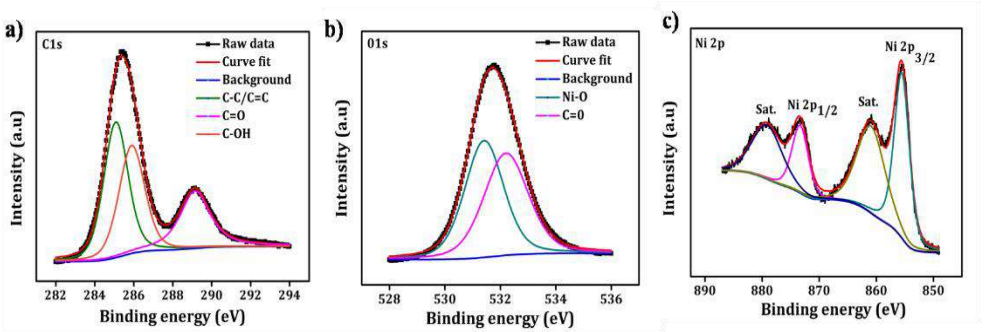

Figure 3.9 *High resolution* ***(a)*** *C1s,* ***(b)*** *O1s,* ***(c)*** *Ni 2p spectrum of Ni MOF*

The high-resolution Ni 2p spectra (Fig. 3.8f) exhibit two predominant peaks at 855.7 and 873.5 eV, accompanied by two corresponding satellite peaks at 861.05 and 879.4 eV. These peaks are attributed to Ni $2p_{3/2}$ and Ni $2p_{1/2}$, respectively, reflecting the spin-orbit characteristics of Ni^{2+} [41-43]. The high-resolution spectra of C1s, O1s, and Ni 2p of Ni MOF are shown in Figure 3.9 (a-c). The EDX results were corroborated by the rising nitrogen content of N-Ni MOF (Figure 3.5).

3.2.9. Electrochemical characteristics

3.2.9.1. Cyclic voltammetry

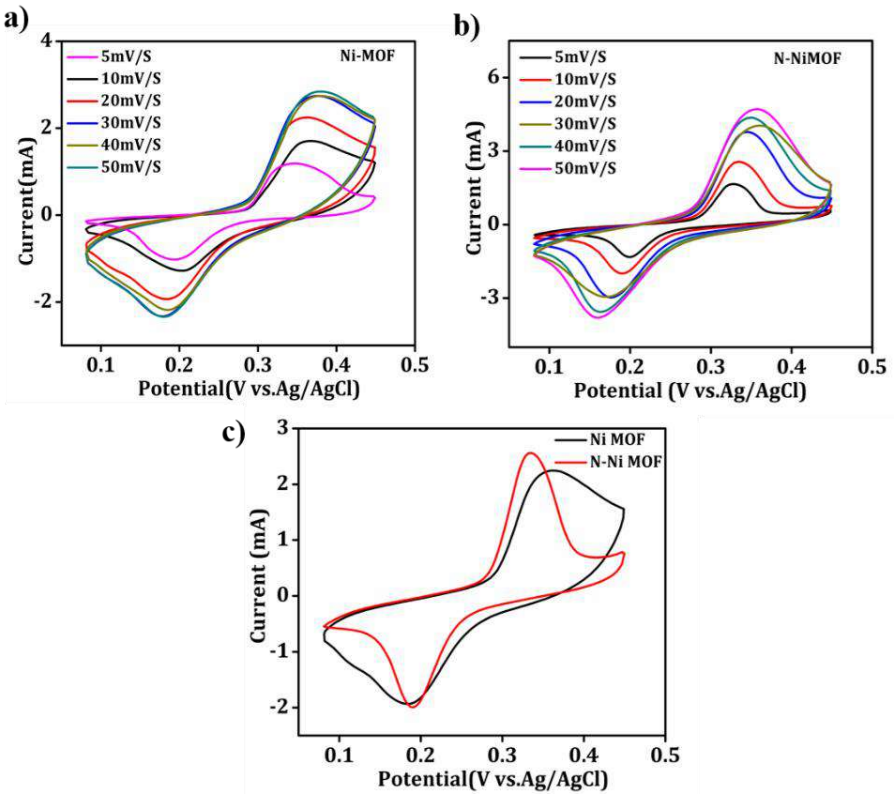

Figure 3.10 *CV curves of* ***(a)*** *Ni MOF and* ***(b)*** *N-Ni MOF at different scan rates* ***(c)*** *comparative CV curves of Ni MOF and N-Ni MOF at 10 mV* s^{-1}

In a three-electrode setup, the electrochemical performance of the Ni MOF and N-Ni MOF were investigated to evaluate whether the samples could be used as the electrode material for a supercapacitor application. The CV profiles of Ni MOF and N-Ni MOF, recorded in 2M KOH at various scan speeds within the voltage range of 0.08V to 0.45V are presented in Figure 3.10 (a) and (b). Please note that Ni MOF can effectively operate only within a narrow potential window, which remains a major limitation for its wider applicability. Equations 5 and 6 describe the reversible conversion between Ni (II) and Ni (III) in the presence of OH^- ions, giving rise to a pair of redox peaks that exhibit pseudocapacitive behavior [3, 42, 44].

$$Ni\ (II) + OH^- \leftrightarrows Ni\ (II)\ (OH) + e^- \quad (3.1)$$

$$Ni\ (II)\ (OH)^- \rightleftharpoons Ni\ (III)\ (OH) + e^- \quad (3.2)$$

The anodic and cathodic peaks shift as the scan rate increases, indicating minimal electrode material resistance and excellent rate capacity. Figure 3.10 (c) compares CV responses of the Ni MOF and N-Ni MOF at a scan rate of 10 mV s^{-1}.

3.2.9.2. Charge storage kinetic studies of N-Ni MOF

According to the power law, $i = av^b$, the current (i) typically relates to the scan rate (υ) where both a and b are constants. The b value can be used to qualitatively gauge the strength of the capacitive effect. A value of b=1 signifies surface redox reactions with non-diffusion-controlled mechanisms and the value of b=0.5 suggests ideal diffusion-controlled faradaic processes. The slope of the linear graph of log (i) versus log (υ) is utilized to assess the parameter b. As depicted in Figure 3.11(a) and 3.12, b values for anodic processes of N-Ni MOF were approximate to 0.5 indicating that the corresponding charge storage was predominantly governed by the diffusion dominated mechanism [36, 45].

The contributions of capacitive-controlled and diffusion-controlled mechanisms as a function of scan rate were determined using the equation.

$$i = k_1 \upsilon + k_2 \upsilon^{1/2} \qquad (3.3)$$

Here, i represents the peak current, υ denotes the scan rate, $k_1\upsilon$ and $k_2\upsilon^{1/2}$ represent the contributions of capacitive and diffusion-controlled processes respectively. The constants k_1 and k_2 at various potentials are obtained by plotting $i/\upsilon^{1/2}$ against $\upsilon^{1/2}$.

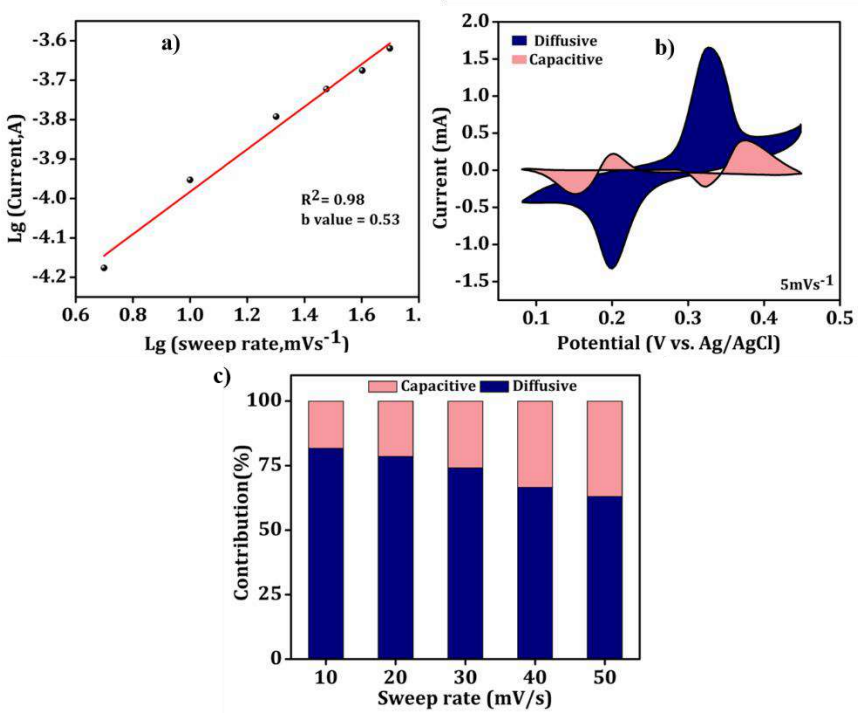

Figure 3.11 ***(a)*** *log I vs. log υ* ***(b)*** *distinction between the pseudo-capacitive and diffusion currents at a scan rate of 5mV* s^{-1} ***(c)*** *ratios of capacitance contributions from surface-controlled pseudocapacitive reactions and diffusion-limited intercalation/de-intercalation reactions at different sweep rates*

Figure 3.11 (b) illustrates the outcome of the analysis for the N-Ni MOF at 5mV s^{-1} with a capacitive (or pseudo-capacitive) contribution of 15.8%. Furthermore, with an increase in the scan rate, the share of the capacitive

(pseudo capacitive) contribution steadily rises, indicating that the N-Ni MOF has more active sites and better electrochemical performance. Figure 3.11(c) illustrates that the contribution of the diffusion-controlled process is reduced because ions have less time to diffuse into the material. Additionally, the polarization of the electrode results in a simultaneous rise in the area of the CV curve and the potential difference between the redox peaks [2].

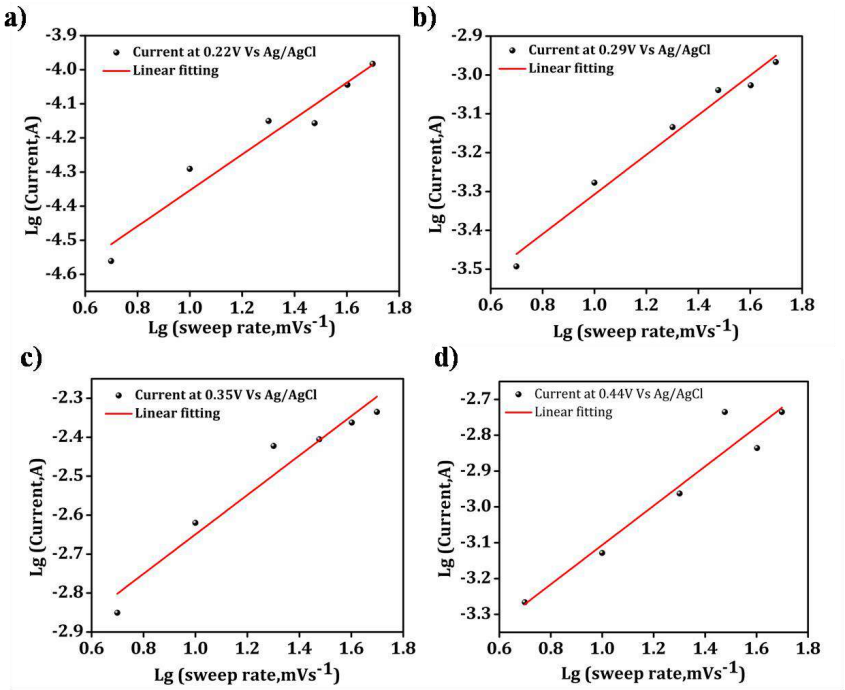

Figure 3.12 *The determination of b values at different potentials*

3.2.9.3. Galvanostatic charge-discharge studies

According to the galvanostatic charge-discharge profiles of the Ni MOF and N-Ni MOF at various current densities shown in Figure 3.13 (a, b), N-Ni MOF has a higher rate capability than Ni MOF. The GCD curves display a substantially asymmetrical charge-discharge pattern in the potential range from 0.08 to 0.45V as a result of pseudocapacitance attributes. The specific capacitance is determined from the GCD curves using Equation (2.1) in

Chapter 2. It is found to be 1519 F g^{-1}, 980 F g^{-1}, 887 F g^{-1}, 748 F g^{-1}, and 489 F g^{-1} for current densities of 1, 1.5, 2.5, 4 and 5 A g^{-1}, respectively (Figure 3.13c). The calculated specific capacitance of the N-Ni MOF is 1519 F g^{-1}, significantly exceeding that of Ni MOF [46, 47].

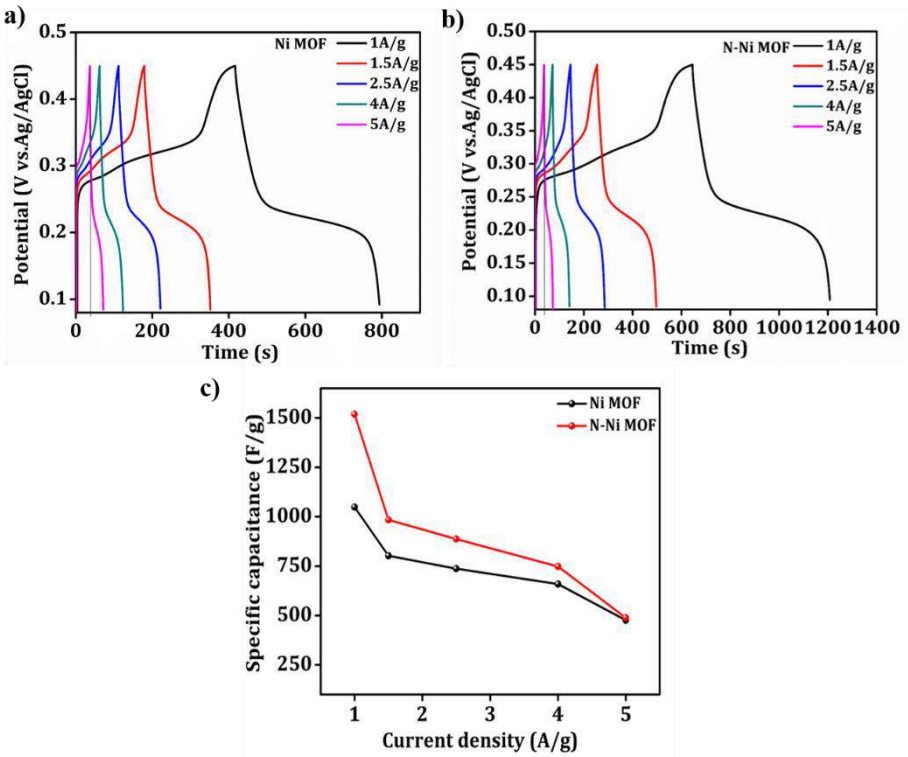

Figure 3.13 *The charge-discharge profiles of* ***(a)*** *Ni MOF,* ***(b)*** *N- Ni MOF,* ***(c)*** *Specific capacitance vs current density for the Ni MOF and N-Ni MOF*

The hierarchical flower-like microsphere structure of N-Ni MOF likely provides an ample specific surface area for faradaic reaction by constricting the OH^- ion diffusion pathway, thereby enhancing reaction potential, as evidenced by the SEM images above. The rich microporous architecture of N-Ni MOF improves the electron transfer and ions diffusion, boosting electrochemical performance, a finding corroborated by the BET measurements (Figure 3.6). The key point is that the C-N bonds in PVP

create favorable environments for faradaic reactions by enhancing electrical conductivity, increasing active site accessibility, improving wettability with electrolytes, and ensuring better electrochemical stability.

3.2.9.4. Electrochemical impedance spectra

The EIS spectral analysis of the samples were performed at frequencies between 10^{-2} to 10^{5} Hz to gain a better understanding of the electrochemical performance. The Nyquist plots of the as-synthesized samples are provided in Figure 3.14. It can be seen that N-Ni MOF possesses lesser charge-transfer resistance than Ni MOF, because the diameter of the semicircle of N-Ni MOF is smaller at high-frequency. Diffusion resistance (Warburg impedance) also decreases as the linear line gets closer to the vertical [48, 49]. N-Ni MOF exhibits lower diffusion resistance and charge-transfer resistance than Ni MOF, indicating that nitrogen incorporation can significantly reduce electrode material resistance, improving reaction kinetics.

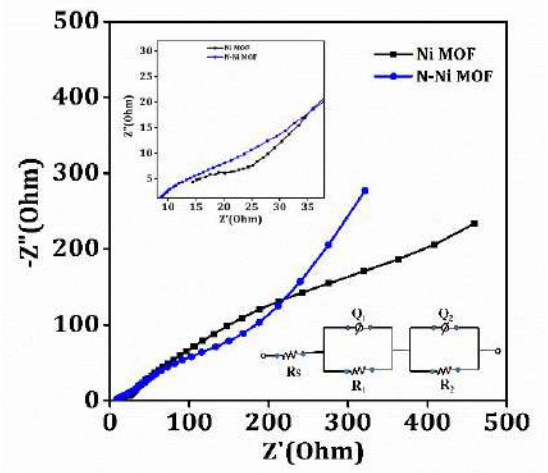

Figure 3.14 *Nyquist plots of the EIS spectra for the Ni MOF and N-Ni MOF (with the equivalent circuit used for fitting shown in the inset)*

The EIS results are fitted to the circuit and it becomes clear that the fitting result is quite similar to our experimental result. To comprehend the character of as-synthesized samples, we suggested an analogue circuit model which fits with the data from the experiments as shown in Figure 3.14. The great accuracy of the fitted results was confirmed through the chi-square value which was found to be around 7.6 $x10^{-3}$. The term R_S in the equivalent circuit denotes the solution resistance. The constant phase components of capacitance concerning the inner layer and diffusion layer are Q_1 and Q_2, respectively. R_1 stands for the resistance of the pore electrolyte and intermediate layer and R_2 is the barrier layer resistance [50].

3.2.9.5. Cyclic stability

Figure 3.15 (a) illustrates the charge-discharge experiments performed at 5 Ag^{-1}current density up to 2000 cycles to explore the cyclic stability of Ni MOF and N-Ni MOF. We have achieved a capacitance retention of 85% for N-Ni MOF, whereas the capacitance retention of N-Ni MOF was found to be 79%.

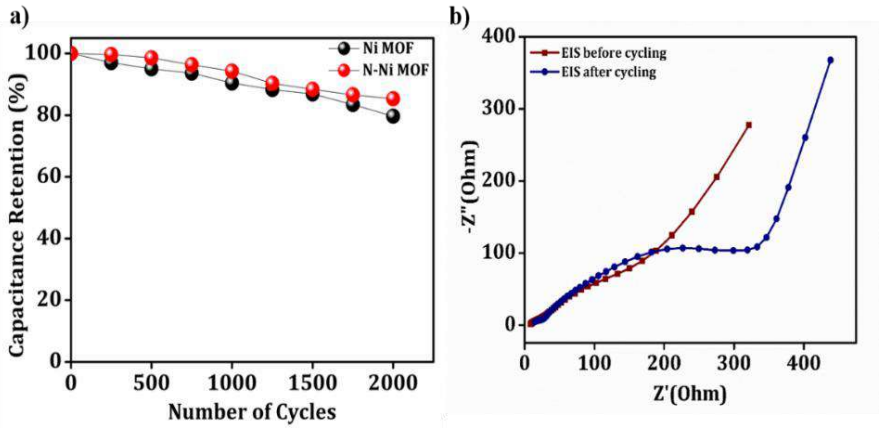

Figure 3.15 (*a*) *Cyclic performance of Ni MOF and N-Ni MOF at a current density of 5A g^{-1} over 2000 cycles* ***(b)*** *Nyquist plot of N-Ni MOF recorded before and after 2000 cycles*

This results show that the cyclic stability of N-Ni MOF has been enhanced significantly in addition to its high specific capacitance and improved rate capability. Figure 3.15 (b) illustrates the EIS spectra of the Ni MOF and N-Ni MOF electrodes before and after the life cycle test. In the high-frequency range, the diameter of the semicircle indicated low cell resistance before cyclic, suggesting a shorter path for ion/electron movement. However, post-cyclic, the EIS spectrum revealed an extended ion/electron transport pathway, as indicated by the increased charge transfer resistance. This may be ascribed to the electrochemical degradation or changes in material performance. Comparative property performance of the N-Ni MOF electrode with previously reported Ni MOF electrode material described in Table 3.2.

3.2.9.6. Symmetric supercapacitor device

We constructed a symmetric supercapacitor device by placing a KOH/Polyvinyl alcohol gel electrolyte between two N-Ni MOF electrodes, each with an area of 2 cm^2 arranged in parallel mode. The schematically illustrated symmetric all-solid-state supercapacitor device is shown in Figure 3.16 (a). CV curves of N-Ni MOF based symmetric supercapacitor devices recorded at various scan rates is presented in Figure 3.16 (b). We further investigated GCD curves at various current densities of the device to study charging-discharging characteristics. The results are shown in Figure 3.16 (c). The device exhibits a higher specific capacitance of 529 Fg^{-1} at a current density of 1A g^{-1}. The device retains 89% of its initial capacitance after 2000 cycles, as demonstrated in Figure 3.16 (d). Figure 3.16 (e) shows the Nyquist plot for the device. Figure 3.16 (f) shows the Ragone plot of the device. The device delivered an exceptional high energy density of 66.12 Wh kg^{-1} at a power density of 900.3 W kg^{-1}. The result demonstrates the potential for the practical applicability of N-Ni MOF-based symmetric supercapacitor device.

This performance is superior to the earlier reported works on Ni MOF-based supercapacitors.

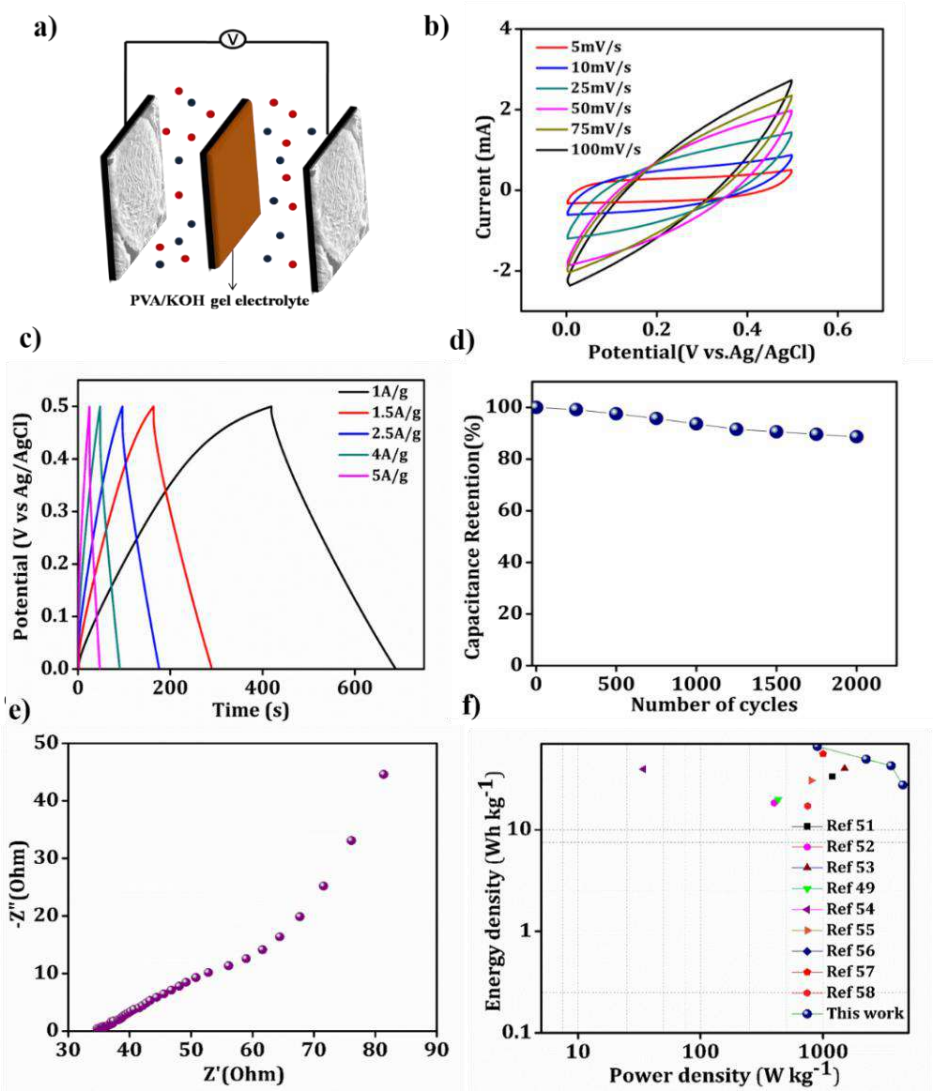

Figure 3.16 (***a***) *Schematic illustration of the assembled symmetric supercapacitor device* ***(b)*** *CV profiles of the device at various scan rates* ***(c)*** *GCD curves of the device at different current densities* ***(d)*** *cyclic performance of N-Ni MOF device at a current density of 5 Ag^{-1}* ***(e)*** *Nyquist plots of the EIS for the N-Ni MOF device* ***(f)*** *Ragone plot of the device in comparison to other Ni MOF-based systems in the literature*

Table 3.2 *A comparison between the related published studies and the current research*

Type of electrode	Specific capacitance ($F\ g^{-1}$)	Maximum Energy density and Power density	Reference
Mn/NiMOF@MWCNT	793.6 F g^{-1}at 1A g^{-1}	33.2Wh kg^{-1} 1198 W kg^{-1}	[51]
Ni-Co MOF	882 F g^{-1} at 0.5A g^{-1}	18.33Wh kg^{-1} 400 W kg^{-1}	[52]
Ni-BDC/PPy	715.6 F g^{-1}at 0.3A g^{-1}	40.1Wh kg^{-1} 1500.6 W kg^{-1}	[53]
Ni-BDC/PANI	938.8 F g^{-1} at 1.8A g^{-1}	19.85Wh kg^{-1} 430.5 W kg-1	[49]
Ni-MOF/graphene	1017 F g^{-1} at 10 mVs^{-1}	39.43Wh kg^{-1} 34.29 Wkg^{-1}	[54]
Zn/Ni-MOF	878 F g^{-1} at 1A g^{-1}	30.51Wh kg^{-1} 800 W kg^{-1}	[55]
NiO/Ni MOF	1176.6 F g^{-1} at 1A g^{-1}	31.3Wh kg^{-1} 374.2 W kg^{-1}	[56]
Ni-Co MOF	980 F g^{-1} at 2.5A g^{-1}	55.7Wh kg^{-1} 1KW kg^{-1}	[57]
Ni MOF/rGO	954F g^{-1} at 1A g^{-1}	17.13Wh kg^{-1} 750W kg^{-1}	[58]
N-Ni MOF	**1519 F g^{-1} at 1 A g^{-1}**	**66.12Wh kg^{-1} 900.3W kg^{-1}**	**This work**

3.3. Conclusion

In summary, we adopted a PVP-assisted approach to synthesize nitrogen-enriched Ni MOF. The effect of PVP on Ni MOF morphology and electrochemical performance was investigated and compared for the first time. The material has an improved supercapacitive performance achieved through morphological control. Here, PVP functioned as both a nitrogen donor and a structure-directing agent. After PVP was introduced, N-Ni MOF has a hierarchical flower-like microspheres morphology that provided considerably high surface area and thus could store more charges, and increase the active metal centers. Moreover, the favorable microporous nature of N-Ni MOF promotes greater diffusion of electrolyte ions and access into the active areas, which enhances the material's excellent rate capability. Compared to Ni MOF, N-Ni MOF showed superior electrochemical performance with a very high specific capacitance of 1519 F g^{-1} at a current density of 1 A $g^{-1,}$ along with capacitance retention of 85% after 2000 cycles. We constructed a symmetric supercapacitor device using N-Ni MOF, which exhibited a greater specific capacitance of 529 F g^{-1} at a current density of 1 A g^{-1}. The device shows a high energy density of 66.12Wh kg^{-1} at a power density of 900.3 W kg^{-1}. Even after 2000 cycles, the device retains 89% stability. Furthermore, N-Ni MOF provided a simple and easy preparation method compared with other novel types of MOFs doped with heteroatoms for supercapacitor applications.

References

[1] H. Gao, H. Shen, H. Wu, H. Jing, Y. Sun, B. Liu, Z. Chen, J. Song, L. Lu, Z. Wu, Review of pristine metal–organic frameworks for supercapacitors: recent progress and perspectives, Energy & Fuels, 35 (2021) 12884-12901.

[2] R. Liang, Y. Du, J. Lin, J. Chen, P. Xiao, Facile-synthesized Ni-Metal–Organic framework/nano carbon electrode material for high-performance supercapacitors, Energy & Fuels, 36 (2022) 7115-7120.
[3] C. Zhang, Q. Zhang, K. Zhang, Z. Xiao, Y. Yang, L. Wang, Facile synthesis of a two-dimensional layered Ni-MOF electrode material for high performance supercapacitors, RSC advances, 8 (2018) 17747-17753.
[4] T. Qiu, Z. Liang, W. Guo, H. Tabassum, S. Gao, R. Zou, Metal–organic framework-based materials for energy conversion and storage, ACS Energy Letters, 5 (2020) 520-532.
[5] X. Pan, Q. Zhu, K. Yu, M. Yan, W. Luo, S.C.E. Tsang, L. Mai, One-dimensional metal-organic frameworks: Synthesis, structure and application in electrocatalysis, Next Materials, (2023) 100010.
[6] Z. Meng, Z. Qiu, Y. Shi, S. Wang, G. Zhang, Y. Pi, H. Pang, Micro/nano metal–organic frameworks meet energy chemistry: a review of materials synthesis and applications, EScience, 3 (2023) 100092.
[7] Y. Zhang, J. Lou, J. Wei, Y. Zhou, H. Wang, L. Wang, Q. Wang, X. Li, X. Song, Dual-outward contraction-induced construction of 2D hollow carbon superstructures, Chemical Communications, 60 (2024) 1567-1570.
[8] H. Zhang, J. Li, Z. Li, Y. Song, S. Zhu, J. Wang, Y. Sun, X. Zhang, B. Lin, Influence of Co-MOF morphological modulation on its electrochemical performance, Journal of Physics and Chemistry of Solids, 160 (2022) 110336.
[9] K.O. Otun, S. Zong, D. Hildebrandt, X. Liu, Self-assembled Zn-functionalized Ni-MOF as an efficient electrode for electrochemical energy storage, Journal of Physics and Chemistry of Solids, 167 (2022) 110779.
[10] A. Murad, J. Liew, M. Yaacob, I. Noor, N. Osman, M. Kamarudin, S. Tan, H. Lee, Z. Talib, M. Alresheedi, Effect of nickel ion concentration on structural, optical and electrical properties towards Ni–H3BTC-MOF formation for nonlinear saturable absorption phenomenon, Journal of Physics and Chemistry of Solids, 167 (2022) 110743.
[11] B. Jia, B. Zhang, Z. Cai, X. Yang, L. Li, L. Guo, Construction of amorphous/crystalline heterointerfaces for enhanced electrochemical processes, eScience, 3 (2023) 100112.
[12] P. Zhang, W. Zhang, Z. Wang, X. Wang, Q. Ren, S. Zhang, Y. Wang, L. He, P. Liu, Q. Zhang, High-voltage, low-temperature supercapacitors enabled by localized “water-in-pyrrolidinium chloride” electrolyte, eScience, 3 (2023) 100184.

[13] F. Xing, Z. Bi, F. Su, F. Liu, Z.S. Wu, Unraveling the design principles of battery-supercapacitor hybrid devices: from fundamental mechanisms to microstructure engineering and challenging perspectives, Advanced Energy Materials, 12 (2022) 2200594.
[14] F. Zhang, J. Zhang, J. Ma, X. Zhao, Y. Li, R. Li, Polyvinylpyrrolidone (PVP) assisted in-situ construction of vertical metal-organic frameworks nanoplate arrays with enhanced electrochemical performance for hybrid supercapacitors, Journal of Colloid and Interface Science, 593 (2021) 32-40.
[15] S. Khokhar, H. Anand, P. Chand, Current advances of nickel based metal organic framework and their nanocomposites for high performance supercapacitor applications: A critical review, Journal of Energy Storage, 56 (2022) 105897.
[16] P.G. Raje, S.R. Gurav, M.R. Waikar, A.S. Rasal, J.-Y. Chang, R.G. Sonkawade, The review of different dimensionalities based pristine metal organic frameworks for supercapacitor application, Journal of Energy Storage, 56 (2022) 105700.
[17] C.-H. Wang, D.-W. Zhang, S. Liu, Y. Yamauchi, F.-B. Zhang, Y.V. Kaneti, Ultrathin nanosheet-assembled nickel-based metal–organic framework microflowers for supercapacitor applications, Chemical Communications, 58 (2022) 1009-1012.
[18] S.A. Hira, K.H. Park, Nitrogen-doped zeolitic imidazolate framework and particle-reduced graphene oxide composites as electrochemical sensors and battery-type supercapacitors, ACS Applied Nano Materials, 4 (2021) 7870-7878.
[19] A. Mohanty, D. Jaihindh, Y.-P. Fu, S.P. Senanayak, L.S. Mende, A. Ramadoss, An extensive review on three dimension architectural Metal-Organic Frameworks towards supercapacitor application, Journal of Power Sources, 488 (2021) 229444.
[20] S.A. Hira, D. Annas, S. Nagappan, Y.A. Kumar, S. Song, H.-J. Kim, S. Park, K.H. Park, Electrochemical sensor based on nitrogen-enriched metal–organic framework for selective and sensitive detection of hydrazine and hydrogen peroxide, Journal of Environmental Chemical Engineering, 9 (2021) 105182.
[21] Y. Ding, Z. Yan, G. Wang, H. Sang, W. Li, Z. Xu, One-pot preparation of La-doped Ni-MOF nanospheres for efficient hybrid supercapacitor electrode material, Materials Chemistry and Physics, 309 (2023) 128340.

[22] D. Fu, H. Li, X.-M. Zhang, G. Han, H. Zhou, Y. Chang, Flexible solid-state supercapacitor fabricated by metal-organic framework/graphene oxide hybrid interconnected with PEDOT, Materials Chemistry and Physics, 179 (2016) 166-173.
[23] S. Chen, C. Wang, M. Zhang, W. Zhang, J. Qi, X. Sun, L. Wang, J. Li, N-doped Cu-MOFs for efficient electrochemical determination of dopamine and sulfanilamide, Journal of hazardous materials, 390 (2020) 122157.
[24] J. Du, A. Chen, Y. Zhang, S. Zong, H. Wu, L. Liu, PVP-assisted preparation of nitrogen doped mesoporous carbon materials for supercapacitors, Journal of Materials Science & Technology, 58 (2020) 197-204.
[25] P. Zhao, R. Li, W. Wu, J. Wang, J. Liu, Y. Zhang, In-situ growth of polyvinylpyrrolidone modified Zr-MOFs thin-film nanocomposite (TFN) for efficient dyes removal, Composites Part B: Engineering, 176 (2019) 107208.
[26] M. Li, X. Jiang, J. Liu, Q. Liu, N. Lv, N. Qi, Z. Chen, A flower-like Co/Ni bimetallic metal-organic framework based electrode material with superior performance in supercapacitors, Journal of Alloys and Compounds, 930 (2023) 167354.
[27] K. Song, X. Qiu, B. Han, S. Liang, Z. Lin, Efficient upcycling electroplating sludge and waste PET into Ni-MOF nanocrystals for the effective photoreduction of CO 2, Environmental Science: Nano, 8 (2021) 390-398.
[28] B. Han, X. Ou, Z. Deng, Y. Song, C. Tian, H. Deng, Y.J. Xu, Z. Lin, Nickel metal–organic framework monolayers for photoreduction of diluted CO2: metal-node-dependent activity and selectivity, Angewandte Chemie International Edition, 57 (2018) 16811-16815.
[29] D. Zhu, C. Guo, J. Liu, L. Wang, Y. Du, S.-Z. Qiao, Two-dimensional metal–organic frameworks with high oxidation states for efficient electrocatalytic urea oxidation, Chemical communications, 53 (2017) 10906-10909.
[30] W. Lu, X. Wu, Ni-MOF nanosheet arrays: efficient non-noble-metal electrocatalysts for non-enzymatic monosaccharide sensing, New Journal of Chemistry, 42 (2018) 3180-3183.
[31] A. Mesbah, P. Rabu, R. Sibille, S. Lebègue, T. Mazet, B. Malaman, M. François, From hydrated Ni3 (OH) 2 (C8H4O4) 2 (H2O) 4 to anhydrous Ni2

(OH) 2 (C8H4O4): impact of structural transformations on magnetic properties, Inorganic chemistry, 53 (2014) 872-881.
[32] P. Arul, S.A. John, Size controlled synthesis of Ni-MOF using polyvinylpyrrolidone: new electrode material for the trace level determination of nitrobenzene, Journal of Electroanalytical Chemistry, 829 (2018) 168-176.
[33] M. Zhao, Y. Wang, Q. Ma, Y. Huang, X. Zhang, J. Ping, Z. Zhang, Q. Lu, Y. Yu, H. Xu, Ultrathin 2D metal–organic framework nanosheets, Advanced Materials, 27 (2015) 7372-7378.
[34] X. Ding, H. Liu, J. Chen, M. Wen, G. Li, T. An, H. Zhao, In situ growth of well-aligned Ni-MOF nanosheets on nickel foam for enhanced photocatalytic degradation of typical volatile organic compounds, Nanoscale, 12 (2020) 9462-9470.
[35] H. Li, F. Meng, S. Zhang, L. Wang, M. Li, L. Ma, W. Zhang, W. Zhang, Z. Yang, T. Wu, Crystal-growth-dominated fabrication of metal–organic frameworks with orderly distributed hierarchical porosity, Angewandte Chemie, 132 (2020) 2478-2485.
[36] H. Guo, H. Zhang, N. Wu, Z. Pan, C. Li, Y. Chen, Y. Cao, W. Yang, Trimesic acid-modified 2D NiCo-MOF for high-capacity supercapacitors, Journal of Alloys and Compounds, 934 (2023) 167779.
[37] Y. Li, Y. Zhao, R. Zhang, G. Lu, PVP-assisted synthesis of monodisperse UiO-66 crystals with tunable sizes, Inorganic Chemistry Communications, 82 (2017) 68-71.
[38] X. Cai, J. Lin, M. Pang, Facile synthesis of highly uniform Fe-MIL-88B particles, Crystal Growth & Design, 16 (2016) 3565-3568.
[39] X. Zhang, J. Wang, X. Ji, Y. Sui, F. Wei, J. Qi, Q. Meng, Y. Ren, Y. He, D. Zhuang, Flake-like nickel/cobalt metal-organic framework as high-performance electrodes for supercapacitors, Journal of Materials Science: Materials in Electronics, 31 (2020) 16260-16268.
[40] X. Quan, Z. Sun, J. Xu, S. Liu, Y. Han, Y. Xu, H. Meng, J. Wu, X. Zhang, Construction of an aminated MIL-53 (Al)-functionalized carbon nanotube for the efficient removal of bisphenol AF and metribuzin, Inorganic Chemistry, 59 (2020) 2667-2679.
[41] C. Yang, X. Li, L. Yu, X. Liu, J. Yang, M. Wei, A new promising Ni-MOF superstructure for high-performance supercapacitors, Chemical Communications, 56 (2020) 1803-1806.

[42] R.R. Bhosale, S. Bhosale, P. Kumbhar, D.K. Narale, R. Ghaware, C.L. Jambhale, S.S. Kolekar, Design and development of porous nanorods-based nickel-metal organic framework (Ni-MOF) for high-performance supercapacitor application, New Journal of Chemistry, (2023).
[43] Q. Cheng, K. Tao, X. Han, Y. Yang, Z. Yang, Q. Ma, L. Han, Ultrathin Ni-MOF nanosheet arrays grown on polyaniline decorated Ni foam as an advanced electrode for asymmetric supercapacitors with high energy density, Dalton Transactions, 48 (2019) 4119-4123.
[44] S. Gao, Y. Sui, F. Wei, J. Qi, Q. Meng, Y. He, Facile synthesis of cuboid Ni-MOF for high-performance supercapacitors, Journal of materials science, 53 (2018) 6807-6818.
[45] A. Thadathil, Y.A. Ismail, P. Periyat, Ternary 3D reduced graphene oxide/Ni 0.5 Zn 0.5 Fe 2 O 4/polyindole nanocomposite for supercapacitor electrode application, RSC advances, 11 (2021) 35828-35841.
[46] Y. Pan, S. Yan, Y. Liu, Z. Tian, D. Li, Y. Chen, L. Guo, Y. Wang, Significantly enhanced electrochemical performance of 2D Ni-MOF by carbon quantum dot for high-performance supercapacitors, Electrochimica Acta, 422 (2022) 140560.
[47] A.D. Salunkhe, P. Pagare, A. Torane, Review on Recent Modifications in Nickel Metal-Organic Framework Derived Electrode (Ni-MOF) Materials for Supercapacitors, Journal of Inorganic and Organometallic Polymers and Materials, (2022) 1-32.
[48] J. Wang, Q. Zhong, Y. Xiong, D. Cheng, Y. Zeng, Y. Bu, Fabrication of 3D Co-doped Ni-based MOF hierarchical micro-flowers as a high-performance electrode material for supercapacitors, Applied Surface Science, 483 (2019) 1158-1165.
[49] Q. Chen, S. Lei, P. Deng, X. Ou, L. Chen, W. Wang, Y. Xiao, B. Cheng, Direct growth of nickel terephthalate on Ni foam with large mass-loading for high-performance supercapacitors, Journal of Materials Chemistry A, 5 (2017) 19323-19332.
[50] M. Yuan, R. Wang, Z. Sun, L. Lin, H. Yang, H. Li, C. Nan, G. Sun, S. Ma, Morphology-controlled synthesis of Ni-MOFs with highly enhanced electrocatalytic performance for urea oxidation, Inorganic Chemistry, 58 (2019) 11449-11457.
[51] Y. Han, J. Zhou, L. Wang, L. Xing, Z. Xue, Y. Jiao, Y. Pang, Redox-active nanostructure electrode of Mn/Ni bimetal organic frameworks

anchoring on multi-walled carbon nanotubes for advanced supercapacitor, Journal of Electroanalytical Chemistry, 882 (2021) 114993.
[52] D. Jiang, C. Wei, Z. Zhu, X. Xu, M. Lu, G. Wang, Preparation of flower-like nickel-based bimetallic organic framework electrodes for high-efficiency hybrid supercapacitors, Crystals, 11 (2021) 1425.
[53] B. Wang, W. Li, Z. Liu, Y. Duan, B. Zhao, Y. Wang, J. Liu, Incorporating Ni-MOF structure with polypyrrole: enhanced capacitive behavior as electrode material for supercapacitor, RSC advances, 10 (2020) 12129-12134.
[54] M. Azadfalah, A. Sedghi, H. Hosseini, Synergistic effect of Ni-based metal organic framework with graphene for enhanced electrochemical performance of supercapacitors, Journal of Materials Science: Materials in Electronics, 30 (2019) 12351-12363.
[55] X. Zhang, Y. Sui, F. Wei, J. Qi, Q. Meng, Y. Ren, Y. He, Self-supported 3D layered zinc/nickel metal-organic-framework with enhanced performance for supercapacitors, Journal of Materials Science: Materials in Electronics, 30 (2019) 18101-18110.
[56] G. Wang, Z. Yan, N. Wang, M. Xiang, Z. Xu, NiO/Ni metal–organic framework nanostructures for asymmetric supercapacitors, ACS Applied Nano Materials, 4 (2021) 9034-9043.
[57] M. Radhika, B. Gopalakrishna, K. Chaitra, L.K.G. Bhatta, K. Venkatesh, M. Sudha Kamath, N. Kathyayini, Electrochemical studies on Ni, Co & Ni/Co-MOFs for high-performance hybrid supercapacitors, Materials Research Express, 7 (2020) 054003.
[58] Y. Zhong, X. Cao, L. Ying, L. Cui, C. Barrow, W. Yang, J. Liu, Homogeneous nickel metal-organic framework microspheres on reduced graphene oxide as novel electrode material for supercapacitors with outstanding performance, Journal of Colloid and Interface Science, 561 (2020) 265-274.

Chapter 4

Polypyrrole Derived Nitrogen-Doped Graphene Quantum Dots /Polypyrrole Composites for High Energy Density Supercapacitor

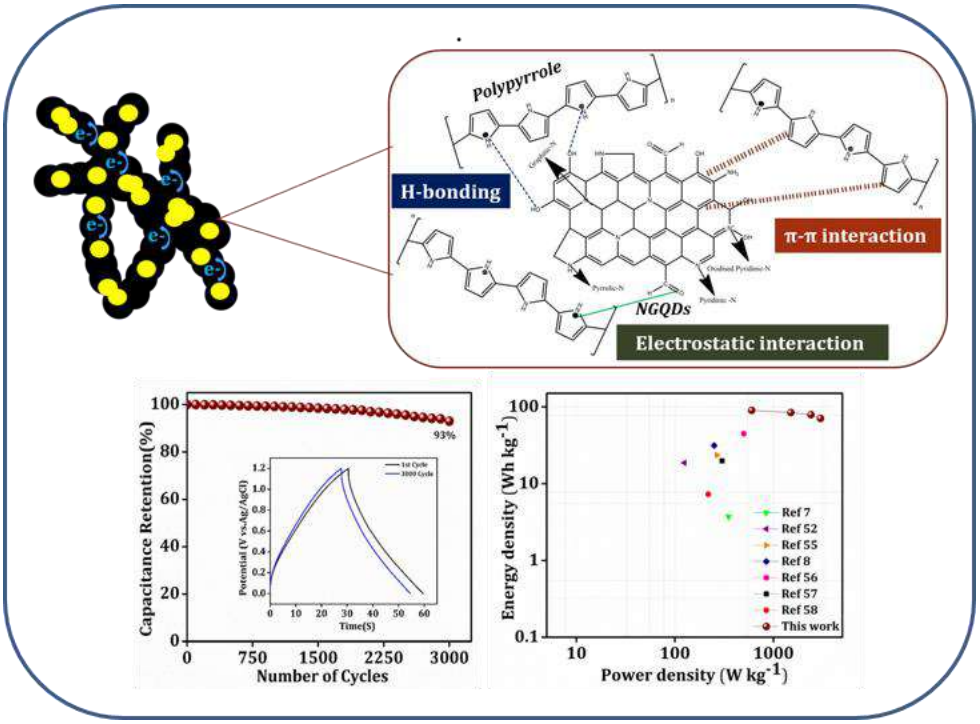

This chapter discusses a novel conducting polymer/GQDs composite for high-performance supercapacitor application. The NGQDs were prepared through a simple one-step solvothermal method using PPy itself as the precursor. The NGQDs/PPy composites of varying composition were systematically studied to understand their supercapacitive behavior. In addition, the practical applicability of the material was demonstrated by fabricating a symmetric supercapacitor device.

4.1. Introduction

Despite their exceptional power delivery and long-term stability, supercapacitors are fundamentally limited by low energy density, which restricts their use for high-demand applications such as electric vehicles and grid-scale energy storage [1, 2]. CPs, including PPy, PANI, PTh, and PEDOT, have emerged as strong candidates for advanced supercapacitor electrode materials. This is primarily due to their ability to undergo fast, reversible faradaic redox reactions, which significantly enhance charge storage efficiency and overall electrochemical performance [3-5]. Among them, PPy is a widely recognized electrode material for designing flexible supercapacitors. This is attributed to its ease of synthesis, environmental stability, excellent biocompatibility, tuneable conductivity, strong redox behavior, and inherent flexibility. The nitrogen atoms in the PPy chain act as active sites for binding negatively charged counterions during the doping process, effectively promoting ion insertion and extraction throughout charging and discharging [6, 7]. Despite these advantages, PPy, like other conducting polymers, suffers from certain drawbacks that hinder its long-term electrochemical performance. During repeated charge-discharge cyclic, PPy undergoes mechanical stress and volumetric changes, leading to cracking, loss of conductivity, and degradation of its electrochemical properties. Additionally, its relatively low surface area limits ion diffusion and reduces the accessibility of redox-active sites, thereby restricting its energy storage capability over time [8, 9].

To overcome the limitations of CPs and exploit their capabilities for energy storage applications. Various strategies have been adopted by researchers, one of the efficient strategies is the integration of carbon nanomaterials to form advanced hybrid composites. Carbon-based materials such as carbon

aerogel [10], carbon quantum dots [11], activated carbon [12], carbon nanotubes [13], graphene [14], GQDs [15, 16], and carbide-derived carbons [16] have garnered widespread attention as supercapacitor electrodes due to their exceptional specific surface area, well-defined porous architecture, excellent chemical stability, and superior electrical conductivity [17]. Among these, the development of GQDs/conducting polymer hybrids has emerged as a powerful approach particularly in enhancing the electrochemical performance, stability, and charge transport properties of PPy-based electrodes paving the way for high-performance supercapacitors [18-20]. Xinmin et al. demonstrated that GQDs/PPy and electrochemically reduced GQDs (ERGQDs/PPy) hybrids deliver high specific capacitance and improved cyclic stability, resulting from the synergistic effect of EDLC behavior from ERGQDs and the pseudocapacitance of PPy [17]. Similarly, Lanxin Wang et al. reported that carbon dots based activated carbon/PPy (AC-CDs/PPy) hybrids exhibited enhanced specific capacitance, energy, and power densities due to the cooperative interaction between the components [7]. Graphene quantum dots**,** nanoscale graphene fragments feature high surface area, quantum confinement, and outstanding electrical conductivity, making them ideal for advanced energy storage [21]. Their ultra-small size (<10 nm) enhances ion diffusion, exposes abundant active sites, and significantly improves charge capacity and cyclic stability [22]. Beyond supercapacitors, GQDs serve in photocatalysis, sensing, drug delivery, and bioimaging, due to their excellent solubility, biocompatibility, photostability, and efficient charge-transfer properties [23]. NGQDs further elevate performance by introducing electron-rich redox centers within the sp^2-carbon lattice through nitrogen atoms. This increases conductivity, accelerates charge transport, and enhancing capacitive behavior, thereby establishing

NGQDs as promising components for next-generation energy storage systems [24].

In this study, a novel NGQDs/PPy composite electrode was successfully developed by integrating NGQDs into a PPy matrix, resulting in significantly enhanced electrochemical performance. NGQDs, known for their ability to facilitate efficient charge transfer, uniform dispersion, and excellent electrical conductivity. NGQDs were synthesized via an innovative one-step hydrothermal method using PPy itself as both the carbon and nitrogen source. Subsequently, these NGQDs were uniformly embedded into the PPy framework to construct a cohesive, porous structure with enhanced surface area, thereby contributing to increased charge storage capacity and rapid-response capability. Within this architecture, NGQDs act as conductive bridges, promoting fast electron transport and enhancing the electrical conductivity and faradaic reaction kinetics of PPy. The resulting synergistic structure exhibits high specific capacitance, excellent rate capability, and outstanding cyclic stability, making it a promising candidate for next-generation supercapacitor applications.

4.2. Results and Discussions

NGQDs were successfully synthesized through a straightforward, one-step hydrothermal strategy employing PPy as the sole nitrogen-rich precursor, as outlined in the experimental section in Chapter 2. During hydrothermal treatment, PPy undergoes controlled decomposition, generating nitrogen-containing aromatic intermediates, which undergo ring closure, resulting in the formation of NGQDs with nitrogen atoms embedded within the aromatic lattice. This approach ensures efficient nitrogen doping and enables the simultaneous incorporation of multiple nitrogen functionalities, including

pyridinic, pyrrolic, and graphitic nitrogen species. These nitrogen functionalities are expected to enhance the electronic properties of the NGQDs. The NGQDs/PPy composites of varying compositions were synthesized by incorporating different volumes of NGQDs into a constant amount of pyrrole monomer. The resulting composites were thoroughly characterized and studied for their applicability as supercapacitors. A schematic representation of the synthesis of NGQDs and NGQDs/PPy composites are illustrated in the chapter 2.

4.2.1. HR-TEM Analysis

The formation of NGQDs was confirmed from HR-TEM analysis. TEM images are presented in Figure 4.1(a-b).

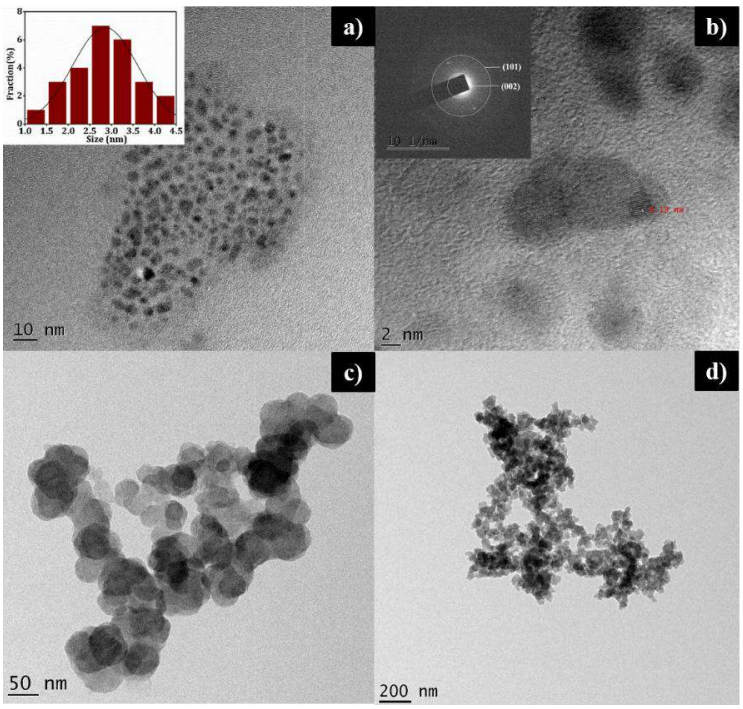

Figure 4.1 ***(a-b)*** *TEM images of NGQDs in two different resolution. The insets in* ***(a)*** *and* ***(b)*** *display the particle size distribution and the SAED pattern of NGQDs respectively.* ***(c-d)*** *TEM images of the NPP-50 composite*

Uniformly sized nanodots observed in the TEM images validate the successful formation of NGQDs from PPy. The embedding of NGQDs within the polypyrrole matrix is also evident from the TEM images shown in Figure 4.1 (c-d). The morphology and internal structure of the as-prepared NGQDs and NGQDs/PPy composite NPP-50 were analysed using HR-TEM. As shown in Figure 4.1(a), the NGQDs exhibit a nearly spherical shape and are uniformly dispersed. The inset of Figure 4.1(a) presents a size distribution histogram obtained through Gaussian fitting, indicating that most NGQDs range from 1 to 5 nm, with an average diameter of 2.8 nm, confirming their quantum size. Figure 4.1(b) reveals well-defined parallel lattice fringes in the NGQDs, signifying their crystalline nature, with an interplanar spacing of 0.19 nm, corresponding to the (101) crystal plane of graphitic carbon [25, 26]. Furthermore, the selected area electron diffraction (SAED) pattern in Figure 4.1(b). SAED results exhibits a distinct concentric ring pattern, further verifying the graphitic-like structure [7, 27].

NPP-50 composite, shown in Figure 4.1(c), reveal that a larger number of NGQDs are embedded within the internal structure of PPy, forming the NGQDs/PPy composite. Based on the TEM analysis, the growth of the NPP-50 composite can be attributed to strong electrostatic interactions between NGQDs and the pyrrole monomer. The NGQDs likely act as nucleation sites due to the abundance of oxygen-containing functional groups (such as hydroxyl and carboxyl) at their edges [8]. Under electrostatic attraction, pyrrole monomer cations (Py^{+}) gradually polymerize on the surface of the NGQDs, leading to the formation of the NGQDs/PPy composites. Consequently, this hybrid structure not only significantly increases the effective interfacial area and thus enhancing the charge transfer, but also facilitates the rapid transport of charge carriers during the charge discharge process [22].

4.2.2. SEM Analysis

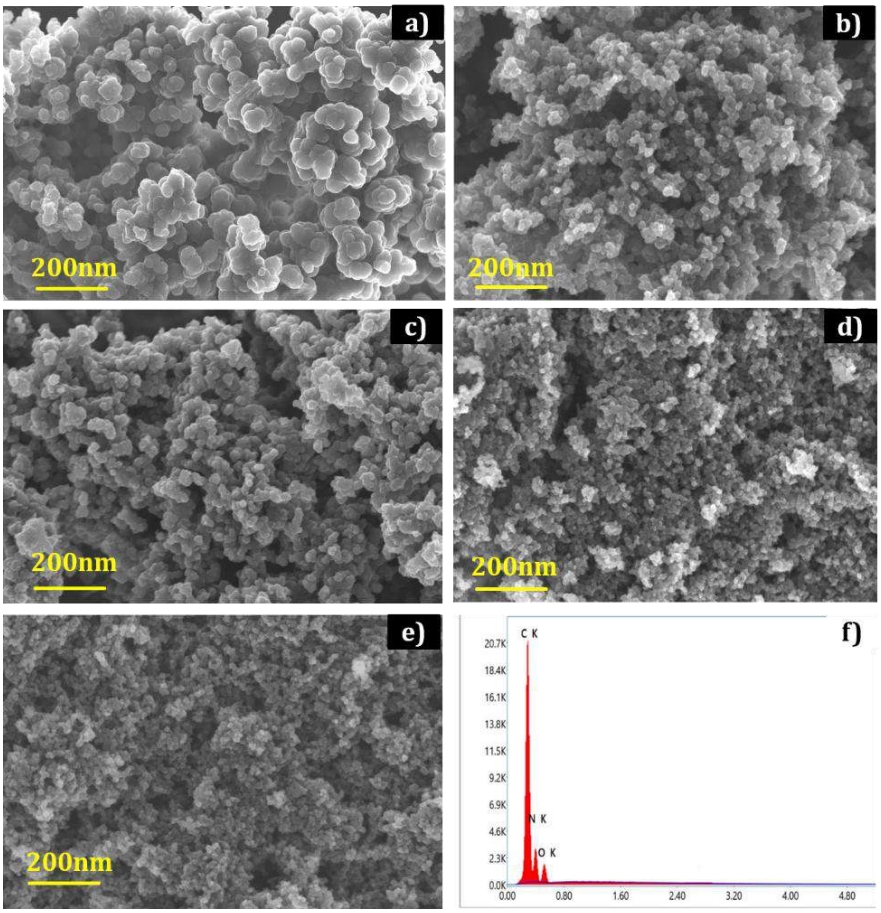

Figure 4.2 *SEM images depicting the morphology of* ***(a)*** *PPy,* ***(b)*** *NPP-25,* ***(c)*** *NPP-50,* ***(d)*** *NPP-75, and* ***(e)*** *NPP-100* ***(f)*** *EDX spectrum of NPP-50 composite showing the presence of elements*

The morphology of PPy and NGQDs/PPy composites were examined using SEM analysis. The results are presented in Figure 4.2(a-e). Pristine PPy exhibits a spherical morphology, whereas the incorporation of NGQDs significantly alters the structural features of PPy [28]. It is also improtant to note that NGQDs act as surfactants due to the presence of numerous hydrophilic functional groups. This results in enhanced conductivity and

promotes the development of a porous architecture in the NGQDs/PPy composites.

Among the composites, the NPP-50 composite in Figure 4.2(c) exhibits a highly porous and well-dispersed structure, which facilitates efficient ion diffusion and charge storage, thereby enhancing electrochemical performance. In contrast, The SEM images corresponding to higher NGQDs loadings, i.e., in NPP-75 and NPP-100 shown in Figure 4.2(d and e) reveals a less porous agglomerated structure, which reduces the effective surface area and consequently diminishes the electrochemical performance. The EDX spectrum of the NPP-50 composite illustrates the atomic ratios of C, N, and O elements, which are 71.09%, 23.49%, and 5.42%, respectively (Figure 4.2 (f)). The significant nitrogen content further confirms the effective nitrogen doping within the composite [8].

4.2.3. UV-Visible absorption and PL spectral analysis

Figure 4.3 (a) displays the UV-Visible absorption spectrum of NGQDs, revealing a prominent absorption band around 256 nm, which corresponds to the π-π^* transitions within the sp^2-hybridized graphitic domains. A secondary absorption band appears near 300 nm, attributed to n-π^* transitions associated with C=O bonds and other surface functional groups containing lone pairs of electrons [29, 30]. The inset photographs in Figure 4.3 (a) show aqueous suspensions of NGQDs under visible light and UV illumination at 365 nm. Under UV light, the pale-yellow solution exhibits a strong cyan blue fluorescence. Figure 4.3 (b) presents the PL spectrum of the NGQDs under 365 nm excitation, showing a distinct emission peak at 462 nm. Moreover, the NGQDs exhibit excitation-dependent PL behavior. As shown in Figures 4.3 (c) and 4.3 (d), increasing the excitation wavelength

from 230 to 440 nm results in a red shift of the emission peak along with a gradual decrease in fluorescence intensity [31, 32].

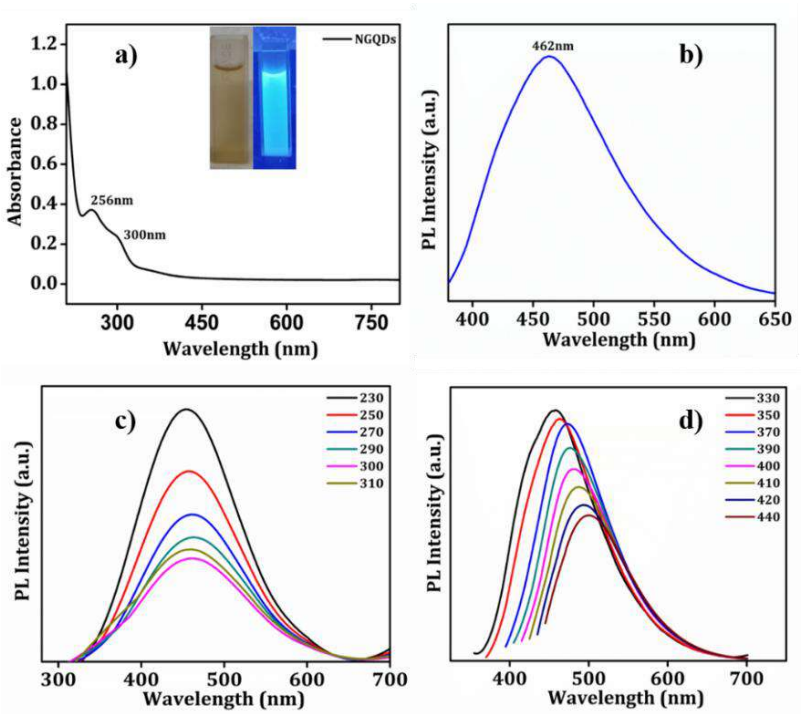

Figure 4.3 ***(a)*** *UV-Visible spectrum of NGQDs; the* inset photographs display NGQDs under visible light (yellow) and UV illumination at 365 nm (cyan blue) ***(b)*** *PL spectrum of NGQDs excited at 365 nm* ***(c, d)*** *Excitation-dependent PL spectra of NGQDs recorded at excitation wavelengths ranging from 230 to 440 nm*

The UV-Vis absorption spectra of PPy and NGQDs/PPy hybrids exhibit prominent optical transitions as shown in Figure 4.4. In the case of PPy, two distinct absorption bands were identified at 287.5 nm and 454.5 nm [33]. The band near 287.5 nm is associated with π-π* electronic transitions along the conjugated polymer chain. The absorption at 454.5 nm is attributed to polaron transition, signifying the generation of mobile charge carriers in doped PPy. For the NGQDs/PPy composite, the π-π* transition band is red shifted to 296 nm which indicates π-π stacking or interaction between

NGQDs and PPy. An additional absorption at 383 nm, attributed to n-π* transitions, arises from nitrogen-containing functional groups present in NGQDs [34].

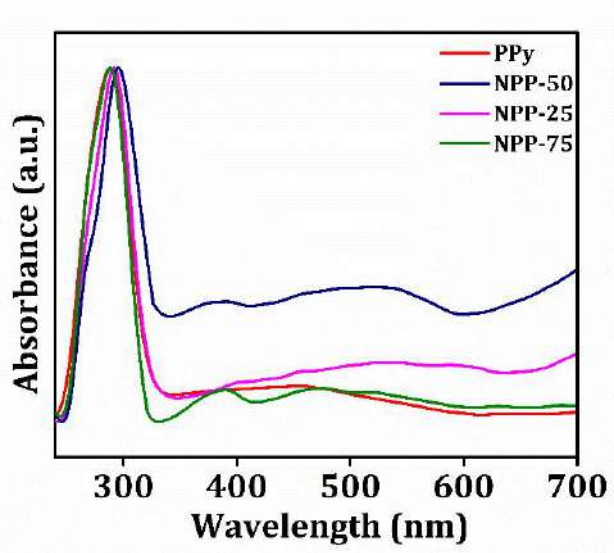

Figure 4.4 *UV-Visible absorption spectra of PPy and NGQDs/PPy composites*

The broad band at 508.5 nm indicates intensified polaron or bipolaron formation within the hybrid structure. This spectral shift and increased absorption intensity are due to enhanced doping effects and stronger electronic coupling. The incorporation of NGQDs promotes greater charge delocalization and alters the energy band structure of PPy. These modifications confirm a synergistic interaction between NGQDs and PPy, which results in improved optical and electrochemical characteristics [35].

4.2.4. FTIR and Raman spectra

Figure 4.5 (a) displays the FTIR spectra of NGQDs. A broad absorption band at 3443 cm^{-1} corresponds to N-H and O-H stretching vibrations, while the

peaks at 2924 cm^{-1} and 2854 cm^{-1} are attributed to the C–H stretching vibrations of aromatic rings.

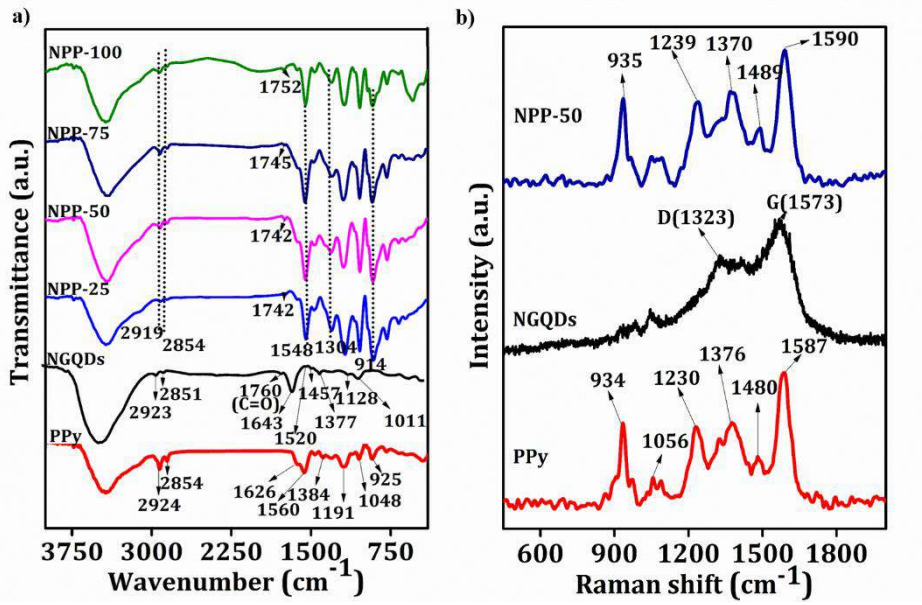

Figure 4.5 (***a)*** *FTIR spectra of the PPy, NGQDs and NGQDs/PPy composites* ***(b)*** *Raman spectra of the PPy, NGQDs and NGQDs /PPy composites*

The presence of N-H stretching near 3443 cm^{-1}, the C-NH-C bending at 1377 cm^{-1}, and the C-N in-plane bending vibration at 1011 cm^{-1} collectively confirms the successful nitrogen doping in the NGQDs [36]. Further, the peak at 1520 cm^{-1} is associated with sp^2-hybridized C-N bonding. Additional peaks appearing at 1643, 1760, 1457, and 1128 cm^{-1} are assigned to aromatic C=C stretching, carboxylate (CO) stretching, and -C-OH bending vibrations, respectively, indicating the presence of aromatic carbon ring structures decorated with hydrophilic functional groups at the edges. Overall, the presence of N-H, C-N, and aromatic C=C stretching bands suggests the retention of the PPy aromatic ring structure in the NGQDs. This provides evidence for the incorporation of nitrogen within the carbon lattice. The

FTIR spectrum of PPy displays several characteristic absorption peaks. The prominent peak at 1560 cm^{-1} is attributed to the C=C ring stretching vibration of the pyrrole structure. Peaks observed at 1384 cm^{-1}, 1191 cm^{-1}, and 1048 cm^{-1} correspond to C-N stretching, C-N in-plane deformation, and C-H in-plane bending vibrations, respectively. The peak at 925 cm^{-1} is associated with C=C in-plane bending within the pyrrole ring, while the absorption band at 784 cm^{-1} corresponds to the N-H out-of-plane bending vibration. These characteristic peaks collectively confirm the successful polymerization of pyrrole [37-39]. In Figure 4.5 (a), the characteristic peaks observed at 1548, 1304, 1178, 1045, and 914 cm^{-1} are attributed to the C=O stretching, C=C stretching, C-N in-plane deformations, C-H vibrations, and C=C in-plane bending vibrations of the pyrrole ring, respectively, in the NGQDs/PPy composites. The sharp peak at 785 cm^{-1} is associated with the PPy in the NGQDs/PPy composite.

Upon the addition of NGQDs, the absorption peaks show no significant shift compared to pure PPy, suggesting that NGQDs are well-dispersed within the PPy matrix. Further, the characteristic peak at 1760 cm^{-1}, attributed to the carbonyl (C=O) group, which also appears in the NGQDs spectrum, confirms that NGQDs are effectively adsorbed onto the surface of PPy [21]. The C=O stretching vibration in the NGQDs/PPy composites shifts from 1760 to 1752 cm^{-1}, which can be attributed to hydrogen bonding interactions between the carbonyl groups of NGQDs and the N-H groups of PPy. Furthermore, the red shift in the absorption peaks corresponds to π-π electronic interactions and hydrogen bonding between the NGQDs and PPy chains. These observations indicate strong interactions between NGQDs and PPy [22, 35].

The Raman spectra provide further insights into the structural features of the synthesized materials. Two pronounced signals are clearly observed in the

NGQDs spectrum in Figure 4.5 (b). The G band at 1573 cm^{-1} due to the presence of an ordered planar sp^2 carbon framework, and the D band at 1323 cm^{-1}, indicative of sp^3 structural imperfections such as edges and functional moieties are observed in the Raman spectra [40]. The substantial intensity of both the G and D bands reflects a high degree of structural order within the NGQD lattice while simultaneously confirming the existence of numerous oxygen-containing groups, predominantly located at the edges.

Notably, the positions of certain signals in the PPy spectrum (Figure 4.5(b)) closely align with the G and D bands, which can be attributed to the presence of unsaturated (C=C) and saturated (C-C) groups within the polymer chains. The characteristic bands identified at 934, 1056, 1376, 1480, and 1587 cm^{-1} correspond to C-C ring deformation, C-H in-plane deformation, C-C in-ring stretching, C-C stretching, and C=C in-ring stretching, respectively, thereby corroborating the formation of PPy. Slight shifts in the position of the bands at 1376 cm^{-1}, 1480 cm^{-1}, and 1587cm^{-1} in the NGQDs/PPy composite spectrum likely due to the strong interactions between the polymeric rings and the carbonaceous nanostructures. Notably, upon formation of the NGQDs/PPy composite, the D band shifts from 1376 to 1370 cm^{-1} indicating π-π interactions along with charge transfer between PPy and NGQDs [3].

4.2.5. XRD Analysis

The XRD pattern of the studied samples display a broad diffraction peak at approximately 2θ = 28.06°, reflecting the amorphous nature of PPy. The diffraction peaks of NGQDs coincide with that of PPy, producing a broad and intensified pattern, as illustrated in Figure 4.6. As the concentration of NGQDs increases, the broad peak gradually This shifts from 2θ = 26.35° to 26.61° [41]. This shift relative to the individual components, indicates a notable interaction between NGQDs and PPy, likely attributed to π-π

stacking or electronic coupling between the two structures. The progressive increase in the 2θ value signifies enhanced structural ordering and an amplified graphitic contribution as the NGQDs content rises from 25 mL to 100 mL [17].

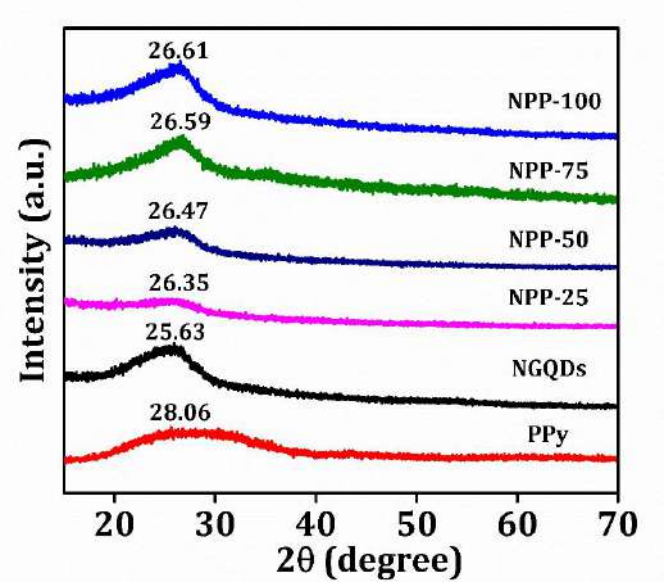

Figure 4.6 *XRD pattern of the PPy, NGQDs and NGQDs/PPy composites*

4.2.6. Conductivity studies

The electrical conductivity of PPy and NGQDs/PPy composites was examined by broadband dielectric spectroscopy. Figure 4.7 illustrates the variation of conductivity with frequency over the range of 10^{-2} to 10^{7} Hz for all the samples. The electrical conductivity of pristine PPy was found to be 1.88×10^{-3} S cm^{-1}. All the samples have electrical conductivity in the semiconducting range.Upon incorporation of NGQDs, the electrical conductivity increased significantly. Among the composites, NPP-50 exhibited the highest electrical conductivity of 7.52×10^{-3} S cm^{-1}.

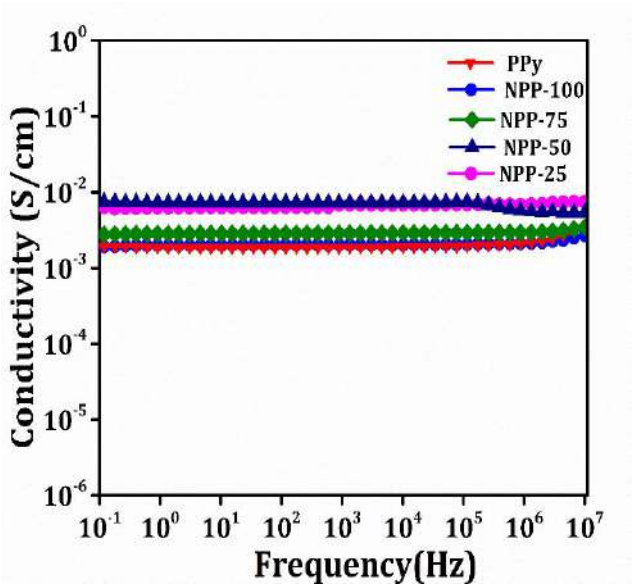

Figure 4.7 *BDS spectra showing the frequency-dependent electrical conductivity*

This notable enhancement is attributed to the synergistic interaction between NGQDs and PPy, which facilitates improved charge transport and electron mobility. However, excessive loading of NGQDs led to a reduction in electrical conductivity due to agglomeration, which disrupts the uniform conductive network and hinders electron transport [22, 42]. The electrical conductivities of PPy and NPP composites are summarized in Table 4.1.

Table 4.1 *Electrical conductivities of PPy and NGQDs/PPy composites*

Material	Conductivity (S cm^{-1})
PPy	1.88×10^{-3}
NPP-25	7.5×10^{-3}
NPP-50	7.52×10^{-3}
NPP-75	4.52×10^{-3}
NPP-100	2.55×10^{-3}

4.2.7. XPS Analysis

XPS was employed to investigate the elemental composition of NGQDs and NGQDs/PPy composites. The results are presented in Figure 4.8 (a and d), the survey spectra reveal three characteristic peaks corresponding to carbon (C 1s, ~285 eV), nitrogen (N 1s, ~400 eV), and oxygen (O 1s, ~530 eV), confirming the major elements present in the electrode materials.

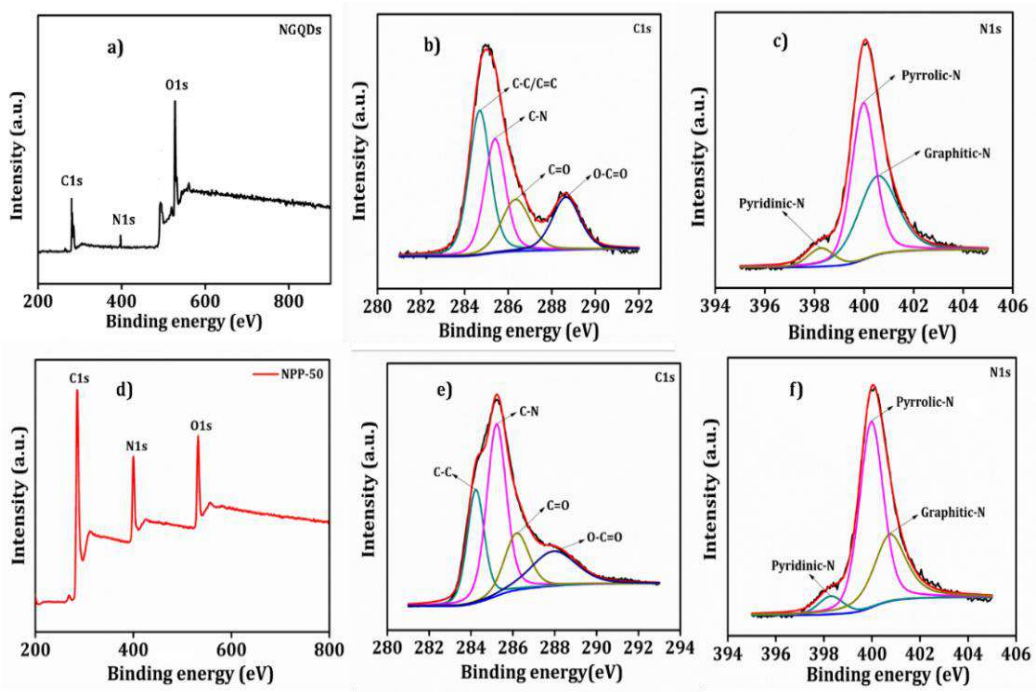

Figure 4.8 *XPS analysis of NGQDs and NPP-50 composite* ***(a, d)*** *survey spectra showing the elemental composition;* ***(b, e)*** *high-resolution C 1s spectra; and* ***(c, f)*** *high-resolution N 1s spectra, highlighting the chemical states of carbon and nitrogen in NGQDs and the NPP-50 composite, respectively*

To gain deeper insight into the chemical states of NGQDs, the C 1s spectrum was deconvoluted (Figure 4.8 (b)). The fitted peaks at 284.6, 285.3, 286.3, and 288.6 eV are attributed to oxygen-containing functional groups, including hydroxyl, carbonyl, and carboxyl moieties, which are distributed

along the edges of the NGQDs [30]. Figure 4.8(c) presents the deconvoluted N 1s spectrum, confirming the successful incorporation of nitrogen into the GQDs framework. The fitted peaks located at 398.3, 399.98, and 400.6 eV are assigned to pyridinic, pyrrolic, and graphitic nitrogen species, respectively. Furthermore, the O 1s spectrum was deconvoluted into two distinct peaks at 531.5 and 533.0 eV, corresponding to C=O and C-OH/C-O-C functionalities, respectively, as shown in Figure 4.9 [43, 44].

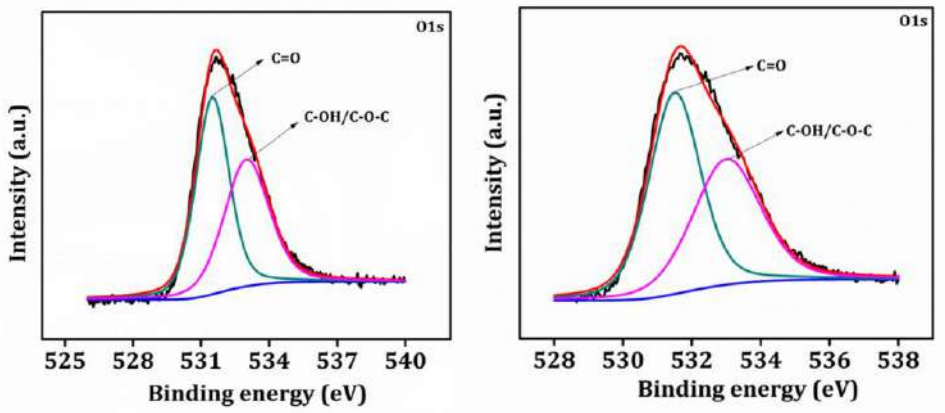

Figure 4.9 *High-resolution O 1s spectra of (a) NGQDs and (b) NPP-50*

The XPS survey spectrum of the NGQDs/PPy composite demonstrates a higher nitrogen content than that of pristine NGQDs, owing to the nitrogen-rich backbone of PPy. In the C 1s spectrum of the NPP-50 composite, four distinct peaks are identified at 284.2, 285.2, 286.2, and 287.9 eV, corresponding to sp^2-hybridized carbon (C=C), C-N, C=O, and COOH groups, respectively. Similarly, the N 1s spectrum of NPP-50 exhibits three peaks at 398.3, 400.0, and 400.8 eV, attributed to pyridinic, pyrrolic, and graphitic nitrogen species. Importantly, the proportion of pyrrolic nitrogen is markedly higher in NPP-50 than in NGQDs, confirming the successful incorporation of PPy and the enrichment of nitrogen functionalities within

the composite. The O 1s spectrum of NPP-50 displays two peaks at 531.5 and 533.0 eV, consistent with those observed in NGQDs, corresponding to C=O and C–OH/C–O–C groups as depicted in Figure 4.9 [45].

4.2.8. BET Surface area Analysis

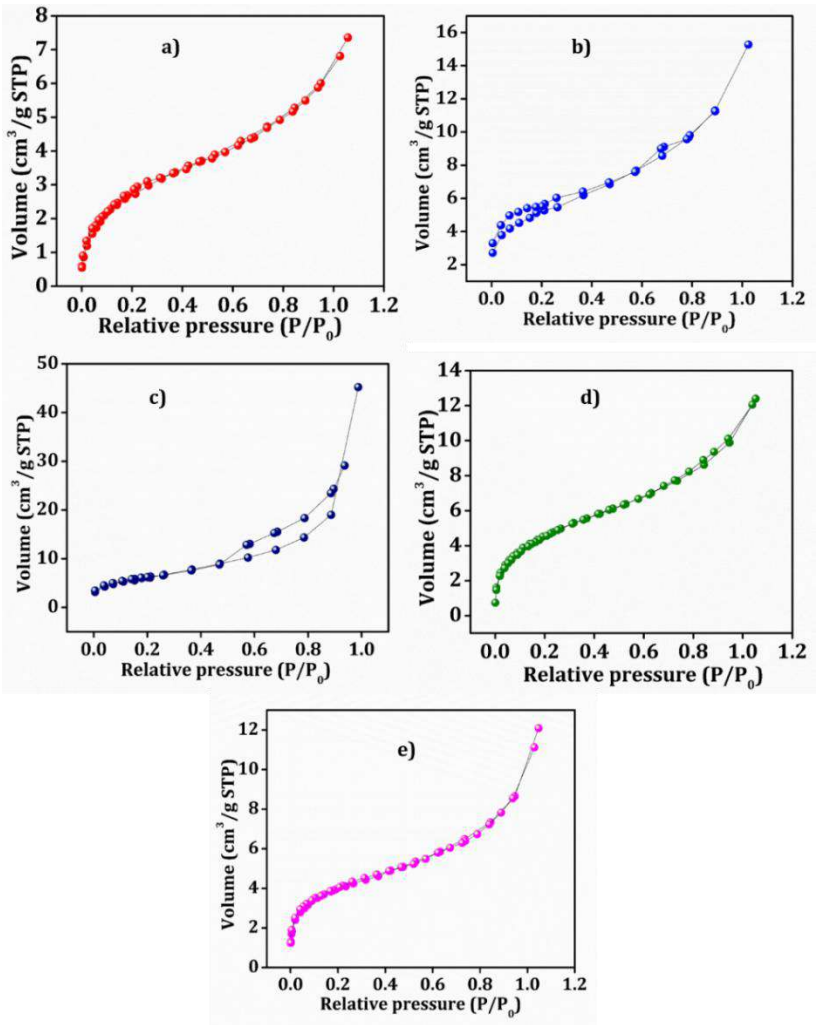

Figure 4.10 *Nitrogen adsorption-desorption isotherms of (a) PPy, and NGQDs/PPy composites with varying NGQDs content: (b) NPP-25, (c) NPP-50, (d) NPP-75 and e) NPP-100*

Figure 4.10 (a-e) presents the nitrogen adsorption-desorption isotherms of PPy and NGQDs/PPy composites, while the corresponding Barrett-Joyner-Halenda (BJH) pore size distribution curves are shown in Figure 4.11. The BET analysis reveals that the specific surface areas of PPy, NPP-25, NPP-50, NPP-75, and NPP-100 are 10, 14, 21, 17, and 16 $m^2 g^{-1}$, respectively. Among these, NPP-50 exhibits the highest surface area, indicating an optimal concentration of NGQDs that facilitates better dispersion and stronger interaction with the PPy matrix. These results are consistent with the SEM images of PPy and NGQDs/PPy composites.

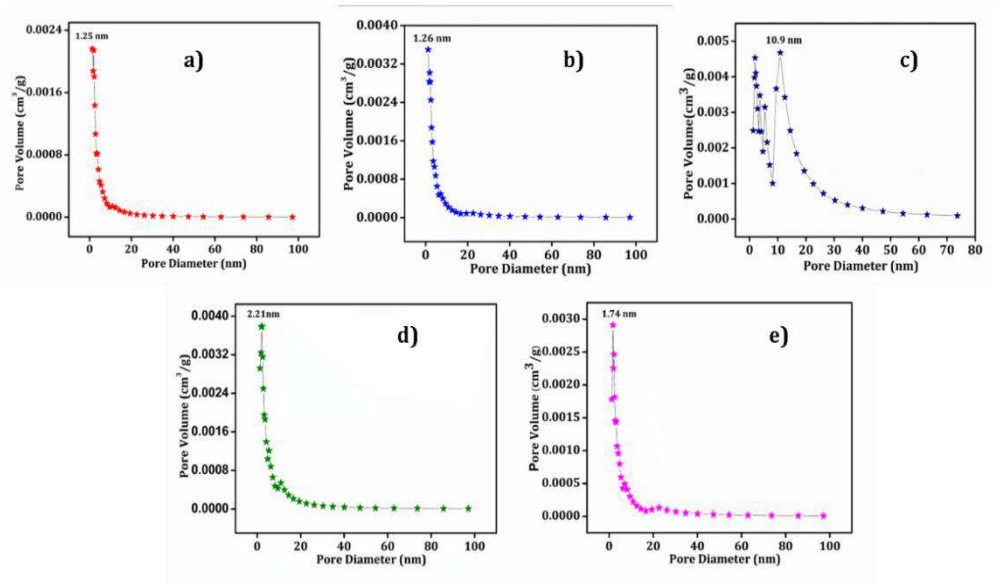

Figure 4.11 *BJH pore size distribution profiles of pure PPy and NGQDs/PPy composites:* ***(a)*** *PPy,* ***(b)*** *NPP-25,* ***(c)*** *NPP-50,* ***(d)*** *NPP-75, and* ***(e)*** *NPP-100*

The pore size distribution, confirms that all samples exhibit mesoporous characteristics, which are advantageous for rapid electrolyte ion diffusion. Notably, the NPP-50 composite demonstrates a well-developed mesoporous structure, offering a synergistic combination of high surface area and

increased pore volume. These features collectively provide more electroactive sites, enhance charge storage capability, and improve electrolyte accessibility. Overall, the superior textural properties of the NPP-50 electrode material suggest its strong potential for high-performance supercapacitor applications, especially in delivering enhanced rate capability and long-term cyclic stability.

4.2.9. Electrochemical Analysis

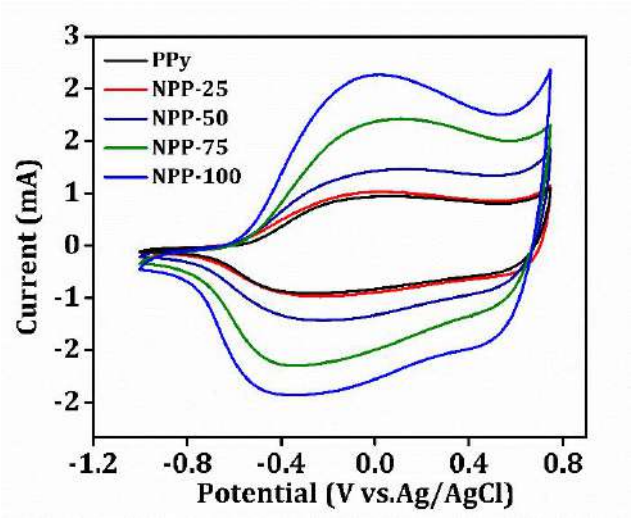

Figure 4.11 *CV curves of PPy and NGQDs/PPy composites recorded at a scan rate of 25mVs^{-1}*

CV measurements were carried out to evaluate the electrochemical behavior of pure PPy, NGQDs, and NGQDs/PPy composites within a potential window ranging from –1.0 to 0.75 V. The experiments employed a three-electrode system with 1 M NaCl as the electrolyte. Figure 4.11 shows the CV curves of both PPy and NGQDs/PPy composites at a scan rate of 25mV/s, which exhibit well-defined redox peaks indicative of prominent pseudocapacitive behavior. Equations (4.1) and (4.2) represent the redox

processes involved in the PPy and NGQDs/PPy composites, which primarily entail the reversible oxidation and reduction of the PPy backbone. During the oxidation process, neutral PPy chain (PPy^0) undergoes electron loss and simultaneously incorporates chloride ions (Cl^-) from NaCl electrolyte to maintain charge neutrality, resulting in the formation of doped PPy (PPy^+Cl^-). Conversely, during the reduction step, the doped polymer accepts electrons and expels Cl^- ions back to the electrolyte, thereby regenerating the neutral PPy structure. This overall redox mechanism enables reversible ion insertion and explusion, contributing to charge storage [20, 46]

$$PPy^0 + Cl^- \leftrightharpoons PPy^+Cl^- + e^- \quad (4.1)$$

$$PPy^+Cl^- + e^- \leftrightharpoons PPy^0 + Cl^- \quad (4.2)$$

The CV curves of PPy, NGQDs, and NGQDs/PPy composites recorded at different scan rates are presented in Figure 4.12 (a-f). As the scan rate increases, both anodic and cathodic peaks shift slightly toward more positive and negative potentials, respectively, indicating kinetic limitations caused by restricted ion diffusion at the electrode-electrolyte interface. The CV curves of NGQDs exhibit a quasi-rectangular shape with broad humps, characteristic of pseudocapacitive behavior. Figure 4.13 depicts a linear correlation of PPy and NGQDs/PPy redox peak currents with the square root of the scan rate. The linear relationship observed, with a high correlation coefficient above (R^2=0.97), confirms that the electrochemical process is predominantly diffusion-controlled up to a scan rate of 200 mV/s [47].The incorporation of NGQDs into the PPy matrix markedly enhanced the current response and significantly increased the area enclosed by the CV curves compared to pure PPy. This response results from rapid and reversible faradaic redox reactions facilitated by surface functional groups such as -OH,

-COOH, and -NH_2, which contribute to efficient charge storage and accelerated electron transfer kinetics. Among all the composites, NPP-50 demonstrated the most pronounced electrochemical performance, exhibiting the largest CV area and highest current response [3]. This indicates that NPP-50 achieved an optimal synergy between electrical conductivity and electroactive surface area.

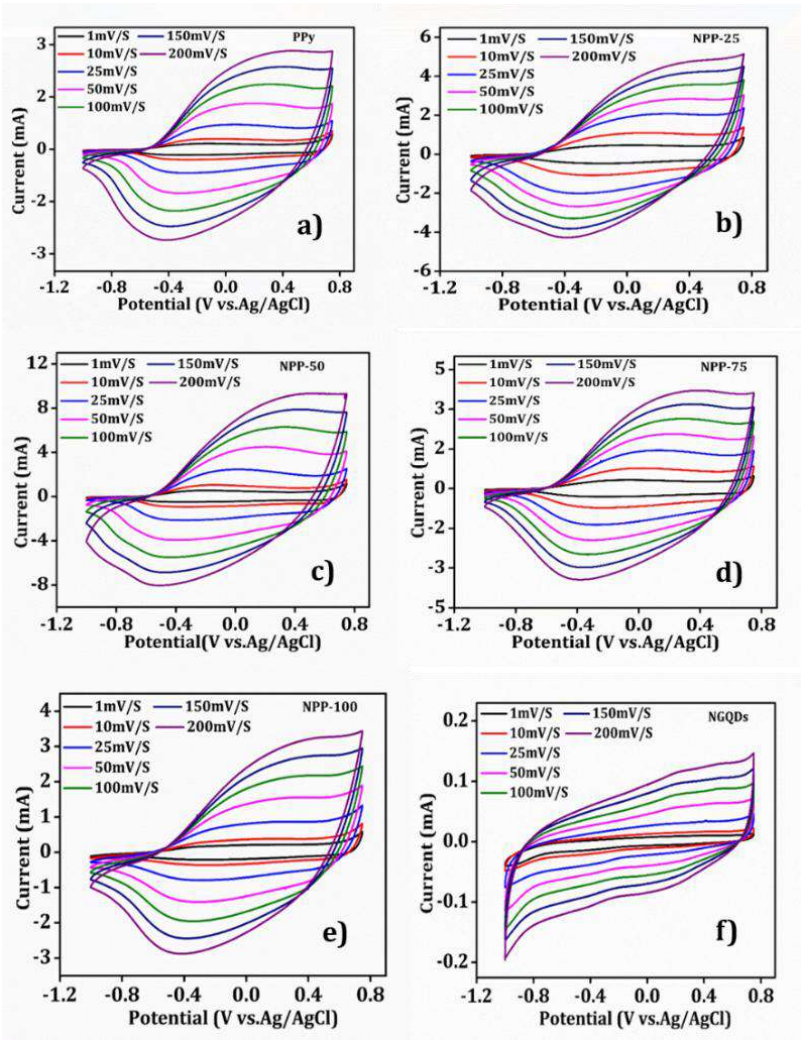

Figure 4.12 *CV curves at different scan rates for* ***(a)*** *NPP-25,* ***(b)*** *NPP-50,* ***(c)*** *NPP-75,* ***(d)*** *NPP-100,* ***(e)*** *pure PPy, and* ***(f)*** *NGQDs*

In contrast, composites with higher NGQD content (NPP-75 and NPP-100) showed current response was lower likely attributed to the aggregation of GQDs at higher concentration of NGQDs. Such aggregation may obstruct active sites and hinder efficient electron transport, thereby limiting the overall capacitive behavior [8].

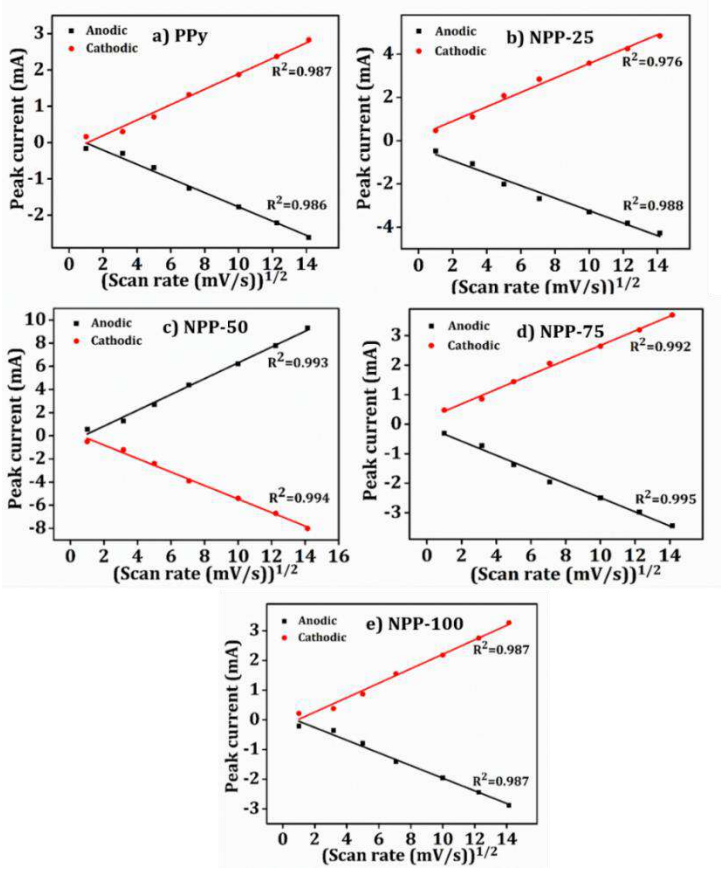

Figure 4.13 *Variation of anodic and cathodic peak currents as a function of the square root of* ***(a)*** *PPy,* ***(b)*** *NPP-25,* ***(c)*** *NPP-50,* ***(d)*** *NPP-75, and* ***(e)*** *NPP-100*

The total capacitance of an electrode results from the combined effects of surface-controlled capacitive processes and diffusion-controlled faradaic

reactions. The current response derived from CV measurements at various scan rates follows a power-law relationship, expressed as $i = av^b$,where i is the current, ν is the scan rate, and a and, b are constants.

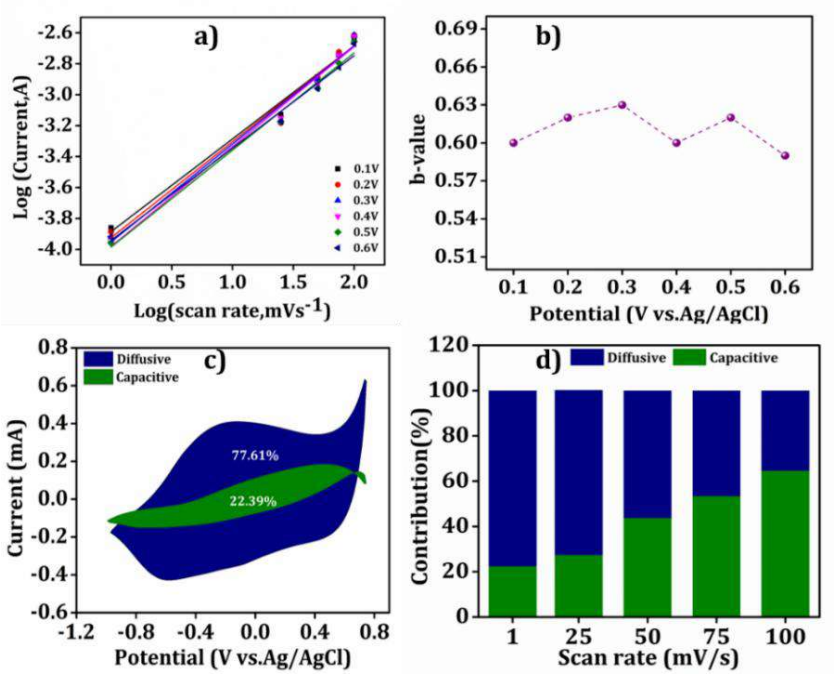

Figure 4.14 ***(a)*** *Log-log plots of current versus scan rate recorded at different potentials;* ***(b)*** *b-values obtained at each potential;* ***(c)*** *analysis showing the separation of pseudocapacitive and diffusion-controlled currents at a scan rate of 1 mV s^{-1} and,* ***(d)*** *variation in the contribution of surface-controlled and diffusion-controlled processes with increasing scan rate.*

A b-value of 0.5 signifies a diffusion-controlled mechanism associated with pseudocapacitive behavior, while b value close to 1 indicates a surface-controlled capacitive process typical of electric double-layer capacitance [48, 49]. Figure 4.14 (a) illustrates the linear dependence of log i on log ν at different potentials, from which the b-values were extracted based on the slopes of the fitted lines. As shown in Figure 4.14 (b) the calculated b-values

for the NPP-50 composite range between 0.5 and 1, confirming the coexistence of both pseudocapacitive and EDLC-type charge storage mechanisms. To further quantify these contributions, the Dunn method was employed, which separates the total current into capacitive ($k_1 v$) and diffusion-controlled ($k_2 v^{1/2}$) components according to the equation.4.3

$$i = k_1 v + k_2 v^{1/2}$$

(4.3)

Here, k_1 and k_2 represent the proportional contributions from the capacitive and diffusion-controlled processes, respectively and can be obtained from the slope and intercept of the plot of $\frac{i}{v^{1/2}}$ versus $v^{1/2}$. As shown in Figure 4.14(c), the electrode delivers a capacitive (pseudocapacitive) contribution of 22.39% and a diffusion-controlled contribution of 77.61% at a scan rate of 1 mV s^{-1}. When the scan rate increases, as illustrated in Figure 4.14(d), the capacitive contribution gradually increases, whereas the diffusion-controlled portion decreases correspondingly. This trend suggests that at higher scan rates, the limited diffusion time of electrolyte ions restricts their access to the inner active sites of the electrode material, thereby enhancing the dominance of surface-controlled capacitive charge storage [50].

GCD analysis was carried out to evaluate the electrochemical behavior of PPy, NGQDs, and NGQDs/PPy composites. The corresponding GCD profiles at various current densities ranging from 0.8 to 5 A g^{-1} are presented in Figure 4.15 (a–f). All samples display nearly ideal, symmetric triangular GCD curves, which is a hallmark of excellent pseudocapacitive characteristics and highly reversible charge-discharge processes. Among all the composites studied, the NPP-50 composite exhibits the most extended discharge duration, as shown in Figure 4.15 (d).

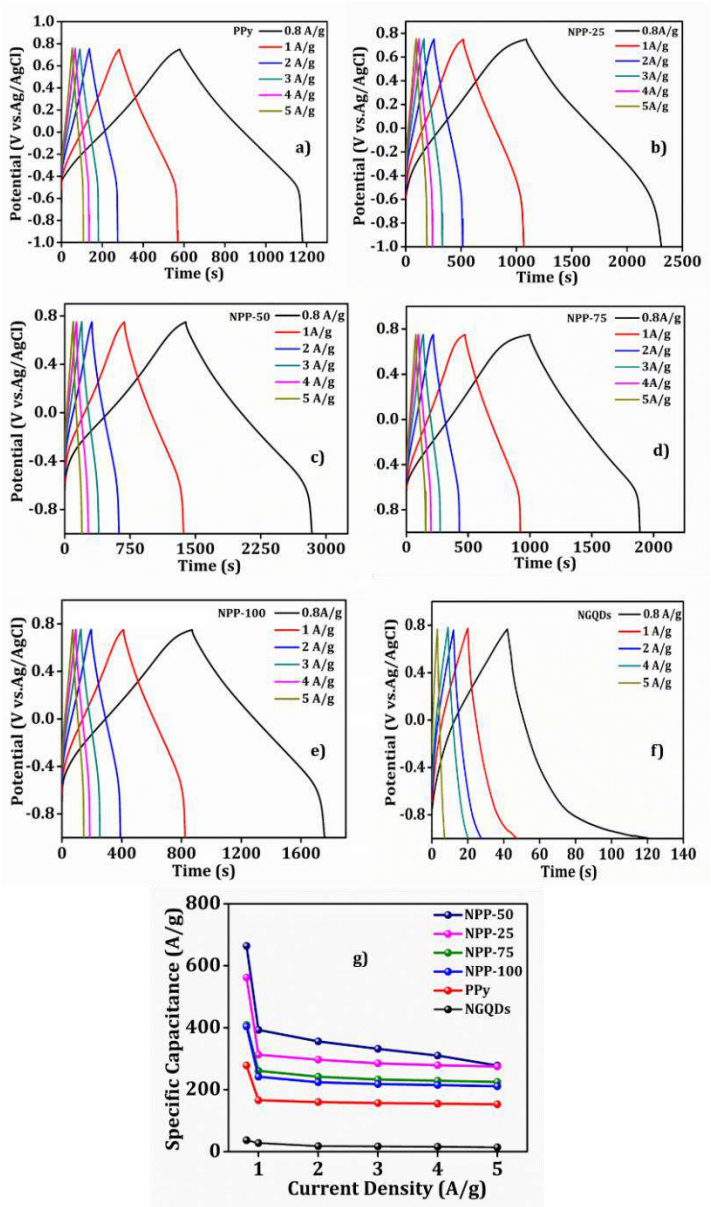

Figure 4.15 *GCD profiles of* ***(a)*** *PPy* ***(b)*** *NGQDs* ***(c)*** *NPP-25* ***(d)*** *NPP-50* ***(e)*** *NPP-75* ***(f)*** *NPP-100* ***(g)*** *specific capacitance of PPy and NGQDs/PPy composites at different current densities*

Indicating its superior charge storage capability. Specific capacitance values, using Eq. (2.8), are 37, 278, 562, 664, 409, and 404 F g^{-1} for PPy, NGQDs, NPP-25, NPP-50, NPP-75, and NPP-100, respectively.

Remarkably, NPP-50 delivers the highest specific capacitance, highlighting the optimized integration of NGQDs, which enhances electrical conductivity, increases electroactive surface area, and promotes more efficient redox activity.Conversely, a decline in capacitance was observed for NPP-75 and NPP-100, primarily due to the agglomeration of excess NGQDs, which hindered ion diffusion and reduced access to active sites. Additionally, the NPP-50 electrode maintains excellent rate capability, with specific capacitance values of 664, 393, 356, 332, 310, and 278 F g^{-1} at increasing current densities of 0.8, 1, 2, 3, 4, and 5 A g^{-1}, respectively, as shown in Figure 4.15 (g). This consistent performance underscores its outstanding electrochemical robustness and potential for high-performance energy storage applications [4, 51].Nyquist plots of all five electrodes, recorded across a frequency range of 0.1 Hz to 100 kHz with an applied potential of 10 mV, are shown in Figure 4.16 [18, 52]. Notably, the NPP-50 electrode exhibits a smaller semicircle, indicating a lower R_{ct} than pure PPy and other NGQDs/PPy composites.

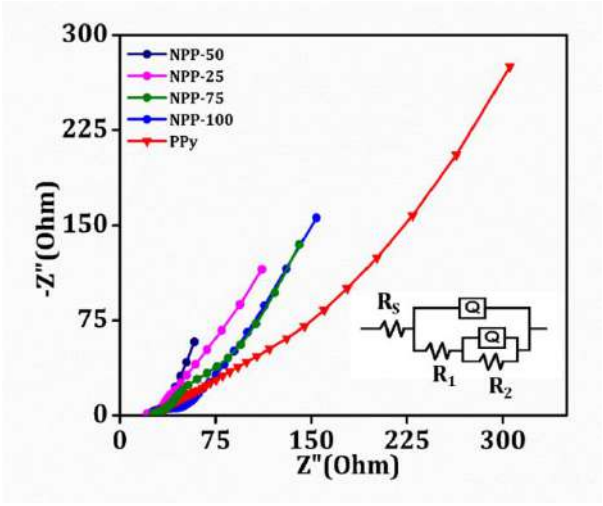

Figure 4.16 *Nyquist plots obtained from EIS measurements of PPy and NGQDs/PPy composites*

In the low-frequency region, the linear segment of the Nyquist plot for NPP-50 approaches the vertical axis more closely, suggesting a reduction in Warburg (diffusion) resistance and thus more efficient ion transport. This reduction in both charge-transfer and diffusion resistances signifies improved electrochemical kinetics and enhanced interfacial contact. The superior performance of NPP-50 can be attributed to the optimal loading of NGQDs, for enhanced electrical conductivity, increase electroactive surface area, and promotes faster ion diffusion within the PPy matrix and thereby for superior electrochemical performance [53]. To gain a deeper understanding of their electrochemical behavior, an equivalent circuit model was proposed to fit the experimental EIS data, as illustrated in the inset of Figure 4.16. The accuracy of the fitting is confirmed by the low chi-square value, calculated to be the order of 4.85×10^{-5}, indicating excellent agreement between the model and experimental data. The equivalent electrical circuit includes components R_S, R_1, R_2, Q_1, and Q_2. Here, R_S represents the solution resistance, R_1 and R_2 denote the charge-transfer or polarization resistances, while Q_1 and Q_2 are constant phase elements (CPEs) used to simulate non-ideal capacitive behavior at the electrode-electrolyte interface [23, 34].

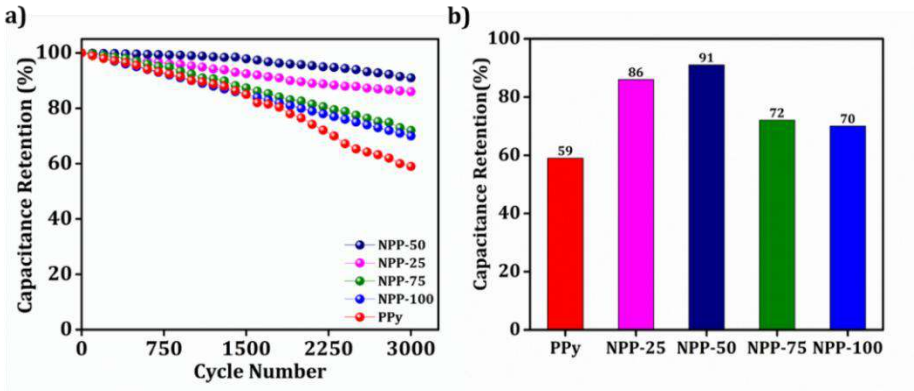

Figure 4.17 (a) *Cyclic stability of PPy and NGQDs/PPy composites* ***(b)*** *effect of NGQDs loading on cyclic stability of NGQDs/PPy composites*

Figure 4.17 (a) illustrates the galvanostatic charge-discharge cyclic performance of PPy and NGQDs/PPy composites over 3000 cycles at a current density of 5 A g^{-1}. It is evident that NGQDs-incorporated composites exhibit substantially superior cyclic stability compared to pristine PPy. Notably, the NPP-50 composite retained approximately 91% of its initial capacitance, underscoring its exceptional durability and structural integrity under repeated cyclic. This remarkable stability is primarily attributed to the synergistic π-π stacking and hydrogen bonding interactions between the conjugated backbone of PPy and surface functional groups (-OH, $-NH_2$) of NGQDs. This interaction are depicted in Figure 4.18. These interactions effectively suppress polymer chain entanglement and inhibit structural degradation, thereby maintaining the integrity of the electroactive network. Moreover, NGQDs serve as conductive nanospacers that not only reduce the aggregation of PPy chains, but also promote efficient electron/ion transport pathways throughout the composite matrix [22].

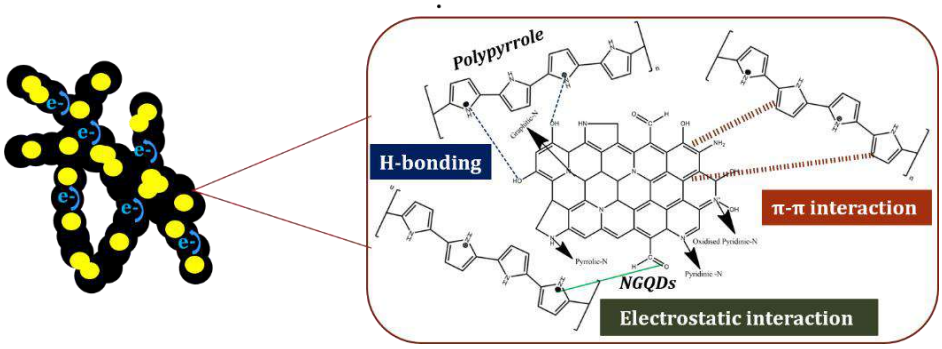

Figure 4.18 *Schematic representation of the proposed interaction between NGQDs and PPy*

The NPP-25 electrode also demonstrated cyclic stability, retaining 86% of its initial capacitance. In contrast, electrodes with higher NGQD loadings (NPP-75 and NPP-100) have decreased cyclic stability. The effect of NGQDs on cyclic stability is presented in Figure 4.17(b). This is due to excess NGQDs impeding access to electroactive sites and hindering charge transfer

dynamics. Pristine PPy, on the other hand, suffered from pronounced electrochemical degradation, retaining 60% of its initial capacitance after 3000 cycles indicative of poor structural degradation under long-term operation. Collectively, these results affirm that the strategic incorporation of NGQDs not only enhances the electrical conductivity but also significantly suppresses degradation during extended cyclic. Thus, NGQDs/PPy composites, particularly NPP-50, emerge as promising candidates for high-performance, long-life supercapacitor applications [54].

4.2.10. Symmetric supercapacitor device

To demonstrate the practical applicability of our material, a symmetric supercapacitor was fabricated by assembling two NPP-50 electrodes (each with an area of 2 cm^2) in a parallel configuration, separated by a NaCl/ PVA gel electrolyte. A schematic illustration of the assembled device is shown in Figure 4.19 (a). The electrochemical performance of the device was evaluated using CV, as depicted in Figure 4.19 (b), with scan rates ranging from 5 to 200 mV/s within a potential window of 0 to 1.2 V. The resulting CV curves displayed well-defined quasi-rectangular profiles, indicative of ideal electrical double-layer behavior and excellent electrochemical reversibility. Further insights were obtained from GCD measurements conducted over the same voltage range at current densities between 1 and 5 A/g. The results are shown in Figure 4.16 (c). The device delivered a high specific capacitance of 451 F/g at 1 A/g. Although a slight decline in capacitance was observed at higher current densities, attributable to restricted ion diffusion, the device maintained a high capacitance of 354 F/g even at 5 A/g. These results underscore the outstanding rate capability and robust performance of the NPP-50-based supercapacitor. EIS was performed on the NPP-50 device both before and after 3000 charge-discharge cycles.

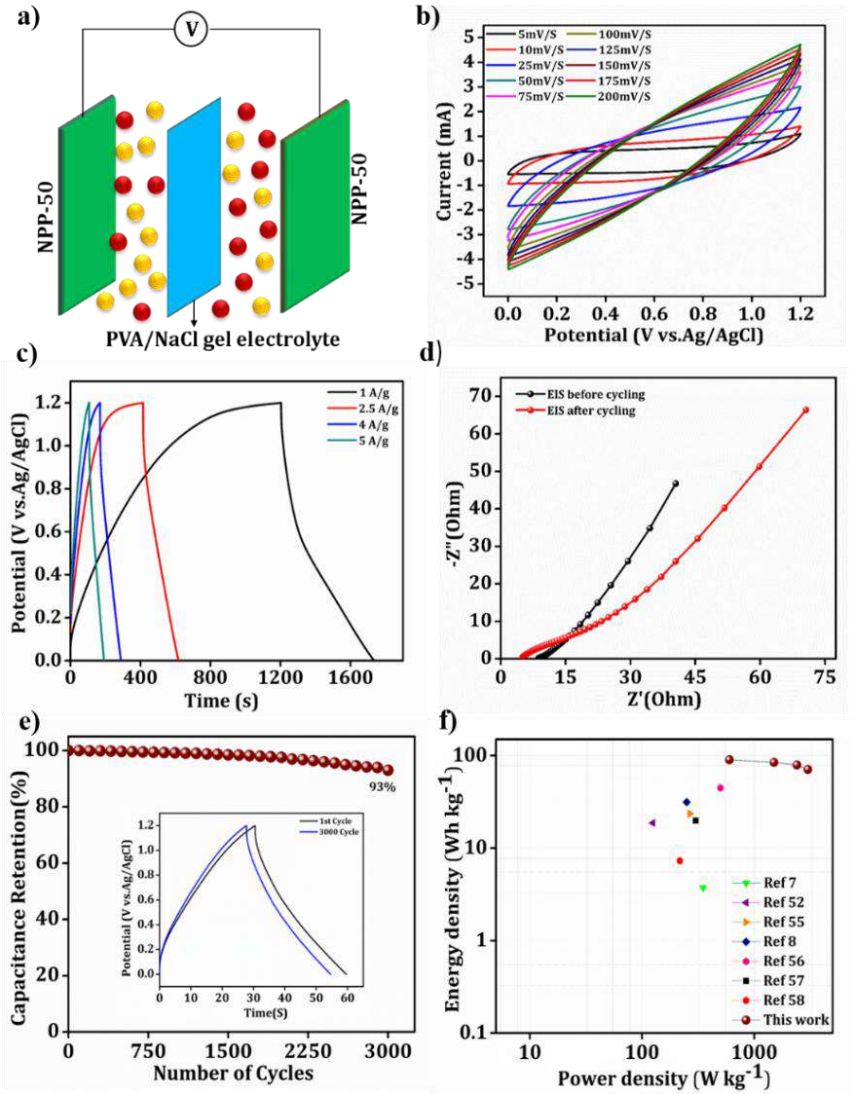

Figure 4.19 ***(a)*** *Schematic illustration of the as-fabricated symmetric supercapacitor device* ***(b)*** *CV curves of the NPP-50 device at various scan rates* ***(c)*** *GCD profiles of the NPP-50 device at different current densities* ***(d)*** *Nyquist plots of the device before and after cyclic* ***(e)*** *cyclic stability of the device over 3000 cycles (inset comparison of the first cycle and 3000 th cycle)* ***(f)*** *Ragone plot comparing the energy and power densities of the NPP-50 device with those of previously reported system.*

The corresponding Nyquist plots, depicted in Figure 4.19 (d), exhibited only minor variations, indicating negligible deterioration and confirming the excellent structural and chemical integrity of the electrode. Cyclic stability of the device was evaluated through 3000 cycles, is shown in the Figure 4.19 (e). The NPP-50 supercapacitor retained high cyclic stability 93% of its initial capacitance.

The energy and power densities of the device was analyzed using a Ragone plot (Figure 4.19 (f)), which demonstrated a high energy density of 90.2 Wh kg^{-1} coupled with a power density of 600.4 W kg^{-1}, surpassing many other NGQDs/PPy based supercapacitors given in Table 4.2. Figure 4.20 shows the photographic images of four symmetric devices fabricated using NPP-50 connected in series to illuminate a red light-emitting diode (LED). The NPP-50-based symmetric supercapacitor demonstrated exceptional energy and power characteristics, along with remarkable cyclic stability, establishing it as a highly reliable supercapacitor device. These results highlight its strong potential for integration into next-generation portable and wearable electronic systems.

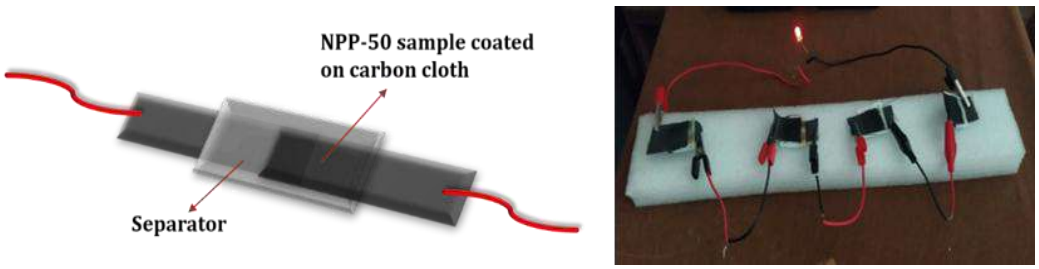

Figure 4.20 *Photographic images of LED light connected to four devices in series.*

Table 4.2 *A comparative analysis of related literature and the current research*

Electrode Material	Specific Capacitance ($F\ g^{-1}$)	Energy density ($Wh\ kg^{-1}$)	Power density ($W\ kg^{-1}$)	References
ZnO@PPy-P(VSANa)/CF	171.8 $F\ g^{-1}$ at 5mV s^{-1}	23.5	266.7	[55]
AC-CDs/PPy	226 $F\ g^{-1}$ at 1 $A\ g^{-1}$	31.4	250	[7]
Bent-Cs-PPy	268 $F\ g^{-1}$ at 1 $A\ g^{-1}$	44.67	500	[56]
CC@CQD @PPy	537.9 $F\ g^{-1}$ at 0.5A g^{-1}	18.7	125	[53]
PPy/PVA/TiO_2/GQDs	219.4 $F\ g^{-1}$ at 1A g^{-1}	3.73	350	[6]
MoO_3/PPy/rGO	412.3 $F\ g^{-1}$ at 0.5A g^{-1}	19.8	301	[57]
TiO_2/PPy	99.42 $mFcm^2$	7.28	217.4	[58]
NPP-50	**664 $F\ g^{-1}$ at 1A g^{-1}**	**90.2**	**600.4**	**This work**

4.3. Conclusions

In conclusion, NGQDs and NGQDs/PPy composites were successfully synthesized through hydrothermal treatment followed by in-situ chemical polymerization. Detailed characterization confirmed that embedding NGQDs

into the PPy framework significantly improved the structural integrity and electrochemical performance of the resulting composites. Among the fabricated composites, the NPP-50 sample demonstrated the most outstanding results, achieving a high specific capacitance of 664 F g^{-1} at 0.8 A g^{-1}, along with excellent rate capability and long-term cyclic stability, maintaining 91% of its initial capacitance after 3000 cycles. The symmetric supercapacitor device constructed using NPP-50 also exhibited impressive specific capacitance of 451 F g^{-1} at 1 A g^{-1}, an energy density of 90.2 Wh kg^{-1}, and a power density of 600.4 W kg^{-1}. Moreover, it retained 93% of its capacitance after 3000 cycles at 5 A g^{-1}, highlighting its excellent durability. Owing to its superior energy storage capability, high power output, cost-effectiveness, and robust stability, the NPP-50 composite emerges as a promising candidate for next-generation energy storage technologies, including batteries, sensors, and other advanced applications.

References

[1] M. Vandana, S. Veeresh, H. Ganesh, Y. Nagaraju, H. Vijeth, M. Basappa, H. Devendrappa, Graphene oxide decorated SnO2 quantum dots/polypyrrole ternary composites towards symmetric supercapacitor application, Journal of Energy Storage, 46 (2022) 103904.
[2] A. Zheng, C. Tao, J. Guo, Z. Shi, X. Cao, Z. Zhang, X. Yang, Phytate-doped polypyrrole/graphene composite aerogel electrodes for supercapacitors, Chemical Engineering Journal, (2025) 164116.
[3] X. Jian, H.-m. Yang, J.-g. Li, E.-h. Zhang, L.-l. Cao, Z.-h. Liang, Flexible all-solid-state high-performance supercapacitor based on electrochemically synthesized carbon quantum dots/polypyrrole composite electrode, Electrochimica Acta, 228 (2017) 483-493.
[4] X. Jian, J.-g. Li, H.-m. Yang, L.-l. Cao, E.-h. Zhang, Z.-h. Liang, Carbon quantum dots reinforced polypyrrole nanowire via electrostatic self-assembly strategy for high-performance supercapacitors, Carbon, 114 (2017) 533-543.
[5] A. Khaleque, M.A.S. Aly, Z.H. Khan, Chemical and electrochemical synthesis of doped conducting polymers and their application in

supercapacitors: An overview, Chemical Engineering Journal, (2025) 160444.
[6] M. Salman, M. Aslam, Z. Mustafa, M. Ahmad, A. Shehzad, Flexible polypyrrole/polyvinyl alcohol/titanium dioxide/graphene quantum dots nanocomposite films for energy storage devices, Diamond and Related Materials, 152 (2025) 111996.
[7] L. Wang, Q. Zeng, Q. Chen, C.M. Li, J. Chen, Synergistically boosting the electrochemical performance of polypyrrole-coated activated carbon derived from carbon dots for a high-performance supercapacitor, Chemical Communications, 57 (2021) 9264-9267.
[8] R. Malik, S. Lata, U. Soni, P. Rani, R.S. Malik, Carbon quantum dots intercalated in polypyrrole (PPy) thin electrodes for accelerated energy storage, Electrochimica Acta, 364 (2020) 137281.
[9] G. Rani, R. Ahlawat, H. Kumar, Green source-based carbon quantum dots, composites, and key factors for high-performance of supercapacitors, Journal of Power Sources, 617 (2024) 235170.
[10] T. Wang, Z. Liu, P. Li, H. Wei, K. Wei, X. Chen, Lignin-derived carbon aerogels with high surface area for supercapacitor applications, Chemical Engineering Journal, 466 (2023) 143118.
[11] S. Sharanappa, S. Vijaykumar, D. Suresh, A.B. Shbil, H. Ganesha, S. Veeresh, Y. Nagaraju, H. Devendrappa, Synthesis of water-soluble nitrogen doped carbon quantum dots-polypyrrole nanocomposite via in-situ polymerization for high performance supercapacitor application, Journal of Energy Storage, 74 (2023) 109371.
[12] O. Soto-Díaz, D.R. Lobato-Peralta, A. Ayala-Cortés, H.I. Villafán-Vidales, S.A. Gamboa-Sanchez, V.H. Collins-Martínez, M. Román-Aguirre, G. González-García, A.K. Cuentas-Gallegos, V.H. Ramos-Sánchez, Solar-driven synthesis of CaS-decorated activated carbon from pecan nutshell agro-industrial waste to assemble green, stable, and electro-activated supercapacitors, Chemical Engineering Journal, 507 (2025) 160743.
[13] A.R. Heiba, M. Abdel-Salam, T. Yoon, E. El Sawy, Zr-MOF composites with zipped and unzipped carbon nanotubes for high-performance electrochemical supercapacitors, Nanoscale, 17 (2025) 459-473.
[14] J. Zhang, W. Liu, M. Du, Q. Xu, M. Hung, R. Xiang, M. Liao, X. Wang, B. Wang, A. Yu, Kinetic investigation of the energy storage process in graphene fiber supercapacitors: Unraveling mechanisms, fabrications,

property manipulation, and wearable applications, Carbon Energy, 7 (2025) e625.
[15] R. Mendoza-Jiménez, L. Garcés-Patiño, C. Rodriguez-Gonzalez, J. Oliva, P. Salas, The role of graphene oxide and graphene quantum dots synthesized from spent lithium-ion batteries for Highly efficient supercapacitors, Electrochimica Acta, (2025) 146499.
[16] M. Paalo, S.S. Yegit, L. Moumaneix, T. Kallio, A. Jänes, Synthesis of zirconium carbide via sol-gel method as a precursor for micro-and mesoporous carbide-derived carbon materials, Carbon Trends, 19 (2025) 100494.
[17] X. Shi, Z.-Z. Yin, J. Xu, S. Li, C. Wang, B. Wang, Y. Qin, Y. Kong, Preparation, characterization and the supercapacitive behaviors of electrochemically reduced graphene quantum dots/polypyrrole hybrids, Electrochimica Acta, 385 (2021) 138435.
[18] K. Rahimpour, R. Teimuri-Mofrad, Novel hybrid supercapacitor based on ferrocenyl modified graphene quantum dot and polypyrrole nanocomposite, Electrochimica Acta, 345 (2020) 136207.
[19] K. Wu, S.-z. Xu, X.-j. Zhou, H.-x. Wu, Graphene quantum dots enhanced electrochemical performance of polypyrrole as supercapacitor electrode, Journal of electrochemistry, 19 (2013) 9.
[20] A. Shabeeba, L. Rajan, M.P. Sidheekha, M.S. Thayyil, Y.A. Ismail, Polypyrrole/hydrogel hybrid films as multi sensing supercapacitor electrodes, Journal of Energy Storage, 55 (2022) 105724.
[21] X. Zhou, P. Ma, A. Wang, C. Yu, T. Qian, S. Wu, J. Shen, Dopamine fluorescent sensors based on polypyrrole/graphene quantum dots core/shell hybrids, Biosensors and Bioelectronics, 64 (2015) 404-410.
[22] P. Wilczewska, J. Breczko, D.M. Bobrowska, M. Wysocka-Żołopa, J. Goclon, A. Basa, K. Winkler, Enhancement of polypyrrole electrochemical performance with graphene quantum dots in polypyrrole nanoparticle/graphene quantum dot composites, Journal of electroanalytical chemistry, 923 (2022) 116767.
[23] M. Muhiuddin, N. Bharadishettar, N.A. Devi, A. Gautam, S.S. Chauhan, A.B. Siddique, M.I. Ahmad, M. Satyanarayan, U. Bhat, W. Akhtar, Neodymium doped graphene quantum dots/PANI composite for supercapacitor application, Journal of Alloys and Compounds, 1012 (2025) 178516.

[24] P. Tian, L. Tang, K. Teng, S. Lau, Graphene quantum dots from chemistry to applications, Materials today chemistry, 10 (2018) 221-258.
[25] R. Das, K.K. Paul, P. Giri, Highly sensitive and selective label-free detection of dopamine in human serum based on nitrogen-doped graphene quantum dots decorated on Au nanoparticles: Mechanistic insights through microscopic and spectroscopic studies, Applied Surface Science, 490 (2019) 318-330.
[26] R. Das, S. Parveen, A. Bora, P. Giri, Origin of high photoluminescence yield and high SERS sensitivity of nitrogen-doped graphene quantum dots, Carbon, 160 (2020) 273-286.
[27] J. Wang, C. Lu, T. Chen, L. Hu, Y. Du, Y. Yao, M.C. Goh, Simply synthesized nitrogen-doped graphene quantum dot (NGQD)-modified electrode for the ultrasensitive photoelectrochemical detection of dopamine, Nanophotonics, 9 (2020) 3831-3839.
[28] Y. Wu, X. Liu, J. Wang, B. Zhang, X. Zhang, O. Hai, Layered double hydroxide/polypyrrole with neural-like transmission network for high-performance supercapacitor electrode, Journal of Energy Storage, 110 (2025) 115295.
[29] S. Ben Aoun, Nanostructured carbon electrode modified with N-doped graphene quantum dots–chitosan nanocomposite: a sensitive electrochemical dopamine sensor, Royal Society open science, 4 (2017) 171199.
[30] M.R. Rahardja, D. Kurniawan, W.-H. Chiang, Microplasma-enabled sustainable synthesis of nitrogen-doped graphene quantum dots for sensitive detection of 4-nitrophenol, Chemosensors, 11 (2023) 390.
[31] R. Vinoth, I.M. Patil, A. Pandikumar, B.A. Kakade, N.M. Huang, D.D. Dionysios, B. Neppolian, Synergistically enhanced electrocatalytic performance of an N-doped graphene quantum dot-decorated 3D MoS2–graphene nanohybrid for oxygen reduction reaction, Acs Omega, 1 (2016) 971-980.
[32] X. Wang, Y. Mo, X. Deng, Y. Cai, C. Guo, J. Chen, W. Wang, G. Li, Multifunctional Nitrogen-doped graphene quantum dots enables Efficient and Stable GaAs/CNT heterojunctions solar cell, Carbon, (2025) 120535.
[33] A. Pasha, S. Khasim, A. Darwish, T.A. Hamdalla, S. Al-Ghamdi, High performance organic coatings of polypyrrole embedded with manganese iron oxide nanoparticles for corrosion protection of conductive copper surface,

Journal of Inorganic and Organometallic Polymers and Materials, 32 (2022) 499-512.
[34] M. Vandana, H. Vijeth, S. Ashokkumar, H. Devendrappa, Hydrothermal synthesis of quantum dots dispersed on conjugated polymer as an efficient electrodes for highly stable hybrid supercapacitors, Inorganic Chemistry Communications, 117 (2020) 107941.
[35] M. Vandana, S. Ashokkumar, H. Vijeth, L. Yesappa, H. Devendrappa, Synthesis and characterization of polypyrrole-graphene quantum dots nanocomposites for supercapacitor application, in: AIP Conference Proceedings, AIP Publishing LLC, 2019, pp. 030535.
[36] Z. Ouyang, Y. Lei, Y. Chen, Z. Zhang, Z. Jiang, J. Hu, Y. Lin, Preparation and specific capacitance properties of sulfur, nitrogen co-doped graphene quantum dots, Nanoscale Research Letters, 14 (2019) 1-9.
[37] J. El Nady, A. Shokry, M. Khalil, S. Ebrahim, A. Elshaer, M. Anas, One-step electrodeposition of a polypyrrole/NiO nanocomposite as a supercapacitor electrode, Scientific Reports, 12 (2022) 3611.
[38] J. Mahmood, N. Arsalani, S. Naghash-Hamed, Z. Hanif, K.E. Geckeler, Preparation and characterization of hybrid polypyrrole nanoparticles as a conducting polymer with controllable size, Scientific Reports, 14 (2024) 11653.
[39] S. Nosheen, M. Irfan, F. Habib, S.Z. Abbas, B. Waseem, F. Iftikhar, B. Soomro, A.K. Aziz, Synthesis and characterization of polypyrrole synthesized via different routes, Int. J. Eng. Res. Technol., 9 (2020) 1630-1633.
[40] V.-P. Thai, D.N. Tran, K. Kosugi, K. Takahashi, T. Sasaki, T. Kikuchi, One-Step Synthesis of N-Doped Graphene Quantum Dots via Plasma Contacting Liquid for Multiple Heavy Metal Ion Detection, ACS Applied Nano Materials, 7 (2024) 12664-12672.
[41] Y. Wang, Y. Wang, D. Liu, Y. Feng, D. Yang, S. Wu, H. Jiang, D. Wang, S. Bi, Study on the Synthesis and Electrochemical Properties of Nitrogen-Doped Graphene Quantum Dots, Materials, 17 (2024) 6163.
[42] A. Mizera, M. Wysocka–Żołopa, S. Zięba, P. Ławniczak, A.T. Dubis, A. Łapiński, New polypyrrole composites with graphene quantum dots as counterions: electrical and spectroscopic properties, Polymer, (2025) 129048.
[43] D. Qu, Z. Sun, M. Zheng, J. Li, Y. Zhang, G. Zhang, H. Zhao, X. Liu, Z. Xie, Three colors emission from S, N co-doped graphene quantum dots for

visible light h2 production and bioimaging, Advanced Optical Materials, 3 (2015) 360-367.
[44] Y.-N. Hao, H.-L. Guo, L. Tian, X. Kang, Enhanced photoluminescence of pyrrolic-nitrogen enriched graphene quantum dots, RSC advances, 5 (2015) 43750-43755.
[45] A. Kashyap, B. Dehingia, R. Ghosh, H. Kalita, Recent Progress on Graphene-Based Derivatives for Enhanced Energy Storage Devices, Chemistry–An Asian Journal, (2025) e202401794.
[46] Y.A. Ismail, J.G. Martínez, A.S. Al Harrasi, S.J. Kim, T.F.F. Otero, Polypyrrol/chitosan hydrogel hybrid microfiber as sensing artificial muscle, in: Electroactive Polymer Actuators and Devices (EAPAD) 2011, SPIE, 2011, pp. 450-461.
[47] A. Shabeeba, M.P. Sidheekha, L. Rajan, Y.A. Ismail, Flexible hybrid film of polypyrrole incorporated chitosan as a biomimetic multistep electrochemical sensor of working temperature: a potentiodynamic study, RSC advances, 12 (2022) 31911-31922.
[48] R. Rajamany, S. Prakash, Y.A. Ismail, Polyvinylpyrrolidone (PVP) assisted synthesis of Ni MOF: Enhanced supercapacitive performance through morphology control, Next Materials, 7 (2025) 100459.
[49] A. Thadathil, Y.A. Ismail, P. Periyat, Ternary 3D reduced graphene oxide/Ni 0.5 Zn 0.5 Fe 2 O 4/polyindole nanocomposite for supercapacitor electrode application, RSC advances, 11 (2021) 35828-35841.
[50] M.Z. Iqbal, S.S. Haider, S. Siddique, M.R.A. Karim, S. Zakar, M. Tayyab, M.M. Faisal, M. Sulman, A. Khan, M. Baghayeri, Capacitive and diffusion-controlled mechanism of strontium oxide based symmetric and asymmetric devices, Journal of Energy Storage, 27 (2020) 101056.
[51] H.S. AlSalem, K.M.S. Katubi, M.S. Binkadem, S.T. Al-Goul, A.M. Wahba, Fabrication of asymmetric supercapacitors (AC@ GQDs//AC) with high electrochemical performance utilizing activated carbon and graphene quantum dots, ACS omega, 8 (2023) 40808-40816.
[52] S. Abinaya, A. Saranraj, S.P. Jose, J. Cherusseri, A. Fatehmulla, Unveiling dynamic insights of nitrogen-doped carbon quantum dots in α-Fe2O3/PANI nanocomposite for supercapattery application, Journal of Materials Science, 59 (2024) 21846-21867.
[53] C. Zhou, G. Liu, F. Wang, H. Liu, J. Nai, J. Hao, Z. Sui, Z. Yang, W. Xu, Growth of CQD/PPy on cotton cloth as a binder-free high-performance

flexible electrode for symmetric supercapacitor, Journal of Alloys and Compounds, 992 (2024) 174618.
[54] P. Chaluvachar, G. Mahesha, V.G. Nair, D.K. Pai, Y. Sudhakar, Graphitic carbon nitride supported metal-free heterostructure embedded with carbon quantum dots and PEDOT as electrodes for supercapacitors, Electrochimica Acta, 513 (2025) 145605.
[55] B. Polat, S. Yazar, M.B. Arvas, C. Ozeroglu, ZnO@ Polypyrrole-P (VSANa) on flexible and wearable carbon felt as electrodes for nonenzymatic H2O2 sensor and supercapacitor applications, Journal of Materials Research, 39 (2024) 913-927.
[56] F. Mashkoor, M. Shoeb, S.M. Adnan, J. Ahmed, C. Jeong, Biomacromolecular engineering of redox-active chitosan–polypyrrole–clay hybrid materials for machine learning-assisted desulfurization and supercapacitor application, International Journal of Biological Macromolecules, (2025) 146304.
[57] H. Deng, J. Huang, Z. Hu, X. Chen, D. Huang, T. Jin, Fabrication of a three-dimensionally networked MoO3/PPy/rGO composite for a high-performance symmetric supercapacitor, ACS omega, 6 (2021) 9426-9432.
[58] H. Cai, Y. Li, D. Liu, X. Yang, D. Zhou, E. Han, X. Li, Q. Li, Y. He, Construction of Moiré-like TiO2/polypyrrole electrodes for high performance photo-assisted supercapacitors, Colloids and Surfaces A: Physicochemical and Engineering Aspects, 703 (2024) 135386.

Chapter 5

Polypyrrole Derived Nitrogen-Doped Graphene Quantum Dots/Polyaniline Composites for Supercapacitor Applications

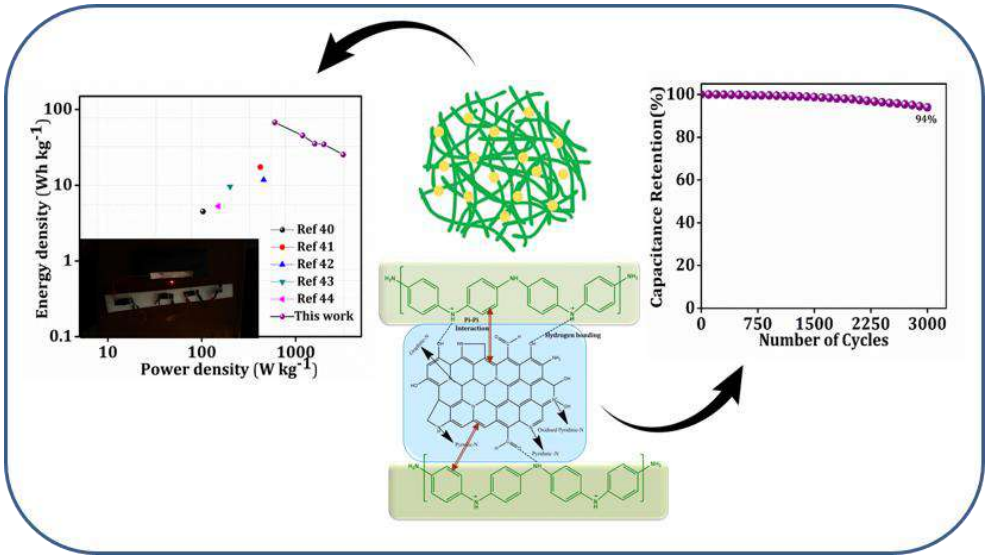

This chapter discusses a novel NGQDs/PANI composites developed for high-performance supercapacitor applications. NGQDs were prepared using PPy as the precursor. The NGQDs/PANI composites for varying compositions of NGQDs were prepared and systematically studied to understand their supercapacitive behavior. Further, the practical applicability of the material was demonstrated by fabricating a symmetric supercapacitor device.

5.1. Introduction

In the previous chapter, the electrochemical characterization and supercapacitive performance of NGQDs/PPy composites were discussed in detail. The enhancement of supercapacitive performance of conducting polymer especially PPy using NGQDs was demonstrated. In the present chapter, the focus is shifted from PPy to PANI. Among various conducting polymers, PANI is one of the most promising material owing to its intrinsically high theoretical capacitance, simple synthesis route, low production cost, and excellent environmental stability [1-4]. Nevertheless, PANI faces a major drawback associated with pronounced volumetric expansion and contraction during the repeated charge-discharge process, due to ion insertion and extraction. Such structural fluctuations inevitably damage the polymer backbone, leading to a substantial decline in cyclic durability [4-6]. To address this limitation, we have explored the NGQDs loading in the development of NGQDs/PANI composites.

In this work, novel NGQDs/PANI composites were prepared through chemical oxidative polymerization method. The NGQDs/PANI composites for varying composition of NGQDs into a constant amount of aniline monomer. The resulting composites exhibit high specific capacitance, excellent rate capability, and moderately high cyclic stability, excellent energy and power density making it a promising candidate for next-generation supercapacitor applications.

5.2. Results and Discussions

The NGQDs/PANI composites were characterized and studied for their potential use in supercapacitor applications. Details of the synthesis process of the NGQDs/PANI composites are given in Chapter 2.

5.2.1. TEM Analysis

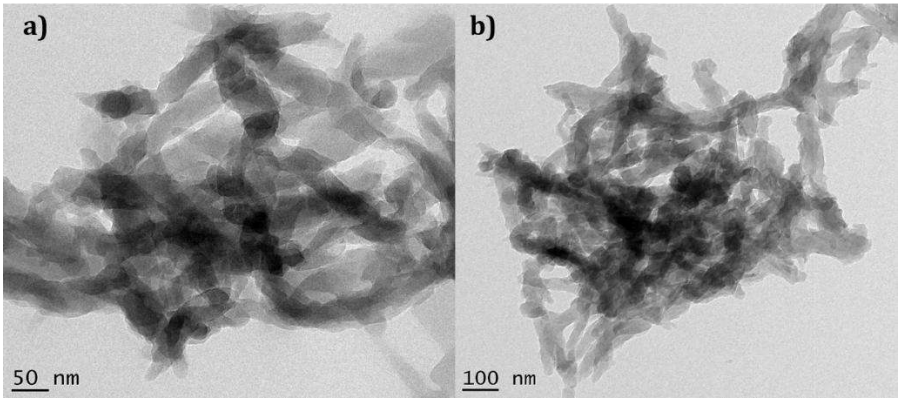

Figure 5.1 *TEM images of the NPA-25 composite*

The detailed description of the TEM images of NGQDs is provided in Chapter 4. TEM images of the NPA-25 composite are shown in Figure 5.1, which reveal a noticeable change in morphology upon incorporation of NGQDs into the PANI matrix. The embedded NGQDs promote the formation of denser and more compact internal structures, which can be attributed to strong π–π interactions between the aromatic backbone of PANI and the conjugated domains of the NGQDs [7, 8].

5.2.2. FTIR Analysis

The FTIR spectra of PANI, NGQDs, and NGQDs/PANI composites are shown in Figure 5.2. The NGQDs exhibit a characteristic absorption peak at 1745 cm^{-1}, corresponding to the carbonyl (C=O) stretching vibration. A detailed discussion of the FTIR spectra of NGQDs has been presented in Chapter 4. The FTIR spectrum of pristine PANI (Figure. 5.2) displays a broad absorption band at 3460 cm^{-1}, due to N-H stretching. Two peaks at 1567 and 1481 cm^{-1}, is attributed to quinoid and benzenoid C=C vibrations, respectively. confirm the formation of the PANI backbone [9].

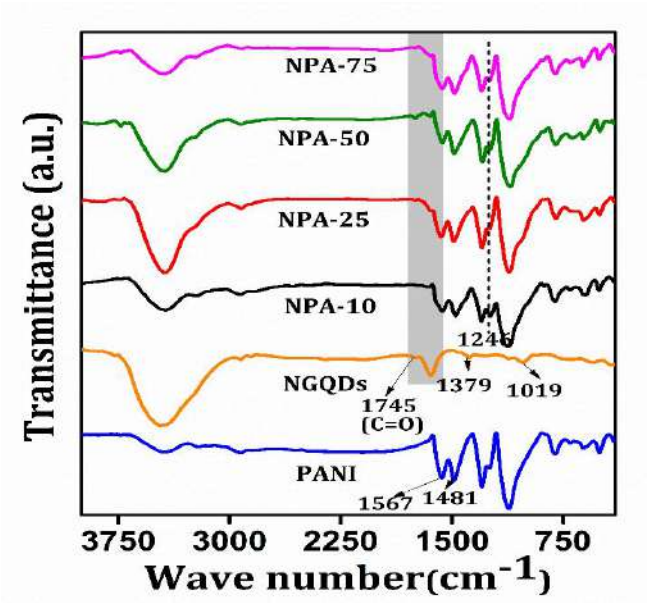

Figure 5.2 *Comparison of the FTIR spectra for PANI, NGQDs, and the NGQDs/PANI composite*

In the composites, the characteristic PANI peaks at 1567 and 1481 cm^{-1} are slightly red shifted, signifying effective interactions between NGQDs and PANI chains. The carbonyl stretching vibration, observed at 1745 cm^{-1} in NGQDs, also appears in the composite but shifts to 1739 cm^{-1}due to hydrogen bonding between the C=O groups of NGQDs and the N-H groups of PANI [10-12].

5.2.3. XRD Analysis

Figure 5.3 shows the XRD pattern for PANI, NGQDs, and NGQDs/PANI composites. The XRD diffraction pattern observed at 26^0 was assigned to (002) plane of graphitic carbon, revealing a graphitic nature of the NGQDs with highly disordered carbon atoms. In the case of pure PANI, distinct reflections appear at $2\theta \approx 14.90°$, 20.62°, and 25.60°, corresponding to the (011), (020), and (200) crystallographic planes, respectively, confirming the

formation of the highly protonated conducting emeraldine salt form [13, 14]. These characteristic peaks are retained in all NGQDs/PANI composite samples. Specifically, the reflections from 20.62° and 25.60°, attributed to the (020) and (200) planes, represent the periodic ordering associated with parallel and perpendicular orientations along the PANI chains [15, 16]. In the composite samples, the peak of pristine PANI at 25.60° appears to overlap with the broad NGQDs peak near 26°, suggesting strong interfacial interactions and structural integration between NGQDs and the PANI matrix.

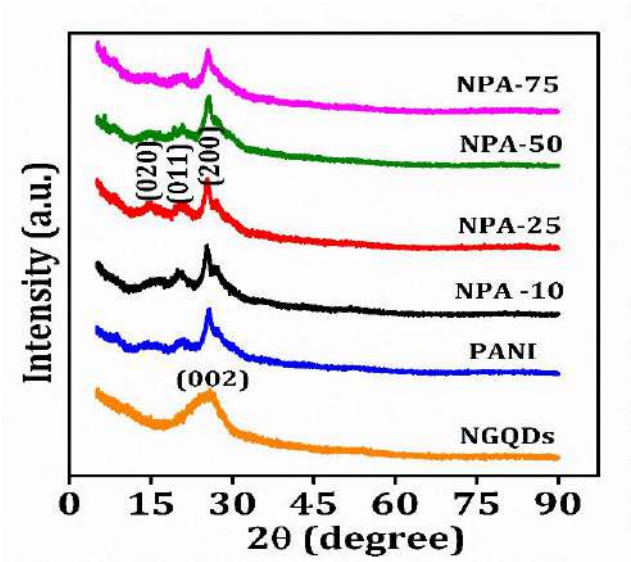

Figure 5.3 *XRD patterns of PANI, NGQDs, and the NGQDs/PPy composites*

5.2.4. UV-Visible Absorption spectra

The UV-Vis spectrum of NGQDs in Figure 5.4(a) exhibited two absorption peaks at 264 nm and 303 nm. This is due to the π-π* transitions within the sp^2-hybridized graphitic structure and n-π* transitions associated with C=O bonds and other surface functional groups containing lone pairs of electrons respectively [17, 18]. The UV-Vis absorption spectra of the PANI and NGQDs/PANI composites are presented in Figure 5.4(b). The spectra shows

three prominent absorption bands centered at approximately 336, 460, and 635 nm . The absorption at 336 nm corresponds to the π → π* transition of the benzenoid rings, whereas the band around 635 nm is attributed to the quinoid segments of PANI. The broad band observed at 460 nm originates from the π* → polaron transition, indicating the oxidized or doped state of PANI [16, 19-21]. The coexistence of both reduced and oxidized bands confirms the presence of mixed electronic states, which is essential for the electrical conductivity of PANI. Compared with PANI, π-π* transition of NGQDs/PANI composites is red shifted from 336 to 350 nm which indicates π-π stacking or interaction between NGQDs and PANI.

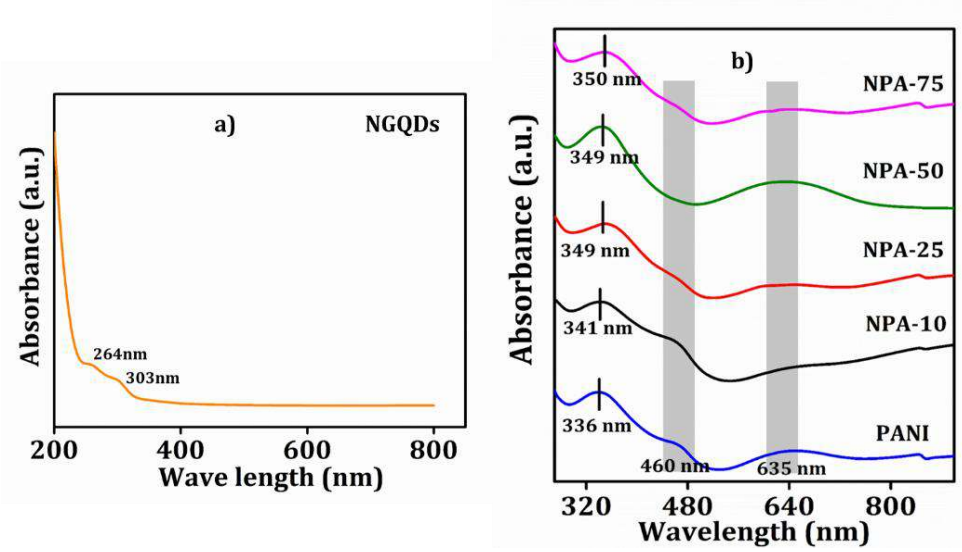

Figure 5.4 (*a*) *UV -Vis spectra of NGQDs* **(*b*)** *UV-Vis spectra of PANI and NGQDs/PANI composites*

5.2.5. SEM Analysis

Figure 5.5 (a-e) presents the FESEM images of pristine PANI and NGQDs/PANI composites. As can be seen from Figure 5.5 (a) PANI exhibits a coral wire-like morphology.

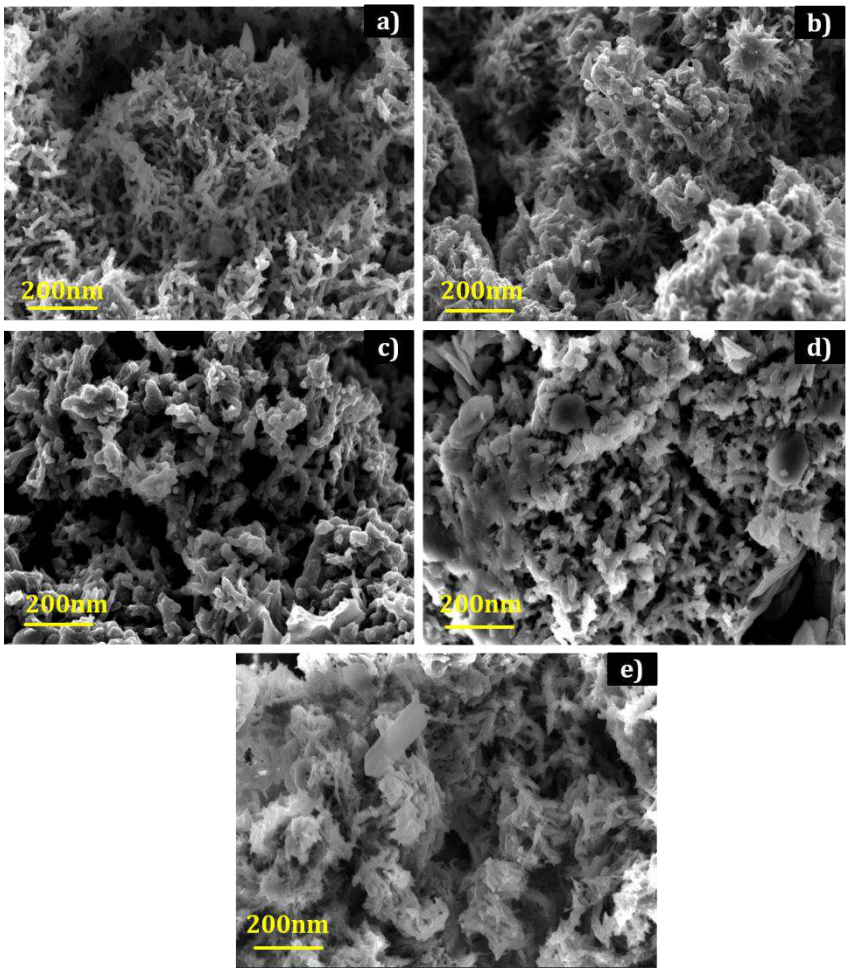

Figure 5.5 *SEM images illustrating the surface morphology of* ***(a)*** *PANI* ***(b)*** *NPA-10,* ***(c)*** *NPA-25,* ***(d)*** *NPA-50, and* ***(e)*** *NPA-75*

Upon incorporation of NGQDs into the PANI matrix (Figure. 5.5(b–e), the morphology evolves into a more porous architecture, which is beneficial for enhancing the specific surface area. Among the composites, NPA-25 shows the most pronounced porous structure, which can enhance electrolyte diffusion. In contrast, the NPA-50 and NPA-75 composites have more agglomerated morphologies, likely due to the increased NGQDs content, which promotes particle aggregation [22-24].

5.2.6. Conductivity Studies

The electrical conductivities of PANI and the NGQDs/PANI composites was evaluated using broadband dielectric spectroscopy. Figure 5.6 shows the variation in conductivity with frequency over the range of 10^{-2} to 10^{7} Hz for all samples.

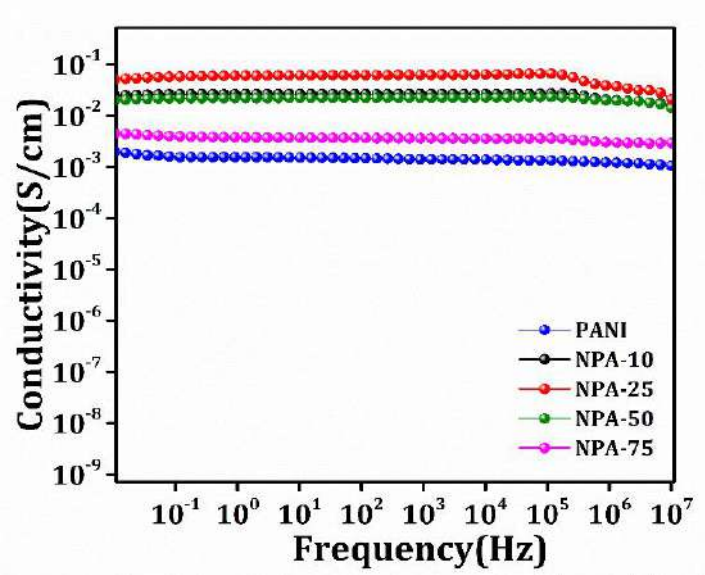

Figure 5.6 *BDS spectra showing the frequency-dependent electrical conductivity of PANI and NGQDs/PANI composites*

PANI exhibited an electrical conductivity of 1.89×10^{-3} S cm^{-1}. All samples exhibited conductivity in the semiconducting region. Notably, the incorporation of NGQDs resulted in a marked enhancement in electrical conductivity. Among the composites, NPA-25 exhibited the highest electrical conductivity of 5.22×10^{-2} S cm^{-1}. This improvement can be attributed to the synergistic interaction between NGQDs and the PANI matrix, which promotes efficient charge transport and enhances electron mobility. In contrast to NPA-50 and NPA-75, increasing NGQDs content, led to a decrease in conductivity. This is due to agglomeration effects, which

disrupt the formation of a continuous conductive network and impede electron transport [25, 26]. The electrical conductivities of PANI and NPA composites are summarized in Table 5.1.

Table 5.1 *Electrical conductivities of PANI and NGQDs/PANI composites*

Material	Conductivity (S cm^{-1})
PANI	$1.89x10^{-3}$
NPA-10	$4.47x10^{-2}$
NPA-25	$5.52x10^{-2}$
NPA-50	$2.05x10^{-2}$
NPA-75	$4.44x10^{-3}$

5.2.7. XPS Analysis

The XPS survey spectrum exhibits three distinct peaks at binding energies of 283.2 eV, 530 eV, and 400 eV, corresponding to the C 1s, O 1s, and N 1s orbitals respectively as shown in Figure 5.7(a). The high-resolution C 1s spectrum, presented in Figure 5.7(b), was deconvoluted into several components. The peak centered at 285.5 eV is attributed to C–N and C=N bonds, while the peak at 284.4 eV corresponds to C–C and C=C bonds in the polymer backbone. Additional peaks observed at 286.5 eV and 287.9 eV are characteristic of C–O/C=O and O–C=O functional groups, respectively.A weak high binding energy tail at 291.6 eV is identified as a shake-up satellite peak, indicating the presence of delocalized π-conjugated aromatic structures [27, 28]. The N 1s spectrum shown in Figure 5.7(c) can be resolved into three distinct peaks at 399.5, 400.2, and 401.3 eV, which are assigned to

pyridinic N, pyrrolic N, and graphitic N species, respectively. Further, the O 1s spectrum of the NPA-25 composite reveals two components at 531 eV and 533 eV, corresponding to C–OH/C–O and C=O groups, respectively [29].

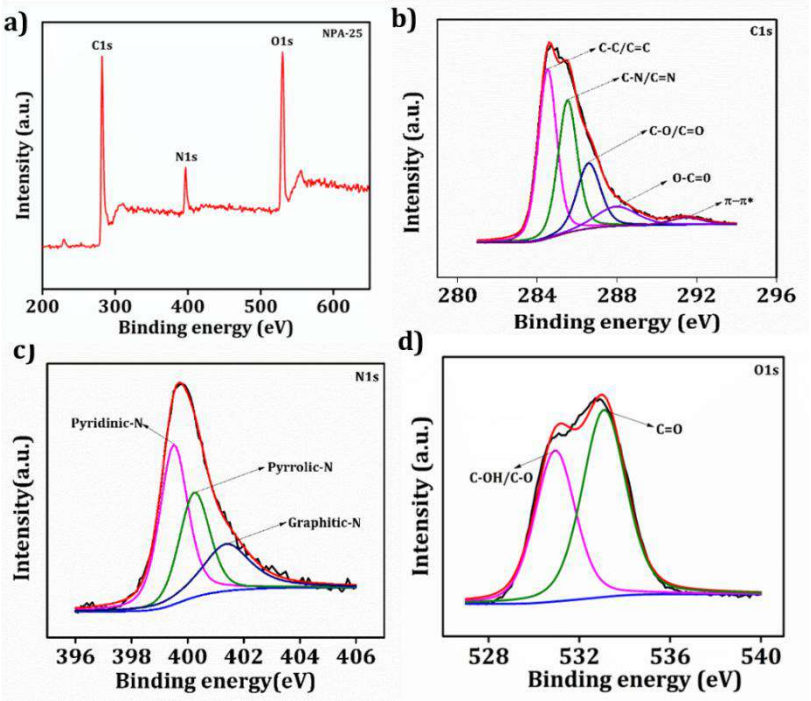

Figure 5.7 *XPS analysis of NPA-25 composite* ***(a)*** *survey spectra showing the elemental composition* ***(b)*** *high-resolution C 1s spectra* ***(c)*** *high-resolution N 1s spectra* ***(d)*** *high-resolution O1s spectra*

5.2.8 BET Surface area Analysis

Figure 5.8 (a-e) presents the nitrogen adsorption-desorption isotherms of PANI and NGQDs/PANI composites. The specific surface areas of PANI, NPA-10, NPA-25, NPA-50 and NPA-75 are 10, 29, 38, 31 and 12 $m^2\ g^{-1}$, respectively. Among these, NPA-25 exhibits the highest surface area. This is due to the optimal concentration of NGQDs that facilitates better dispersion and stronger interaction with the PANI matrix [30, 31].

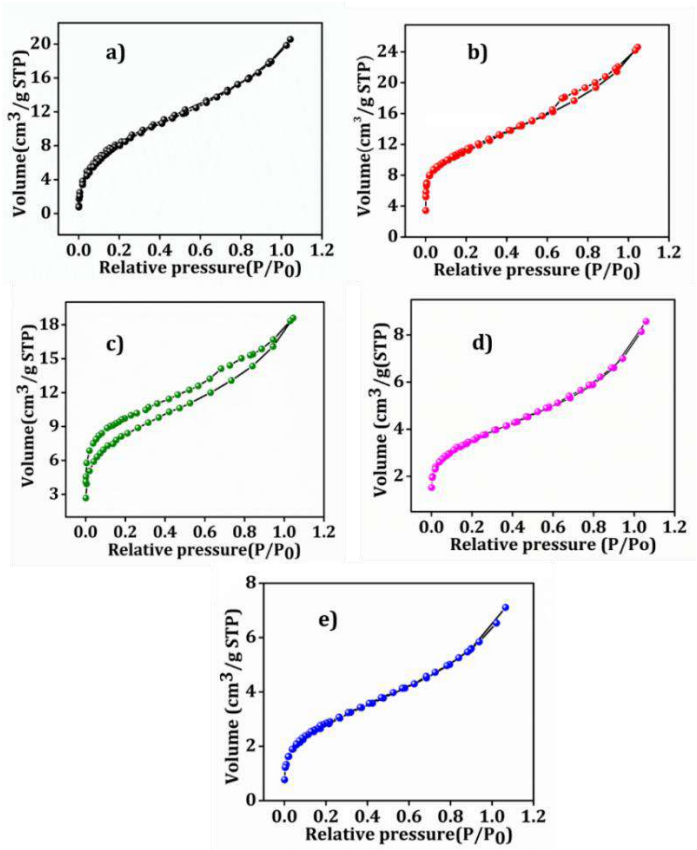

Figure 5.8 *Nitrogen adsorption-desorption profiles for* ***(a)*** *pristine PANI and the NGQDs/PANI composites containing different NGQDs loadings* ***(b)*** *NPA-10,* ***(c)*** *NPA-25,* ***(d)*** *NPA-50,* ***(e)****NPA-75*

5.2.9 Electrochemical Characteristics

The electrochemical behavior of pristine PANI and PANI/NGQDs composites was studied by recording their CV. The experiments were carried out in a three electrode setup using 1M H_2SO_4 window ranging from -0.2 to 0.8V. The CV profiles of pristine PANI as well as NGQDs/PANI composites display two redox peaks. These peaks originate from faradaic reactions involving the leucoemeraldine to emeraldine transition and the subsequent conversion of emeraldine to pernigraniline forms of PANI resulting in

improved faradaic charge storage [32, 33]. The CV curves of PANI and NGQDs/PANI composites are depicted in Figure 5.9.

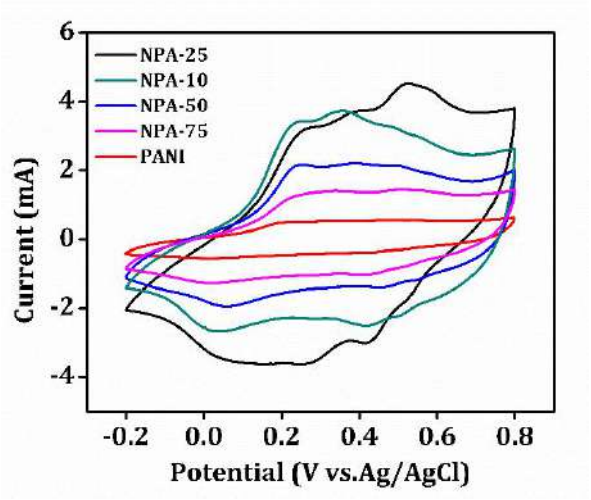

Figure 5.9 *CV profiles of PANI and NGQDs/PANI composites recorded at 25 mV s^{-1}*

The CV curves at different scan rates from 5 to 200 mVs^{-1} are shown in Figure 5.9(a-f). There is a positive shift in the anodic peaks and a negative shift in the cathodic peaks, with increasing scan rate. This response can be attributed to restricted ion diffusion and limited electrolyte accessibility at higher scan rates. It can been seen that the redox properties remain unchanged even at higher scan rates, demonstrating the good rate capability and stable pseudocapacitive behavior of the NGQDs/PANI composites. The CV curve of NGQDs exhibits a quasi-rectangular shape with broad humps, indicating the presence of pseudocapacitive behavior in Figure 5.10(f). Among all the composites, NPA-25 has the the largest CV area and the highest current response, indicating its enhanced electrochemical response. This behavior can be attributed to fast and reversible faradaic redox reactions enabled by surface functional groups including -OH, -COOH, and $-NH_2$

of NGQDs, thereby enhancing charge storage efficiency. This highlights superior charge storage capacity and fast electron transfer kinetics in the composites.

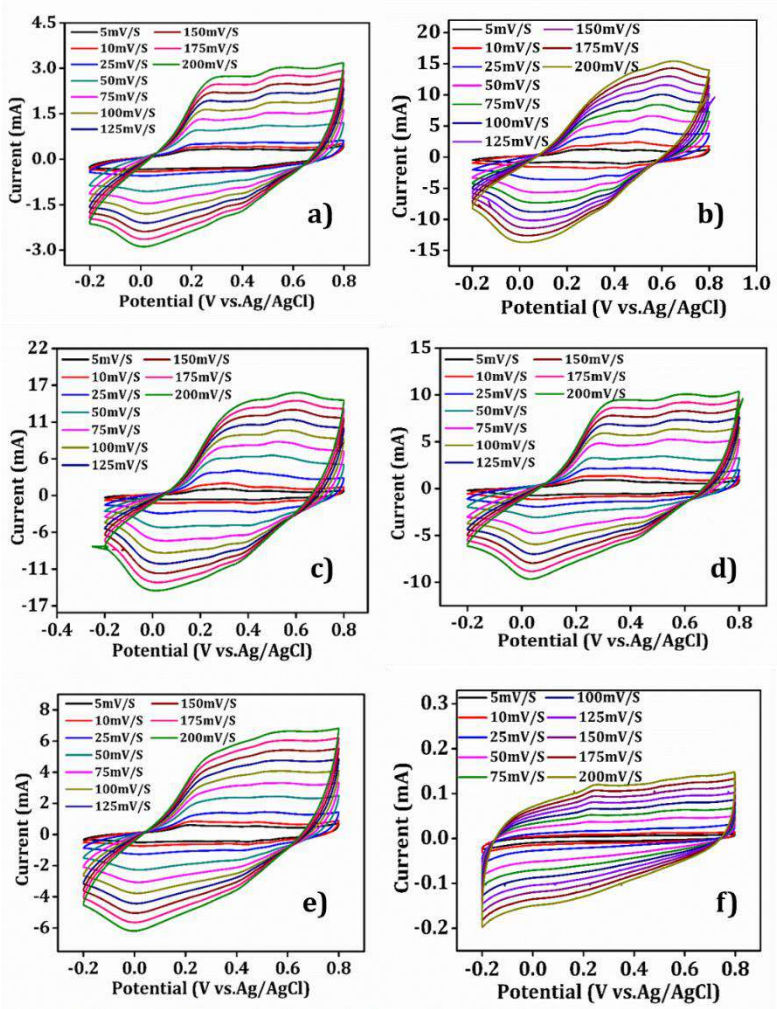

Figure 5.10 *CV profiles for varying scan rates for* ***(a)*** *PANI,* ***(b)*** *NPA-10,* ***(c)*** *NPA-25,* ***(d)*** *NPA-50,* ***(e)*** *NPA-75, and* ***(f)*** *NGQDs.*

Figure 5.11 shows linear dependence of the redox peak current of PANI and NGQDs/PANI composites on the square root of the scan rate. The strong

correlation above R^2=0.97 for all material confirms that diffusion-controlled kinetics dominate the electrochemical process up to 200 mV s^{-1}.

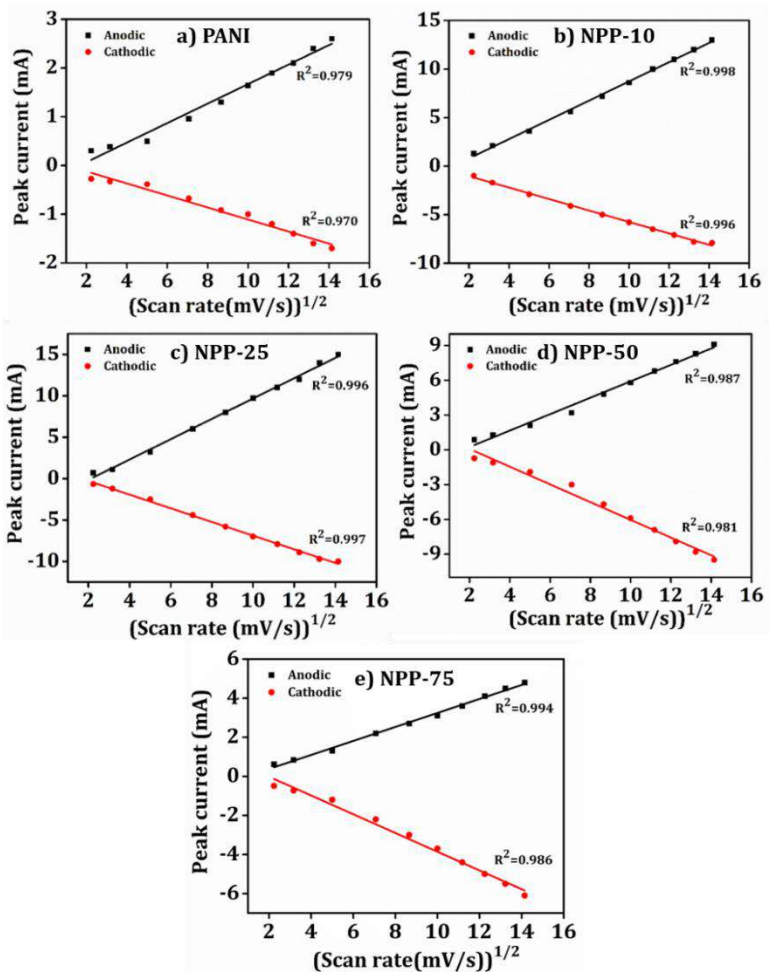

Figure 5.11 *Plot of anodic and cathodic peak currents of* ***(a)*** *PANI* ***(b)*** *NPA-10,* ***(c)*** *NPA-25,****(d)*** *NPA-50 and* ***(e)*** *NPA-75 as a function of square root of scan rates.*

The charge-storage mechanism of the NPA-25 composite was further analyzed using the power-law relationship that correlates the current response (i) at a given potential with the scan rate (ϑ), expressed as:

$$i = av^b \qquad (5.1)$$

$$\log(i) = \log(a) + b\log(v) \quad (5.2)$$

Where a and b are constants. The b values at different potentials were obtained from the slope of the log i versus log (ϑ) plots, as shown in Figure 5.12(a).

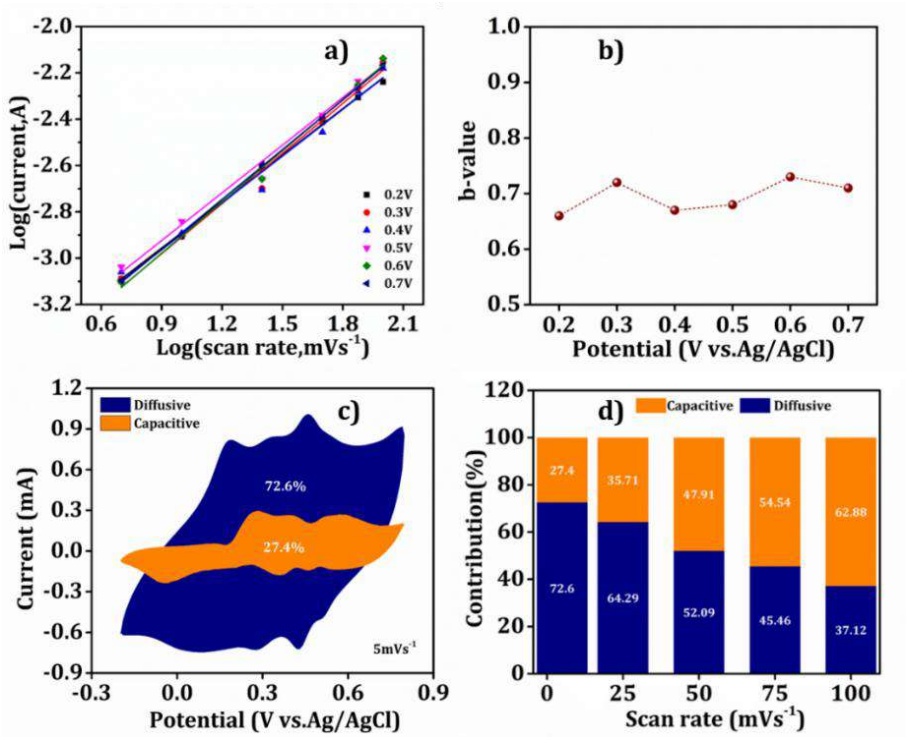

Figure 5.12 ***(a)*** *Relationship between log(current) and log(scan rate) across different potentials* ***(b)*** *corresponding b-values extracted from the slopes* ***(c)*** *separation of capacitive and diffusion-driven currents for NPA-25 at 5 mV* s^{-1}*, and* ***(d)*** *percentage contributions from surface-controlled pseudocapacitance and diffusion-controlled processes as a function of scan rate*

Typically, $b \approx 0.5$ indicates a diffusion-controlled faradaic process, whereas $b \approx 1$ signifies a surface-controlled capacitive process (double-layer behavior). The b values obtained from the anodic region in Figure 5.12(b)

fall between 0.5 and 1. This suggested that NPA-25 exhibits a mixed charge-storage behavior involving both diffusion-dominated faradaic reactions and capacitive processes. To further quantify, Dunn's method was employed to calculate the capacitive and diffusion-controlled contributions. According to this method, can be explained in the previous chapter the measured current at a specific potential can be expressed as:

$$i = k_1 v + k_2 v^{1/2} \quad (5.3)$$

Plotting $\frac{i}{v^{1/2}}$ versus $v^{1/2}$ allows the extraction of k_1 (capacitive contribution) and k_2 (diffusion-controlled contribution). Figure 5.12(c) displays the separation of capacitive and diffusive currents at a scan rate of 5 mV s^{-1}, where the shaded region highlights the capacitive contribution. At this scan rate, NPA-25 exhibits 72.6% diffusion-controlled contribution and 27.4% capacitive contribution. The capacitive and diffusion-controlled contributions at various scan rates are presented in Figure 5.12 (d). As the scan rate increases, the capacitive portion steadily becomes more dominant, while the diffusion-controlled contribution correspondingly diminishes. At the maximum scan rate of 100 mV s^{-1}, the NPA-25 electrode exhibits a capacitive contribution of 62.88%, with the remaining 37.12% arising from diffusion-dominated processes. This trend happens because electrolyte ions do not have sufficient time to diffuse into the electrode matrix and complete redox reactions at higher scan rates, thereby decreasing the faradaic contribution.

Figure 5.13 (a–f) present the GCD profiles recorded at different current densities ranging from 0.8 to 5 A g^{-1}. All electrodes exhibit nearly symmetric triangular charge-discharge curves, indicating excellent pseudocapacitive behavior.

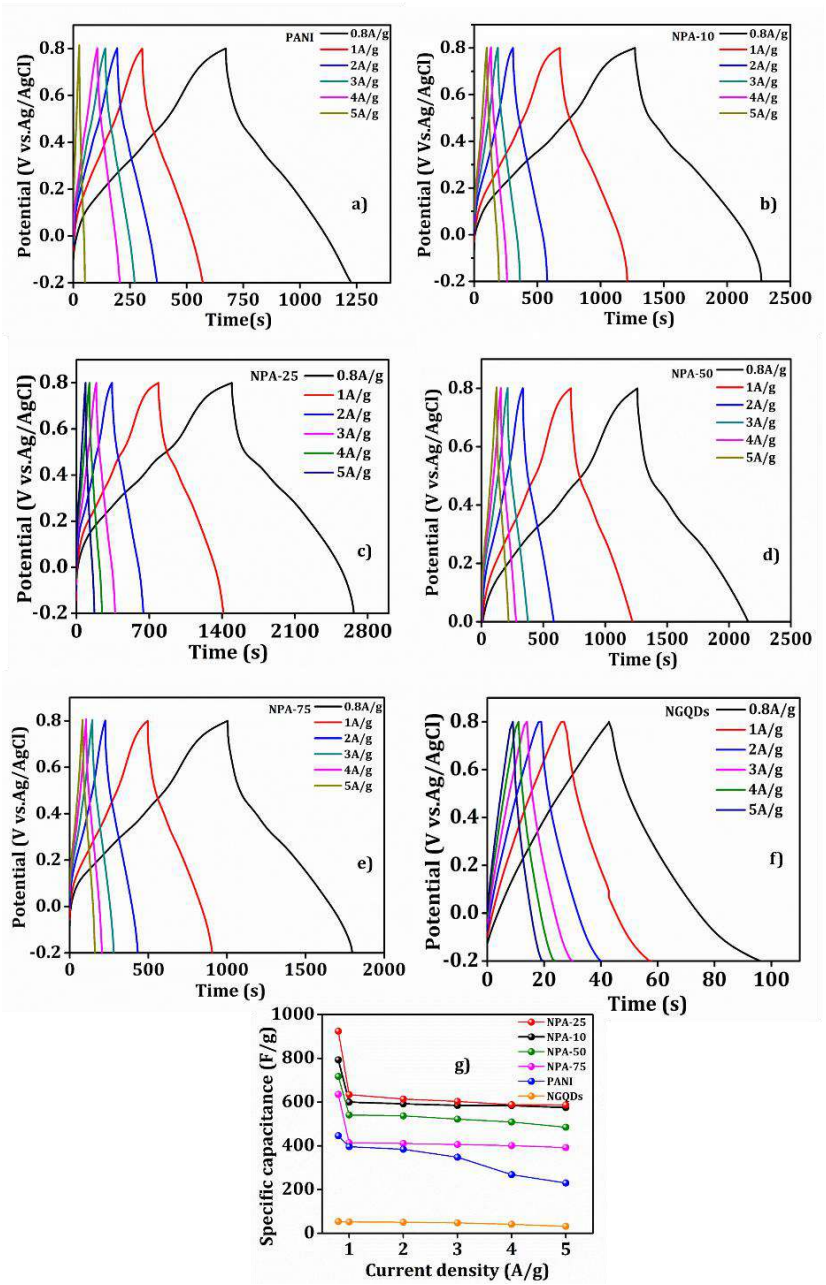

Figure 5.13 *GCD profiles of (a) PANI, (b) NGQDs, (c) NPA-10, (d) NPA-25, (e) NPA-50, and (f) NPA-75 (g) comparison of specific capacitance values at different current densities.*

From the GCD curves, the calculated specific capacitances at a current density of 0.8 A g^{-1} are 446, 793, 924, 717, 635, and 54 Fg^{-1} for PANI, NPA-10, NPA-25, NPA-50, NPA-75, and NGQDs, respectively. Among the composites, NPA-25 has the longest discharge time (Figure 5.13c), reflecting its superior capacitive performance. An optimal loading of NGQDs enhances electrode-electrolyte interfacial contact and increase the specific capacitance. In contrast, NPA-50 and NPA-75 exhibit reduced specific capacitance. Because at higher NGQD loading, the agglomeration increases, which impedes ion transport and electron diffusion, thereby increasing internal resistance [34]. Pristine PANI shows the shortest discharge time and the lowest capacitance. Upon NGQDs loading capacitance increases effectively modifies the conjugated structure of PANI and significantly enhances its electrochemical performance. This results corroborate with the UV-Visible absorption spectra observations [35]. The NPA-25 electrode exhibits excellent rate capability, delivering specific capacitance values of 924, 634, 614, 603, 588, and 587 F g^{-1} at current densities of 0.8, 1, 2, 3, 4, and 5 A g^{-1}, respectively, as illustrated in Figure 5.13(g). This stable performance over a wide range of current densities highlights its strong electrochemical robustness and its promise for high-performance energy storage applications.

Figure 5.14 shows the Nyquist plots of five electrodes recorded over a frequency range of 0.1 Hz to 100 Hz with an AC perturbation of 10 mV. The impedance spectra display two characteristic regions: a high-frequency region corresponding to charge-transfer resistance and a low-frequency region associated with Warburg resistance resulting from the ion diffusion/transport in the electrolyte. Among all electrodes, the NPA-25 composite exhibits a more vertical line in the low-frequency region. This indicates near-ideal capacitive behavior and shortened ion diffusion

pathways, which facilitate efficient electrolyte ion accessibility. In the high-frequency region, the smaller semicircle diameter of NPA-25 reflects a reduced charge-transfer resistance (Rct), attributed to enhanced faradaic reactions and improved double-layer capacitance (C_{dl}) at the electrode-electrolyte interface.

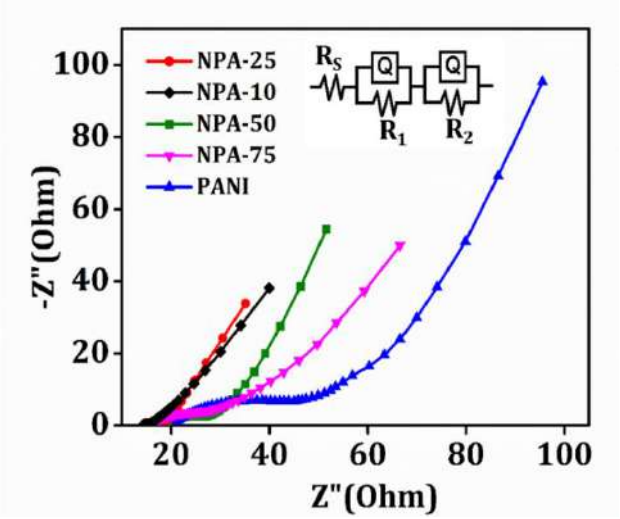

Figure 5.14 *Nyquist plot of PANI and NGQDs/PANI composites with the corresponding fitted equivalent circuit of NPA-25 shown in the inset.*

To better understand the electrochemical behavior of the as-prepared samples, the experimental EIS data were fitted using an equivalent circuit model as shown in the inset of Figure 5.14. The reliability of the fitting is evidenced by the very low chi-square value (~2.26×10^{-5}), which indicates excellent agreement between the experimental results and the proposed model. The equivalent circuit consists of Rs, R1, R2, Q1, and Q2, as explained in the previous chapter.where Rs corresponds to the solution resistance, R1 and R2 represent the charge-transfer (or polarization) resistances, and Q1 and Q2 are constant phase elements (CPEs) introduced to

account for the non-ideal capacitive behavior at the electrode-electrolyte interface [36, 37].

Figure 5.15(a) illustrates the galvanostatic charge-discharge cyclic performance of PANI and NPA composites for up to 3000 cycles at a current density of 5 A g^{-1}. As evident from the plot, the NGQDs/PANI incorporated composites exhibit superior cyclic stability compared to pristine PANI.

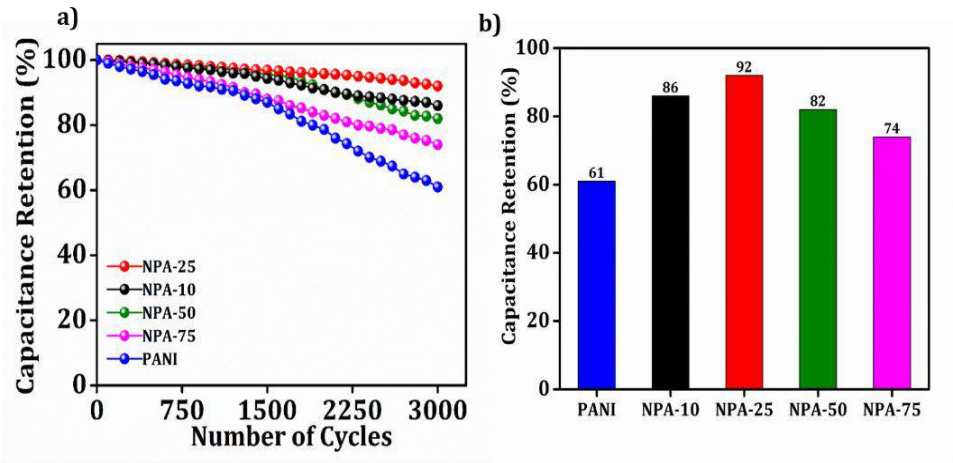

Figure 5.15 ***(a)*** *Cyclic stability performance evaluated through repeated charge-discharge measurements* ***(b)*** *effect of NGQDs loading on cyclic stability of NGQDs/PANI composites*

The NPA-25 composite have showed highest cyclic stability 92%, highlighting its exceptional durability and structural integrity under repeated cycles. This remarkable stability is primarily attributed to the synergistic π-π stacking and hydrogen bonding interactions between the conjugated backbone of PANI and surface functional groups (-OH, -NH_2) of NGQDs, as shown in Figure 5.16. These interactions help to prevent polymer chain entanglement and reduce structural damage, allowing the polymer networks to remain unchanged. In addition, NGQDs act as conductive nanospacers

that limit the aggregation of PANI chains and create continuous pathways for efficient electron and ion transport [15, 22, 38].

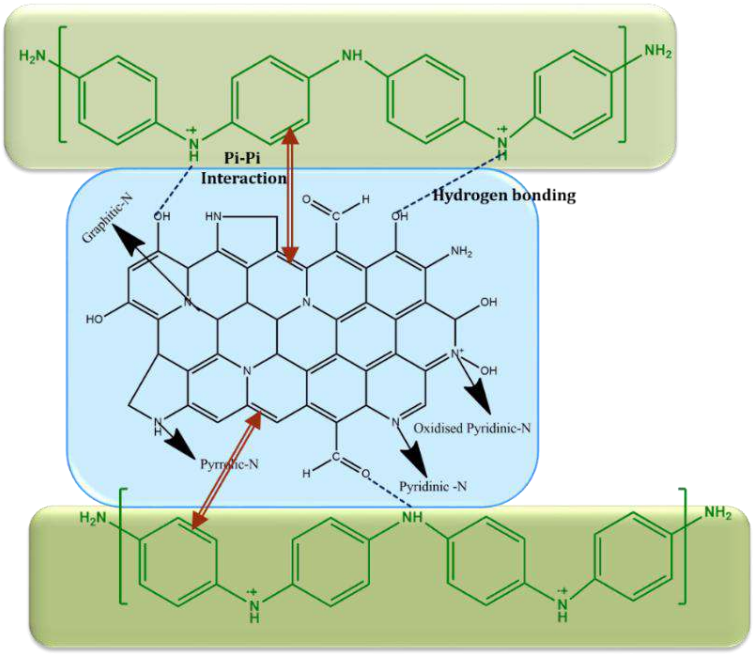

Figure 5.16 *Schematic representation of the proposed interaction between NGQDs and PANI*

5.2.10 Symmetric supercapacitor device

A symmetric solid-state supercapacitor was fabricated using NPA-25 by sandwiching two carbon cloth coated with NPA-25,each with an area of 2 cm^2 using PVA/H_2SO_4 gel as the electrolyte [39]. The assembled device was analyzed in a two-electrode configuration using CV, GCD, and EIS techniques. As shown in Figure 5.17(a), the CV curves recorded at different scan rates shows moderely good capacitive response and reversibility for the device. The GCD curves at different current densities are presented in Figure 5.17(b). The specific capacitance was calculated from the GCD curves. The device delivers a high specific capacitance of 760 Fg^{-1} at a current density of

1.5 Ag^{-1}, which is much higher than that of previously reported PANI/NGQDs based supercapacitors (Table 5.2).

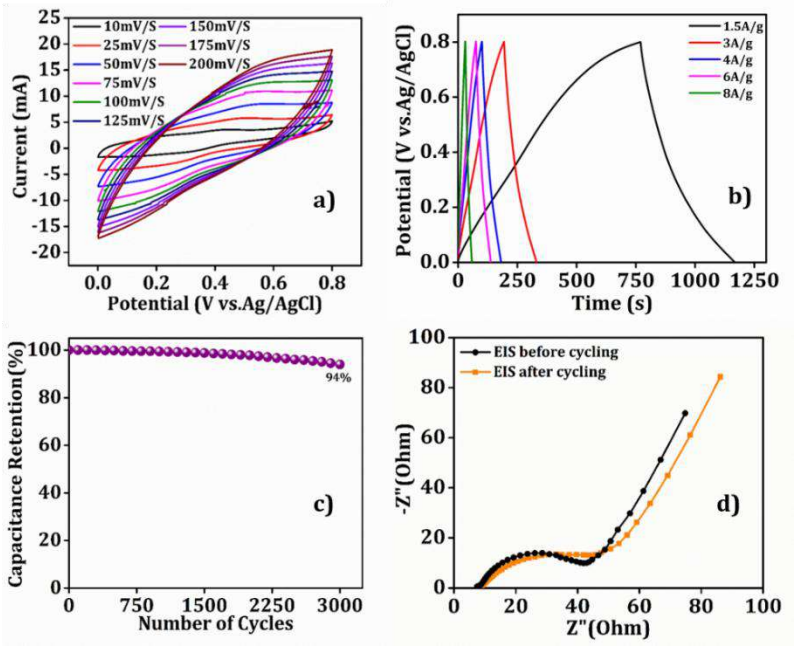

Figure 5.17 *a) CV profile of the NPA-25 symmetric supercapacitor device at different scan rates. b) GCD characteristics at various current densities c) long-term cyclic stability is measured up to 3000 cycles d) Nyquist plots before and after cycling*

The long-term cyclic stability was examined at a current density of 5 A g^{-1} for 3000 consecutive cycles. As depicted in Figure 5.17(c), the device retains 94% of its initial capacitance, demonstrating remarkable cyclic stability. To further assess the electrochemical kinetics, EIS spectra were collected before and after the stability test. The corresponding Nyquist plots, depicted in Figure 5.17(d), exhibited only minor changes, indicating negligible degradation and confirming the good structural and chemical integrity of the electrode. The Ragone plot in Figure 5.18(a) illustrates the correlation between the energy and power densities of the device using the respective

equations provided in chapter 2. The device delivers an energy density of 67.6 Wh kg^{-1} at a power density of 599.7 W kg^{-1}, indicating its ability to sustain high energy output even under elevated power demands.

Table 5.2 *A comparative analysis of related literature and the current research*

Electrode Material	Specific Capacitance ($F\ g^{-1}$)	Energy density ($Wh\ kg^{-1}$)	Power density ($W\ kg^{-1}$)	References
CNFs/PANI	201 $F\ g^{-1}$ at 0.25 $A\ g^{-1}$	4.5	103	[40]
PAni@CuO-ZnO MnO	882.7 $F\ g^{-1}$ at 1 $A\ g^{-1}$	17.4	420	[41]
Mc/PANI	107.8 $F\ g^{-1}$ at 0.5 $A\ g^{-1}$	9.59	200.1	[42]
E-RGO12/PANI	398 $F\ g^{-1}$ at 0.6 $A\ g^{-1}$	5.3	150	[43]
PANI/CNT/eMoS2	532 $F\ g^{-1}$ at 1 $A\ g^{-1}$	11.8	457	[44]
NPA-25	**947 $F\ g^{-1}$ at 1 $A\ g^{-1}$**	**67.6**	**599.7**	**This work**

To demonstrate the practical applicability of the fabricated supercapacitor, four supercapacitor cells were assembled in series achieve a total working voltage of 3V, as shown in Figure 5.18(b). The assembled device was charged for 10 s and subsequently discharged by powering a red LED. The LED remained illuminated for approximately 40s, confirming the device's capability for real-world applications. Overall, these results confirm that the fabricated device outperforms many reported PANI/GQDs supercapacitors and holds strong promise for practical applications.

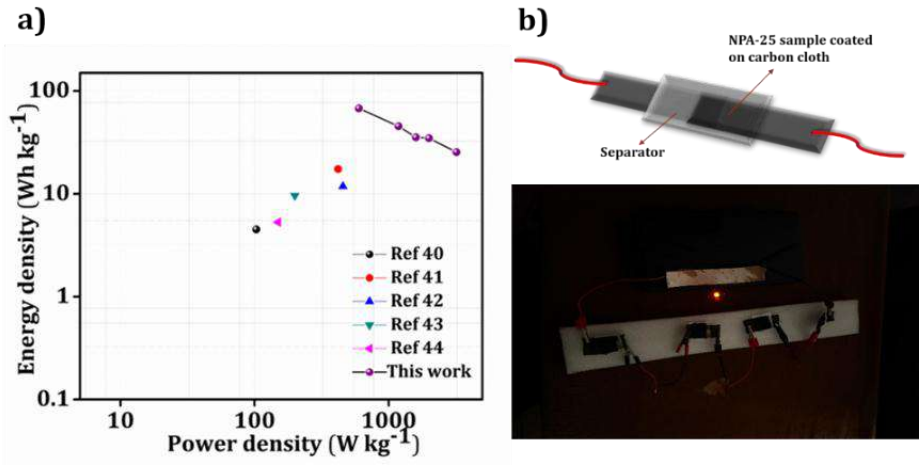

Figure 5.18 ***a)*** *Ragone plot comparing the energy and power densities of the NPA-25 device with previously reported supercapacitor systems* ***b)*** *schematic representation of symmetric supercapacitor device and photographic image of a red LED illuminated by connected to four devices in series*

5.3. Conclusions

In the present study, NGQDs and NGQDs/PANI composites were successfully synthesized via a single step hydrothermal route followed by chemical oxidative polymerization. NGQDs/PANI The integration of NGQDs into the polyaniline matrix, markedly enhanced charge transfer kinetics and increases the effective surface area of the electrode, thereby, contributing significantly to the overall capacitance. Among the investigated electrodes, the NPA-25 composite with an optimized NGQDs concentration delivered the best performance. This is due to the optimum synergistic interaction between NGQDs and the PANI framework. The NPA-25 electrode achieved a high specific capacitance of 947 Fg^{-1} at a current density of 1A g^{-1}, along with excellent cyclicstability, retaining approximately 92% of its initial capacitance after 3000 cycles. In addition, the symmetric supercapacitor device fabricated using NPA-25 electrode

exhibited a specific capacitance of 760 F g^{-1} at 1.5 A g^{-1}, with a high energy density of 67.6 Wh kg^{-1} and a power density of 599.7 W kg^{-1}. These results clearly demonstrate that the NGQDs/PANI hybrid electrode material is a highly promising candidate for advanced supercapacitor applications.

References

[1] S. Prakash, R. Rajamany, P. Anjana, R. Rakhi, Y.A. Ismail, Covalently bonded polyaniline-nitrogen doped rGO macromolecules for superior supercapacitors with enhanced energy density and long-term cyclic stability, Journal of Power Sources, 665 (2026) 239079.
[2] S. Prakash, R. Rajamany, S.M. Varghese, R. Rakhi, Y.A. Ismail, Polyaniline-Functionalized Sulfur and Nitrogen Co-Doped rGO: Toward Sustainable, Ultra-Stable Supercapacitors with Superior Energy Density and High Retention Rate, Materials Research Bulletin, (2025) 113966.
[3] N. Punnakkal, S. Naneena, S.L. CP, A. Pradeep, S.B. TG, P.V. Suneesh, Nitrogen-doped graphene quantum dot embedded polyaniline for the fabrication of high-performance flexible supercapacitor with enhanced cycling stability, Journal of Energy Storage, 100 (2024) 113527.
[4] A.H. Majeed, L.A. Mohammed, O.G. Hammoodi, S. Sehgal, M.A. Alheety, K.K. Saxena, S.A. Dadoosh, I.K. Mohammed, M.M. Jasim, N.U. Salmaan, A review on polyaniline: synthesis, properties, nanocomposites, and electrochemical applications, International Journal of Polymer Science, 2022 (2022) 9047554.
[5] M.P. Sidheekha, L. Rajan, Y.A. Ismail, Reaction driven biomimetic sensing characteristics of polyaniline/chitosan hybrid film: sensing chemical and electrical reaction conditions, Materials Chemistry and Physics, 279 (2022) 125769.
[6] M. Beygisangchin, S. Abdul Rashid, S. Shafie, A.R. Sadrolhosseini, H.N. Lim, Preparations, properties, and applications of polyaniline and polyaniline thin films—A review, Polymers, 13 (2021) 2003.
[7] Q. Wang, H. Wang, D. Liu, P. Du, P. Liu, Synthesis of flake-shaped nitrogen-doped carbon quantum dot/polyaniline (N-CQD/PANI) nanocomposites via rapid-mixing polymerization and their application as electrode materials in supercapacitors, Synthetic Metals, 231 (2017) 120-126.

[8] C. Luk, B. Chen, K. Teng, L. Tang, S.P. Lau, Optically and electrically tunable graphene quantum dot–polyaniline composite films, Journal of Materials Chemistry C, 2 (2014) 4526-4532.
[9] Y.A. Ismail, S.R. Shin, K.M. Shin, S.G. Yoon, K. Shon, S.I. Kim, S.J. Kim, Electrochemical actuation in chitosan/polyaniline microfibers for artificial muscles fabricated using an in situ polymerization, Sensors and Actuators B: Chemical, 129 (2008) 834-840.
[10] M. Beygisangchin, S.A. Rashid, S. Shafie, S.K. Kamarudin, Synthesis and characterization of polyaniline-graphene quantum dots and their potential for Pyrene detection using photoluminescence spectroscopy, Research on Chemical Intermediates, 50 (2024) 3869-3898.
[11] Y.-H. Chang, C.-C. Chang, L.-Y. Chang, P.-C. Wang, P. Kanokpaka, M.-H. Yeh, Self-powered triboelectric sensor with N-doped graphene quantum dots decorated polyaniline layer for non-invasive glucose monitoring in human sweat, Nano Energy, 112 (2023) 108505.
[12] S. Mondal, U. Rana, S. Malik, Graphene quantum dot-doped polyaniline nanofiber as high performance supercapacitor electrode materials, Chemical Communications, 51 (2015) 12365-12368.
[13] S. Bhadra, D. Khastgir, Determination of crystal structure of polyaniline and substituted polyanilines through powder X-ray diffraction analysis, Polymer Testing, 27 (2008) 851-857.
[14] E. El-Sharkaway, R.M. Kamel, I.M. El-Sherbiny, S.S. Gharib, Removal of methylene blue from aqueous solutions using polyaniline/graphene oxide or polyaniline/reduced graphene oxide composites, Environmental technology, (2020).
[15] H. Kuzhandaivel, S. Manickam, S.K. Balasingam, M.C. Franklin, H.-J. Kim, K.S. Nallathambi, Sulfur and nitrogen-doped graphene quantum dots/PANI nanocomposites for supercapacitors, New Journal of Chemistry, 45 (2021) 4101-4110.
[16] A. Ramadan, M. Anas, S. Ebrahim, M. Soliman, A. Abou-Aly, Effect of Co-doped graphene quantum dots to polyaniline ratio on performance of supercapacitor, Journal of Materials Science: Materials in Electronics, 31 (2020) 7247-7259.
[17] A. Thadathil, D. Thacharakkal, Y.A. Ismail, P. Periyat, Polyindole-derived nitrogen-doped graphene quantum dots-based electrochemical sensor for dopamine detection, Biosensors, 12 (2022) 1063.

[18] A. Ramachandran, A.N. JS, S. Karunakaran Yesodha, Polyaniline-derived nitrogen-doped graphene quantum dots for the ultratrace level electrochemical detection of trinitrophenol and the effective differentiation of nitroaromatics: structure matters, ACS Sustainable Chemistry & Engineering, 7 (2019) 6732-6743.
[19] R. Xing, X. Gong, X. Zhuang, Y. Li, C. Bulin, X. Ge, B. Zhang, Synthesis and improved electrochemical properties of nitrogen-doped graphene quantum dot–modified polyaniline, Journal of Nanoparticle Research, 24 (2022) 32.
[20] P.T. Patil, R.S. Anwane, S.B. Kondawar, Development of electrospun polyaniline/ZnO composite nanofibers for LPG sensing, Procedia Materials Science, 10 (2015) 195-204.
[21] P.-Y. Wong, S.-W. Phang, A. Baharum, Effects of synthesised polyaniline (PAni) contents on the anti-static properties of PAni-based polylactic acid (PLA) films, Rsc Advances, 10 (2020) 39693-39699.
[22] Y.-H. Chiu, M. Rinawati, L.-Y. Chang, Y.-T. Guo, K.-J. Chen, H.-C. Chiu, Z.-H. Lin, W.-H. Huang, S.-C. Haw, M.-H. Yeh, Carbon nitride quantum dots/polyaniline nanocomposites for non-invasive glucose monitoring using wearable sweat biosensor, ACS Applied Nano Materials, 8 (2025) 2340-2351.
[23] B. Chen, Q. Yang, Y. Yang, J. Chen, B. Yan, Y. Gu, R. Fu, S. Chen, PANI doped with carbon quantum dots for the asymmetric high-performance solid-state electrochromic supercapacitor, Journal of Power Sources, 633 (2025) 236407.
[24] Y.-F. Wang, D.-L. Liu, J.-J. Han, A.-R. Guo, Detection of formaldehyde by cyclic voltammetry using a PANI/GO composite film–modified electrode, Ionics, 28 (2022) 2457-2468.
[25] A.B. Siddique, K. Morrison, G. Venkat, A.K. Pramanick, N. Banerjee, M. Ray, Charge transport through functionalized graphene quantum dots embedded in a polyaniline matrix, ACS Applied Electronic Materials, 3 (2021) 1437-1446.
[26] G.G. Gebreegziabher, A.S. Asemahegne, D.W. Ayele, D. Mani, R. Narzary, P.P. Sahu, A. Kumar, Polyaniline–graphene quantum dots (PANI–GQDs) hybrid for plastic solar cell, Carbon Letters, 30 (2020) 1-11.
[27] A. Ganguly, S. Sharma, P. Papakonstantinou, J. Hamilton, Probing the thermal deoxygenation of graphene oxide using high-resolution in situ X-

ray-based spectroscopies, The Journal of Physical Chemistry C, 115 (2011) 17009-17019.
[28] Y. Guo, J. Li, F. Meng, W. Wei, Q. Yang, Y. Li, H. Wang, F. Peng, Z. Zhou, Hybridization-induced polarization of graphene sheets by intercalation-polymerized polyaniline toward high performance of microwave absorption, ACS Applied Materials & Interfaces, 11 (2019) 17100-17107.
[29] C. Ratlam, S. Phanichphant, S. Sriwichai, Development of dopamine biosensor based on polyaniline/carbon quantum dots composite, Journal of Polymer Research, 27 (2020) 183.
[30] J. Breczko, B. Grzeskiewicz, E. Gradzka, D.M. Bobrowska, A. Basa, J. Goclon, K. Winkler, Synthesis of polyaniline nanotubes decorated with graphene quantum dots: Structural & electrochemical studies, Electrochimica Acta, 388 (2021) 138614.
[31] R. Regueira, R.Y. Suckeveriene, I. Brook, G. Mechrez, R. Tchoudakov, M. Narkis, Investigation of the electro-mechanical behavior of hybrid polyaniline/graphene nanocomposites fabricated by dynamic interfacial inverse emulsion polymerization, Graphene, 4 (2015) 7-19.
[32] E. Song, J.-W. Choi, Conducting polyaniline nanowire and its applications in chemiresistive sensing, Nanomaterials, 3 (2013) 498-523.
[33] S.A. Ansari, Graphene quantum dots: novel properties and their applications for energy storage devices, Nanomaterials, 12 (2022) 3814.
[34] S. Guo, H. Shen, Z. Tie, S. Zhu, P. Shi, J. Fan, Q. Xu, Y. Min, Three-dimensional cross-linked polyaniline fiber/N-doped porous carbon with enhanced electrochemical performance for high-performance supercapacitor, Journal of Power Sources, 359 (2017) 285-294.
[35] K. Kakaei, S. Khodadoost, M. Gholipour, N. Shouraei, Core-shell polyaniline functionalized carbon quantum dots for supercapacitor, Journal of Physics and Chemistry of Solids, 148 (2021) 109753.
[36] B. Balakrishnan, S.K. Balasingam, K.S. Nallathambi, A. Ramadoss, M. Kundu, J.S. Bak, I.H. Cho, P. Kandasamy, Y. Jun, H.-J. Kim, Facile synthesis of pristine FeS2 microflowers and hybrid rGO-FeS2 microsphere electrode materials for high performance symmetric capacitors, Journal of industrial and engineering chemistry, 71 (2019) 191-200.
[37] L.-Y. Chang, M. Rinawati, Y.-T. Guo, Y.-C. Lin, C.-Y. Chang, W.-N. Su, H. Mizuguchi, W.-H. Huang, J.-L. Chen, M.-H. Yeh, Nitrogen-doped

graphene quantum dots incorporated into MOF-derived NiCo layered double hydroxides for nonenzymatic lactate detection in noninvasive biosensors, ACS Applied Nano Materials, 7 (2024) 14431-14442.
[38] S.u. Haque, A. Nasar, Inamuddin, M.M. Rahman, Applications of chitosan (CHI)-reduced graphene oxide (rGO)-polyaniline (PAni) conducting composite electrode for energy generation in glucose biofuel cell, Scientific Reports, 10 (2020) 10428.
[39] R. Rajamany, S. Prakash, Y.A. Ismail, Polyvinylpyrrolidone (PVP) assisted synthesis of Ni MOF: Enhanced supercapacitive performance through morphology control, Next Materials, 7 (2025) 100459.
[40] F. Miao, C. Shao, X. Li, N. Lu, K. Wang, X. Zhang, Y. Liu, Polyaniline-coated electrospun carbon nanofibers with high mass loading and enhanced capacitive performance as freestanding electrodes for flexible solid-state supercapacitors, Energy, 95 (2016) 233-241.
[41] N. Boutaleb, G.M. Al-Senani, S.D. Al-Qahtani, A. Benyoucef, B.D. Alkoudsi, Investigation and properties of PAni-coated CuO–ZnO–MnO quaternary hybrid as electrode material for supercapacitor application, Colloids and Surfaces A: Physicochemical and Engineering Aspects, 718 (2025) 136867.
[42] J. Noh, S. Jekal, C.M. Yoon, Polyaniline-Coated Mesoporous Carbon Nanosheets with Fast Capacitive Energy Storage in Symmetric Supercapacitors, Advanced Science, 10 (2023) 2301923.
[43] Y. Wang, Y. Wang, Y. Wang, J. Liu, Facial preparation of covalent modified reduced graphene oxide/polyaniline composite and its stable-enhanced electrochemical performance, Heliyon, 9 (2023).
[44] M. Jasna, M.M. Pillai, A. Abhilash, P. Midhun, S. Jayalekshmi, M. Jayaraj, Polyaniline wrapped carbon nanotube/exfoliated MoS2 nanosheet composite as a promising electrode for high power supercapacitors, Carbon Trends, 7 (2022) 100154.

Chapter 6

NGQDs integrated Polypyrrole and Polyaniline as Sensors of Electrical Energetic Condition

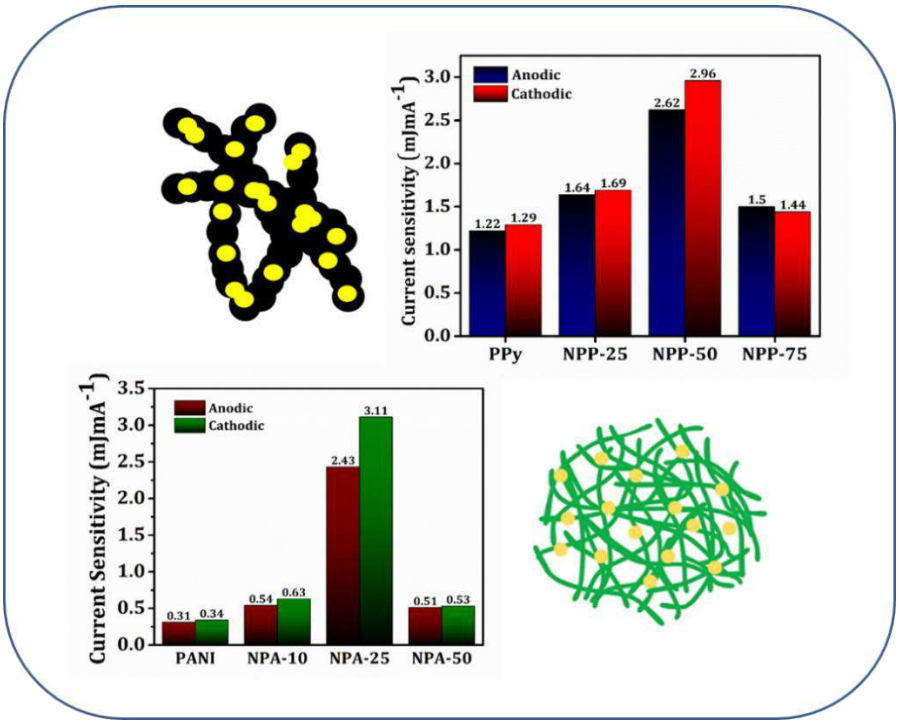

This chapter presents a detailed investigation of the reaction-driven sensing behavior of NGQDs/PPy and NGQDs/PANI composites towards working electrical energetic conditions using chronopotentiometry. The electrical energy consumed during the redox processes of NGQDs/PPy and NGQDs/PANI is employed as the sensing parameter. The results illustrate how the amount of NGQDs in the composites influences their sensing characteristics. Overall, the findings demonstrate the strong potential of these materials to function as an efficient current sensor.

6.1. Introduction

In the preceding two chapters, the supercapacitive performance of NGQDs/PPy and NGQDs/PANI composites was discussed in detail. In this chapter, we focus on exploring their reactive sensing ability towards their working electrical energetic condition, i.e., their ability to function as a current sensor. In conventional electrochemical sensors, the target analytes are either present in the electrolyte or adsorbed onto the electrode surface, where the electrode materials primarily function as electrode supports or electrocatalysts for sensing applications.

The biomimetic and reactive sensing nature of conducting polymer was introduced by Otero and co-workers, based on the concept of composition-dependent characteristics of conducting polymers [1, 2]. CPs can be regarded as multistep electrochemical molecular motors or machines. During electrochemical reactions, ions and solvent molecules are reversibly exchanged with the electrolyte to maintain charge neutrality and osmotic pressure balance. This exchange induces reversible swelling and shrinking of the polymer matrix, corresponding to expansion and contraction of the polymer chains. Under electrochemical reaction control, CPs can undergo redox process through *n* successive steps or pass through *n* discrete conformational energetic states progressively and reversibly, thereby functioning as multistep macromolecular motors [3-5].

Since electron extraction during oxidation occurs through multiple consecutive steps, infinitesimally small changes in polymer composition can be achieved by applying minute anodic or cathodic potential variations. As a result, all properties coupled to the volume changes (composition variation) of CPs during electrochemical reactions, such as temperature, applied current, mechanical force or pressure, and chemical environment in the surrounding

electrolyte, also undergo corresponding changes. These variations directly influence the electronic energy levels and potential evolution within the polymer. Consequently, CPs and CP-based devices designed on this principle are expected to operate as highly sensitive sensors that respond to changes in their surrounding environment [6].

A theoretical framework and experimental evidence describing the reactive sensing nature of CPs with respect to their working variables and the variation in consumed electrical energy have also been proposed by our research group [7-9]. Since electrochemical reactions in CPs occur outside the equilibrium conditions, any perturbation in the working variables that affects the reaction rate leads to a shift in the consumed electrical energy, which can be readily sensed by the polymer without the need for additional connectivities. In this context, the principle suggested by Otero that any physical or chemical variable (such as current, active site concentration, electrolyte concentration, mechanical stress, or temperature) disturbing the electrochemical reaction rate must modify the reaction overpotential to self-adapt to the newly imposed energetic requirements has been validated for a wide range of conducting polymers [10]. Although this reactive sensing behavior of CPs has been explored previously, the ability of NGQDs-based composites of polypyrrole has not yet been investigated. Only a few recent studies, notably by Ismail *et al.*, have reported on the reactive sensing behavior of polyaniline and its composites [11]. The objective of this work is to demonstrate the reactive sensing capability of NGQDs/PPy and NGQDs/PANI towards electrical energetic condition ie., to prove their applicability as a current sensor. Specifically, the current sensing properties of these composites are investigated and reported here for the first time. This study is significant for the development of CP-based soft, wet, and reactive sensing devices.

6.2. Results and Discussion

The detailed electrochemical characterization of both NGQDs/PPy and NGQDs/PANI composites has been discussed in the respective chapters 4 and 5. The results of coulovoltammometry (QV) and chronopotentiometry analysis are discussed in this chapter.

6.2.1. Coulovoltammogram of NGQDs/PPy composites

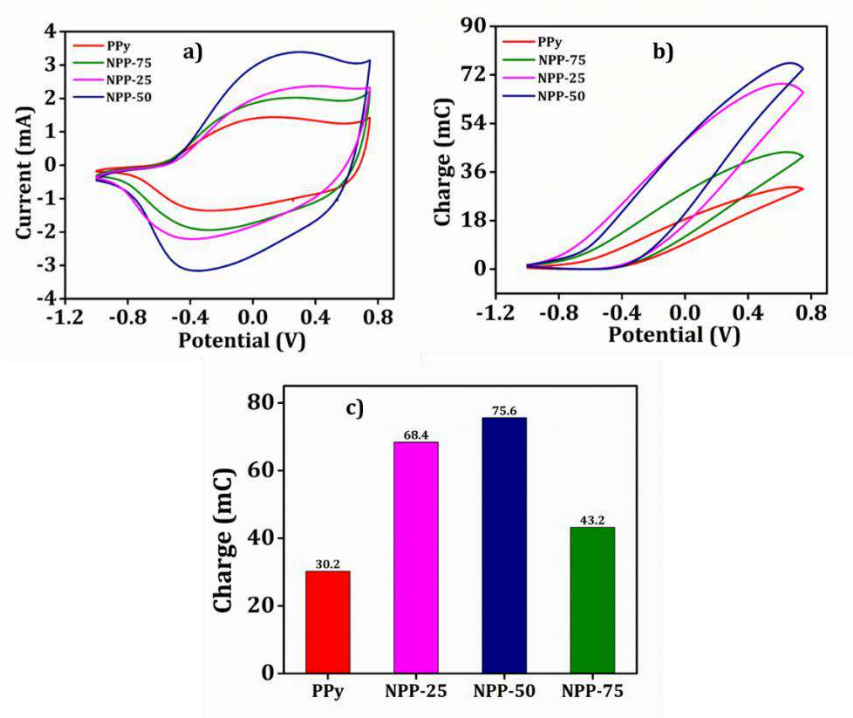

Figure 6.1 ***a)*** *CV profiles of PPy and NGQDs/PPy composite* ***b)*** *QVs of PPy and NGQDs/PPy composites obtained by integrating corresponding CVs* ***c)*** *redox charges of PPy and NGQDs/PPy composites obtained from QVs.*

Coulovoltammogram (QV) is a plot of consumed charge versus potential obtained by integrating the CV. The minimum of QV is considered as the zero-charge reference, and the difference between the maximum and minimum points in the closed QV loop defines the charge consumed during

the reversible oxidation-reduction reaction.The CV profiles of the PPy and NGQDs/PPy composites recorded in 1M NaCl at a scan rate of 25mV s^{-1} are shown in Figure 6.1(a). Figure 6.1(b) depicts the QV curves obtained by integrating corresponding CVs. The redox charges associated with the reversible processes of PPy, NPP-25, NPP-50, and NPP-75 composites are calculated to be 30.2 mC, 68.4 mC, 75.6 mC, and 43.2 mC, respectively, as shown in Figure 6.1(c).

Among these composites, NPP-50 exhibits the highest redox charge. For the NPP-50 composite, the optimal NGQD concentration, as explained in Chapter 4, provides a greater number of accessible active sites. This facilitates enhanced ion exchange during the redox process, leading to a higher consumption of oxidation-reduction charge.

6.2.2. Sensing working electrical energetic condition: Current Sensor

The reactive sensing behavior of the materials towards their electrical working conditions was investigated using chronopotentiometry. In this approach, a constant current, anodic and/or cathodic, was applied to the material, thereby regulating the reaction rate, inducing a systematic change in the polymer composition, and monitoring the evolution of the electrode potential. The sensing response was evaluated by recording the corresponding chronopotentiograms. Variations in physical or chemical parameters that influence the electrode reaction kinetics were reflected in the potential evolution of the PPy chains in the composite. To assess the material's ability to sense electrical stimuli, the PPy and NGQDs/PPy composite electrode was subjected to square-wave constant current signals. Before recording the CP, the electrode was electrochemically stabilized by recording 20 consecutive CVs. The application of successive square current magnitude yielded well-defined CP responses under constant charge

conditions. The potential evolution during the electrochemical reaction changes systematically with a change in the applied current.

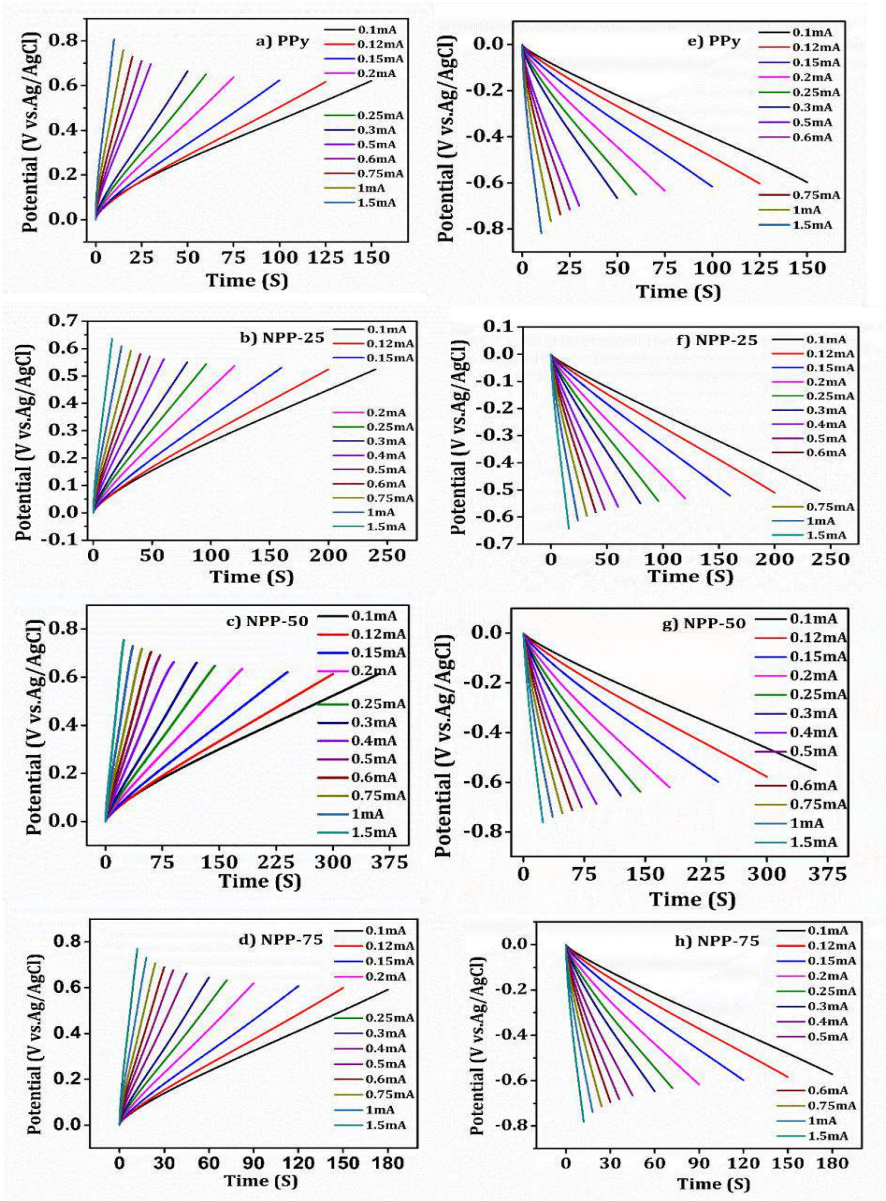

Figure 6.2 *Chronopotentiograms of PPy and NGQDs/PPy composites obtained by applying various constant anodic* ***(a-d)*** *and cathodic* ***(e-h)*** *currents at a constant electrical charge in 1 M NaCl aqueous solution.*

The current sensing characteristics of the material were investigated in a 1 M NaCl aqueous electrolyte. Square current pulses with amplitudes between ±0.1 mA and ±1.5 mA were applied sequentially. The pulse duration was varied to maintain a constant oxidation and reduction charge (Q = i·t), so that the same oxidation state or reaction extension was achieved in each measurement. The chronopotentiometric studies of the PPy and NGQDs/PPy composites were performed at a constant charge approximately equal to half of their redox charge obtained from the QVs (Figure 6.1b). The normalized anodic and cathodic chronopotentiometric responses of PPy and NGQDs/PPy composites are shown in Figure 6.2 (a-d) and Figure 6.2 (e-h), respectively. An increase in the applied current results in a shift of the potential toward more positive values during oxidation and more negative values during reduction [12]. The electrical energy consumed during the reaction was obtained using the following equation by integrating the corresponding chronopotentiograms.

$$U = I \int E dt \qquad (6.1)$$

Figure 6.3(a) shows that the consumed electrical energy during the redox reaction has a linear dependence on the applied electric current for all the samples. Therefore, the reaction energy senses or responds to locally imposed electrical energetic conditions. The slope of the curve in Figure 6.3(a) denotes the sensitivity of the material. Therefore, the material can act as a sensor of the applied electrical current. The current sensitivities corresponding to the anodic and cathodic processes of PPy and NGQDs/PPy composites are depicted in Figure 6.3(b).

The highest sensitivity is obtained for the NPP-50 composite. The values are found to be 2.62 mJ mA^{-1} and -2.96 mJ mA^{-1} for the anodic and cathodic processes, respectively. The highest sensitivity of NPP-50 was attributed to

the optimal concentration of NGQDs that provides a larger number of active sites. The EIS analysis further supports this observation. Among all the composites, NPP-50 shows the lowest solution resistance and Warburg resistance, enabling more efficient diffusion of anions and solvent molecules. This improved ion transport facilitates faster intercalation and de-intercalation processes, ultimately enhancing the sensing response. Therefore, the superior current sensitivity of the NPP-50 composite can be convincingly explained by its high electrical conductivity along with its minimal solution and diffusion resistances.

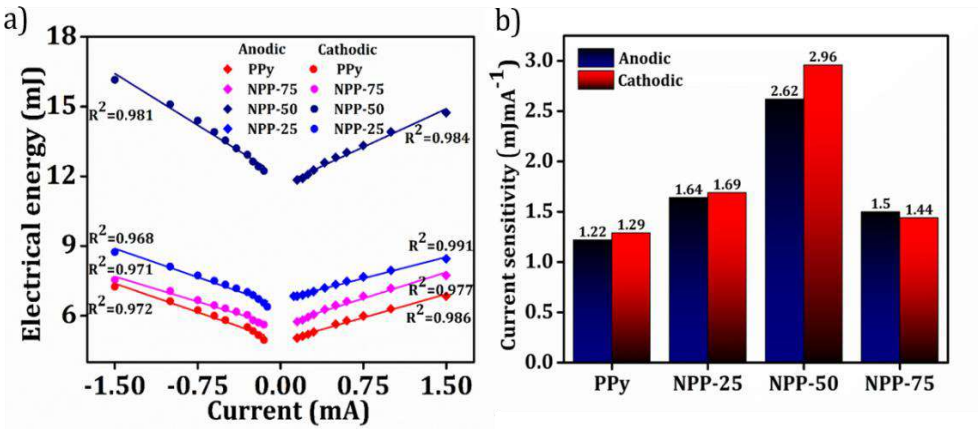

Figure 6.3 ***a)*** *Variation of electrical energy consumed by the PPy and NGQDs/PPy composites with the applied current* ***b)*** *Effect of NGQDs loading on the current sensitivity of NGQDs/PPy composites*

. 6.2.3. Theoretical description

The PPy and PANI are the active materials responsible for sensing characteristics of the NGQDs/PPy and NGQDs/PANI composites. The theoretical description of both PPy and PANI is presented in the following equations.

The electrochemical reaction of PPy is expressed as

$$(PPy^*)_s + n(X^-)_{sol} + m(H_2O) \rightleftharpoons [PPy^{n+}(X^-)_n(H_2O)_m]_{gel} + ne^- \quad (6.2)$$

In the case of PANI,

$$(PANIH_{X^*})_s + n(A^-)_{aq} + m(H_2O) \rightleftharpoons [(PANI)^{n+}(A^-)_n(H_2O)_m]_{gel} + xH^+ + (n+x)e^- \quad (6.3)$$

Under equilibrium conditions, the potential of the PPy and PANI electrode is represented by the Nernst equation, as given below [13],

$$E = E_0 - \frac{RT}{nF}\ln\frac{[X^-][PPy^*]}{[(PPy)^{n+}(X^-)_n(H_2O)_m]} \quad (6.4)$$

$$E = E_0 - \frac{RT}{nF}\ln\frac{[X^-][PANIH_{X^*}]}{[(PANI)^{n+}(X^-)_n(H_2O)_m]} \quad (6.5)$$

Here, E denotes the evolved potential, E⁰ is the standard electrode potential, R represents the universal gas constant, and F is the Faraday constant. The anion concentration is expressed as $[X^-]$, while $[PPy^*]$ *and* $[PANIH_x^*]$ corresponds to the concentration of active polymer centres. The concentration of oxidised PPy polymer centres is given by $[(PPy)^{n+}(X^-)_n(H_2O)_m]$, and that of PANI is given as$[(PANI)^{n+}(X^-)_n(H_2O)_m]$.

Unlike equilibrium systems, the electrochemical redox reactions of both PPy and PANI working outside the equilibrium conditions. Otero et al. proposed an alternative interpretation of the Le-Châtelier principle for such systems, suggesting that changes in reaction rate result in a redistribution of reaction energy to meet new energetic requirements. As a result, variations in the reaction's working energetic conditions are reflected in the material's electrode potential.

The reaction rate of PPy can be expressed as [10, 14]

$$r = k[PPy^*]^a[X^-]^b \quad (6.5)$$

In the case of PANI,

$$r = k[PANIH_x^*]^a[A^-]^b[H^+]^{-C}$$

(6.6)

In this expression, r represents the specific reaction rate, while k denotes the kinetic coefficient. The parameters a and b correspond to the reaction orders associated with the active polymer centres and the anion (electrolyte) concentration, respectively. When a steady current is applied to the PPy and PANI electrode, a direct relationship between the applied current and the reaction rate can be established.

$$r = \frac{q}{FV} = \frac{it}{FV} \leftrightarrow i = \frac{rFV}{t}$$

(6.7)

The parameters q (charge), i (current), t (duration of current flow), F (Faraday's constant), and V (volume of the PPy or PANI polymer) are interrelated. To correlate the rate constant with the evolution of electrode potential, the Butler-Volmer equation, central to electrochemical kinetics, is used to describe both anodic and cathodic processes [15].

$$i_a = FVk_\alpha[PPy^*]^a[X^-]^b \quad (6.8)$$

$$i_a = FVk_{\alpha 0}[PPy^*]^a[X^-]^b \exp\left(\frac{(1-a)nF(E-E_0)}{RT}\right) \quad (6.9)$$

In the case of PANI,

$$i_a = FVk_\alpha[PANIH_x{}^*]^a[X^-]^b[H^+]^{-C}$$

(6.10)

$$i_a = FVk_{\alpha 0}[PANIH_x{}^*]^a[X^-]^b\,[H^+]^{-C}\exp\left(\frac{(1-a)nF(E-E_0)}{RT}\right) \quad (6.11)$$

In this part, the potential developed during the reaction depends on several factors, such as the electrolyte concentration, applied current, and temperature. An equation can therefore be derived to describe the relationship between these parameters and the resulting electrode potential.

$$E_a = E_0 + \frac{RT}{(1-a)nF}\left(In\left(\frac{i_a}{FV}\right) - bln[X^-] - \alpha \ln[PPy^*] - Ink_{\alpha 0}\right) \quad (6.12)$$

For PANI,

$$E_a = E_0 + \frac{RT}{(1-a)nF}\left(In\left(\frac{i_a}{FV}\right) - bln[A^-] - \alpha \ln[PANIH_x{}^*] - cpH - Ink_{\alpha 0}\right) \quad (6.13)$$

Equations 6.9 and 6.12 explain the sensor-like behavior of PPy, and same as Equations 6.11 and 6.13 explain the sensor like behavior of PANI during the anodic process. A similar expression can be derived for the cathodic process. During oxidation, the material proceeds through n successive steps, which enables the formulation of a generalized equation describing the overall process [16].

$$E_n(t) = E_0 + i_aZ + (n-1)\Delta E + \frac{RT}{(1-a)F}\{\ln\left(\frac{i_a}{FV}\right) - bln[X^-] - aln\left(\left[PPy^*\right]_{initial} - \frac{i_at}{FV}\right) - lnk_{\alpha 0}\} \quad (6.14)$$

For PANI,

$$E_n(t) = E_0 + i_aZ + (n-1)\Delta E + \frac{RT}{(1-a)F}\{\ln\left(\frac{i_a}{FV}\right) - bln[A^-] - aln\left(\left[PANIH_x{}^*\right]_{initial} - \frac{i_at}{FV}\right) - cpH - lnk_{\alpha 0}\} \quad (6.15)$$

Equations 6.9, 6.12 and 6.14 for PPy and the same as Equations 6.11, 6.13 and 6.15 establish the relationship between the electrical energy consumed during the material's reaction and key experimental parameters, such as the

applied current, electrolyte concentration, and temperature. These findings confirm the material's reactive sensing behavior under working conditions. This general equation demonstrates the strong potential of PPy and PANI as an electrochemical sensor, capable of detecting changes in electrical, chemical, and thermal environments.

6.2.4. Coulovoltammogram of NGQDs/PANI Composites

The CV curves of PANI and NGQDs/PANI composites recorded at a scan rate of 25 mV s^{-1} in 1 M H_2SO_4 at room temperature are shown in Figure 6.4(a). The detailed description of these CV curves is explained in Chapter 5. The corresponding QV curves are presented in 6.4(b).

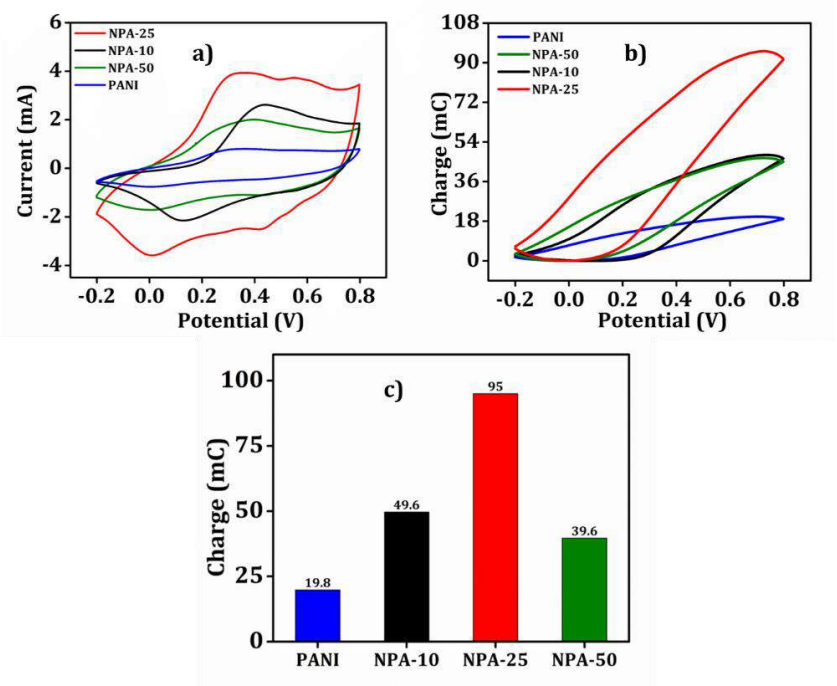

Figure 6.4 ***a)*** *CV profiles of PANI and NGQDs/PANI composites* ***b)*** *QVs of NGQDs/PANI composites obtained by integration of CVs* ***c)*** *Redox charges obtained from QVs.*

The reversible redox charges were found to be 19.8 mC for PANI and 49.6 mC, 95 mC, and 39.6 mC for the NPA-10, NPA-25, and NPA-50 composites, respectively, as shown in Figure 6.4(c). Among the composites, NPA-25 consumed more redox charge due to the optimal incorporation of NGQDs into the PANI. As discussed in Chapter 5, NPA-25 has a larger number of electrochemically active sites, which facilitate greater ion exchange during the redox process and consequently, higher charge consumption. The slope observed in the QV profiles indicates faster oxidation-reduction kinetics, with the highest reaction rate observed for the NPA-25 composite.

6.2.5. Sensing working electrical energetic condition: Current Sensor

The reaction-driven sensing characteristics of PANI and NGQDs/PANI composites towards electrical working conditions were investigated. It is found that demonstrating that the electrical energy consumed during the reaction can serve as the sensing parameter.

Normalized chronopotentiometric responses were recorded by applying square current pulses of varying magnitude (±0.1 mA to ±1.5 mA) in an aqueous 1 M H_2SO_4 electrolyte, while maintaining all other experimental parameters constant. The anodic and cathodic responses of all studied materials are presented in Figures 6.5(a-d) and 6.5(e-h), respectively. The chronopotentiometric studies of the PANI and NGQDs/PANI composites were performed at a constant charge approximately equal to half of their redox charge obtained from the QVs. Following the initial potential step, an increase in the applied anodic or cathodic current results in a shift in the potential evolution toward more anodic or more cathodic values. As shown in Figure 6.6(a), the electrical energy consumed during the redox reactions of PANI and NGQDs/PANI composites exhibits a linear dependence on the applied current. This linear relationship confirms that the consumed

electrical energy can sense the imposed electrical energetic conditions, particularly the driving current, as shown in 6.6 (a).

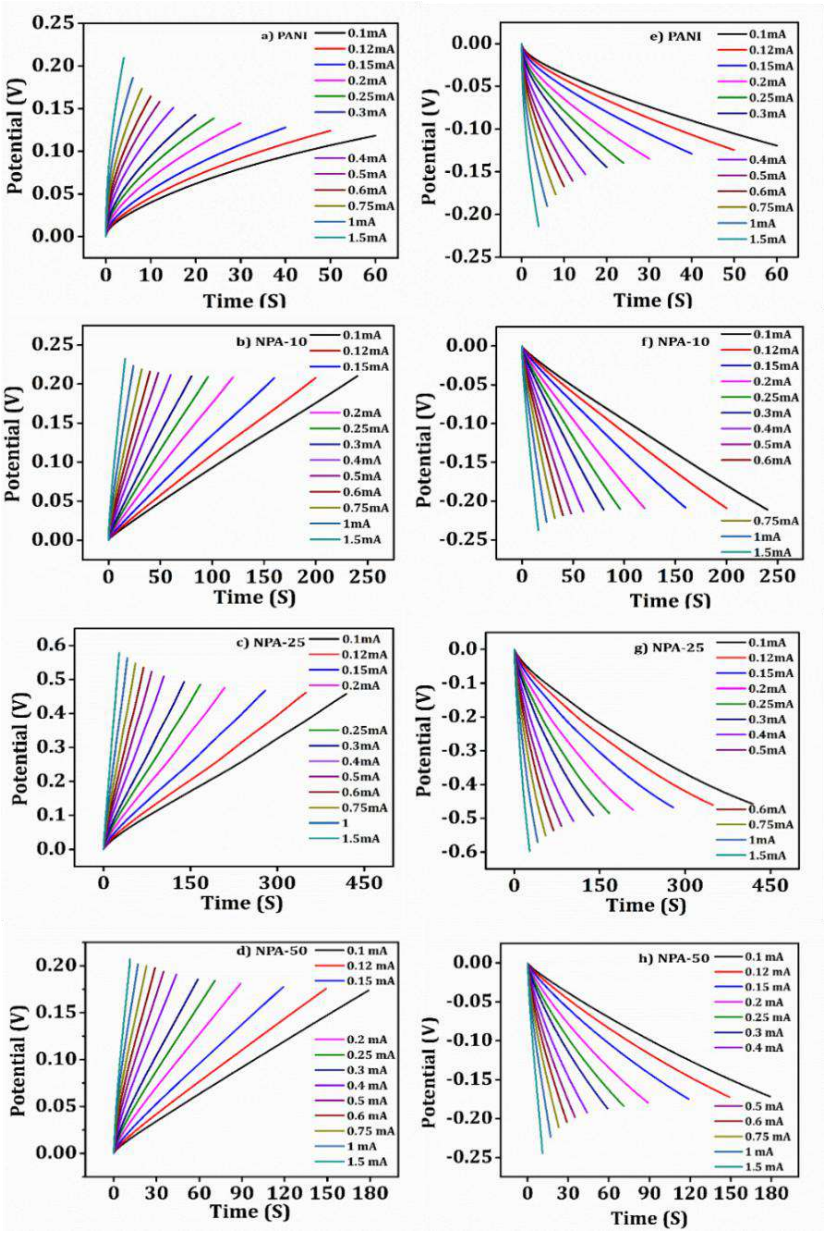

Figure 6.5 *Anodic **(a-d)** and cathodic **(e-h)** chronopotentiograms were obtained when different currents were applied to NGQDs/PANI composites by passing a constant electrical charge in 1M H_2SO_4*

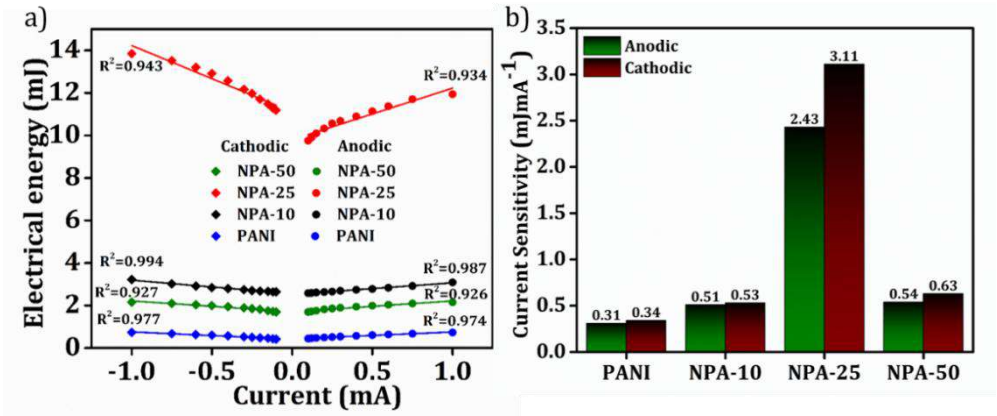

Figure 6.6 ***a)*** *Electrical energy consumed for PANI and NGQDs/PANI composites at different applied current* ***b)*** *dependence of current sensitivity on NGQDs loading in NGQDs/PANI composites*

This confirms that material serves as current sensor. Among the investigated composites, NPA-25 shows the highest sensitivity, with values of 2.43 mJ mA^{-1} and −3.11 mJ mA^{-1} for the anodic and cathodic processes, respectively. The sensitivity curve is presented in 6.6(b). The NPA-25 composite exhibits higher sensitivity, which can be attributed to the optimal NGQD concentration that provides a larger number of electroactive sites. As discussed earlier in Chapter 5, the EIS spectra further corroborate this behavior.

Among all the composites, NPA-25 shows the lowest solution resistance and Warburg resistance, enabling more efficient diffusion of anions and solvent molecules. This enhanced ion transport facilitates faster intercalation and deintercalation processes, thereby improving the overall sensitivity of the material. Consequently, the superior current sensitivity of the NPA-25 composite can be justified by its high electrical conductivity combined with minimal solution and Warburg resistances.

6.3. Conclusion

The reactive sensing characteristics of the NGQDs/PPy and NGQDs/PANI composites towards their electrical working conditions were systematically investigated. The sensing performance was explored using chronopotentiometry. The electrical energy consumed during the electrochemical reaction was proven to be the sensing parameter. The consumed electrical energy during the reaction increases as the applied current increases. Thus, shows a linear dependence on the applied current.

The study clearly demonstrates that the presence of NGQDs plays a crucial role in governing the sensing behavior of both PPy and PANI composites. An optimum amount of NGQDs helps stabilize the polymer chains through strong chemical interactions, which improves the interfacial integrity and electronic coupling between NGQDs and PPy or PANI. As a result, both electrochemical stability and charge transport are enhanced, leading to improved sensing performance. Hence, both NGQDs/PPy and NGQDs/PANI composites open new avenues for sensing motor innovations.

References

[1] T.F. Otero, M.J. Ariza, Revisiting the electrochemical and polymeric behavior of a polypyrrole free-standing electrode in aqueous solution, The Journal of Physical Chemistry B, 107 (2003) 13954-13961.
[2] T.F. Otero, M.J. Ariza, S. Costa, M. Marquez, Revisiting the electrochemical properties of conducting polymers, in: Smart Structures and Materials 2004: Electroactive Polymer Actuators and Devices (EAPAD), SPIE, 2004, pp. 221-229.
[3] T.F. Otero, Soft, wet, and reactive polymers. Sensing artificial muscles and conformational energy, Journal of Materials Chemistry, 19 (2009) 681-689.

[4] T.F. Otero, J.G. Martinez, Physical and chemical awareness from sensing polymeric artificial muscles. Experiments and modeling, Progress in Polymer Science, 44 (2015) 62-78.
[5] T.F. Otero, J.G. Martinez, Structural and biomimetic chemical kinetics: kinetic magnitudes include structural information, Advanced Functional Materials, 23 (2013) 404-416.
[6] A. Shabeeba, M.P. Sidheekha, L. Rajan, Y.A. Ismail, Flexible hybrid film of polypyrrole incorporated chitosan as a biomimetic multistep electrochemical sensor of working temperature: a potentiodynamic study, RSC advances, 12 (2022) 31911-31922.
[7] L. Rajan, M.P. Sidheekha, A. Shabeeba, T.F. Otero, Y.A. Ismail, Structural electrochemistry of poly (3, 4-ethylenedioxythiophene) and its applicability as simultaneous sensor of environmental surroundings: self-sensing electrical, thermal, and chemical working conditions, Journal of Materials Chemistry A, 12 (2024) 4583-4600.
[8] L. Rajan, M.P. Sidheekha, A. Shabeeba, Y.A. Ismail, Conducting polymers as bio-mimetic multistep macromolecular sensors of working conditions: polyindole/polyvinyl alcohol hybrid film senses electrical and chemical working ambient, Materials Chemistry Frontiers, 6 (2022) 1706-1718.
[9] A. Shabeeba, Y.A. Ismail, Chitosan/polypyrrole hybrid film as multistep electrochemical sensor: sensing electrical, thermal and chemical working ambient, Materials Research Bulletin, 152 (2022) 111817.
[10] T.F. Otero, J.J. Sanchez, J.G. Martinez, Biomimetic dual sensing-actuators based on conducting polymers. Galvanostatic theoretical model for actuators sensing temperature, The Journal of Physical Chemistry B, 116 (2012) 5279-5290.
[11] A. Ajayan, L. Rajan, S. Prakash, Y.A. Ismail, Macromolecular sensing motors from conducting polymers: Polyaniline/methylcellulose composites as stable current sensing supercapacitors, International Journal of Biological Macromolecules, 279 (2024) 135312.
[12] Y.A. Ismail, J.G. Martínez, T.F. Otero, Fibroin/Polyaniline microfibrous mat. Preparation and electrochemical characterization as reactive sensor, Electrochimica Acta, 123 (2014) 501-510.

[13] Y.A. Ismail, J.G. Martinez, T.F. Otero, Polyurethane microfibrous mat templated polypyrrole: Preparation and biomimetic reactive sensing capabilities, Journal of Electroanalytical Chemistry, 719 (2014) 47-53.
[14] K.J. Vetter, Electrochemical kinetics: theoretical aspects, Elsevier, 2013.
[15] J.G. Martinez, T.F. Otero, Biomimetic dual sensing-actuators: theoretical description. Sensing electrolyte concentration and driving current, The Journal of Physical Chemistry B, 116 (2012) 9223-9230.
[16] T.F. Otero, J.G. Martinez, L. Valero, K. Asaka, Y.A. Ismail, One actuator and several sensors in one device with only two connecting wires: mimicking muscle/brain feedback, Advances in Science and Technology, 79 (2013) 16-25.

Chapter 7

Conclusions and Future Outlook

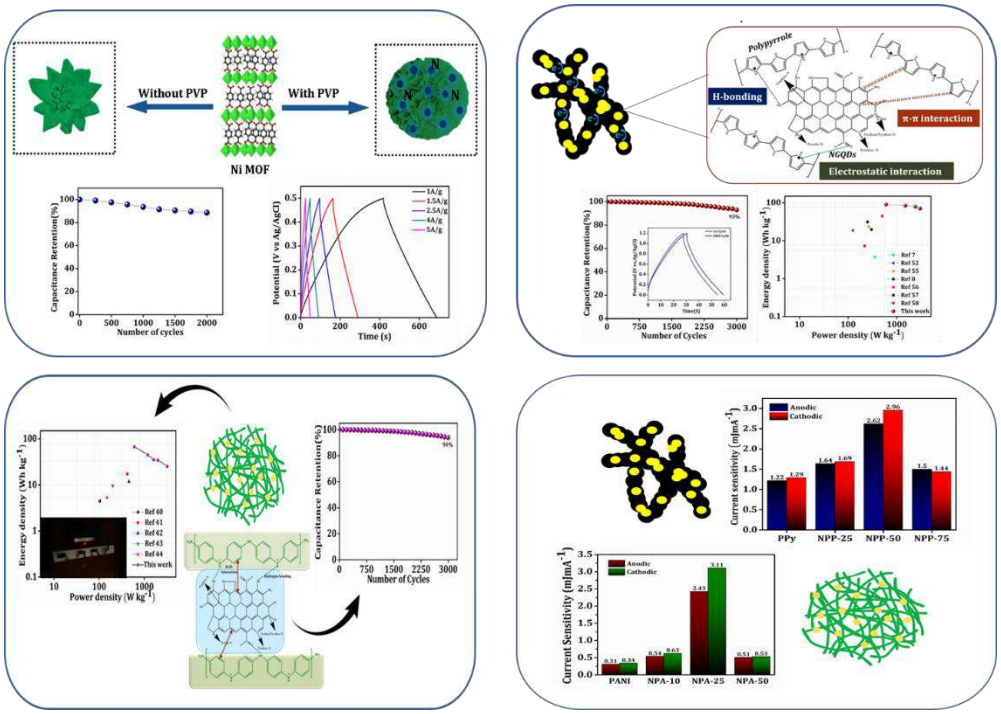

The entire thesis summarized in this chapter. The major highlights of the research work and the future scope of the materials studies are also presented here.

7.1. Conclusions

The growing demand for clean, efficient, and sustainable energy resources has intensified interest in advanced energy storage technologies. Among these, supercapacitors have attracted considerable attention for use in portable electronics, electric vehicles, and large-scale industrial applications. Supercapacitors stand out because of their ability to deliver high power, rapid charge and discharge, and maintain good performance over long operational lifetimes. The effectiveness of these devices largely depends on key factors such as the choice of electrode materials, the nature of the electrolyte, and the available surface area of the electrodes.

The first part of the thesis explores MOF-based material as an electrode material for supercapacitors. MOFs are a combination of metal ions or clusters and organic linkers. Owing to its remarkable surface area, tunable pore size and pore volume, it stands out as a promising candidate in supercapacitor applications. Ni MOFs are regarded as a highly favourable candidate, due to their well-ordered porous architecture, flexible oxidation state (Ni^{2+}, Ni^{3+}), tunable frameworks, and high theoretical capacitance. One of the major drawbacks of MOFs is their low electrical conductivity, which limits their active usage as a supercapacitor. In this work, nitrogen-enriched Ni MOF was prepared via the solvothermal technique using PVP. Here, PVP acted as a nitrogen source as well as a morphology controlling agent. The introduction of PVP altered the flower-like structure of Ni MOF into hierarchical microspheres, resulting in an expanded surface area. Compared with Ni MOF, N-Ni MOF exhibited a high specific capacitance of 1519 F g^{-1} at a current density of 1A g^{-1}. A symmetric supercapacitor was fabricated using N-Ni MOF delivered high specific capacitance of 529 F g^{-1} and a high energy density of 66.12Wh kg^{-1} at a power density of 900.3 W kg^{-1}.

The second part of the thesis explores the supercapacitor application along with the reactive sensing capabilities of conducting polymers and graphene quantum dot-based materials. Among the conducting polymers, PPy and PANI have been widely used as electrode materials for supercapacitor applications, due to their ease of synthesis, environmental stability, excellent biocompatibility, tunable electrical conductivity, and strong redox behavior. However, both PPy and PANI suffer from certain drawbacks. During repeated charge-discharge cycling, PPy undergoes mechanical stress and volumetric changes, leading to cracking, loss of conductivity, and degradation of its electrochemical properties. In this thesis, we explored the enhancement of the supercapacitive performance of PPy and PANI by preparing composites with NGQDs. Here, a novel single-step hydrothermal method was used for preparing NGQDs using PPy as a precursor. PPy itself is used as a carbon as well as a nitrogen source. First, NGQDs/PPy composites of varying compositions of NGQDs were prepared by using the chemical oxidative polymerization technique. The formation of NGQDs and NGQDs/PPy composites was confirmed through structural and morphological characterizations. The CV and GCD tests were conducted to evaluate the supercapacitive performance. Among the composites, NPP-50 exhibited a higher specific capacitance of 664 F g^{-1} at 0.8 A g^{-1} and improved cyclic stability of 91% after 3000 cycles. Finally, a symmetric supercapacitor was fabricated using NPP-50 composite and showed a high energy density of 90.2 Wh kg^{-1}, at a power density of 600.4 W kg^{-1}.

Next, we investigated the enhancement of the supercapacitive performance of PANI through compositing with NGQDs. Here also, the NGQDs/PANI composites of varying composition were prepared using the chemical oxidative polymerization technique. Among the composites, NPA-25 exhibited a higher specific capacitance of 924 Fg^{-1} and cyclic stability than

the other composites and PANI. A symmetric supercapacitor was fabricated using NPP-25 composite exhibited specific capacitance of 760 F g^{-1} at 1.5 A g^{-1}, with a high energy density of 67.6 Wh kg^{-1} and a power density of 599.7 W kg^{-1}.

The reactive sensing characteristics of the NGQDs/PPy and NGQDs/PANI composites towards their electrical working conditions were studied using CP. It was proven that the consumed electrical energy during the electrochemical reaction is a sensing parameter. The consumed electrical energy during the redox reaction has a good linear dependence on the applied current. Notably, the sensing and charge storage properties were derived from a single faradaic electrochemical reaction of the NGQDs/PPy and NGQDs/PANI composites. This finding suggests that the construction of self-sensing super capacitors is possible in future using both NGQDS/PPy and NGQDs/PANI composites as active electrode materials.

7.2. Future outlook

We have successfully developed a symmetric supercapacitor device based on NGQDs/PPy and NGQDs/PANI composites. This achievement opens up numerous possibilities for exploring their application in advanced level, such as flexible and wearable supercapacitors, solid state microsupercapacitors etc. In this work, we demonstrated that these composites also have current sensing property. They have the ability to sense their surrounding environment while working. As a result devices exploiting the electrochemical reactions of PPy and PANI composites can function as a sensors, biosensors, smart windows, sensing membranes. This discovery holds a promise for the evolution of biomimetic sensing motors. By utilizing the inherent self-sensing capabilities of PPy and PANI-based materials, it is possible to mimic the functions of biological organs, where both working

signals and feedback are transmitted through the same two connecting wires. This advancement enables the development of advanced biomimetic systems with integrated self-sensing ability, leading to enhanced performance and efficiency.

LIST OF PUBLICATIONS

International Journals

	Rajamany, R., Prakash, S., & Ismail, Y. A. (2025). Polyvinylpyrrolidone (PVP) assisted synthesis of Ni MOF: Enhanced supercapacitive performance through morphology control. Next Materials, 7, 100459. https://doi.org/10.1016/j.nxmate.2024.100459
	Prakash, S., **Rajamany, R.**, Anjana, P. M., Rakhi, R. B., & Ismail, Y. A. (2026). Covalently bonded polyaniline-nitrogen doped rGO macromolecules for superior supercapacitors with enhanced energy density and long-term cyclic stability. Journal of Power Sources, 665, 239079. https://doi.org/10.1016/j.jpowsour.2025.239079
	Prakash, S., **Rajamany, R.**, Varghese, S. M., Rakhi, R. B., & Ismail, Y. A. (2025). Polyaniline-Functionalized Sulfur and Nitrogen Co-Doped rGO: Toward Sustainable, Ultra-Stable Supercapacitors with Superior Energy Density and High Retention Rate. Materials Research Bulletin, 113966. https://doi.org/10.1016/j.materresbull.2025.113966
	Rajamany, R., Prakash, S., & Ismail, Y. A. (2022). Synthesis and characterisation of polyaniline/polyvinyl alcohol composites as supercapacitor electrode materials. Plastics, Rubber and Composites, 51(5), 240-249. https://doi.org/10.1080/14658011.2021.1981090

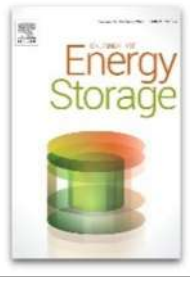	**Roopasri Rajamany**, Sivakrishna Prakash, Y.A. Ismail, Hierarchial polypyrrole derived nitrogen-Doped graphene quantum dots /polypyrrole composites for high energy density supercapacitor applications, Journal of energy storage (under revision)

LIST OF PRESENTATIONS

1. **Paper presentation (poster)** in Frontiers in Chemical Sciences (FCS 2022), International Conference organized by the Department of Chemistry, University of Calicut.

2. **Paper presentation (Poster)** in Frontiers in Chemical Sciences (FCS 2024) National Seminar organized by the Department of Chemistry, University of Calicut (**awarded Best Poster**.)

3. **Paper presentation (Poster)** in Emerging Frontiers in Chemical sciences (EFCS-2024) organized by the Farook College

4. **Paper presentation (Poster)** in Frontiers in Chemical Sciences (FCS 2025) National Seminar organized by the Department of Chemistry, University of Calicut.